Oil & Natural Gas Technology

DOE Award No.: DE-NT0005638

Final Report

October 1, 2008 to May 31, 2011

Remote Sensing and Sea-Truth Measurements of Methane Flux to the Atmosphere (HYFLUX project)

Submitted by:
Texas A&M University - Corpus Christi
6300 Ocean Dr.
Corpus Christi, TX 78412

Principal Author: Ian R. MacDonald

Prepared for:
United States Department of Energy
National Energy Technology Laboratory

Office of Fossil Energy

DISCLAIMER

This report was prepared as an account of work sponsored by an agency of the United States Government. Neither the United States Government nor any agency thereof, nor any of their employees, makes any warranty, express or implied, or assumes any legal liability or responsibility for the accuracy, completeness, or usefulness of any information, apparatus, product, or process disclosed, or represents that its use would not infringe privately owned rights. Reference herein to any specific commercial product, process, or service by trade name, trademark, manufacturer, or otherwise does not necessarily constitute or imply its endorsement, recommendation, or favoring by the United States Government or any agency thereof. The views and opinions of authors expressed herein do not necessarily state or reflect those of the United States Government or any agency thereof.

ABSTRACT

A multi-disciplinary investigation of distribution and magnitude of methane fluxes from seafloor gas hydrate deposits in the Gulf of Mexico was conducted based on results obtained from satellite synthetic aperture radar (SAR) remote sensing and from sampling conducted during a research expedition to three sites where gas hydrate occurs (MC118, GC600, and GC185). Samples of sediments, water, and air were collected from the ship and from an ROV submersible using sediments cores, niskin bottles attached to the ROV and to a rosette, and an automated sea-air interface collector.

The SAR images were used to quantify the magnitude and distribution of natural oil and gas seeps that produced perennial oil slicks on the ocean surface. A total of 176 SAR images were processed using a texture classifying neural network algorithm, which segmented the ocean surface into oil-free and oil-covered water. Geostatistical analysis indicates that there are a total of 1081 seep formations distributed over the entire Gulf of Mexico basin. Oil-covered water comprised an average of 780.0 sq. km (sd 86.03) distributed with an area of 147,370 sq. km. Persistent oil and gas seeps were also detected with SAR sampling on other ocean margins located in the Black Sea, western coast of Africa, and offshore Pakistan.

Analysis of sediment cores from all three sites show profiles of sulfate, sulfide, calcium and alkalinity that indicated anaerobic oxidation of methane with precipitation of authigenic carbonates. Difference among the three sampling sites may reflect the relative magnitude of methane flux.

Methane concentrations in water column samples collected by ROV and rosette deployments from MC118 ranged from ~33,000 nM at the seafloor to ~12 nM in the mixed layer with isolated peaks up to ~13,670 nM coincident with the top of the gas hydrate stability field. Average plume methane, ethane, and propane concentrations in the mixed layer are 7, 630, and 9,540 times saturation, respectively. Based on the contemporaneous wind speeds at this site, contemporary estimates of the diffusive fluxes from the mixed layer to the atmosphere for methane, ethane, and propane are 26.5, 2.10, and 2.78 μmol/m^2d, respectively.

Continuous measurements of air and sea surface concentrations of methane were made to obtain high spatial and temporal resolution of the diffusive net sea-to-air fluxes. The atmospheric methane fluctuated between 1.70 ppm and 2.40 ppm during the entire cruise except for high concentrations (up to 4.01 ppm) sampled during the end of the occupation of GC600 and the transit between GC600 and GC185. Results from interpolations within the survey areas show the daily methane fluxes to the atmosphere at the three sites range from 0.744 to 300 mol d-1.

Considering that the majority of seeps in the GOM are deep (>500 m), elevated CH_4 concentrations in near-surface waters resulting from bubble-mediated CH_4 transport in the water column are expected to be widespread in the Gulf of Mexico.

TABLE OF CONTENTS

Disclaimer ..... **ii**
Abstract ..... **i**
Executive Summary **1**
Background and Geologic Setting 5
Marine Methane Sources and Importance 6
Formation of Seafloor Carbonates and Chemosynthetic Communities at Seeps 7
Stability and Occurrence of Gas Hydrate at Seeps 7
Completion of Proposed Tasks 9
Section 1: Gulf of Mexico Hydrocarbon Seep: Regional Inventory 9
Section 2: Completion of Other Regions Hydrocarbon Seep Inventory 9
Section 3: Completion of Bubble Flux Analysis 9
Section 4: Completion of Water Column Flux Analysis 9
Section 5: Completion of Air-Sea Flux Analysis 9
Section 6: Completion of Sediment Analyses 9
Project Results Dissemination 10
Results **12**
1. Gulf of Mexico Hydrocarbon Seep: Regional Inventory 12
1.1 Satellite data acquisition and processing 12
1.2 Materials and Methods 13
Image data and processing 13
Clustering Methodology 14
1.3 Results 15
SAR image archive processed 15
Abundance and distribution of oil and gas seeps in the Gulf of Mexico 18
Comparison of oily versus non-oily seeps 24
2. Other Regions' Hydrocarbon Seep Inventory 26
2.5 Conclusions 29
3. Bubble Flux Analysis 30
3.1 Bubbles an Bubble Plumes in the Hydrate Zone 30
3.2 Bubble Size 31
3.3 Bubble Processes During Rise 34
Bubble Plume Processes 34
3.4 Numerical Bubble Studies 34
3.5 Next Efforts 39
4. Water Column Flux Analysis 40
4.1 Introduction 40
4.2 Site Description 43
4.3 Methods 45
Water Column Sampling and Analysis 45
Estimation Diffusive Hydrocarbon Fluxes 46
4.4 Results 48
4.5 Summary and Discussion 51

5. Air-Sea Flux Analysis 54
5.1. Introduction 54
5.2 Method 54
Net sea-to-air flux calculation 59
5.3. Results 59
5.4. Discussion 61
Elevated atmospheric methane 61
Impact of small area high concentration hotspots on the regional air-sea flux 66
5.5 Conclusions 69
6. Sediment Analysis 70
6.1 Introduction 70
6.2 Regional Setting 71
6.3 Materials and Methods 72
6.4 Results 73
Pore water analysis 73
Sediment Analysis 80
6.5 Discussion 82
Numerical Modeling 84
6.6 Conclusions 84
References 86
List of Acronyms and Abbreviations 94
Appendices 95
Appendix I: HYFLUX cruise report
Appendix II: Inventory of SAR images analyzed for HYFLUX results
Appendix III: Preliminary report on persistent oil seep and gas hydrates in the Black Sea
Appendix IV: Analytical results of water column samples
Appendix V: Analytical results of air-sea continuous sampling

LIST OF TABLES

Table i.1. Principal investigators and major contributors for HYFLUX project with reference to results sections in the final report. 1

Table 1.1. Summary statistics for inventory of oil-covered water detected in 176 independent SAR image samples of the Gulf of Mexico. Mean and standard deviations were calculated from a bootstrap-sampling of 2000 re-samplings 22

Table 4.1. Estimated contemporary diffusive fluxes of methane, ethane, and propane to the atmosphere at MC 118. 52

Table 5.1: Mean atmospheric methane mixing ratios, seawater methane concentrations, saturation anomalies and net sea-to-air fluxes of methane at the three seep sites (ranges of values in parentheses). . 60

Table 5.2: Diffusive net sea-to-air fluxes of methane from different environments. 60

Table 5.3. Mass fluxes over the survey area using different interpolation gridding methods. The boundaries for the gridded fluxes are shown in Figure 4.6. 65

Table 5.4. The integrated net mass flux of methane from each survey area each day and the total potential mass flux from hotspots at those sites. 68

Table 6.2. Sediment analyses from Gulf of Mexico sites GC 600, GC 185, and MC 118. PC 1, PC3, and PC 4 were collected with a piston corer, GC 8. 80

GRAPHICAL MATERIALS LIST

Figure i.1: The locations of study sites MC118 (900 m depth), GC600 (1200 m depth) and GC185 (also known as Bush Hill, 550 m depth), as well as the track followed by the research ship. 2

Figure 1.1: The locations of study sites MC118 (900 m depth), GC600 (1200 m depth) and GC185 (also known as Bush Hill, 550 m depth), as well as the track followed by the research ship. 12

Figure 1.2: Gridded distribution of satellite SAR coverage among 1135 image collections. Frequency scale indicates the number of times each grid cell was sampled. Grid size is 10 km. Higher sampling frequency reflects collection bias by satellite imaging clients. 16

Figure 1.3: Observation density for the 408 TCNNA processed SAR images selected from the total image archive shown in Figure 1.2. Coastal bays and inlets were not included even when the satellite images provided coverage 17

Figure 1.4: Sampling frequency in TCNNA processed images for the gridded map areas shown in Figure 1.3. The mean samplings per cell was 15.3. Zero samplings were confined to bay and coastal waters where natural seeps do not occur 17

Figure 1.5: Locations of seep formations in the Gulf of Mexico detected by analysis of SAR image data base. These are sites where continuing flux of methane and higher hydrocarbon compounds would support accumulation of gas hydrate at the seafloor. 18

Figure 1.6: Gridded frequency of oil and gas venting in the Gulf of Mexico based on frequency of oil slick origins detected in SAR data. The grid scale is 10 km. 19

Figure 1.7: Average areas of oil covered water gridded to a 10-km scale and normalized to the frequency of observation for each grid cell. 20

Figure 1.8: Average area of oil-covered water for 10-km grid filtered to remove coastal anomalies and isolated events. Vertical and horizontal lines divide the Gulf region into quadrants along 90° west and 25° north, respectively. 21

Figure 1.9: Archive of CTD profiles and bottom water temperature measurements from NODC records for the Gulf of Mexico. A. locations of measurements; B. summary plot for the bottom measurement, truncated for depths 200 m. Compiled by N. Guinasso, Geochemical and Environmental Research Group, Texas A&M University. 22

Figure 1.10: Stability horizons for gas hydrate formed from (methane) (CH_4) (structure I) and mixtures of C_2H_6 (ethane) and C_3H_8 (propane) as calculated by M. Reagen, Lawrence Livermore Lab, University of California, Berkeley. Points show the expected temperature and pressure conditions for the gridded locations of the gas hydrate region (Figure 1.8). 23

Figure 1.11: Oil and gas seeps detected by satellite SAR with TCNNA analysis compared to gas bubble acoustic targets detected by NOAA survey during August 2011. Inset map shows regional area southeast of Mississippi Delta. Labeled features include domes and the blow out site at Macondo Prospect wellhead. Bathymetric swath map shows extend of NOAA survey. Contours at 100, 500, 1000, 1500, 2000, and 2500 m. 24

Figure 2.1: SAR images from West African Margin. Flares mark locations of gas bubble plumes detected by acoustic surveys. 27

Figure 2.2: SAR images processed offshore Pakistan. Upper panel shows regional setting and position of processed images. Lower panel shows TCNNA processed results. 28

Figure 3.1: Schematic showing bubble plume processes. 30

Figure 3.2: Bubble emission size distribution from MC118. 31

Figure 3.3: Volume emission size distribution from MC118 bubble plume 32

Figure 3.4: Relationship between power law exponent, a, and bubble flux, Q, for major bubble plumes. From Leifer [2010]. 32

Figure 3.5: Time and radius dependent bubble size distribution for the MC118 plume 33

Figure 3.6: Vertical velocity of MC118 bubble plume bubbles, clean and dirty rise velocity parameterization in stagnant water, and curve fit. Outliers are also noted on this figure. 33

Figure 3.7: Flowchart of numerical bubble model. Modified from Leifer and Judd [2002]. 35

Figure 3.8: Single bubble simulations for 2500 μm and 5000 μm radius bubbles with and without deep sea effects. (inv = invasion, ev = evasion). 36

Figure 3.9: MC118 bubble plume simulation of methane **A)** content and **B)** dissolution fluxes for no deep sea processes, and **C)** dissolution flux including deep sea processes. 37

Figure 3.10: Plume integrated dissolution rate to the water column absent **A)** no deep sea effects, and **B)** deep sea processes 37

Figure 3.11: A) Plume-integrated bubble gas content with depth for simulation of MC118 bubble including deep sea effects for a range of gases, and **B)** contribution of different bubble sizes to pentane bubble content. 38

Figure 3.12: Plume size and depth dependent dissolution flux for a bubble plume from **A)** 200 m, **B)** 500 m, **C)** 1000 m, and **D)** 1500 m. Depth effects simulated for all depths. 38

Figure 3.13. A) Integrated plume content for a range of release depths and **B)** Dissolution fluxes. 39

Figure 4.1: Location of the MC 118 seep site. 42

Figure 4.2. The Max Rover ROV used to sample immediately adjacent to the bubble plumes at MC 118. Water samples were collected by an array of 14 bottles (7 on each side of the ROV) attached to the chassis. The Niskin bottles were tripped remotely one-by-one from the control room onboard the research vessel. 42

Figure 4.3 A: Bathymetric image of MC 118 (from [Lutken et al., 2006]) showing region of irregular topography to the southwest. **B.** Hydrocast grid collected above a bubble plume emitted from the mound at MC 118. The distance between stations is 50 m, and the cross represents the plume origin. 44

Figure 4.4: Profiles of temperature (green), salinity (blue), and methane concentrations (red) in the upper 120 m of the water column. 47

Figure 4.5. Methane concentration profiles sampled by CTD/hydrocast and ROV. 48

Figure 4.6: Water column $\delta^{13}C$-CH_4 (red) and CH_4 profiles sampled by CTD/hydrocast and ROV 49

Figure 4.7: Profiles of ethane, propane, and n-butane. 50

Figure 5.1: Cruise track (red line) of HYFLUX cruise in July of 2009 (4 July – 19 July, 2009). Colored surface of the map indicates the water depths and land surface elevations. The bathymetric data are from the NOAA National Geophysical Data Center (http://www.ngdc.noaa.gov/mgg/bathymetry/relief.html). White circles denote the locations of the three seep sites; black circles mark the year days (YD) along the cruise track; red stars stand for the ports where the ship departed or arrived. 55

Figure 5.2: (a) Atmospheric mixing ratios (blue) and surface seawater concentrations (red) of methane; the scales for surface seawater methane in ranges of 0 – 30 nmol L^{-1} and 30 – 200 nmol L^{-1} are different. **(b - c)** Atmospheric mixing ratios (blue) and surface seawater concentrations (red) of ethane (b) and propane (c). **(d)** Sea surface salinity (blue) and temperature (red); **(e)** 24 hour averaged wind speeds at 10 m above sea level prior to sampling (blue) and ship speeds along the cruise track (red). **(f)** Saturation anomalies (blue) and net sea-to-air fluxes (red) of methane; different scales for saturation anomalies in ranges of -40 – 2000 % and 2000 – 10000 % and fluxes in ranges of -20 – 100 μmol m^{-2} d^{-1} and 100 - 400 μmol m^{-2} d^{-1}; dash line marks zero saturation anomaly and zero flux. Concentrations of zeros for panels a – c indicate concentrations below the instrument detection limit. Grey shadows mark the time periods over three seep sites. X-axis is the year day of 2009 and the corresponding month/day is labeled in the brackets. 56

Figure 5.3: 24-hour back-trajectories of air masses (dot lines) and locations of oil platforms (black dots) in the northern Gulf of Mexico. Back-trajectories downloaded from the NOAA Air Resources Laboratory (http://www.ready.noaa.gov/ready/open/hysplit4.html) and platform locations are from MMS GOM regional database (http://www.gomr.mms.gov/homepg/pubinfo/repcat/arcinfo/index.html). White circles denote the locations of three seep sites. Red stars stand for the ports where the ship departed or arrived. 61

Figure 5.4: Vertical profiles of density at MC118 (a), GC600 (b) and GC185 (c). Red and blue lines stand for two randomly selected CTD casts from each site. 62

Figure 5.5: Methane concentrations in surface seawater at MC118 (a-b), GC600 (c-d) and GC185 (e-f). Grey rectangles in the lefthand panels indicate the blown-up regions, which are plotted in the righthand panels. Red stars indicate the locations of the seeps. 63

Figure 5.6: Contour plots of methane net sea-to-air fluxes at the three seep sites using natural neighbor. Red stars indicate the locations of the seeps. Black circles stand for the locations of the flux measurements. 64

Figure 5.7: Corrected seawater methane concentration (C_w) as a function of a hotspot concentration and a hotspot size. **(a)** A scenario when the ship crosses a hotspot from a background concentration of 2 nmol L^{-1} at a ship speed of 4 knots (e.g. when ship is doing coarse survey). **(b)** A scenario when the ship crosses a hotspot from a background concentration of 2 nmol L^{-1} at a ship speed of 0.1 knots (e.g. when ship is holding station). **(c) and (d)** are the blown-up plots for (a) and (b). White lines indicate 4 nmol L^{-1} contours. 4 nmol L^{-1} is our defined boundary for an observable hotspot signal. 67

Figure 5.8: Hotspots potentially missed between sampled locations at GC185 as a function of assumed total hotspot area. Probability that a hotspot was missed during the survey (n = 71) (solid line). CH_4 flux from the total integrated hotspot area (dashed line). CH_4 flux from the 50- times the background (i.e. non-hotspot) area at GC185 (dashed-dotted line). 69

Figure 6.1: SO_4^{2-}, HS^-, Alkalinity and Ca^{2+} concentrations for PC 1 at site GC 600..... 74

Figure 6.2: SO_4^{2-}, HS^-, Alkalinity and Ca^{2+} concentrations for PC 3 at site GC 600..... 75

Figure 6.3: SO_4^{2-}, HS^-, Alkalinity and Ca^{2+} concentrations for PC 4 at site GC 185..... 76

Figure 6.4: SO_4^{2-}, HS^-, Alkalinity and Ca^{2+} concentrations for GC 8 at site MC 118. 78

Figure 6.5: SO_4^{2-}, HS^-, Alkalinity and Ca^{2+} concentrations for RC 8 at site MC 118. 79

Figure 6.6: Percent carbonate, bulk sedimentary carbonate $\partial^{13}C$, and percent authigenic carbonate by weight calculated from simple mass balance plotted versus depth. See text for discussion. 81

Figure 6.7: SO_4^{2-} and DIC concentrations for PC 1 at site GC 600..... 84

EXECUTIVE SUMMARY

Rapid flux of hydrocarbons through seafloor sediments creates conditions under which shallow deposits of gas hydrate can form at or near bottom waters. These deposits probably represent a small fraction of the global reservoir of gas hydrate, but due to their exposed setting, seafloor gas hydrates are subject to varying ocean conditions. The Gulf of Mexico (GOM) is a region in which many such shallow gas hydrates are known to occur. A working hypothesis is that these circumstances could produce significant fluxes of methane into the water column and potentially to the atmosphere. Changes in bottom water conditions due to climate trends might amplify this process. This investigation was undertaken to determine the distribution, abundance, and methane fluxes from the shallow gas hydrate reservoir in the Gulf of Mexico and other regions of the world.

The full name of this project reflects the multidisciplinary character of the total effort: *"Remote sensing and sea-truth measurements of methane flux to the atmosphere from near-surface gas hydrates in continental margins."* For convenience, the project was dubbed HYFLUX (for HYdrate FLUX) and will be so named throughout this report. The project was awarded to Texas A&M University - Corpus Christi (TAMUCC) in June 2008 and was completed in September 2011. Principal investigators (Table i.1) included researchers from the following institutions: Florida State University (FSU), Scripps Institute for Oceanography (SIO), Texas A&M University (TAMU), and University of California Santa Barbara (UCSB). The University of Southern Mississippi provided technical support during the research cruise. The research ship was chartered from TDI Inc. and the remote operated vehicle (ROV) was provided by Oceaneering Inc.

Table i.1. *Principal investigators and major contributors for HYFLUX project with reference to results sections in the final report.*

Project investigator email address	Result Section	Institution and contact	Tasks and work product
Asper, Vernon vernon.asper@usm.edu	App. I	University of Southern Mississippi	Cruise logistics & *In-situ* sonar
Chanton, Jeffery jchanton@fsu.edu	4	Florida State University	Water column methane flux
Garcia-Pineda, Oscar oscar.oggp@gmail.com	1, 2	Florida State University	Satellite remote sensing
Hu, Lei lhu@ocean.tamu.edu	5	Texas A&M University-College Station	Air-sea methane flux
Kastner, Miriam mkastner@ucsd.edu	4	Scripps Oceanographic Institute	Water column methane flux
Leifer, Ira ira.leifer@bubbleology.com	3	University of California, Santa Barbara	Bubble flux quantification
MacDonald, Ian imacdonald@fsu.edu	1	Florida State University	Project leader, Remote sensing
Naehr, Thomas thomas.naehr@tamucc.edu	6	Texas A&M University-Corpus Christi	Sediment geochemistry
Solomon, Evan esolomn@u.washington.edu	4	University of Washington	Water column methane flux
Yvon-Lewis, Shari syvon-lewis@ocean.tamu.edu	5	Texas A&M University-College Station	Air-Sea methane flux

Figure i.1: *The locations of study sites MC118 (900 m depth), GC600 (1200 m depth) and GC185 (also known as Bush Hill, 550 m depth), as well as the track followed by the research ship.*

Major activities included completion of research cruise using a ship and ROV to collect samples from the seafloor, water column and surface ocean at three known hydrocarbon seeps in the Gulf of Mexico. The research cruise was completed in June-July 2009. *Figure i.1* shows the locations of study sites MC118 (900 m depth), GC600 (1200 m depth) and GC185 (also known as Bush Hill, 550 m depth), as well as the track followed by the research ship. A detailed narrative of the cruise activities and a complete inventory of the sampling stations is provided in ***Appendix I***. The results obtained from sample collection during the research cruise comprise a large fraction of the work described in this report. In a separate effort, project participants compiled and analyzed a large collection of satellite image data from the Gulf of Mexico and other regions of the world. The purpose of this effort was to compile inventories of natural oil and gas seeps that host gas hydrate at deposits near the seafloor.

The HYFLUX project confirmed the widespread occurrence of gas hydrate across the Gulf of Mexico basin and provided evidence to support its significant impact on seafloor geology and geochemistry. The stability of gas hydrate in the Gulf of Mexico may be significantly enhanced, even under conditions of climate change, if structure II hydrate is as predominant as other research would suggest. Transfer of methane to the water column well into the mixed layer was clearly demonstrated. However, extreme flux rates (1000s μm m^{-2} d^{-1}), which were suggested by some previous studies, were not replicated in these investigations. Sea surface to air fluxes were relative modest for the major part of the sea surface observations. Water column measurements were at least superficially consistent with limited fluxes to the atmosphere. However, dynamics of the bubble plumes and the structure of methane concentrations at the thermocline suggest that larger fluxes could occur.

Continuous measurements of air and sea surface concentrations of methane were made over the three sampling sites to obtain high spatial and temporal resolution of the diffusive net sea-to-air fluxes by the investigators from TAMU. The atmospheric methane fluctuated between 1.70 ppm and 2.40 ppm during the entire cruise except for high concentrations (up to 4.01 ppm) sampled during the end of the occupation

of GC600 and the transit between GC600 and GC185. In conjunction with air-mass back trajectory analysis, these high concentrations are likely from a localized methane source to the atmosphere. Methane concentrations in surface seawater and methane net sea-to-air fluxes show high temporal and spatial variability within and between sites. The presence of ethane and propane in the surface seawater indicates a thermogenic source in the plume areas, suggesting the surface methane could be at least partly attributable to transport from the deepwater hydrocarbon seeps. Results from interpolations within the survey areas show the daily methane fluxes to the atmosphere at the three sites range from 0.744 to 300 mol d-1. Extrapolating the highest daily sea-to-air flux of methane to other deepwater seeps in the northern Gulf of Mexico suggests that the net diffusive sea-to-air flux from deepwater hydrocarbon seeps in this region is not a significant source to the atmospheric methane.

Methane flux from shallow gas hydrate deposits takes the form of bubble plumes released from discrete vents and fissures where gas hydrate is exposed to seawater. Investigators at UCSB made careful measurement of bubble behavior using high definition video and sonar to track rising bubbles with the ROV. Theoretical models developed from these measurements indicate that bubble size and degree of contamination strongly influence bubble behavior and fate. The three sampling sites investigated, as well as the majority of the known hydrocarbon seeps in the Gulf of Mexico and those detected with satellite remote sensing (see below), release significant quantities of liquid hydrocarbon with the gas bubbles.

This oil coats the bubble interior walls and is carries upward by the buoyant plume. Gas in contact with seawater may also form transient layers of gas hydrate. The combination of gas hydrate and oil coatings has effect of increasing the travel distance prior to dissolution. Upwelling effects generated by the rising bubbles will have the further effect of transporting relative methane-rich water upward in the water column and potentially enhancing flux to the atmosphere in localized areas.

Dissolved hydrocarbon concentrations and $\delta^{13}C\text{-}CH_4$ were measured in samples obtained with an ROV immediately adjacent to bubble plumes at the three sampling sites under the direction of the investigators from SIO. Water samples were also collected from a dense grid of CTD and hydrocasts above the plume targeting the thermocline and mixed layer. Methane concentrations range from ~33,000 nM at the seafloor to ~12 nM in the mixed layer with isolated peaks up to ~13,670 nM coincident with the top of the gas hydrate stability field. Water column ethane, propane, and n-butane profiles show the same trends. Methane/(propane + ethane) ratios and $\delta^{13}C\text{-}CH_4$ values suggest a mixture between a thermogenic and a biogenic source for the methane. Average plume methane, ethane, and propane concentrations in the mixed layer are 7, 630, and 9,540 times saturation, respectively. Based on the contemporaneous wind speeds at this site, contemporary estimates of the diffusive fluxes from the mixed layer to the atmosphere for methane, ethane, and propane are 26.5, 2.10, and 2.78 $\mu mol/m^2d$, respectively. These results highlight the importance of hydrate skins and bubble-driven processes for enhancing hydrocarbon transfer through the water column, and show that methane and heavier hydrocarbons can be deposited in the mixed layer from a ~900-m seep. Considering that the majority of seeps in the Gulf of Mexico are deep (>500 m), elevated CH_4 concentrations in near-surface waters resulting from bubble-mediated CH_4 transport in the water column are expected to be widespread in the Gulf of Mexico.

Sediment samples obtained by coring from the research ship showed evidence for anaerobic oxidation of methane at the three study sites. Pore water gradients of dissolved sulfate, sulfide, alkalinity, and calcium were also indicative of active hydrocarbon seepage. Among the sites studied, GC600 showed the most active upward flux of hydrocarbons, leading to a complete depletion of pore water sulfate below 20 cm below seafloor (cmbsf). Sulfide, alkalinity, DIC, and calcium gradients corroborate these findings and are indicative of authigenic carbonate precipitation in shallow subsurface sediments. Pore water data from site MC118 also showed evidence for active hydrocarbon seepage, although pore water gradients indicate lower methane flux rates, which lead to sulfate reduction and the development of a SMI at roughly 40 cmbsf. Finally, site GC185 revealed pore water gradients typical of background sediments in the area,

demonstration the small lateral extent of active hydrocarbon seepage. Geochemical profiles from site GC600 indicate that microbially-driven anaerobic oxidation of methane is active now. Microbial production rates of dissolved inorganic carbon (DIC) are controlled by the diffusion of sulfate to the zone of anaerobic oxidation of methane) AOM and the overall stochiometry of the anaerobic oxidation of methane process. Modeled rates of DIC production (~10^{-14} mol DIC/cm^3 s) are comparable to published rates from field studies and laboratory incubations. Anaerobic oxidation of methane will produce DIC pore water gradients that will lead to subsurface carbon sequestration through authigenic carbonate precipitation in geologically short time intervals of several thousand years.

Effervescent hydrocarbons that rise naturally from hydrocarbon seeps in the Gulf of Mexico reach the ocean surface after minimal lateral transport. This oil forms thin (~0.1 µm) layers that enhance specular reflectivity and have been widely used to quantify the abundance and distribution of natural seeps using synthetic aperture radar (SAR). SAR data allow direct comparison of the areas of the ocean surface covered by oil from natural sources and the discharge. After reviewing more than 1,000 SAR images, the investigators at FSU used a texture classifying neural network algorithm to quantify the areas of naturally occurring oil-covered water in 176 SAR image collections from the Gulf of Mexico obtained between May 1997 and November 2007. Analysis removed pollution events and transient oceanographic effects by including only the reflectance anomalies that that recurred in the same locality over multiple images. The analysis identified a total of 1,081 geologic formations from which oil and gas was observed to emanate in multiple images.

Validity of the method for predicting the location of shallow gas hydrate deposits was tested during the research effort at the GC 600 site. This locality was known from satellite observations and preliminary exploration with submarine ALVIN during a previous research project, which had targeted the seismic features thought to be associated with seepage. However, exposed gas hydrate and hydrocarbon venting had not been observed. This project targeted the seafloor location indicated by the time-averaged position of surface oil slicks, which was approximately 1 km south from the ALVIN dive sites. The ROV quickly located highly active hydrocarbon vents and very large exposures of gas hydrate.

For a regional comparison of where seeps and gas hydrate is likely to occur, the Gulf of Mexico was divided into four quadrates along 90° west longitude, and 25° north latitude. The largest number of seep formations was observed in the northwest quadrate at 754, followed by the northeast quadrate at 125, the southwest quadrate at 59 and the southeast quadrate at 1. The output of these formations could be estimated by measuring the size of the floating oil layers discharged. Confidence intervals on these estimates could be obtained by bootstrap statistical techniques. Floating oil layers were observed in only a fraction of the total Gulf area amounting to 1.22×10^5 km^2. In a bootstrap sample of 2000 replications, the combined average area of these layers was 7.80×10^2 km^2 (sd 86.03). The northwest quadrate received on average 68.0% of this total (5.30×10^2 km^2, sd 69.67). The northeast quadrate, where the BP discharge occurred, received on average 7% of the total natural seepage in the Gulf of Mexico (5.24×10^2 km^2, sd 21.99). The southwest quadrate received an average of 25% of the total natural discharge (18.9×10^2 km^2, sd 46.03), while the southeast quadrate received less than 1% of naturally discharged oil.

The distribution of seeps and presumed gas hydrate deposits predicts the frequency of occurrence for gas hydrate over the range of depths in the Gulf of Mexico. Depth (pressure) and water temperature will control the stability of gas hydrate and influence the crystal structures of the material. Structure I gas hydrate is comprised of methane alone and has a more restricted range of pressure and temperature than does structure II hydrate, which comprises methane mixed with higher hydrocarbon gases such as propane. The analysis suggests that above 1500 m, structure II hydrate will predominate in inverse proportion to depth. Below 1500 m, bottom water temperatures are very stable in the Gulf of Mexico and structure I hydrate may be the dominant form. The result of this distribution would enhance the overall stability of the gas hydrate reservoir in the Gulf.

Satellite indicators of natural seeps that would host gas hydrates were found in the eastern and northern Black Sea, along the margin of Pakistan, and off the coast of Congo. Results shared by collaboration with investigators at the MARUM group, University of Bremen, Germany made it possible to confirm regional occurrence of gas hydrate in all three of these areas. Samples of gas hydrate were obtained from the seafloor in direct association with the seeps detected by satellite in the Black Sea. Off Pakistan and Congo, gas hydrates were obtained in the general region, but sampling has not yet been completed in the areas were seeps were detected in the satellite images.

The complete dataset of satellite observations was compiled in a web-accessible form (*www.sarsea.org*) and measures were implemented to link this line of evidence with the geophysical records available through Department of Interior compilations of geophysical data gathered by the energy industry. The satellite tools for detecting floating oil developed during the project as well as the data on historic levels of natural oil seepage are proving invaluable in assessing the impact of the BP oil blowout of April-July 2010.

Background and Geologic Setting

The northern Gulf of Mexico is a prolific hydrocarbon province where rapid migration of oil, gases, and brines from deep subsurface petroleum reservoirs occurs through faults generated by salt tectonics [*H. H. Roberts and Carney*, 1997]. In the Gulf of Mexico, the focused expulsion of hydrocarbons is manifested at the seafloor by gas vents, gas hydrates, oil seeps, chemosynthetic biological communities, and mud volcanoes [*De Beukelaer et al.*, 2003]. Hydrocarbon gas is emitted as bubble plumes from focused gas vents within larger hydrocarbon seep sites. The bubble plumes are visible throughout the water column on acoustic profiles and echo-sounder records [*De Beukelaer et al.*, 2003; *I. R. MacDonald et al.*, 1994; *H. H. Roberts and Carney*, 1997], and the bubbles are commonly coated with a thin layer of oil [*I. Leifer and MacDonald*, 2003]. Upon reaching the sea surface, this oil forms targets that are easily detected by satellite remote sensing methods such as SAR. SAR imagery shows ~350 perennial oil slicks associated with hydrocarbon plumes offshore Louisiana [*De Beukelaer et al.*, 2003; *I.R. MacDonald et al.*, 2005; *I. R. MacDonald et al.*, 2002], and ~100 slicks in the southern Gulf of Mexico [*I.R. MacDonald et al.*, 2005; *I.R. MacDonald et al.*, 2004]. These are minimum estimates that exclude the non-oily plumes in the Gulf of Mexico, which may be equally as abundant as the oily ones [*De Beukelaer et al.*, 2003; *I. Leifer and MacDonald*, 2003]. Recent seismic studies and ground-truth observations estimate that there may be 5,000 geologically active seep sites in the northern Gulf of Mexico [*Frye*, 2008]. However, the present day release rates from these sites have not been well-constrained and cannot be confirmed from seismic evidence alone.

Research during the late 1990s and the early 2000s examined the upper continental slope (depths < 1000 m) of the Gulf of Mexico and demonstrated that chemosynthetic communities occupy discrete regions affected by persistent and protracted flux of hydrocarbons. Ground truth operations reported by [*De Beukelaer et al.*, 2003; *Frye*, 2008; *I. R. MacDonald*, 1997; *A.V. Milkov and Sassen*, 2001; *H. H. Roberts and Carney*, 1997] demonstrated that active oil seeps universally include shallow deposits of gas hydrate. In many ways the Gulf of Mexico has also served as a case study for understanding gas hydrate deposits and hydrocarbon seeps, which have more recently been investigated on other continental margins. Gas hydrates have similarly been reported from active oil seeps in the South China Sea [*Chen et al.*, 2006; *Huang et al.*, 2006], the west coast of Africa [*Ben-Avraham et al.*, 2002; *Gay et al.*, 2006; *Sahling et al.*, 2008], and the Black Sea [*Bohrmann et al.*, 2003]. We argue that conditions or rapid, focused flux of oil and gas that prevail at hydrocarbon seeps will necessarily produce shallow deposits of gas hydrate that are metastable under prevailing oceanographic conditions.

The findings from the northern Gulf of Mexico on the upper slope were extended and replicated by multi-disciplinary in the southern Gulf of Mexico, which found gas hydrate and carbonates in a 3200 m setting

that included extensive seafloor asphalt deposits and seep-generated carbonates [*Ding et al.*, 2010a; *Stephan A. Klapp et al.*, 2010; *I.R. MacDonald et al.*, 2004; *T. H. Naehr et al.*, 2009].

Marine Methane Sources and Importance

Submarine gas hydrate represents a large pool of greenhouse gas that may interact with the atmosphere over geologic time to affect climate cycles. In the near term, the magnitude of methane reaching the atmosphere from gas hydrate on continental margins is poorly known because 1) gas hydrate is exposed to metastable oceanic conditions in shallow, dispersed deposits that are poorly imaged by standard geophysical techniques, and 2) the consumption of methane in marine sediments and in the water column is subject to uncertainty. This project will address this problem with a combined effort of satellite remote sensing and data collection at proven sites in the Gulf of Mexico where gas hydrate releases gas to the water column.

Methane is an important trace gas in the atmosphere playing a significant role in greenhouse warming and ozone destruction. The current global CH_4 source strength is relatively well constrained at ~582 Tg CH_4 yr^{-1} (1 Tg = 10^{12} g), but the methane flux from individual sources is not [*K L Denman et al.*, 2007]. The current budget contains a fossil (^{14}C-depleted) CH_4 flux from fossil fuel-related anthropogenic emissions such as coal mining and crude oil exploitation of ~100 Tg CH_4 yr^{-1} [*K L Denman et al.*, 2007]. This flux is based on the ^{14}C-dead methane in the atmosphere, thus is a top-down estimate. A significant fraction of natural methane from geologic sources is also ^{14}C-depleted, yet is not included in the atmospheric methane budget because the methane fluxes from these sources remain poorly quantified. From a geologic perspective, however, the flux from these sources such as marine gas hydrates and mud volcanoes, terrestrial methane seeps, and geothermal/volcanic emissions are likely to comprise a significant fraction of the fossil methane flux to the atmosphere. Of these geologic sources, the flux of methane from marine hydrocarbon seeps and mud volcanoes, probably the most significant sources, is the least constrained because they are difficult to detect. Thus, the distribution of these marine sources is not well known and they are difficult to sample with traditional techniques. A significant fraction of the methane that migrates from subbottom reservoirs to the water column is sequestered in shallow deposits of gas hydrate that can interact with the water column at the margin of the hydrate stability regime [*I.R. MacDonald et al.*, 2005; *I. R. MacDonald et al.*, 1994; *A.V. Milkov and Sassen*, 2001; *A.V. Milkov et al.*, 2000].

Recent literature reviews have indicated that the CH_4 flux from marine seeps could be as high as 20-40 Tg CH_4 yr^{-1}, which would amount to ~1/3 of the current estimated fossil fuel-related anthropogenic emission to the atmosphere [*A. G. Judd et al.*, 2002; *Kvenvolden and Rogers*, 2005]. These estimates, however, are mainly based on approximations of seafloor CH_4 fluxes and water column acoustic surveys, thus are not constrained by direct water column sampling and flux determinations from the oceanic mixed layer to the atmosphere. These estimates also do not account for possible changes in the stability of shallow gas hydrate due to increased water temperatures [*Kennett and Cannariato*, 2000] or cascading pressure changes resulting from slope failure and turbidity flow [*Dillon and Max*, 2000a].

There are several processes that consume methane as it ascends from seafloor seeps to the sea surface. The most important of these CH_4 loss processes are anaerobic oxidation of methane in the sediment column, bubble dissolution, aerobic CH_4 oxidation in the water column, and gas transfer across the bubble-water interface with N_2 and O_2 during bubble ascent through the water column. Most recent studies focused on direct plume sampling in the water column have occurred at water depths <100 m, and in particular have concentrated on the prolific seeps at Coal Oil Point, California. These studies have indicated that the bubble plumes at Coal Oil Point retain a significant fraction of the CH_4 during water column transit and that they emit a considerable amount of methane locally [*Hornafius et al.*, 1999; *Mau et al.*, 2007]. The aerial extent of the Coal Oil Point seeps, however, is small at ~280 km^2, thus, with ~1.3

Gg CH_4 yr^{-1}, these seeps do not contribute a significant amount of methane to the atmosphere [*Hornafius et al.*, 1999; *Mau et al.*, 2007]. There have been only a few studies quantifying CH_4 fluxes from deepwater (>200 m) hydrocarbon seeps [*Kessler et al.*, 2006; *Reeburgh et al.*, 1991; *Schmale et al.*, 2005; *Valentine et al.*, 2001; *Yoshida et al.*, 2004], which cover a much larger area than the shallow water seeps. These preliminary studies have indicated that CH_4 in bubble plumes emanating from water depths greater than 200 m is entirely consumed before reaching the mixed layer as a result of bubble dissolution, aerobic methane oxidation, and gas exchange, thus are not a significant source of methane to the atmosphere [*Greinert et al.*, 2006; *McGinnis et al.*, 2006; *Valentine et al.*, 2001]. However, these studies that are limited in spatial extent, relied on inaccurate sampling techniques that typically fail in sampling the bubble plumes, but sample the background concentrations instead, thus the question of whether marine hydrocarbon plumes represent a significant source of CH_4 to the atmosphere that should be included in the global atmospheric methane budget remains unresolved.

Formation of Seafloor Carbonates and Chemosynthetic Communities at Seeps

Natural oil and gas seeps are a localized phenomenon that occurs in numerous, wide-spread settings on the Gulf of Mexico slope. The flux of reduced, organic carbon through seafloor sediments causes profound alteration of the benthic environment, with the result that substantial fractions of the carbon is mineralized in place. Free-living , microbial fauna oxidize the hydrocarbons in coupled or sequential heterotrophic and chemoautotrophic modes that are related to the *anaerobic oxidation of methane* (AOM) [*A. Boetius et al.*, 2000] and of higher hydrocarbons [*Joye et al.*, 2004]. Alteration of pore fluid alkalinity resulting from this activity leads to authigenic precipitation of carbonate and carbonate cements [*Thomas H. Naehr et al.*, 2007b], which comprise a wide range of mineralogical compositions in Gulf of Mexico sediments [*Harry H. Roberts et al.*, 2010]. Endosymbiotic bacteria allow diverse metazoan species to achieve substantial biomass and to support an associated fauna of fish and invertebrates [*Lessard-Pilon et al.*, 2010]. The chemosynthetic host species tend to be prominent and to function as ecosystem engineers by altering the environment in ways that produce habitat for characteristic communities [*Bergquist et al.*, 2003; *Cordes et al.*, 2007]: bush-like aggregations of siboglinid tube worms stand above the bottom with a relief of 1 m or more and can extend for tens of meters; mussels beds (*Bathymodilous* sp.) often comprise thousands of individuals in contiguous assemblages covering tens of square meters, and mats of bacteria (*Beggiatoa*) create large areas of distinctive patterning in the seafloor.

Stability and Occurrence of Gas Hydrate at Seeps

Gas hydrate forms in marine sediments at active oil and gas seeps where the water content of pore volumes and the flux of free gas allows the accumulation of methane-saturated water under appropriate conditions of temperature and salinity [*Buffett and Zatsepina*, 2000; *Dillon and Max*, 2000b; *A. V. Egorov et al.*, 1999]. These conditions prevail across large areas of the ocean margins at depths of 100 to 300 m subbottom. Gas hydrate and a trapped layer of free gas have been widely detected as bottom simulating reflectors (BSR), i.e. regions of high acoustic contrast that track the ocean bottom and cut across geologic strata. This gives rise to the hypothesis that the global gas hydrate methane reservoir is large [*Ginsburg*, 1998; *Kvenvolden*, 2000], although some authors have suggested that initial estimates of the global magnitude were too high [*A. V. Milkov*, 2000; *Alexei V. Milkov*, 2004]. Because the continued stability of gas hydrate depends on submarine temperature and pressure, changes in these variables could theoretically destabilize gas hydrate over large regions, with the potential to release large magnitudes of methane and increase greenhouse climate forcing [*Kvenvolden*, 2000]. Episodes of large scale destabilization of gas hydrate distinct periods of Earth history including the "blast in the past" Eocene thermal maximum [*Dickens et al.*, 1995] and Quarternary glacial interstadials resulting from the "clathrate-gun hypothesis" [*Kennett and Cannariato*, 2000].

Whether the Gulf of Mexico would be subject to similar destabilization events depends on the magnitude of the gas hydrate reservoir in the basin and its mode of occurrence. Some authors have noted the high heat flow and the frequent perforation of the sealing strata in the Gulf of Mexico and have concluded that the subbottom occurrence of gas hydrate in BSR-style deposits is limited in this region compared to other margins [*A. V. Milkov and Sassen*, 2000]. Geophysical evidence suggests that this view may be too conservative and that there are substantial resources, albeit in more complex settings [*Frye*, 2008]. One facet of this issue is how active gas seepage through the seafloor causes gas hydrate to form not in zones buried under 100s of meters of sediment, but at the sediment water interface. This phenomenon was first observed in piston cores collected for surface geochemical exploration in the Gulf of Mexico [*Brooks et al.*, 1984] and has subsequently been observed in diverse global settings including the Black Sea [*Bohrmann et al.*, 2003], the Congo margin [*Kasten et al.*, 2003], and the Pakistan margin [*Delisle*, 2004]. In this type of setting, gas hydrate is subject to much more variable temperature conditions than it is emplaced in BSR deposits [*I. R. MacDonald et al.*, 1994] and preliminary evidence suggested that in the upper slope depths (~500m), where many of the Gulf of Mexico hydrates have been documented, brief excursions in bottom water temperature could induce decomposition of shallow gas hydrate deposits. Subsequent work showed that due to the low thermal conductivity of gas hydrate, most gas hydrate deposits at intermediate depths are effectively insulated against decomposition due to transient changes in water temperature [*I.R. MacDonald et al.*, 2005]. Therefore, large-scale destabilization of shallow gas hydrate deposits in the would require a persistent change in bottom water temperatures like those that have been posited for glacial interstadials [*Kennett and Cannariato*, 2000]. Because shallow gas hydrate deposits are prevalent in the Gulf of Mexico, this region might be subject to climate induced destabilization of gas hydrate.

However, the composition of Gulf of Mexico gas hydrate deposits must be considered in evaluating this possibility. While many of the gas hydrate deposits that have been investigated world-wide are formed from methane in with water molecules arranged in cubic lattice forms, called structure one (sI), thermogenic gas reservoirs in the Gulf of Mexico oil province provide significant sources of ethane and propane. These gases allow formation of structure two (sII) gas hydrate, which has a significantly larger stability horizon with respect to temperature and pressure [*Sloan.*, 1998]. The effect of ethane and propane availability upon gas hydrate structures has been investigated at deep and shallow sites in the Gulf of Mexico [*Stephan A. Klapp et al.*, 2010; *S. A. Klapp et al.*, 2010]. The results showed that in the deeper site (3400 m) gas hydrate structures were exclusively sI, while in a shallow (540 m) site, the gas hydrate was exclusively sII.

This background indicates that the susceptibility of the entire gas hydrate pool in the Gulf of Mexico to climate-induced destabilization will depend on the distribution of shallow deposits with respect to depth and to availability of higher hydrocarbon gases (ethane and propane) that would form sII gas hydrate. Furthermore, when gas is released from the seafloor, either by persistent background seepage or by destabilization of gas hydrate deposits, transfer to the atmosphere will depend on dynamic processes in the water column as gas bubbles rise and dissolve before reaching the sea surface. This multidisciplinary investigation used satellite remote sensing to inventory the sites of persistent natural oil and gas seeps, where thermogenic ethane and propane would invariably be a component of the discharging gas. The dissolution of gas released from typical seeps was investigated during a field study at three natural seeps representing moderate (1200 m), intermediate (900 m), and shallow (540 m) depths of occurrence in the northern Gulf of Mexico. The project investigators collected sediment cores to measure the rates of carbonate precipitation in the sediments due to microbial consumption of methane. They also used an ROV to follow rising bubbles of gas from the seafloor to the near the surface, observing the behavior of bubbles and collecting discrete water samples along this interval. Finally, they made high-frequency collections of water and air over the seep sites to measure directly the flux of methane to the atmosphere.

Completion of Proposed Tasks

The tasks enumerated below were proposed for the DE-NT0005638 Phase 2 Budget Period 2 that concludes with this report. The following summary outlines the progress toward completion for each of these tasks. The orginal numbering of these tasks from the project management is indicated in *italics*. Results sections or appendices in this report that fulfill these tasks are listed in ***bold italics***.

Section 1: Gulf of Mexico Hydrocarbon Seep: Regional Inventory

The goal of this task (*Management Plan Task 5*) is to complete a regional inventory of active CH_4 sources in the Gulf of Mexico basin that are associated with gas hydrate. This will be accomplished by geo-spatial analysis of satellite synthetic aperture radar (SAR) images. Goal of analysis was to detect persistent oil slicks on ocean surface associated with natural seeps, CH_4 releases, and gas hydrate. Gulf of Mexico regional results are detailed in datasets available at the *www.sarsea.org* website. This task was completed as described in ***Appendix II*.**

Section 2: Completion of Other Regions Hydrocarbon Seep Inventory

The goal of this task (*Management Plan Task 13*) is to complete the remote sensing inventory of CH_4 flux on continental margins from other global regions. Most detailed results were obtained in the Black Sea as reported in ***Appendix III***. Results from other regions seep surveys are detailed in datasets available in the *www.sarsea.org* website.

Section 3: Completion of Bubble Flux Analysis

The goal of this task (*Management Plan Task 14*) is to evaluate the visual and sonar records of bubble activity to constrain the flux of CH_4 due to this process. Dr. Ira Leifer at UCSB was the investigator for this task. The sonar sensor deployed on the HYFLUX research cruise did not function as planned and produced no data. The visual analysis of bubble flux

Section 4: Completion of Water Column Flux Analysis

The goal of this task (*Management Plan Task 16*) is to model CH_4 flux through the water column based on the water samples and other information. A provisional version of these results was compiled using analyses completed at sea (see ***Section 4***). A more detailed presentation will be given a manuscript in preparation.

The goal of this task (*Management Plan Task 15*) is to analyze the water samples for CH_4 concentration. Dr. Miriam Kastner at Scripps was the investigator for this task, assisted by Dr. Evan Solomon at University of Washington. These analyses included analysis of ethane, propane, and butane concentrations. The task has been completed for samples collected at the MC118 study site and are compiled in ***Appendix IV***.

Section 5: Completion of Air-Sea Flux Analysis

The goal of this task (*Management Plan Task 17*) was to control for flux from the water into the atmosphere by analyzing CH_4 concentrations in synoptic sea-surface water samples and samples of ambient air. Results are described in ***Section 5***.

Section 6: Completion of Sediment Analyses

The goal of this task (*Management Plan Task 18*) was analysis of the pore fluids and carbonates from the sediment samples and description of the sediment cores. These analyses have been completed as detailed in ***Section 6***.

The goal of this task (*Management Plan Task 19*) was to model the effect of anaerobic oxidation of methane on the flux of gas from gas hydrate deposits to the water column and to examine how carbon derived from AOM is sequestered in seafloor carbonate deposits. As of the present, this task remains in progress.

Project Results Dissemination

Project results (*Management Plan Task 20*) have been detailed in a final report to the government which describes the final disposition of each task outlined above. In addition, project investigators have made presentations to national and international scientific associations to describe and discuss their findings. Final results will be published as peer-reviewed scientific that acknowledge the support of DOE-NETL.

Published Abstracts

MacDonald, I. R., V. Asper, O. P. Garcia, M. Kastner, I. Leifer, T. Naehr, E. Solomon, S. Yvon-Lewis and B. Zimmer, 2008. HyFlux - Part I: Regional Modeling of Methane Flux From Near-Seafloor Gas Hydrate Deposits on Continental Margins. Eos Trans. AGU 89(53): OS33A-1322.

Naehr, T. H., V. L. Asper, O. Garcia, M. Kastner, I. Leifer, I. R. MacDonald, E. A. Solomon, S. Yvon-Lewis and B. Zimmer, 2008. HyFlux - Part II: Subsurface sequestration of methane-derived carbon in gas-hydrate- bearing marine sediments. Eos Trans. AGU, 89(53), Fall Meet. Suppl., 89(53): OS33A-1323.

Garcia, O., I. R. MacDonald, B. Zimmer, W. Shedd and M. Frye, 2009. Satellite SAR inventory of Gulf of Mexico oil seeps and shallow gas hydrates. Geophysical Research Abstracts 11: EGU2009-11633.

Garcia-Pineda, O.G., MacDonald, I.R., Shedd, W., and Zimmer, B., 2009, HYFLUX: Satellite Exploration of Natural Hydrocarbon Seeps and Discovery of a Methane Hydrate Mound at GC600: Eos Trans. AGU, 90(52), p. OS31A-1185 Poster.

Hu, L., Yvon-Lewis, S.A., Kessler, J.D., and MacDonald, I., 2009, Air-sea flux of methane from selected marine hydrate/seep sites in the northern Gulf of Mexico during HYFLUX: Eos Trans. AGU, 90(52), p. OS23B-04.

MacDonald, I.R., Garcia-Pineda, O.G., Chanton, J., Kastner, M., Solomon, E.A., Leifer, I., Naehr, T.H., Yvon-Lewis, S.A., and Kessler, J.D., 2009, HYFLUX: Satellite Inventory and Sea-Truth for Gulf of Mexico Gas Hydrate System: Eos Trans. AGU, 90(52), p. OS23B-03.

Shapiro, R.A., Naehr, T.H., MacDonald, I., Kastner, M., Robertson, G., and Solomon, E.A., 2009, Pore Water Data From Three Gas Hydrate Sites in the Gulf of Mexico: First Results From the HyFlux Project: Eos Trans. AGU, 90(52), p. OS31A-1186 Poster.

Solomon, E.A., Kastner, M., and Leifer, I., 2009, Ethane and propane emissions to the ocean and atmosphere from 550-1200 m seeps in the Gulf of Mexico: Eos Trans. AGU, 90(52), p. OS31A-1182 Poster.

Peer-reviewed Publications

Garcia-Pineda, O., I. R. MacDonald, et al. (2010). Remote sensing evaluation of geophysical anomaly sites in the outer continental slope, northern Gulf of Mexico. Deep-sea Research Part II 57(21-23): 1859-1869.

Solomon, E. A., M. Kastner, G. Robertson, I. Leifer, I. MacDonald, and J. Chanton (2011), Sea-air hydrocarbon fluxes associated with a 900-m seafloor gas hydrate deposit in the Gulf of Mexico, Proceedings of the 7th International Conference on Gas Hydrates, Edinburgh, Scotland, U.K.(17-21 July 2011).

Hu, L., S. A. Yvon-Lewis, J. D. Kessler, and I. R. MacDonald (2012), Methane fluxes to the atmosphere from deepwater hydrocarbon seeps in the northern Gulf of Mexico, J. Geophys. Res., 117(C1), C01009.

Manuscripts In-preparation

Title: **Methane emissions from 550-1200 m seeps in the Gulf of Mexico**
Authorship: E. Solomon, M. Kastner, I. Leifer, I. MacDonald, J. Chanton
For submission to: *Science*

Title: **Natural oil and gas sources in the Gulf of Mexico: Quantification by satellite remote sensing**
Authorship: I. R. MacDonald O. Garcia-Pineda, and F. Huffer
For submission to: *Nature Geoscience*

Title: **Carbonate precipitation in gas hydrate sediments of the Gulf of Mexico**
Authorship: T. Naehr and co-authors
For submission to: *Geomarine Letters*

Title: **Natural and Unnatural Oil in the Gulf of Mexico: Comparing the fate of Macondo oil discharges with natural hydrocarbon sources**
Authorship: O. Garcia-Pineda, S. Morey, F. Huffer, I.R. MacDonald,
For submission to: *Environmental Research Letters*

Title: **Basin-wide stability estimates for shallow gas hydrate deposits in the Gulf of Mexico.**
Authorship: I.R. MacDonald, O. Garcia-Pineda, M. Regan, N. Guinasso
For submission to: *Geology*

RESULTS

1. GULF OF MEXICO HYDROCARBON SEEP: REGIONAL INVENTORY

1.1 SATELLITE DATA ACQUISITION AND PROCESSING

The Gulf of Mexico is one of several continental margins where much of the larger hydrocarbon systems occur in the uppermost portion of the sediment column [*I. R. MacDonald et al.*, 2002]. Over the last half century, offshore exploration for hydrocarbons in the northern Gulf of Mexico has advanced from the bays and inner shelf to the continental slope-to-continental rise transition. Evidence of natural hydrocarbon seepage in the continental slope of this semi-enclosed sea has been documented through remote sensing analysis correlating oil slick signatures on the sea surface to natural seepage and chemosynthetic communities on the sea floor [*Hood et al.*, 2002; *I MacDonald et al.*, 1996]. Major hydrocarbon accumulations on the slope are also commonly associated with intense seepage at the seafloor intersection of the corresponding cross-stratal migration pathways as shown in *Figure 1.1*.

Figure 1.1: *The locations of study sites MC118 (900 m depth), GC600 (1200 m depth) and GC185 (also known as Bush Hill, 550 m depth), as well as the track followed by the research ship.*

Optical satellite remote sensing depends on sunlight illuminating the Earth in order to obtain useful imagery. Its performance is restricted by the presence of clouds, fog, smoke or darkness. However, SAR sensors does not have this limitation [*Jingxuan et al.*, 2002]. Compared to real aperture radar, SAR synthetically increases the antenna's size or aperture to increase the azimuth resolution though the same pulse compression technique as adopted for range direction. Synthetic aperture radar processing uses the motion of the radar platform to increase the effective aperture of a small antenna [*Raney et al.*, 1991]. SAR-based technology provides its own microwave illumination and thus operates day or night, regardless of weather conditions [*Alpers and Hühnerfuss*, 1988].

Interactions between the sea surface and microwaves are very sensitive to variations in sea surface roughness [*Fortuny-Guasch*, 2003]. Rough surfaces scatter large amounts of energy back to the antenna and have bright signatures, while smooth surfaces reflect the energy away from the antenna and have dark signatures [*Gordon et al.*, 1998; *Ivanov Andrei*, 2002].

The high reflectivity of the sea surface is due to Bragg scattering from capillary and short gravity waves, and for this reason, the backscatter intensity in sea water is stronger than in surfactants (surfactant = surface active agents) [*Henschel et al.*, 1997]. The detection of oil slicks with single-polarization signals from SAR sensors has been found to be optimal at small incidence angles and under moderate wind speeds, ranging from 3-8 m/s [*Fortuny-Guasch*, 2003], and in some cases extended to 3-10 m/s [*Quintero-Marmol et al.*, 2003].

Because favorable conditions prevail during many months of the year in the Gulf of Mexico, SAR data have an excellent potential for detecting hydrocarbon seeps (*Figure 1.3*). Where multiple images detect hydrocarbons in the same locality, one can assert with confidence that the site is associated with a seafloor hydrocarbon seep [*De Beukelaer et al.*, 2003; *I.R. MacDonald et al.*, 1993; *I R MacDonald et al.*, 1996]. Field trials and modeling efforts have demonstrated that oil reaches the sea surface as inner coatings on bubbles of methane [*I. Leifer and MacDonald*, 2003; *I. R. MacDonald et al.*, 2002]. Where hydrocarbon seeps occur in depths beyond the hydrate stability zone (~500m), the rapid flux of gas will feed shallow deposits of gas hydrate that potentially interact with water column temperature changes [*I.R. MacDonald et al.*, 2005; *I. R. MacDonald et al.*, 1994; *Vardaro et al.*, 2005]. Satellite SAR therefore provides a means to inventory the abundance, distribution, and activity of shallow gas hydrate deposits at an ocean-basin scale.

1.2 MATERIALS AND METHODS

Image data and processing

Through a data sharing agreement with National Aeronautic Space Administration (NASA), and the European Space Administration (ESA), SAR images were analyzed and processed for detection of image targets consistent persistent oil discharge from fixed points on the seafloor (***Appendix II***). All images were collected either by RADARSAT-1 or Envisat in different beam modes. Images were analyzed and interpreted following a series of processing steps. After converting analog SAR signals from the satellites into binary SAR signal data, converter tools software (MapReady and VISAT) provided by Alaska Satellite Facility (ASF) and ESA were then used to construct GeoTIFF (8bit-grayscale) images from the raw binary SAR data. The GeoTIFF format has the embedded georeferencing information required to project the data in a GIS application (Arcmap).

After these preparatory steps, SAR images were ready to be interpreted. First, a general overview on the image was made to understand the overall weather conditions to evaluate ocean features based on the evident roughness of the sea surface and to pinpoint potential geographic errors. Initially, the analyst would examine the points of geographic reference (e.g. coast lines, platforms). The texture of the image was then examined in order to estimate the wind conditions present during the time of the collection of radar data and to make a judgment whether an image had been collected under sea-state conditions that were compliant with detection of floating oil layers. Based on previous experience, oil layers can be detected in SAR images when wind speeds were between 2 and 10 m/s [*Garcia-Pineda et al.*, 2010]. For wind speeds higher than this range, the layers of oil tended to fragment and disappear into the heightened backscatter caused by chop and rough seas. Under low-wind conditions, there may not be sufficient wind to cause capillary waves in unoiled water, making it impossible to detect the reflectance contrast caused by floating oil layers. If contemporary wind speed data were available for an image, an objective evaluation could be made about whether to proceed with analysis. Lacking this information analysis proceeded according to the analyst's subjective evaluation of the image. Sea states under conditions of

wind speeds higher than the allowable limit typically created high contrast speckle, more or less uniformly distributed over the image area. Additionally, under high-wind conditions, a complete absence of oil slicks particularly from areas known to host persistent seeps would contribute to the judgment that the image in question was outside of the compliant limits. Under low-wind conditions, large, mostly uniform areas of the sea surface would appear radar-dark. If low wind cells were present, upwelling and other biogenic films are common to congregate on the surface and then drift, false targets. If low-wind regions were restricted to discrete portions of an image, these regions could be selectively excluded from the analysis, while oil slick features were counted in the majority of the image.

The search target for oil layers generated by seafloor sources was a linear or curving, radar-dark region with an approximate 1:10 width to length ratio. Typically, the Oil Slick Origin (OSO) was dark with sharp boundaries. OSO points were identified by the shape of floating oil layers following particular characteristics (i.e. origins tend to be wider and more distinct ends of curvilinear features, which narrow and attenuate with increasing distance from the point where fresh oil reaches the sea surface). The down-wind portions of slicks tended to thin, gradually becoming fainter, and finally dissipating completely into the background (*Figure 1.1*). Following the image analysis, if dark signatures in the SAR image were identified as potential oil slicks generated from natural hydrocarbon seeps, two GIS layers were created related using the georeference information of SAR image using the ET GeoWizards attachment for Arcmap. The first layer is a polygon shape file that will contain the area of the SAR image footprint. This footprint layer is given all the attributes of the image (i.e. beam mode, date and time of collection, etc). The second layer is a point shapefile that will contain OSO points, which are single points within detected oil slicks. After determining the OSO points in the image, the depth data is then merged with each OSO attribute. This merged information was used to determine the deflection through the water column. In most regions, OSO points are clustered in two modes: clusters within a single image and clustering that becomes apparent when the results of multiple image analyses are combined in a GIS. Within a single image, seep formations with multiple discharge vents would produce a collection of adjacent OSO points offset from their seafloor source by the horizontal distance traveled during vertical transit between the bottom and the surface. The geographic average of a set of OSO points would be the best estimate for the center of the formation. The average distances among OSOs from a common seep formation would also provide a measure of the geologically determined scale of the active seep. The challenge is how to determine the clustering radius. Following the methodology on [*Garcia-Pineda et al.*, 2010], we analyzed the tendency of OSO points to cluster within each individual image to determine characteristic spatial scales.

Clustering Methodology

A Hierarchical Cluster Tree (HCT) based on pair-wise distances between OSO points was constructed for each image. In such a tree, points close together are grouped together in a cluster. Depending on the definition of ‘‘close,’’ different clusters may emerge. The ideal maximal distance within a cluster was used when grouping. The reasoning behind this grouping is the fact that in an individual satellite image, OSO points that originate from the same sources on the ocean floor will be encompassed by a radius characteristic of seep-formation geology. The clustering starts by grouping the closest two points together and then regarding these two points as a new point and repeating the process. Each clustering step involves a distance matrix that contains all of the distances between the current set of points. With each step the distance matrix shrinks by one row and one column. The art when clustering is deciding at what distance things should no longer fall under the same cluster. We opted to use the Inconsistency Coefficient (IC), also called ‘‘factor of inconsistency’’ [*Jain and Dubes*, 1988; *Zahn*, 1971], to decide the maximal distances within a cluster. Other authors use the index of clumping [*Ripley*, 1981] to decide on cutoffs, but the results are shown to be equivalent. The inconsistency coefficient for a grouping of two points or sub-clusters into a new cluster is similar to a z-score. It uses the mean distance between all the original unclustered points in both sub-clusters and the standard deviation of all those distances. The

distance between the two sub-clusters (for us, the maximum distance between any two elements of the sub- clusters) is normalized by subtracting the mean of all distances and dividing the result by the standard deviation of all the sub- clusters. A small inconsistency value means that the distance between the two sub-clusters combined into a new cluster is similar to distances encountered in previous clustering steps, or, said differently, that there is no large jump in distances caused by combining the sub-clusters. If the inconsistency index exceeds one, those items should not be clustered together. Even if the index is less than one, the inconsistency index is not a sufficient method for deciding on cluster size. We also look for a jump in maximal distances within a cluster to decide at which maximal distance we want to stop the clustering. Background information on hierarchical clustering can be found in [*Deonier et al.*, 2005] and [*Ripley*, 1981]. After determination of clustering radii for individual images, the centroids of OSO clusters were assumed to be estimates for the location of active seep formations for the conditions occurring at each image collection time. When centroid locations were compared among multiple images covering the same region, a second scale of clustering was determined by repeating the pair- wise distance comparison for centroids.

1.3 RESULTS

SAR image archive processed

The project obtained a total of 1,135 SAR images collected between 1997 and 2007 covering the Gulf of Mexico with a cutoff imposed from the Caribbean Sea along a line between the southern-most point of the Florida mainland and the northern tip of the Yucatan peninsula. (*Figure 1.2*). A complete listing of images downloaded and processed is provided in ***Appendix II***. Relative frequency of coverage was calculated by gridding the Gulf region at a 10-km scale and counting the frequency with which each grid cell was imaged. Linear trends in the sampling are an artifact of the orbital paths of the satellites. The distribution of these images shows distinctly higher frequency of observations in the central region of the northern Gulf of Mexico, with a second area of high frequency of the western coast of the Yucatan Peninsula. Coastal bays and inlets were in masked off in this inventory. The collection bias toward the central and southern regions results from monitoring requirements of the energy industry for the U.S. and Mexico, respectively.

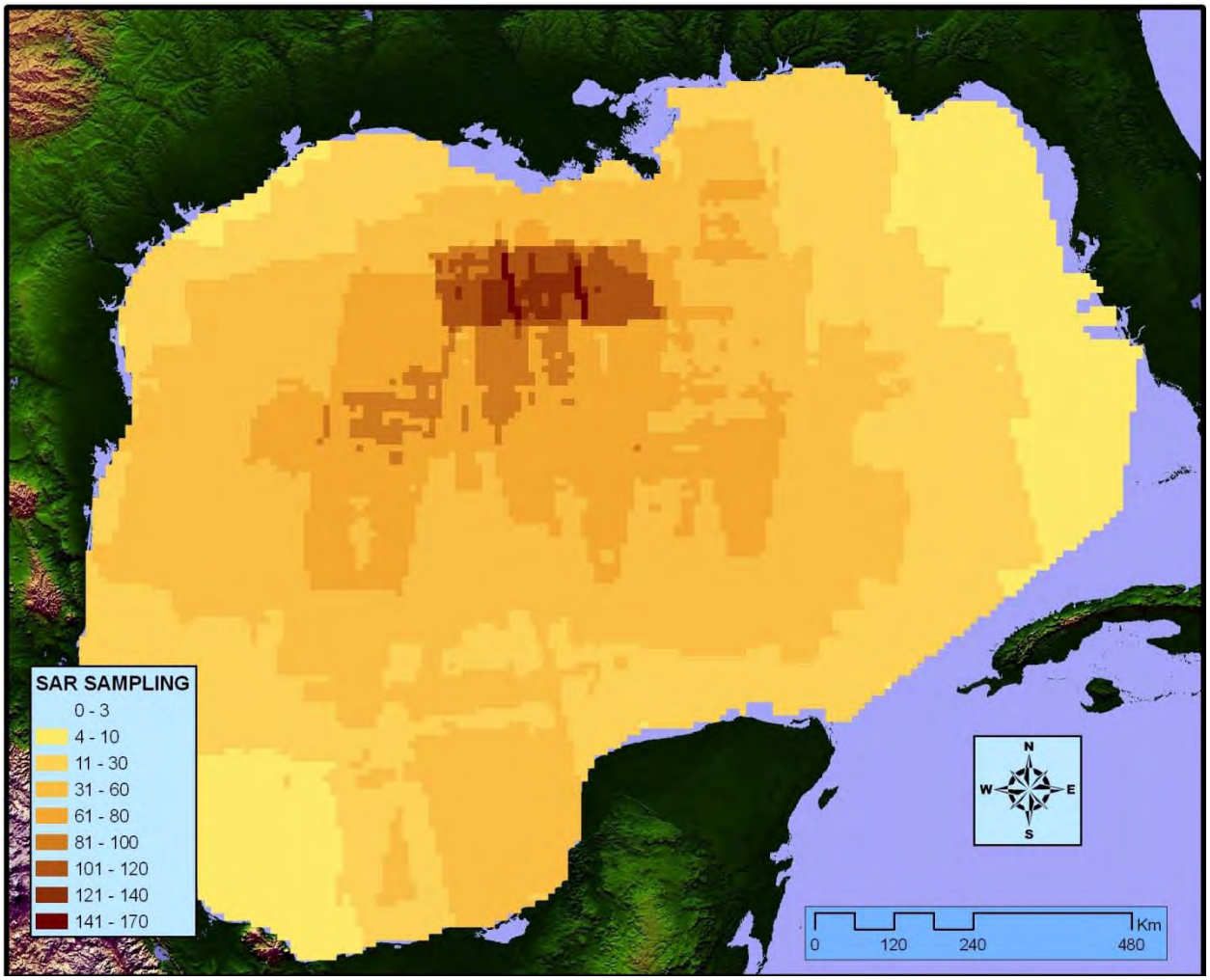

Figure 1.2: *Gridded distribution of satellite SAR coverage among 1135 image collections. Frequency scale indicates the number of times each grid cell was sampled. Grid size is 10 km. Higher sampling frequency reflects collection bias by satellite imaging clients.*

After review, a total of 408 images were processed with the TCNNA algorithm (*Figure 1.3*). This resulted in a sampling of the Gulf of Mexico covering 147,370 km2 of ocean area of the Gulf of Mexico. Processing was concentrated in the regions of greatest observed seepage in order to detect temporal variations and maximize replication of observation. More than 95% of the Gulf area was imaged a minimum two times, with the un-sampled areas restricted to the coastal bays and inlets. Very high sampling frequencies were obtained for the areas surrounding the region offshore Louisiana, where previous results have shown that abundant and prolific seeps occur [*De Beukelaer et al.*, 2003; *I R MacDonald et al.*, 1996]. On average, each cell was imaged 15.3 times; *Figure 1.4* shows the overall frequency distribution of TCNNA processed images covering the entire Gulf region.

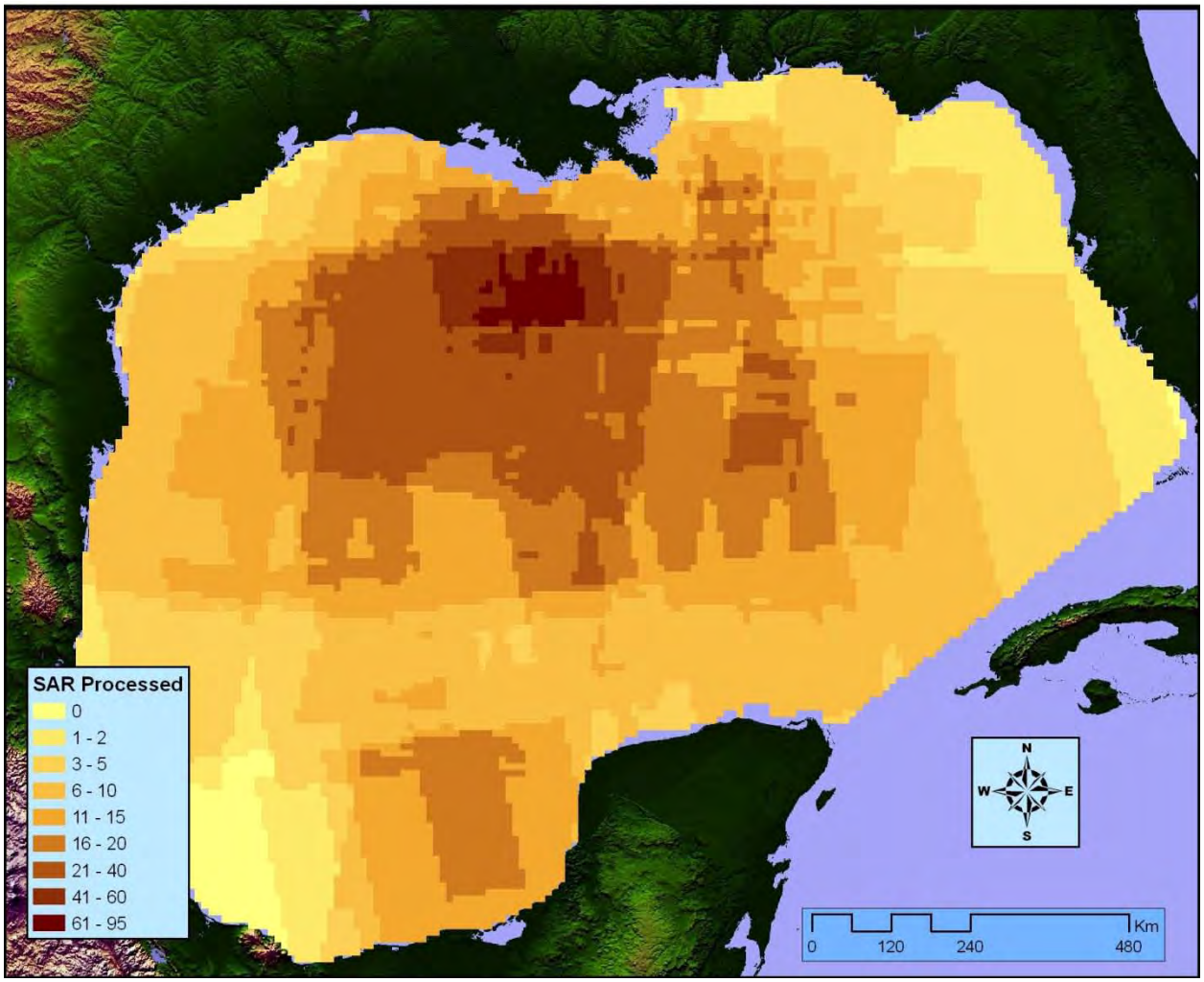

Figure 1.3: *Observation density for the 408 TCNNA processed SAR images selected from the total image archive shown in Figure 1.2. Coastal bays and inlets were not included even when the satellite images provided coverage.*

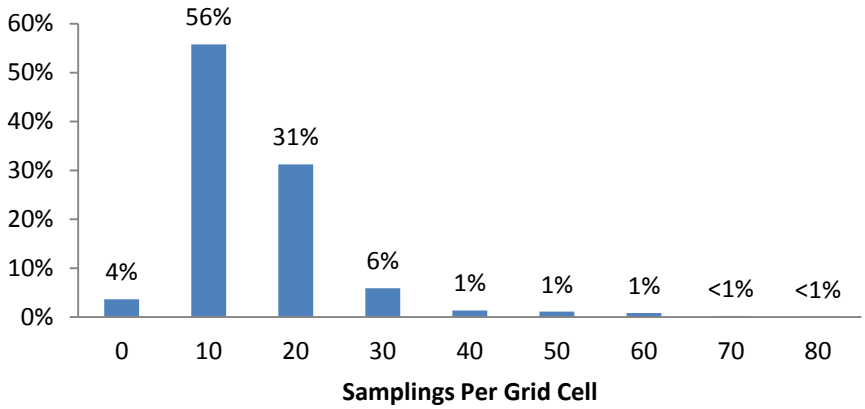

Figure 1.4: *Sampling frequency in TCNNA processed images for the gridded map areas shown in Figure 1.3. The mean samplings per cell was 15.3. Zero samplings were confined to bay and coastal waters where natural seeps*

do not occur

Abundance and distribution of oil and gas seeps in the Gulf of Mexico

Results from the processed archive of SAR images were used to compile a comprehensive inventory of persistent oil and gas sources in the Gulf of Mexico (*Figure 1.5*). This product is developed from detection of individual vents, which when observed in any given SAR image will generate an OSO on the ocean surface. Analysis of the clustering scale for OSOs over multiple images yields the predicted location of seep formations, which are the geologic features where hydrocarbons are escaping to the water column, presumably from an individual reservoir through a fault or similar conduit. The analysis finds that there are 1,081 geologic formations, which are concentrated in north to south trend from the Texas-Louisiana Slope, through the Sigsbee Knolls and the Campeche Knolls [*Bryant et al.*, 1991], to a cluster of sources that occur with the super-giant Cantarell oil field on the Campeche Bank of the Yucatan Peninsula [*de Miranda et al.*, 2004]. The association of seep formations with salt-tectonic stratigraphy of the Gulf of Mexico [*Watkins et al.*, 1978] is underscored by relative the hiatus in the frequency of seep formations in the Mississippi Canyon area and the relative curtailment of the process eastward along the Mississippi-Alabama Slope toward the Florida Platform [*Hine et al.*, 2003].

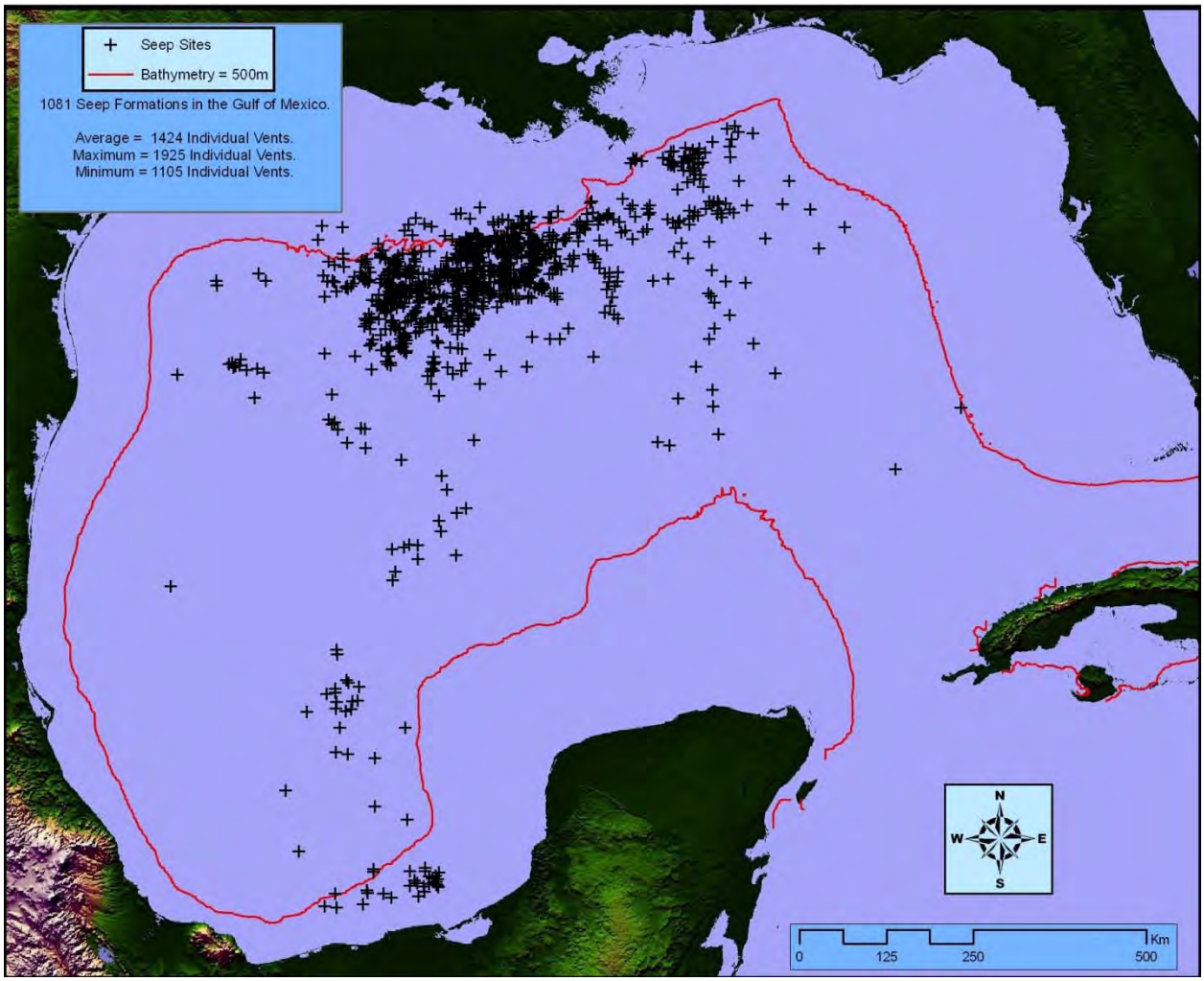

Figure 1.5: *Locations of seep formations in the Gulf of Mexico detected by analysis of SAR image data base. These are sites where continuing flux of methane and higher hydrocarbon compounds would support accumulation of gas hydrate at the*

seafloor.

Previous observations of the seafloor characteristics of seepage sites, including the HYFLUX sampling site at GC185 (Bush Hill) has shown that an such single formation will support one to several vents and generate a comparable number of OSOs in remote sensing images. [*De Beukelaer et al.*, 2003]. These findings were supported by the observations made during the HYFLUX research cruise, when multiple vents were observed at MC118, GC600, and at GC185. The number of vents (OSOs) observed per formation depends on wind direction and sea-state effects on the SAR images. Taking the average number of OSOs observed per formation, the analysis indicates that there are about 1,424 persistent oil and gas vents across the entire Gulf of Mexico (maximum 1,925, minimum 1,105). This variability suggests that not all vents are active continually, and that there may be episodic occurrences of higher activity within formations or across multiple formations. A measure of the prevalence of gas hydrate near the seafloor would be the prevalence of venting. To provide a regional overview this indicator, the number of vents was summarized over a 10-km gridded array covering the entire Gulf (*Figure 1.6*). This result can be interpreted as a minimum estimate for the region of the Gulf that will host shallow gas hydrate deposits. The drawback of this presentation is that it does not show gas vents or mud volcanoes that do not discharge sufficient oil to create a surface slick.

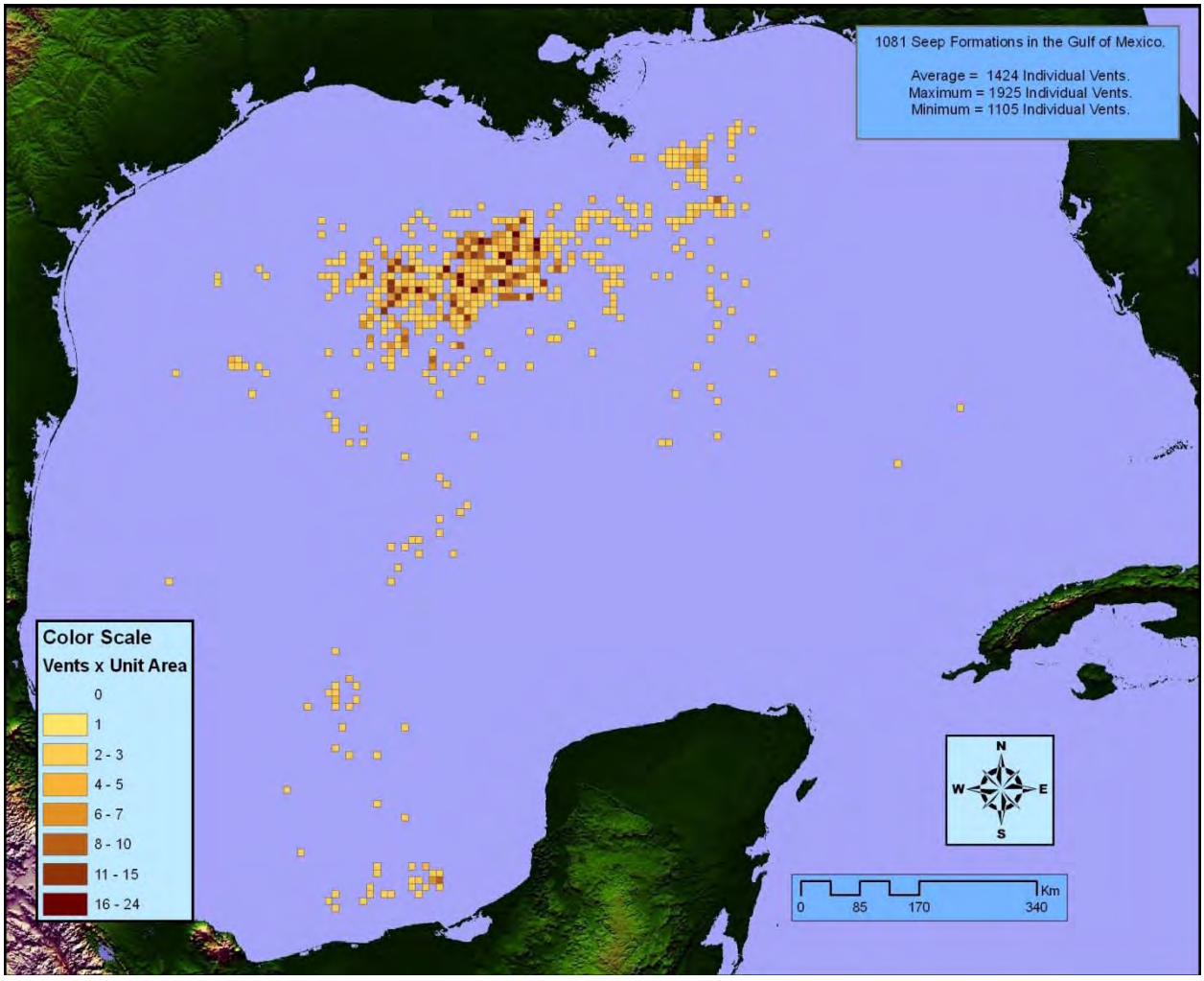

Figure 1.6: *Gridded frequency of oil and gas venting in the Gulf of Mexico based on frequency of oil slick origins detected in SAR data. The grid scale is 10 km.*

The distribution and frequency of seep formations with one or more active vents indicates where, at a minimum, gas hydrate deposits will occur in the deep Gulf of Mexico. The abundance of gas hydrate in these formations will depend on the magnitude of gas flux at each site [*A.V. Egorov et al.*, 1999; *I.R. MacDonald et al.*, 2005; *A. V. Milkov and Sassen*, 2000]. Although acoustic methods might be used to compare gas fluxes from individual vents [*Klaucke et al.*, 2006; *Nikolovska et al.*, 2008], they would not provide a regional summary of the process. Geophysical data has been used to delineate seep formations [*Sager et al.*, 1999] and to inventory the geologic total extent of the gas hydrate province [*Frye*, 2008]. However these data do not distinguish between areas where active, ongoing seeps would support shallow gas hydrate deposits and the relict features that may have been generated by seeps that were active in the past, but are no longer discharging gas. Satellite remote sensing data detect the presence of floating oil and can be used to compare the relative output of hydrocarbons from natural sources that might host shallow gas hydrates. The theory is that areas producing greater amounts of oil will have a greater tendency to host shallow hydrate deposits. *Figure 1.7* shows the average areas of floating oil layers displayed in the same 10-km grid used previously. The drawback with this result is that it includes oil from possible pollution sources as well as coastal processes that may produce false-positive targets.

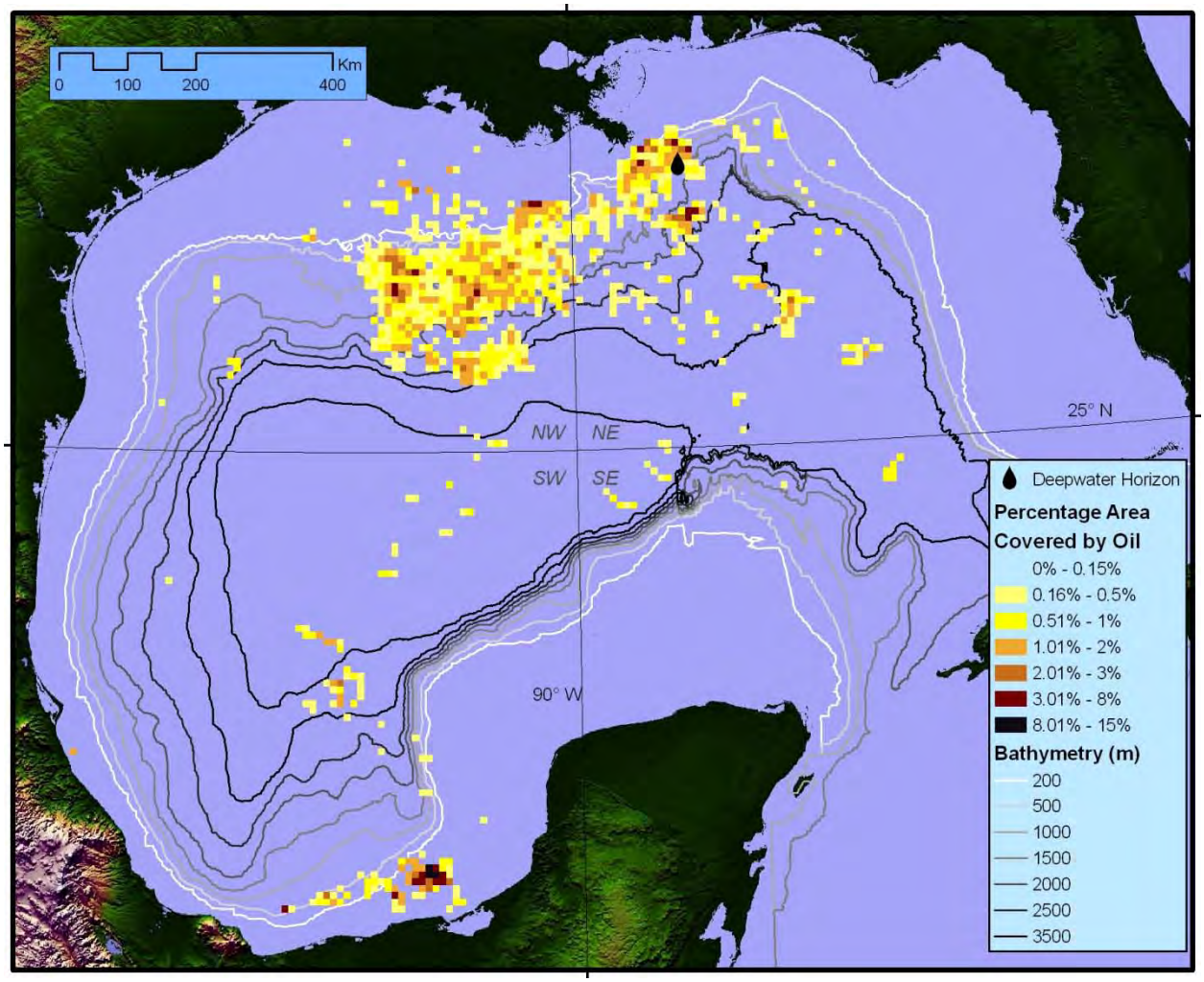

Figure 1.7: *Average areas of oil covered water gridded to a 10-km scale and normalized to the frequency of observation for each grid cell.*

The analysis was extended in order to: 1) estimate the average rates of discharge for natural oil seeps in the Gulf and 2) develop a "best estimate" of region where shallow gas hydrates occur in the Gulf of

Mexico. Oil slicks or similar features were eliminated from the inventory unless a seep formation (*Figure 1.5*) had been within the grid cell where the slicks were observed or within a one-cell buffer surrounding that cell. This had the result of removing the coastal anomalies and defining consolidated regions where floating oil on the surface indicates persistent seafloor sources of oil and gas (*Figure 1.8*). These results were then analyzed to estimate rates of discharge and to consider how depth and expected water temperatures would affect the formation and stability of shallow gas hydrate deposits.

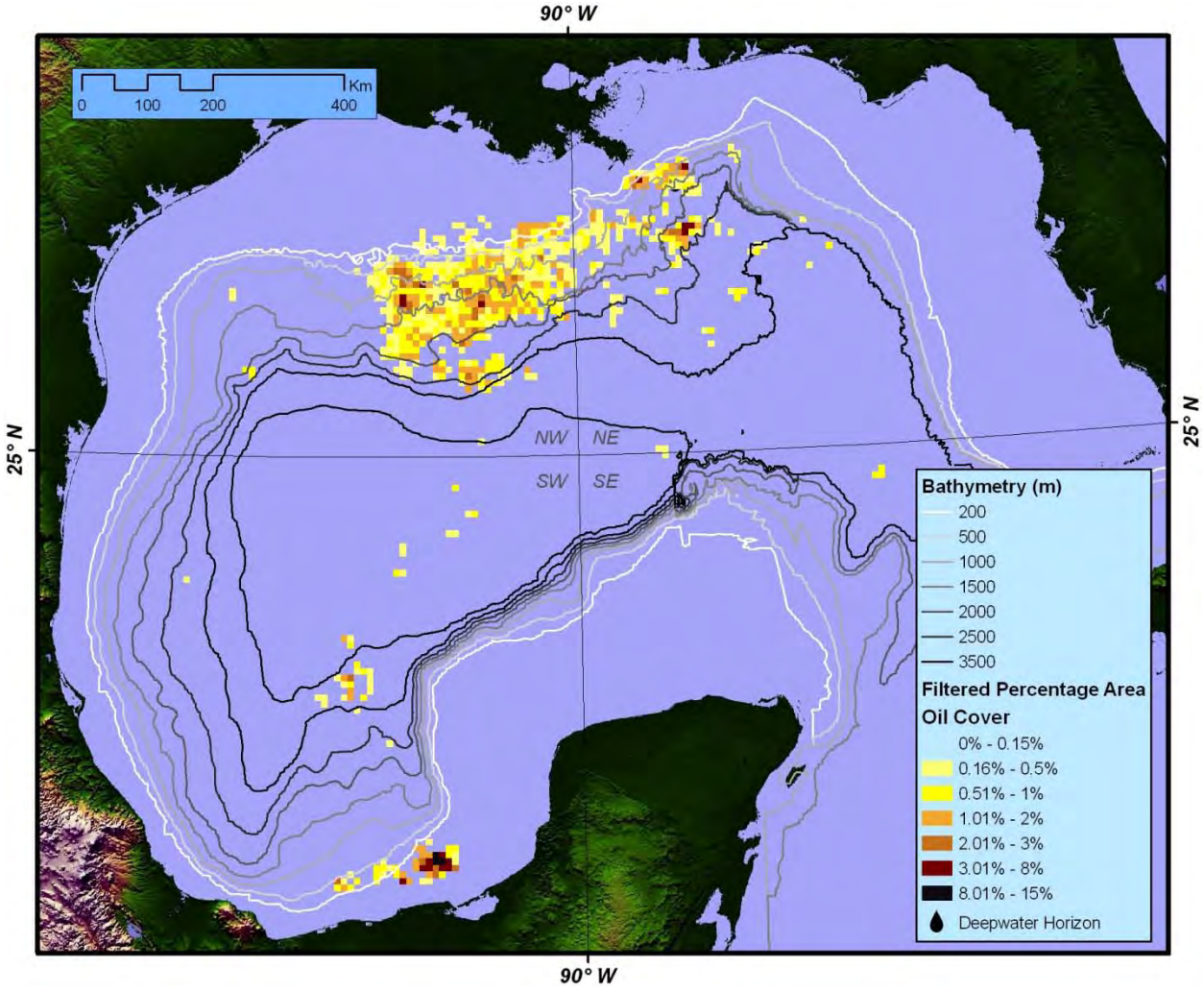

Figure 1.8: *Average area of oil-covered water for 10-km grid filtered to remove coastal anomalies and isolated events. Vertical and horizontal lines divide the Gulf region into quadrants along 90° west and 25° north, respectively.*

To estimate the average amount of oil-covered water in the Gulf, each SAR image was considered a separate, independent sample of the offshore area of an arbitrary size. In doing this, it was found that many images listed as distinct files in the SAR archives were actually collections made during a single orbital transit of the Gulf region that had been divided into separate files for cataloging purposes. The TCNNA outputs images were joined into single image strips and any overlapping regions between adjacent frames were consolidated. This yielded 176 satellite SAR samplings of the Gulf within the region delineated in *Figure 1.8*, with one or more OSO features present in each sampling.

A simple division of the Gulf into four quadrants along 90° west longitude and 25° north latitude provides a basis for comparing the scale of oil seepage in the northwest, northeast, southeast, and southwest

regions (*Table 1.1*). The four regional quadrants comprised between 16% and 34% of the total Gulf 147,370 km2 area. Sampling frequency was also reasonably dense, with an average of 29.4 image samples per seep cell. Sampling frequency for seep cells was higher than it was for the entire Gulf (*Figure 1.4*). Sampling frequency was lower in the southwest quadrant because the predominant image types available for this region were Scansar Wide-mode images that covered 400 x 400 km.

To estimate the significance of the mean area of oil-covered water and the differences between quadrants, the complete set of 176 images was resampled following a bootstrap methodology that chose at random a image sample of size 176 [*Chernick*, 1999]. This was possible because the resampling method allow for repeated selection of each image until the sample set was completed. Repeating the procedure 2,000 times allowed for the estimation of standard error and for comparison of different subregions of the Gulf. This analysis shows that the northwestern quadrant, comprising most of the Texas-Louisiana Slope and Sigsbee Escarpment areas, with an average of 68% of the total, was the major source of floating oil in the Gulf. The southwestern quadrant, containing the Cantarell field and the Campeche Knoll seeps [*I.R. MacDonald et al.*, 2004] contributed an average of 25% of the total. The northeastern quadrant, where the Deepwater Horizon blowout and oil discharge of 2010 occurred [*National Commission*, 2011], contributed only 7% of the background oil seepage into the Gulf of Mexico.

Table 1.1. *Summary statistics for inventory of oil-covered water detected in 176 independent SAR image samples of the Gulf of Mexico. Mean and standard deviations were calculated from a bootstrap-sampling of 2000 re-samplings*

Region	Size of Gulf Region (km^2)	Percent of Total Area	Mean Images per Seep Cell	Mean Area of Oil-Covered Water (km^2)	S.D. of Mean	Percent of Total Oil-Cover
NE	42,120	29%	22.5	54.4	21.99	7.0%
NW	32,120	22%	39.3	529.0	69.67	68%
SE	23,030	16%	14.9	193.8	46.03	25%
SW	50,100	34%	12.2	3.7	10.96	0.5%
Total Gulf	147,370	100%	29.4	780.0	86.03	100%

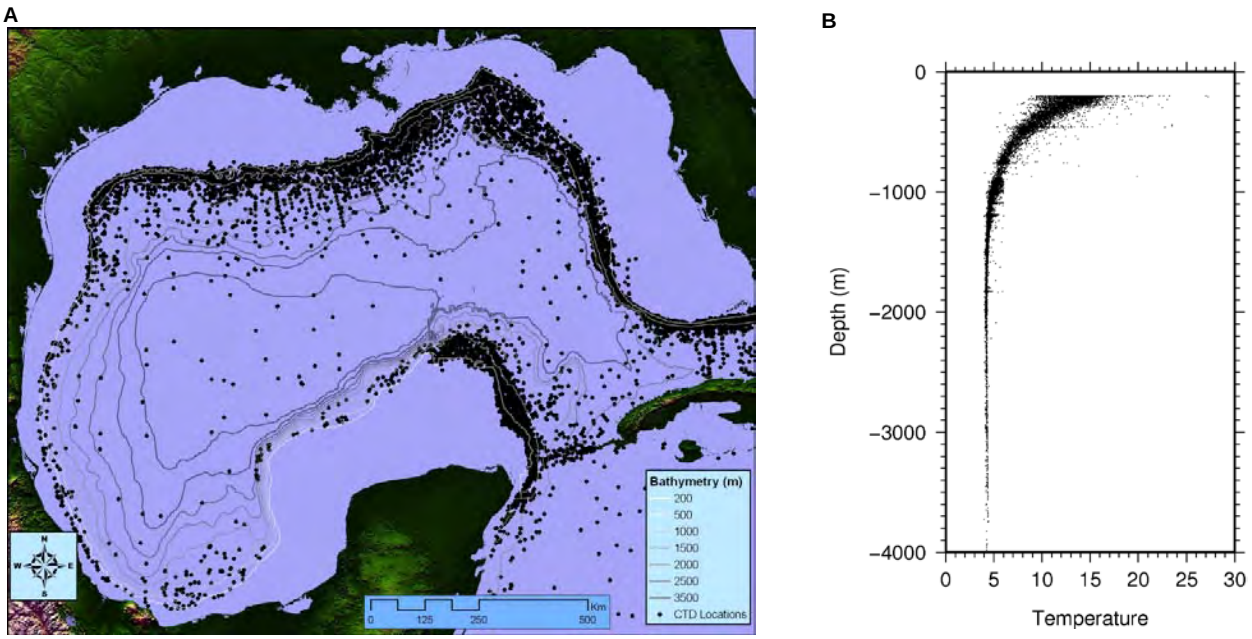

Figure 1.9: *Archive of CTD profiles and bottom water temperature measurements from NODC records for the Gulf of Mexico. A. locations of measurements; B. summary plot for the bottom measurement, truncated for depths 200 m. Compiled by N. Guinasso, Geochemical and Environmental Research Group, Texas A&M University.*

Defining the province in which shallow gas hydrates can occur allows for an examination of the environmental conditions that affect formation and stability. Stability of gas hydrate is defined by ambient pressure and water temperature [*Sloan Jr.*, 1998]. Although a relatively small proportion of the gas hydrate hosting seeps have been occupied by investigators, there is a large archive of temperature profiles for the region available from the National Ocean Data Center (NODC). The complete archive of temperature profiles from surface ships and drifters is shown in *Figure 1.9-A*.

The compiled data show a mixed layer above 200 m and a temperatures decreasing below the thermocline to about 5 °C. The Gulf of Mexico has a sill-depth of about 1500 m for both the Yucatan Straits and the Florida Straits, so the deeper portion of the Gulf basin is filled by a mixture of North Atlantic Deep water and Antarctic Intermediate water and lacks thermohaline circulation that would replace these waters with colder deep waters. The minimum bottom water temperature of the Gulf reported in the NODC archive was 4.0 °C. There is a slight increase in potential temperature with depth due to adiabatic effects. To relate the temperature database to the gas hydrate, the bottom values for each temperature profiles were taken. Because of the monotonic temperature values below 1500 m, it was possible to include the bottom measurements for profiles in deeper water even when they did not extend to the actual ocean bottom. Depths (pressure) was taken from the Admiralty bathymetric chart for the Gulf of Mexico. *Figure 1.10* shows the temperature and pressure predictions for the gridded gas hydrate locations overlain with the stability horizons for gas hydrate formed from pure methane (sI) and for mixtures of methane plus ethane and propane (sII). Strikingly, the overwhelming majority of gas hydrate localities are well to the left and below the stability horizon, i.e. highly stable with respect to effects of temperature and salinity.

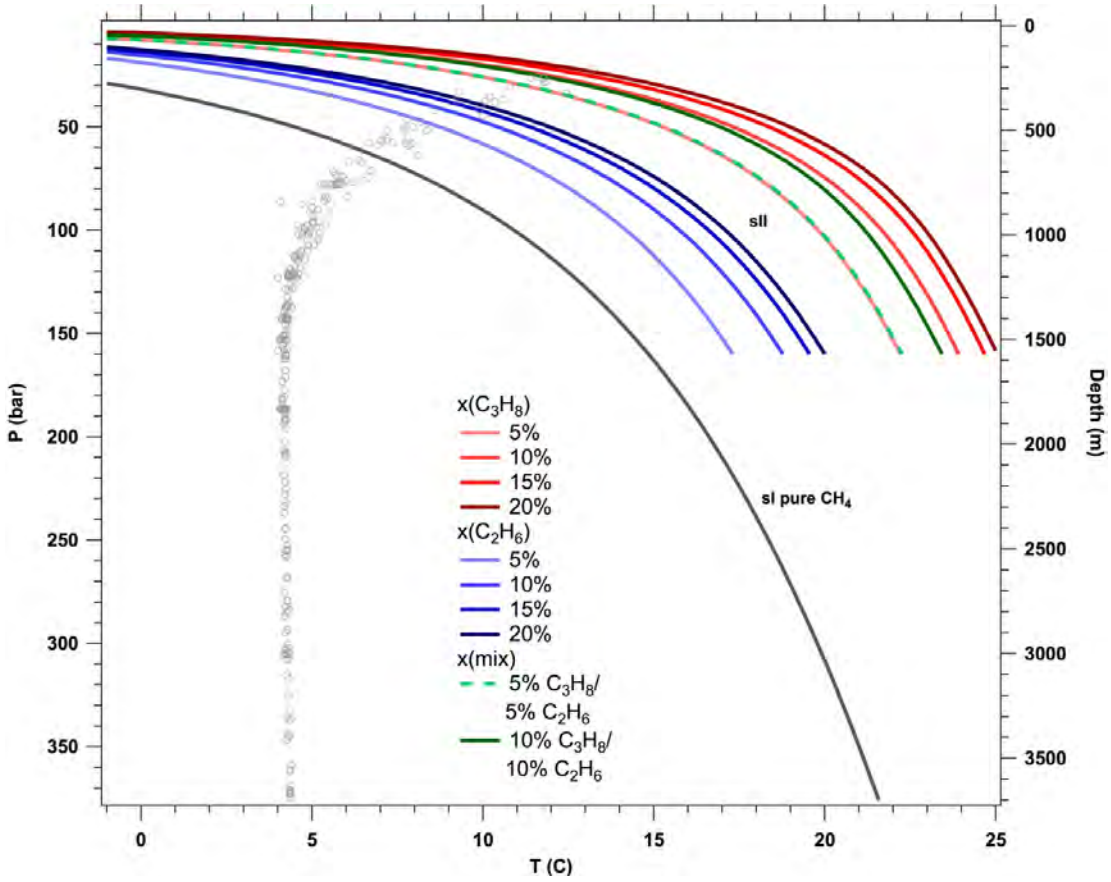

Figure 1.10: *Stability horizons for gas hydrate formed from (methane) (CH_4) (structure I) and mixtures of C_2H_6 (ethane) and C_3H_8 (propane) as calculated by M. Reagen, Lawrence Livermore Lab, University of California, Berkeley. Points show the*

expected temperature and pressure conditions for the gridded locations of the gas hydrate region (Figure 1.8).

Comparison of oily versus non-oily seeps

Satellite remote sensing methods for detecting persistent hydrocarbon seeps require a flux of oil to the sea surface. Methane fluxes without oil, no matter how vigorous they might be, do not generate a signal that can be seen by SAR or presently available sensors [*De Beukelaer et al.*, 2003]. The results shown in *Figures 1.7 and 1.8* do not reflect seeps where gas predominates. This implies that there may be a large number of methane sources that are not represented in the SAR data. At the outset of the HYFLUX project, there was no option to test this supposition. Due to the interest in natural seeps prompted by the BP oil discharge, an acoustic survey was conducted in the vicinity of the well head in August of 2011 (Larry Mayer, personal communication, 2011). The survey vessel (RV Okeanus Explorer) used a SeaBeam swath-mapping system to interrogate the water column for the presence of bubbles, oil drops and acoustic anomalies. These results, although they are still in preliminary form at this time, make it possible directly to compare detection of gas in the water column with persistent oil slicks on the surface detected by SAR using the method described in this section (*Figure 1.11*).

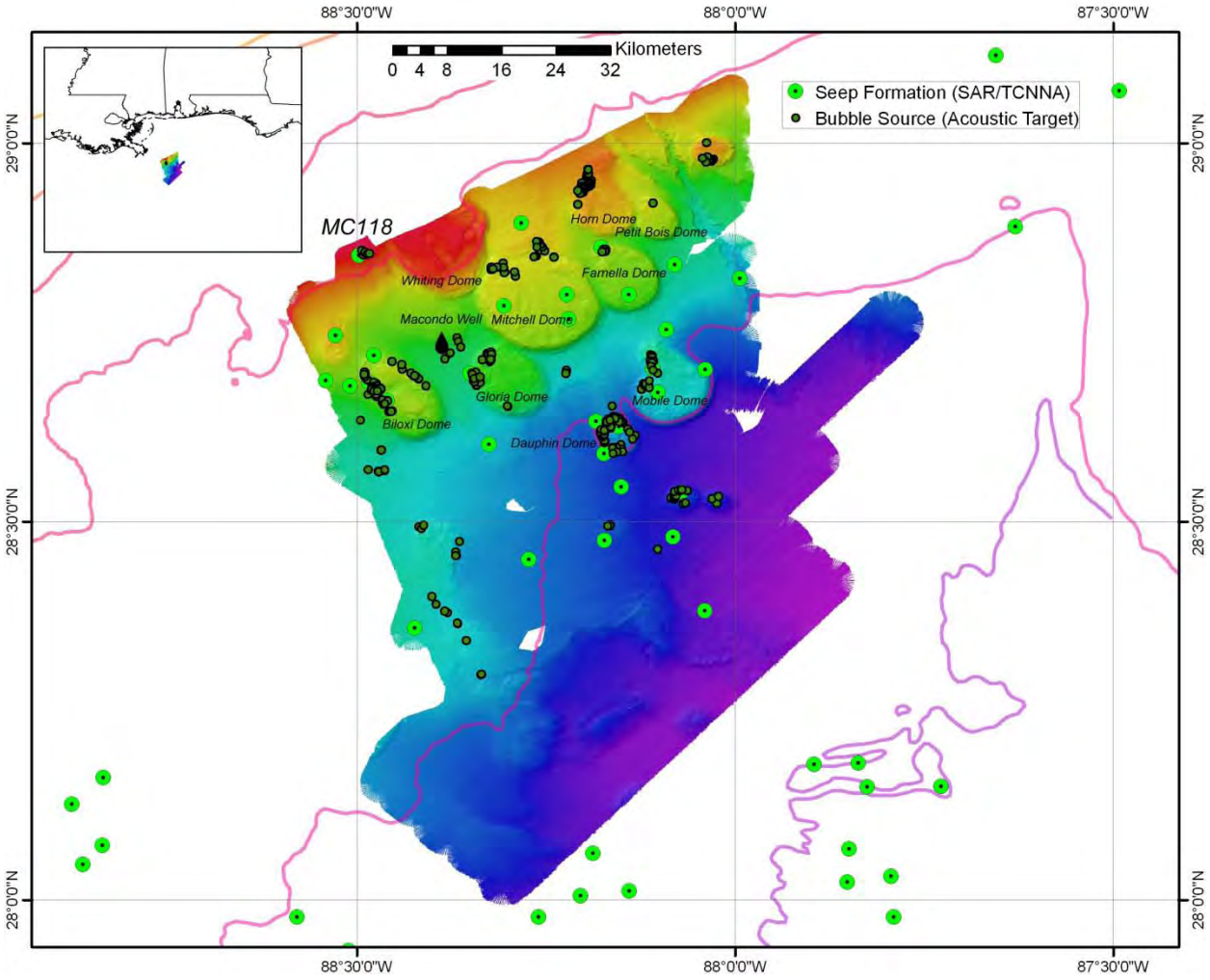

Figure 1.11: *Oil and gas seeps detected by satellite SAR with TCNNA analysis compared to gas bubble acoustic targets detected by NOAA survey during August 2011. Inset map shows regional area southeast of Mississippi Delta. Labeled features include domes and the blow out site at Macondo Prospect wellhead. Bathymetric swath map shows extend of NOAA survey. Contours at 00 1000 1 00 000 n 00 m*

100, 500, 1000, 1500, 2000, and 2500 m.

Results of this comparison illustrate how different seep processes and potential differences in fluid characteristics will lead to potentially divergent findings depending on what method is used for remote detection of seeps and possible gas hydrate deposits. Moreover, intermittent releases may confound the findings if a survey or satellite observation happens when individual sources are either unusually active or temporarily quiescent. In general, however, there was good correspondence between The NOAA acoustic survey detected abundant gas venting and apparent bubble sources at the MC118 study site, as well as the Biloxi, Dauphin, Farnella, Mitchell, and Mobile Domes. These occurrences corresponded closely to the seep formations detected by satellite SAR analysis. This suggests that the bubble sources at these sites were associated with oil transport to surface waters. The abundance of bubble sources indicates that seafloor gas hydrate deposits are more widespread than is indicated with analysis of the SAR data. For example, on Biloxi Dome, the satellite results indicate that there are seep sources on the northern portion of the feature, while the acoustic survey results show multiple bubble sources along the northeastern and southwestern sides of the dome. In the northeastern portion of the NOAA acoustic survey, bubble sources were detected in areas without matching satellite SAR oil signatures. The Destin Dome and Desoto Canyon region of the eastern Gulf of Mexico is known for hosting gas and condensate reservoirs as opposed to petroleum [*Mink et al.*, 1989]. If the venting fluids are relatively oil-free, bubbles would be less likely to reach the surface and would not transport sufficient oil to generate targets that can be detected by SAR. For some reservoirs, therefore, SAR could significantly underestimate or fail to detect gas seeps and associated gas hydrate deposits. Estimates of the abundance and distribution of gas hydrate based on satellite surveys is there for a lower boundary on its occurrence.

2. OTHER REGIONS' HYDROCARBON SEEP INVENTORY

Natural marine oil seeps that produce layers of oil floating on the ocean surface have been reported in many oceanic regions worldwide. Preliminary surveys of oil and gas seeps were undertaken in several other international regions as a component of the HYFLUX project. The objective of this effort was not to compile an exhaustive inventory of seep formations comparable to the results achieved in the Gulf of Mexico. Instead the team attempted to verify whether hydrocarbon reservoirs in other regions can be detected using the SAR analysis techniques perfected in the Gulf. Three regions were chosen, based on underlying background knowledge of the basin geological properties in the respective regions: the Black Sea offshore Ukraine and Georgia, the Makran accretionary prism in the Arabian Sea offshore Pakistan, and the eastern Atlantic Ocean offshore the Republic of Congo and Angola. Collaboration with the MARUM Marine Geology and Geophysics group at the University of Bremen, Germany made it possible to verify that SAR targets were generated by floating oil and were associated with exposed gas hydrate. These studies are ongoing and are brief described for this report.

The most extensive results were obtained in the Black Sea and are described in detail in a preliminary report attached as Appendix III. In this region, numerous persistent oil slicks were observed in surface waters in the eastern portion of the basin near the Georgian city of Poti and in the north central region near the Ukrainian city of Savastopol. Seafloor sampling confirmed presences of extensive gas hydrate deposits and large gas vents. Although the total density of active OSO was not as great as has been observed in the Gulf of Mexico, and there were quite a number of gas seeps that did not produce surface oil signatures, SAR technology was a demonstrated success in identifying regions where seafloor gas hydrates could be found.

Active gas seeps that support chemosynthetic communities have been explored by several submersible expeditions [*Sibuet and Vangriesheim*, 2009]. Locations where gas discharge generates bubble plumes or flares that can be detected acoustically have been reported in preliminary results [*Spiess*, 2008] and generally agreed with the submersible observations of chemosynthetic communities. The goal of the HYFLUX project was to determine whether archived SAR images indicated persistent oil seeps that corresponded to the locations of bubble plumes and chemosynthetic communities. Results from the eastern Atlantic Ocean were limited by the availability of SAR imagery with acceptable geographic coverage and weather conditions conducive to viewing floating oil. Over 50 possible images were reviewed for suitability. Three RADARSAT SAR images and three ENVISAT images were selected for geoprocessinf (*Figure 2.1*). These results indicated presence of oil seeps in the shallow coastal waters, but were inconclusive in the deep water areas where gas flares had been detected.

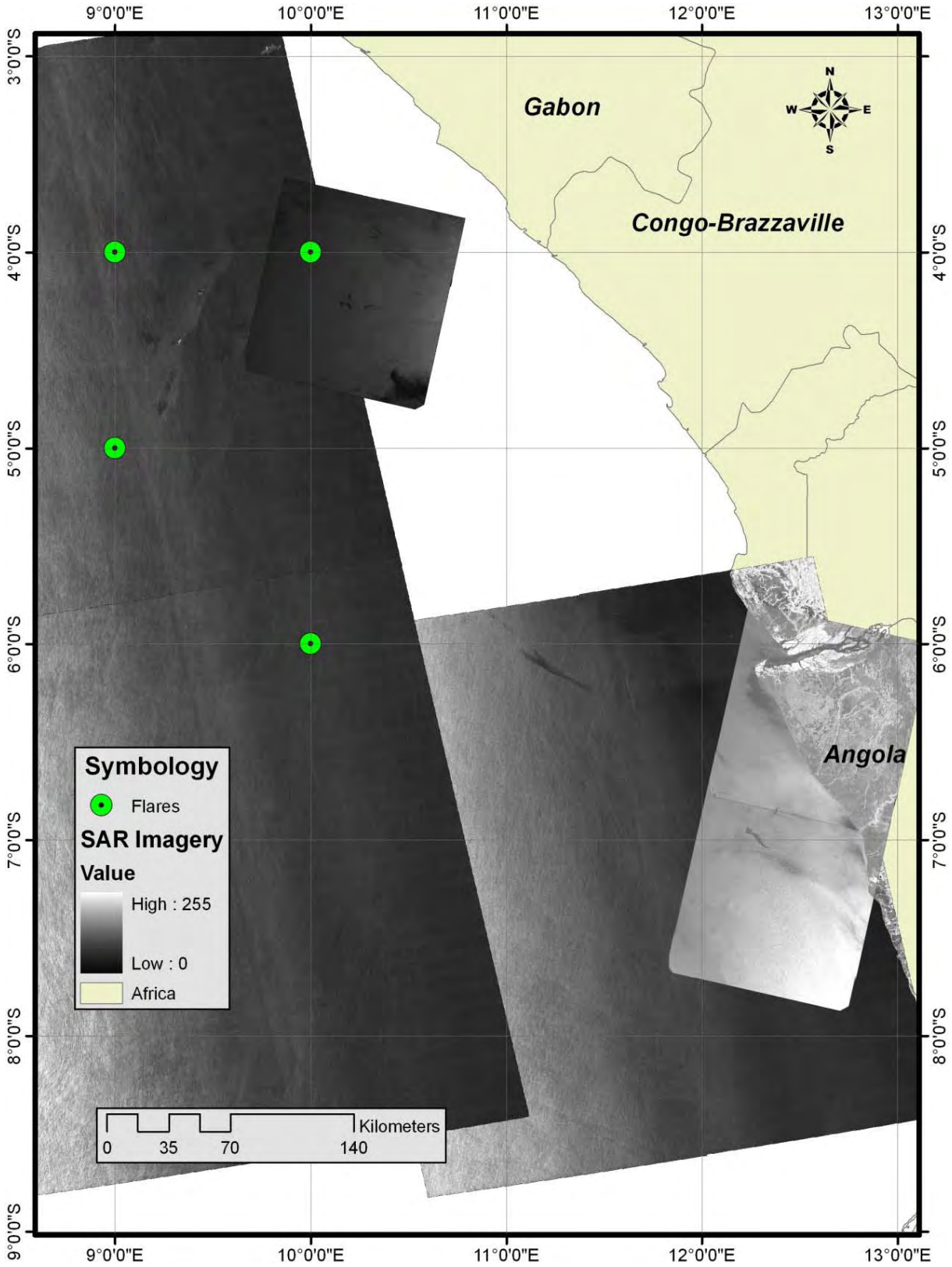

Figure 2.1: *SAR images from West African Margin. Flares mark locations of gas bubble plumes detected by acoustic surveys.*

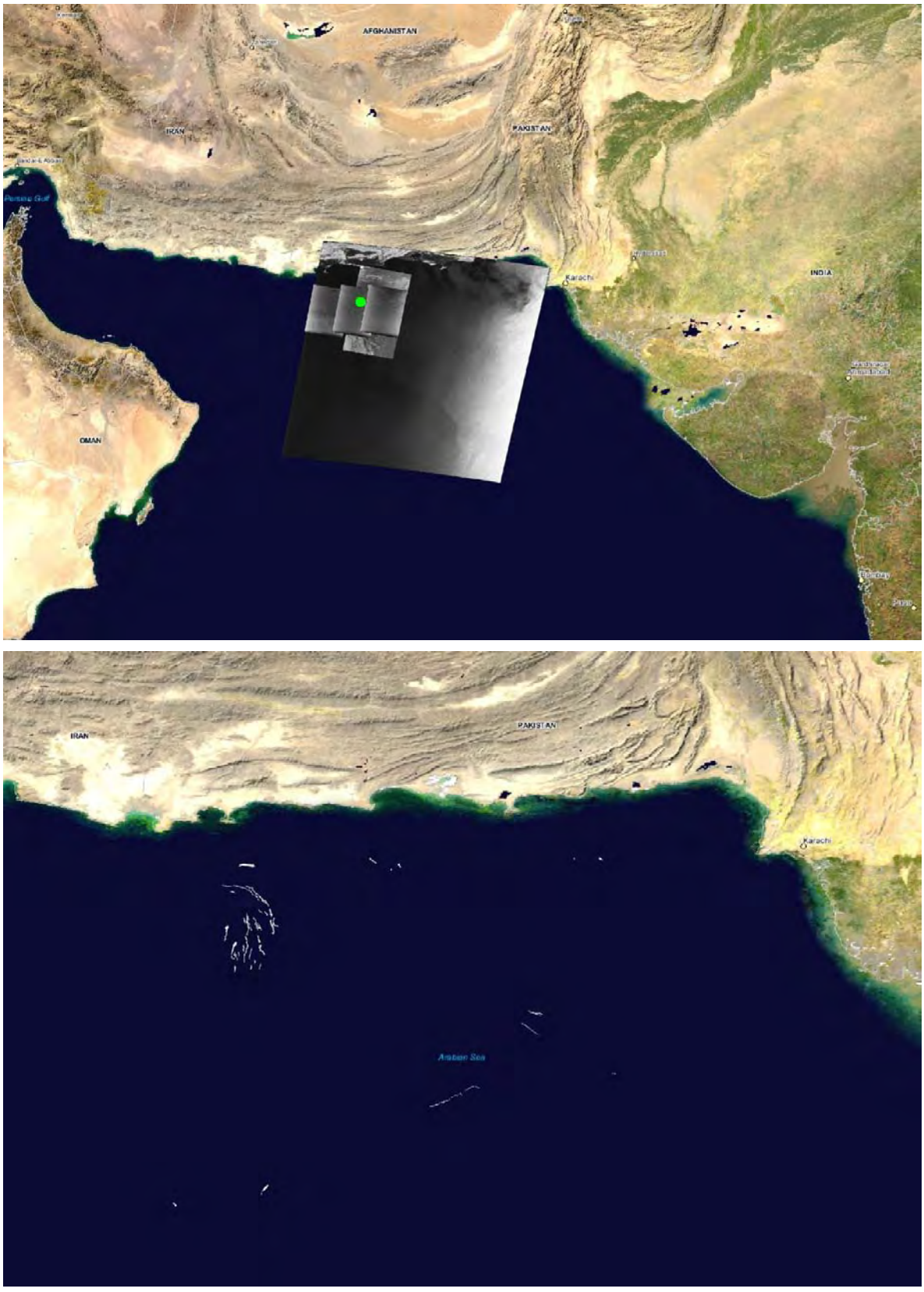

Figure 2.2: *SAR images processed offshore Pakistan. Upper panel shows regional setting and position of processed images.*

Lower panel shows TCNNA processed results.

Hydrocarbon fluid seepage has been detected in the thrust faulting regime generated in the Makran subduction zone offshore Pakistan [*Ding et al.*, 2010b] and active gas venting was observed in depths of 1020 m [*Thomanek et al.*, 2010]. The HYFLUX project examined the archive of SAR images with the goal of determining whether the SAR technique of detecting potential gas hydrate bearing areas would be effective on a geologically active margin. Similarly to the effort for the west coast of Africa, the HYFLUX team reviewed over 100 potential images and successfully geoprocessed six separate images. This review detected repeated oil targets over areas of the thrust fault. Although the MARUM group confirmed gas hydrates and gas venting in the general region, sampling to date has been focused to the east of the principal concentration of seep targets. Future effort will be required to provide detailed seafloor data regarding the sources of the oil detected in the SAR analysis.

2.5 CONCLUSIONS

Satellite remote sensing offers a comprehensive overview of the distribution and magnitude of natural oil and gas seeps in the Gulf of Mexico. Automated processing techniques make it possible to rapidly analyze the occurrence of floating oil discharged by natural seeps. With automated techniques, the available archive of images was sufficient to cover the search for evidence of seeps over the entire Gulf of Mexico and reliably to eliminate areas where seeps did not occur, as well as to distinguish natural seeps from probable pollution or transient events. Focusing efforts on the regions where seeps were prevalent, the satellite image archive provided enough repeat coverage so that statistical techniques could be used to identify the probable locations of geologic formations where oil and gas venting and shallow gas hydrates were likely to occur. A total of 1,081 such formations were detected. These sites share the general geographic extent predicted by geophysical records [*Frye*, 2008], but are far fewer in number. This suggests that the satellite methods are delineating seeps which are active in the present, while the geologic effects of seep (e.g. hard grounds, reflectance anomalies) will persist for features that have become inactive.

The depth distribution of these features and their associated gas hydrate deposits can be used to predict their disposition with respect to the hydrate stability horizon. Two findings emerge from this: first that consistent with recent geochemical analyses [*Stephan A. Klapp et al.*, 2010; *S. A. Klapp et al.*, 2010], gas hydrate structure in the shallower settings of the Gulf of Mexico basin would be constrained to structure II with structure I hydrate confined to depths >1000 m, and second that if this is in fact confirmed, gas hydrate stability is probably not challenged by variation in bottom water temperature within its present range.

An opportune comparison of satellite detection of seep formation versus acoustic survey confirms that there is broad overlap between the techniques. However, mismatches between seeps that have an acoustic signal indicates that satellite surveillance will be at best a minimum estimate for the magnitude and distribution of seeps. Preliminary investigations margins with very different geological styles from what is found in the Gulf of Mexico, show that these estimates can provide global information on natural seeps and gas hydrate. Posting of results on the www.sarsea.org website provides a mechanism for promoting wider investigation of shallow gas hydrate deposits by other investigators.

3. BUBBLE FLUX ANALYSIS

The HYFLUX mission sought to understand the importance of plume processes to methane flux from the seabed to the sea-surface for seepage in the Gulf of Mexico and to use these values to better understand total global fluxes. Plume processes are summarized schematically in *Figure 3.1*.

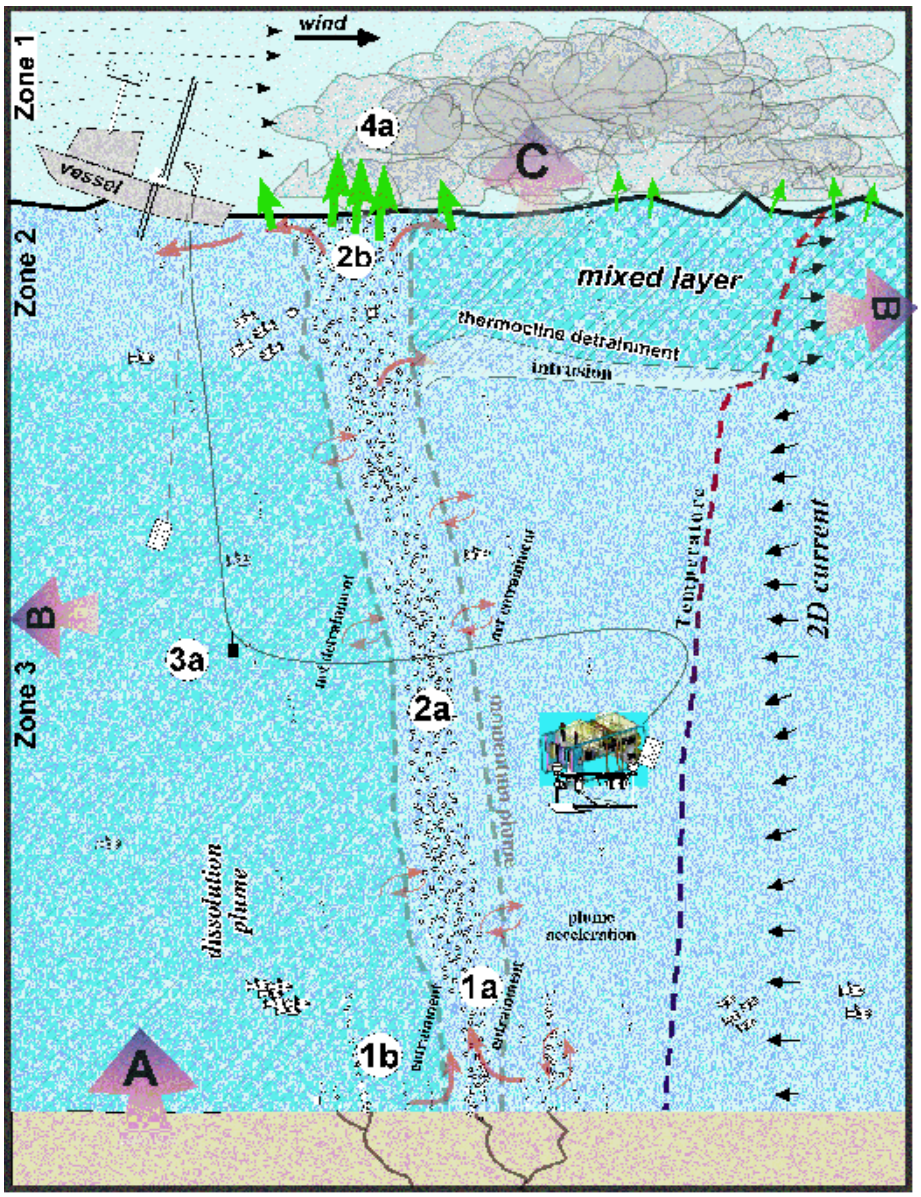

Figure 3.1*: Schematic showing bubble plume processes.*

3.1 BUBBLES AN BUBBLE PLUMES IN THE HYDRATE ZONE

Observations of natural seepage at hydrate depths provide insights into the behavior of large oily and gas bubbles in the hydrate stability zone. For example, sonar shows that bubbles can rise distances of hundreds of meters [*Granin et al.*, 2010; *Greinert et al.*, 2006; *Sauter et al.*, 2006] or even to more than two kilometers [*Spiess and Artemov,* 2010], indicating that bubble dissolution may not occur rapidly.

Underlying these observations of bubble survival is the deep sea process whereby methane bubbles develop hydrate skins that "separate" the methane from the water, preventing rapid conversion into hydrate particles. Importantly, the hydrate skin slows diffusion of methane from the bubble with its geochemistry controlled (to first order) by hydrate solubility rather than its gas phase diffusion rate. The result is dramatically enhanced bubble survival and reduced dissolution and hence increased flux to shallower waters [*G. Rehder et al.*, 2009; *Gregor Rehder et al.*, 2004].

Marine hydrocarbon seepage escapes from the seabed (Compartment 1) through one or more connected or unconnected pathways, rising towards the sea surface. During rise, dissolution causes methane loss to the water column at a rate that is determined by the bubble size, aqueous concentration, and high-pressure effects, such as hydrate skins, and bubble plume effects such as the upwelling flow (area 1a in *Figure 3.1*).

Various processes, including currents and stratification, affect the upwelling flow and the aqueous concentration in the plume; however, ADCP data were unavailable for the HYFLUX cruise. At various depths where buoyancy changes, such as the thermocline or at the top of the hydrate stability field, the potential exists for significant plume detrainment, e.g., as observed by Solomon et al. (2009) for Bush Hill. Such pooling in upper waters near the thermocline is also evident in data shown in *Figure 3.4* and cannot be explained by bubble processes, but rather only by bubble plume processes.

The plume also lifts colder, deeper water leaving a density signature that can be detected in CTD profiles (Zone 2). Dissolved methane in the deep sea is advected downcurrent, while in the mixed layer (Zone 2) it also sea-air gas exchanges into the atmosphere (Zone 1). Errors occur in interpretation of wind speed measurements and concentration measurements if they are strongly influenced by the boat's structure.

3.2 BUBBLE SIZE

Bubble size and seep depth are critical parameters for predicting the fate of seabed methane bubbles, and therefore bubble size distribution measurements are critical. Video from MC118 was analyzed and the bubble emission size distribution derived. The overall size distribution showed similarities both to size distributions reflective of vents with single bubble emissions (*Figure 3.2*, at 2483 µm) and a broad size distribution characteristic of a bubble plume with breakup (major plume), with a power law exponent of 0.79. A secondary poorly characterized single bubble vent that produced large bubbles with a fundamental radius of ~4900 µm was identified as well, but could simply be the result of poor resolution of the fall-off distribution of the major bubble plume. Bubble size distributions were calculated as in [*I. Leifer*, 2010].

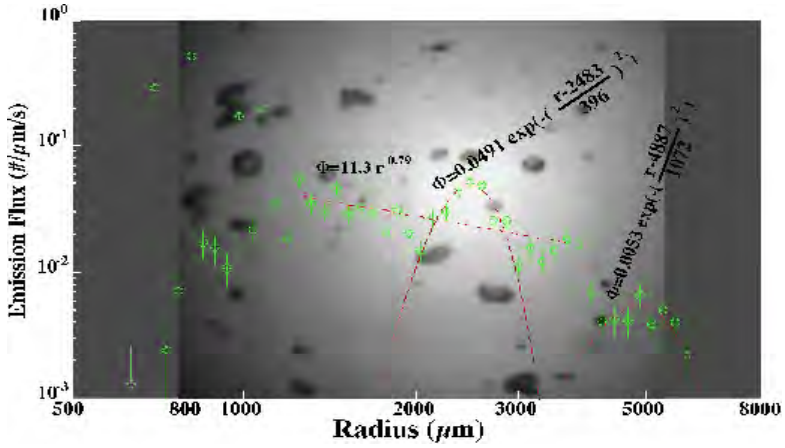

***Figure 3.2**: Bubble emission size distribution from MC118.*

Although the highest concentration of bubbles occurred for very small (800 µm) bubbles, they comprise a negligible fraction of the bubble mass (*Figure 3.3*). The 2500 µm emission mode contributes approximately equally to two other larger emission modes. Overall, this plume had a flux of 10.25 (cm^3/s), which at a depth of 980 m translates to a molar flux of 4419 mMol/s.

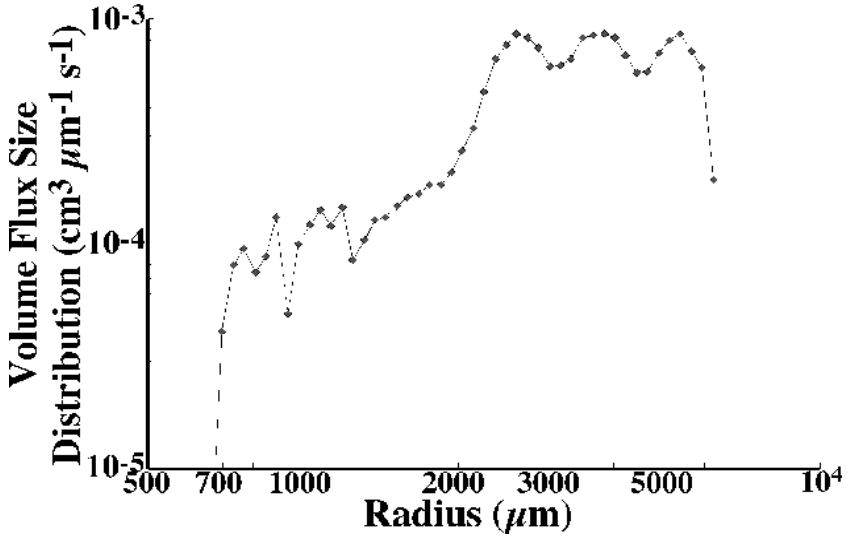

Figure 3.3: *Volume emission size distribution from MC118 bubble plume.*

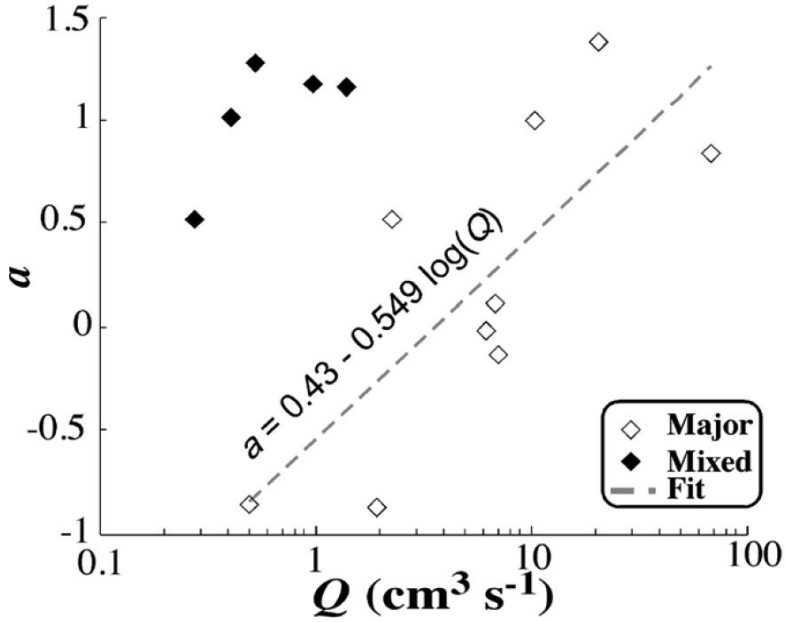

Figure 3.4: *Relationship between power law exponent, a, and bubble flux, Q, for major bubble plumes. From Leifer [2010].*

Based on the relationship between power law exponent and bubble flux in [*I. Leifer*, 2010] for the Santa Barbara Channel, the observed power law of 0.73 corresponds to a flux of a bit more than 22 cm^3 s^{-1} for non-oily bubbles (see *Figure 3.4)* in good agreement given the temporal variability in emission for this plume. Specifically, as is common with major bubble plumes of this magnitude, it pulses. This is both because larger bubbles rise faster and therefore reach the camera level sooner, and because of internal dynamics. The pulsing also is apparent in the time-size distribution which shows not only that pulses are

associated with the larger bubbles, but that the strong emission mode of the single bubble vent at 2250 µm was activated halfway through this data set. The largest bubbles were associated with pulses, and the appearance of smaller bubbles corresponded with larger pulses, consistent with higher flows and stronger turbulence bubble fragmentation. These results are summarized in *Figure 3.5*.

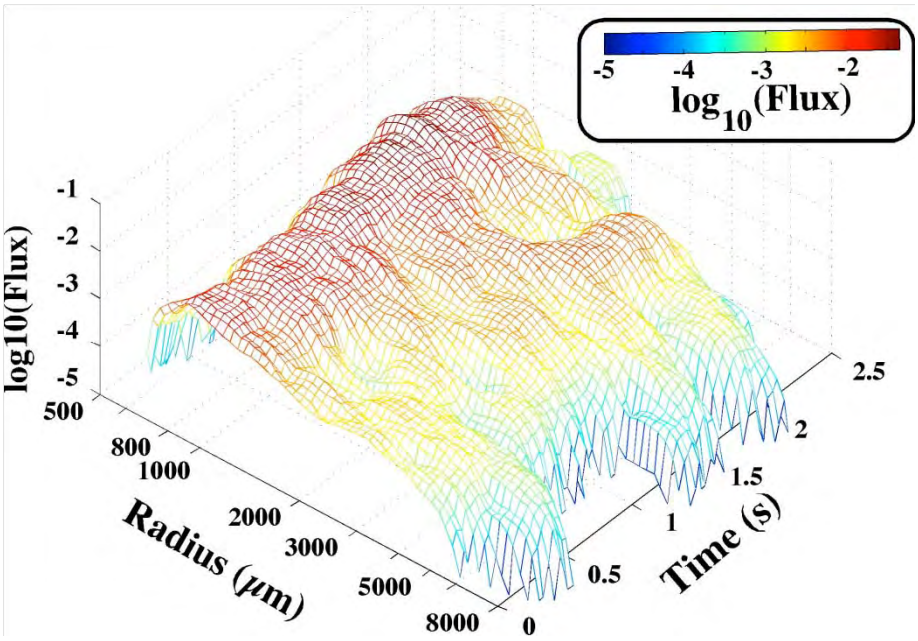

Figure 3.5: *Time and radius dependent bubble size distribution for the MC118 plume.*

Calculation of the emission size distribution depends on the rate bubbles are rising vertically. Based on an examination of the radius dependent rise speed (*Figure 3.6)*, the curve fit to the data roughly parallels the oily-bubble rise velocity parameterization, suggesting a consistent offset of approximately 10 cm/s for all bubble sizes. Based on a curve fit, this translates to an upwelling flow of 10.3 cm/s. Additionally, a few small bubbles were observed to rise very slowly, which can be due to turbulence, but the presence of some larger, very slow rising bubbles (r > 2000 µm), suggests that some bubbles are either oily, are aggregated with sediment, or have hydrate flakes attached.

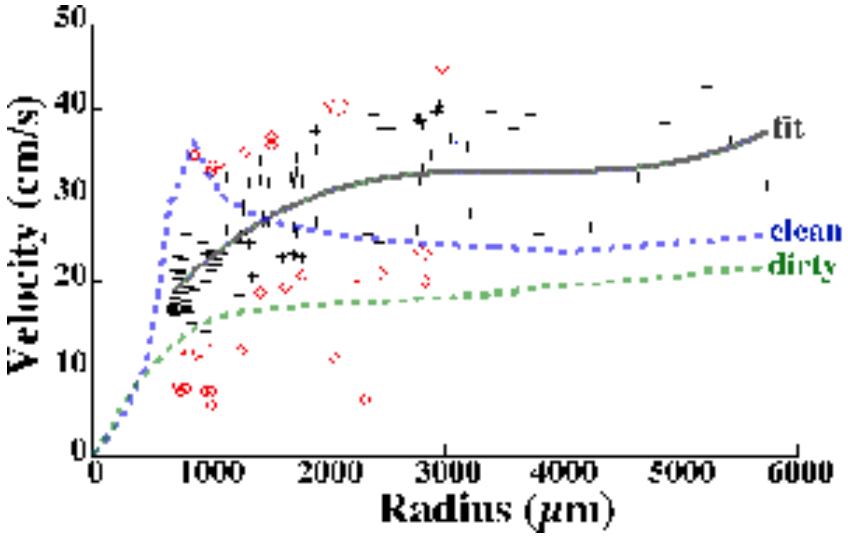

Figure 3.6: *Vertical velocity of MC118 bubble plume bubbles, clean and dirty rise velocity parameterization in stagnant water, and curve fit. Outliers are also noted on this figure.*

3.3 BUBBLE PROCESSES DURING RISE

As the bubble rises, the internal gases diffuse into the surrounding water leading to shrinkage, with gases having lower diffusivity (higher Schmidt number) evading the bubble slower. This will lead to progressive enhancement of larger n-alkane components until the bubble begins to dissolve (i.e., shrink) and trace gas evasion becomes controlled by the mass loss of the dominant gas (methane). In the deep sea, decreasing hydrostatic pressure is negligible. Furthermore, as a bubble rises, air inflows leading to bubble growth; however, [*G. Rehder et al.*, 2009] found the air inflow impact was negligible for typical hydrate depths.

Bubble Plume Processes

Some of these observations suggest plume processes associated with fluid detrainment are important. Furthermore, studies of natural seepage [*I. Leifer and Judd*, 2002; *E Solomon et al.*, 2009] and engineered plumes [*Ira Leifer et al.*, 2009] confirmed that strong stratification, such as at the thermocline/pycnocline, leads to large-scale plume fluid loss or detrainment, a phenomenon identified in the laboratory as distinct to two phase flows – bubbles [*McDougall*, 1978]. Upwelling flows associated with seep bubble plumes are effective at fluid-flow transport of water enhanced with elevated concentrations of dissolved gases and marine particles [*Ira Leifer et al.*, 2009]. Detrainment leads to deposition of these droplets as well as enhanced dissolved natural gas and oil components into intrusion layers [*Lemckert and Imberger*, 1993].

Other marine processes can affect the interaction between stratification and plume detrainment and a hydrocarbon flux to the surrounding ocean. For example, currents play an important role. Thus, during ROV tests in the Coal Oil Point seep field in June 2010 for slack current conditions, dye injections demonstrated that seabed fluid was transported across the thermocline and reached the sea surface. In contrast, for conditions earlier in the day under strong current conditions, no dye reached the sea surface.

3.4 NUMERICAL BUBBLE STUDIES

The deep sea fate of hydrocarbons from natural marine seepage was investigated with a numerical bubble propagation model. The model includes several deep sea processes including hydrate skin effects based on analysis of single-bubble release data, depth-dependent solubility, compressibility, and enhanced bubble density that slows bubble rise (note bubble density includes compressibility) and is described in [*G. Rehder et al.*, 2009]. Because the parameterization of individual bubble gas exchange depends on the rise velocity, enhanced density affects the gas exchange parameterization; however, second order effects on gas exchange are not considered, primarily due to an absence of literature. Results presented in [*G. Rehder et al.*, 2009] suggested that for depths to 1500 m these effects are small. Specifically, there were no “tunable parameters,” with all parameterizations based on the best understanding of deep sea CH_4 chemistry and bubble behavior, with the simulations performing extremely well for most conditions, the exception being hydrate skin covered bubbles deep in the HSF, which data showed had a tendency after ~10 minutes to dissolve at a far slower rate. This process was proposed to relate to a thickening of a hydrate skin. Because such processes are unknown, no effort was made to simulate them and model and data diverged in [*G. Rehder et al.*, 2009].

Initially, physical, fluid dynamical, plume, and chemical parameters are loaded (see model flowchart, *Figure 3.7*). The model can simulate a bubble plume or single bubbles. Where feasible, look-up tables are used for computational speed, including parameterizations for the individual bubble gas exchange rate, k_B, bubble rise velocity, V_B, diffusivity, etc. Bubbles in each size class are simulated including an imposed upwelling flow, V_{up}. The model then solves the coupled differential equations describing bubble rise and gas exchange [*I. Leifer et al.*, 2006; *G. Rehder et al.*, 2009]. Integration of the stiff set of differential equations is by a third-fourth order Runge-Kutta approach (a leap frog approach tends not to converge numerically), with integration tolerances chosen based on parameters affecting bubble

evolution, such as bubble size and depth. Integration continues until the bubble surfaces or dissolves to a set size, or for a set time. Model output for each bubble size is interpolated to a smooth depth grid, and the mass flux (to the water column) for the bubble (or plume) at each depth is calculated. The entire model is implemented in MATLAB (Mathworks, MA).

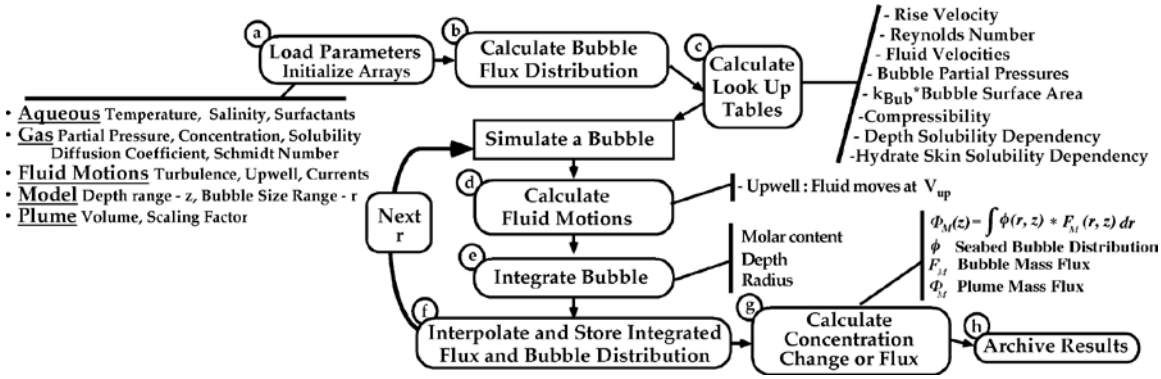

Figure 3.7: *Flowchart of numerical bubble model. Modified from Leifer and Judd [2002].*

In addition to the details described in [*G. Rehder et al.*, 2009], an oiliness parameter was added which arbitrarily reduced the rise velocity and gas exchange by the same amount. Given the absence of field (or laboratory) data on oily bubbles, this effect is explored as a sensitivity parameter rather than accurately simulating real world effects.

Two simulation cases were run, one with hydrate effects and one without, for simulations from 980 m. One improvement of the model is incorporation of temperature profiles, as well as allowing simulation of bubble oiliness, not used in these simulations. Simulations were run with a suite of alkanes C1-C5 (methane – pentane), as well as dissolved air which inflows the bubbles. Both simulations also incorporate an upwelling flow of 15 cm/s, which might be a little fast.

Single bubble simulations showed that absent deep sea effects, bubbles dissolve very rapidly, with a 2500 µm bubble dissolving in just a couple of hundred meters. The addition of hydrate and other deep sea effects almost doubled the bubble lifetime, but did not allow it to rise significantly further, only about another 100 m, still dissolving in the deep sea.

A significant amount of the mass flux also was contained in larger bubbles with a mode at about 5000 µm. Simulations of these very large bubbles showed they were able to rise to far shallower depths, reaching almost 250 meters before dissolving, although by 400 m depth, bubbles had shrank to almost 500 µm. This was in contrast to ROV bubble tracking observations, which suggested smaller bubbles (due to the regular sinusoidal oscillations; characteristic of bubbles smaller than 2000 µm, whereas 5000 µm bubbles exhibit irregular oscillations). Furthermore, tracked bubbles did not show signs of dissolving to such small radii at even 250 m – bubbles with a 500-µm radius cease oscillations, which was not observed.

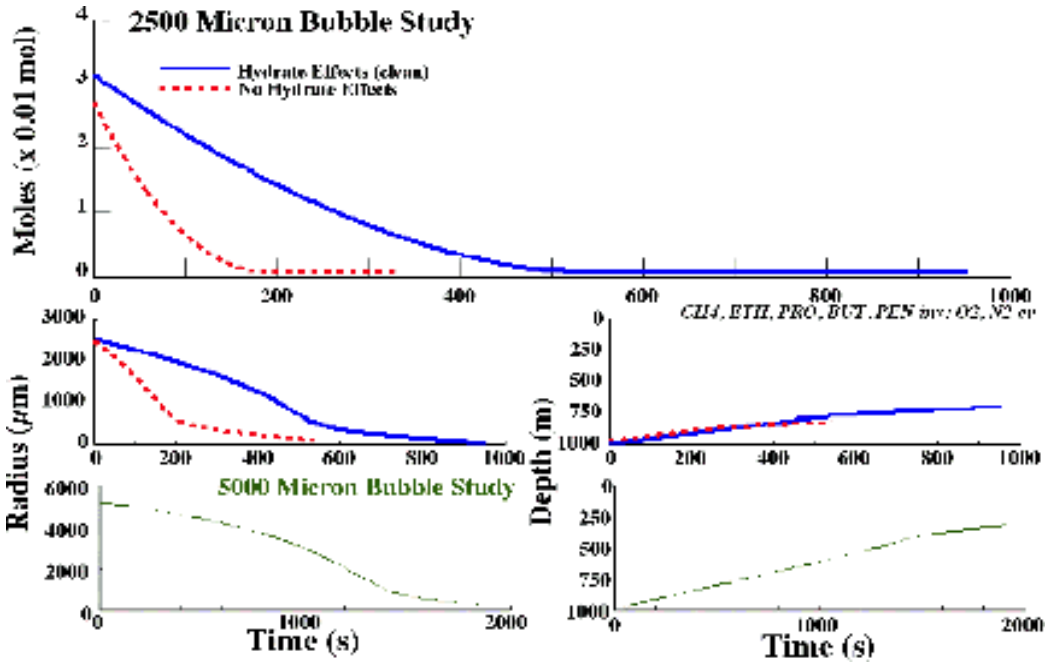

Figure 3.8: *Single bubble simulations for 2500 µm and 5000 µm radius bubbles with and without deep sea effects. (inv = invasion, ev = evasion).*

The single bubble simulations (*Figure 3.8*) showed that different bubble sizes exhibit distinct behavior, resulting in methane (and other trace gases) deposition with different depth profiles. Because a bubble plume comprises a range of different bubble sizes with different emission fluxes, bubble plume simulations were conducted (*Figure 3.9)*. Absent deep sea processes, methane bubble content decreases rapidly with depth, approximately uniformly split between the dominated by the 2500, 3700, and 5000 µm modes, but rapidly shifts towards the larger bubble plumes. As a result, the dissolution flux mirrors the pattern, with smaller emission modes depositing methane at a faster rate into the deeper water column. Incorporation of deep sea processes yields greater bubble survivability for bubbles of all sizes, and as a result, a shift in the deep sea dissolution relative importance to the smaller bubbles (larger bubbles survive better) as well as larger bubbles surviving to shallower depths. These changes also are seen in the integrated plume dissolution profile (*Figure 3.10*), with a quasi-exponential decrease where deep sea effects are included and much less so for the case where they are neglected, likely due to very rapid dissolution. This rapid dissolution is apparent in the pentane trend where the outgassing increases as the methane-driven outflow/dissolution forces the pentane to outflow at a rate faster than pure diffusion. This process also causes progressive enhancement of larger molecular components.

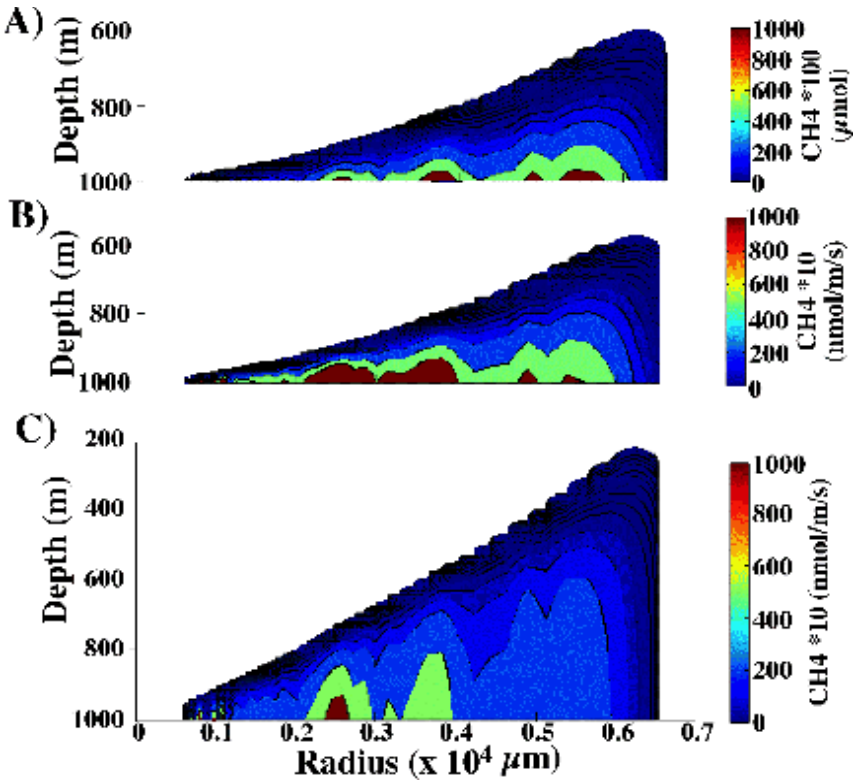

Figure 3.9: *MC118 bubble plume simulation of methane* ***A)*** *content and* ***B)*** *dissolution fluxes for no deep sea processes, and* ***C)*** *dissolution flux including deep sea processes.*

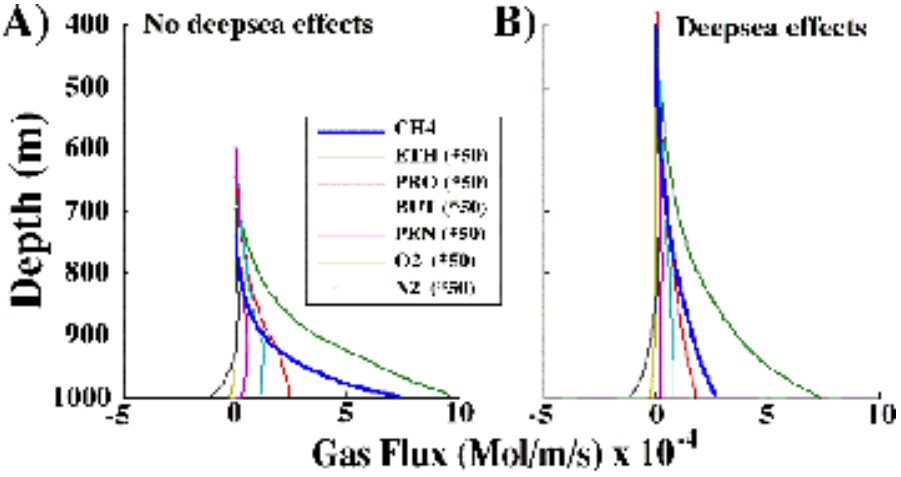

Figure 3.10: *Plume integrated dissolution rate to the water column absent* ***A)*** *no deep sea effects, and* ***B)*** *deep sea processes.*

For larger molecules, such as pentane, larger bubbles become far more important (*Figure 3.11)* with the largest reaching the sea surface (although they have lost more than 99% of their initial pentane and a greater fraction of their initial methane). The influx and subsequent dissolution force the outflow of the airgases and also is apparent. For the alkane tracer gases, the relative ratios vary with depth due to different diffusivities and solubilities, although uncertainty in parameters like solubility also play a role.

This demonstrates that measurements of trace gas ratios are a powerful diagnostic tool to unravel the importance of bubble and bubble plume processes and to predicting the deep sea methane's fate.

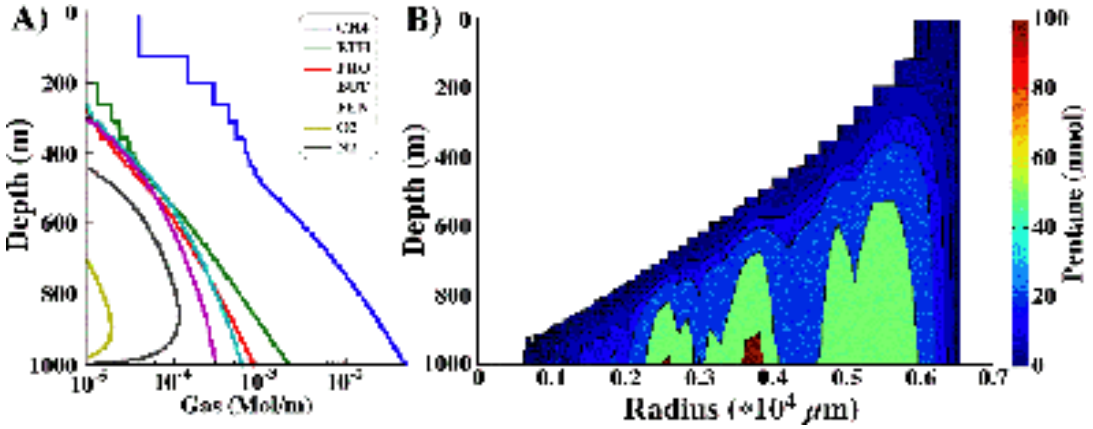

Figure 3.11: ***A)*** *Plume-integrated bubble gas content with depth for simulation of MC118 bubble including deep sea effects for a range of gases, and* ***B)*** *contribution of different bubble sizes to pentane bubble content.*

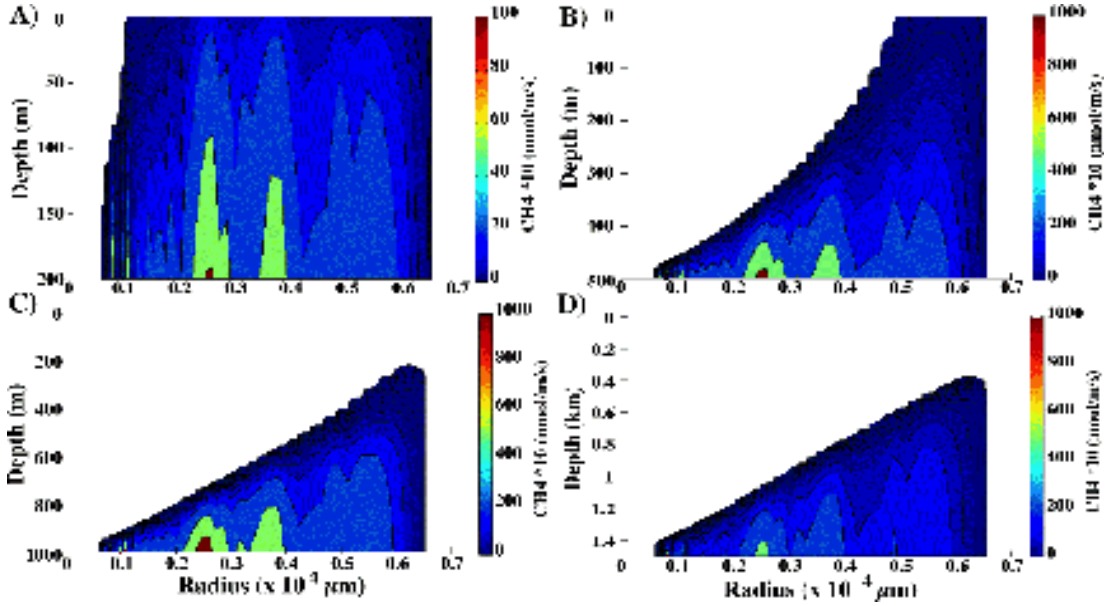

Figure 3.12: *Plume size and depth dependent dissolution flux for a bubble plume from* ***A)*** *200 m,* ***B)*** *500 m,* ***C)*** *1000 m, and* ***D)*** *1500 m. Depth effects simulated for all depths.*

The same plume exhibits very different behavior at different depths, with larger bubbles becoming more important as the depth increases (*Figure 3.12*). At 200 m, bubbles larger than about 1800 μm are able to transport methane to the sea surface, while at 500 m only quite large bubbles can, and at 1 and 1.5 km even the largest bubbles in the MC118 plume dissolve subsurface.

The total plume content for different release depths does not show a simple trend with increasing depth (*Figure 3.13*). From 200 m, much of the methane reaches the sea surface, while from 500 m, dissolution is faster (even for the first few hundred meters). As the plume is released deeper in the hydrate stability zone the dissolution rate slows down. As a result, a plume from 1500 m has the same amount of methane at 450 m (top of the hydrate stability field in the Gulf of Mexico) as a plume from 1000 m, despite having

risen a far greater distance. The inverse of these trends is captured in the dissolution flux rates (*Figure 3.13B*).

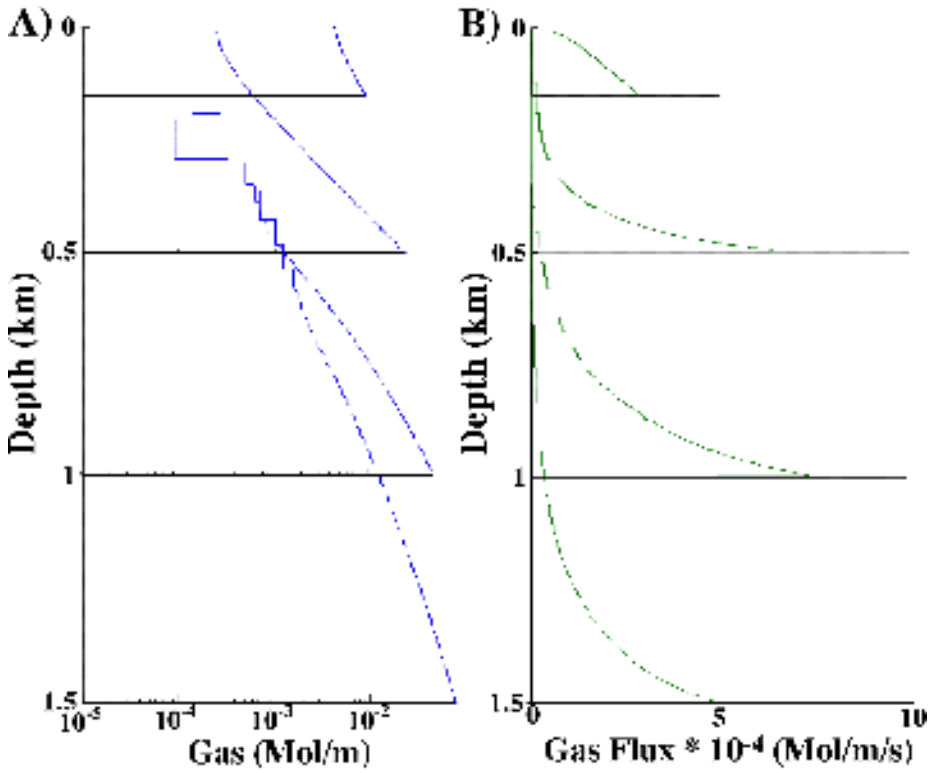

Figure 3.13. A) *Integrated plume content for a range of release depths and* ***B)*** *Dissolution fluxes.*

3.5 NEXT EFFORTS

Next efforts will focus on comparing water column measurements of methane and trace gases with model predictions, analysis of other bubble plume emission size distributions, and improvements in the bubble model to include Structure II hydrate skins, more realistic, multicomponent compressibility, and to simulate plume stratification processes.

What is clear from the simulations is that absent plume processes, the observed, top heavy methane profile cannot be re-created in the field. Secondly, the observations strongly suggest that smaller bubbles are surviving to very shallow depths, which cannot be explained absent either (unobserved) very strong upwelling flows, thick oil coatings (not observed), or Structure II hydrate processes.

A planned publication for submission in early Fall 2011 will tie together the modeling and observational data sets to characterize the importance of Structure II hydrate processes to deep sea bubble and bubble plume processes, the fate of the released methane and other hydrocarbons, and the connection between.

4. WATER COLUMN FLUX ANALYSIS

The information in results in this chapter have been published in the following journal article:
Solomon, E. A., M. Kastner, G. Robertson, I. Leifer, I. MacDonald, and J. Chanton (2011), Sea-air hydrocarbon fluxes associated with a 900-m seafloor gas hydrate deposit in the Gulf of Mexico, Proceedings of the 7th International Conference on Gas Hydrates, Edinburgh, Scotland, U.K.(17-21 July 2011).

4.1 INTRODUCTION

Methane is an important trace gas in the atmosphere playing a significant role in greenhouse warming and ozone destruction. The current global CH_4 flux to the atmosphere is relatively well constrained at ~582 Tg/yr (1 Tg = 10^{12} g), however the methane fluxes from many individual sources are not [*K L e a Denman*, 2007]. The current budget contains a fossil (^{14}C-depleted) CH_4 flux from fossil fuel-related anthropogenic emissions such as coal mining and crude oil exploitation of ~100 Tg CH_4/yr [*K L e a Denman*, 2007]. This flux estimate is based on the fossil methane in the atmosphere, thus is a top-down estimate. A significant fraction of natural methane emissions from geologic sources is also ^{14}C-depleted, but it is not currently included in the fossil methane budget because the methane fluxes from geologic sources remain poorly quantified. Of the various geologic sources of methane, it is likely the flux from marine seeps and mud volcanoes are the most significant e.g [*Kvenvolden and Rogers*, 2005]. The methane flux to the atmosphere from marine seeps and mud volcanoes are the least constrained of the geologic sources because they are difficult to identify and sample with traditional techniques.

Recent literature reviews have indicated that the global flux of CH_4 from marine seeps could be as high as 20-40 Tg/yr, which amounts to 1/3 of the current estimated anthropogenic fossil fuel-related emission to the atmosphere [*Etiope et al.*, 2008b; *Hornafius et al.*, 1999; *A. G. Judd et al.*, 2002; *Kvenvolden and Rogers*, 2005]. These estimates, however, are mainly based on approximations of seafloor methane fluxes and water column acoustic surveys, and rough estimates of the amount of CH_4 lost from bubbles during transit through the water column and the amount of methane that is oxidized aerobically. To move from first-order approximations of the flux of methane from marine seeps to the atmosphere to a more quantitative estimate, comprehensive tracking of methane from seafloor vent sources to the sea surface by direct sampling for methane concentrations in the water column is required, as well as direct flux measurements from the oceanic mixed layer to the atmosphere.

Most recent studies on constraining the fate of methane released from marine seeps have been carried out at the prolific hydrocarbon seeps at Coal Oil Point, California. These studies have indicated that the bubble plumes emitted at depths <100 m retain a significant fraction of their methane during water column transit and that they emit a considerable amount of CH_4 to the atmosphere locally [*Hornafius et al.*, 1999; *I. Leifer et al.*, 2006; *Mau et al.*, 2007].

There have only been a few studies quantifying CH_4 fluxes to the atmosphere from deepwater seeps (e.g. [*Greinert et al.*, 2006; *Kessler et al.*, 2006; *Reeburgh et al.*, 1991; *Schmale et al.*, 2005; *Valentine et al.*, 2001; *Yoshida et al.*, 2004]), which are more ubiquitous and cover a much larger area than the shallow water seeps. Most of these preliminary studies have indicated that CH_4 emitted from bubble plumes emanating from water depths greater than 200 m is almost entirely consumed before reaching the mixed layer as a result of bubble dissolution, aerobic methane oxidation, and gas exchange, thus are not a significant source of CH_4 to the atmosphere. However, these studies are limited in spatial extent, and most relied on traditional shipboard hydrocasts to sample the water column over the seeps. These traditional sampling techniques are inefficient at targeting seafloor vents and bubble plumes. Furthermore, some of the previous studies focused on areas where seepage occurs as single bubbles (e.g.[*McGinnis et al.*, 2006]). Single bubbles dissolve and lose most of their methane near the seafloor where it is oxidized by

microbes. The timescale of microbial methane oxidation in the deep sea is ~1 year [*Valentine et al.*, 2001; *Watanabe et al.*, 1995], which is short relative to the time it would take CH_4 to diffuse to the winter mixed layer (~50 yr;[*G. Rehder et al.*, 1999]). Most seafloor seeps, however, emit flares or plumes of bubbles in which the vertical methane transport is significantly enhanced by a wide bubble size distribution, upwelling flows, and surfactants such as hydrate skins and oil [*I. Leifer et al.*, 2006; *I. R. MacDonald et al.*, 2002; *G. Rehder et al.*, 2009; *E Solomon et al.*, 2009].

Using a new technique where methane concentrations and $\delta^{13}C$-CH_4 isotope profiles were directly collected immediately adjacent to bubble plumes in the Gulf of Mexico by manned submersible, Solomon et al. [*E Solomon et al.*, 2009] observed elevated methane concentrations throughout the water column. The $\delta^{13}C$-CH_4 profiles indicate that methane oxidation in the bubble plumes was negligible. Using new numerical bubble models that take into account methane solubility, compressibility, and multiple bubbles (e.g.[*G. Rehder et al.*, 2009]), they showed that bubble size, upwelling flows, and the presence of surfactants inhibit bubble dissolution. Consequently, CH_4 concentrations in the mixed layer above the 550-m seeps were 30-950 times saturated with respect to air in equilibrium with seawater at the in situ conditions, and contemporary diffusive methane fluxes to the atmosphere were 1-3 orders of magnitude greater than estimates from other deepwater seep sites [*E Solomon et al.*, 2009]. These results contradict the conventional wisdom that CH_4 emitted at deep seeps does not reach the mixed layer, and expands the depth range where bubble-mediated transfer of methane to the mixed layer is possible. Thus, the question of whether marine hydrocarbon seeps represent a significant source of methane to the atmosphere that should be included in the global atmospheric methane budget remains unresolved.

In the Gulf of Mexico, bubble plumes are visible throughout the water column on echograms, and the bubbles are often coated with a thin layer of oil [*I. Leifer and MacDonald*, 2003]. On reaching the sea surface, this oil is detected by satellite remote sensing methods such as synthetic aperture radar [*I. R. MacDonald et al.*, 2002]. Satellite imagery in the Gulf of Mexico shows ~1,100 perennial oil slicks associated with plumes [*I R. MacDonald*, 2011]. This is a conservative estimate that excludes the non-oily bubble plumes, which may be equally abundant as the oily plumes. Of the 1,100 seeps identified to date, ~76% of them occur at depths greater than ~550 m.

Accordingly, the main objective of the July 2009 HyFlux expedition was to investigate the sea-air CH_4 flux from deepwater (550-1200 m) hydrocarbon seeps associated with seafloor gas hydrate deposits in the northern Gulf of Mexico. Here we focus on tracking methane in bubble plumes emitted at 900-m depth from a 1 km^2 mound in MMS lease block Mississippi Canyon 118 (MC 118). This site is also the location of the DOE Gulf of Mexico Hydrates Research Consortium long-term gas hydrate observatory (*Figure 4.1*). The water column immediately adjacent to the bubble plumes emitted at MC 118 was sampled with an array of rosette bottles attached to a Max Rover ROV (*Figure 4.2*). In addition, traditional hydrocast profiles were collected at background locations and adjacent to the plumes, and a 150 × 150 m grid of shallow water hydrocasts (through the pycnocline) were collected above the seafloor source. The ROV and hydrocast samples were analyzed for C_1-C_4 hydrocarbons and $\delta^{13}C$-CH_4 to constrain the source of the methane, the dissolution depth of the bubbles, the extent of CH_4 oxidation in the water column, and the fraction of CH_4 that reaches the mixed layer. From the spatial distribution and abundance of methane in the mixed layer, diffusive fluxes to the atmosphere are estimated. This dataset provides constraints on the efficiency of bubble-mediated transfer of methane from deep (~1000 m) seeps to the mixed layer, and provides insight into the importance of deep seeps (the majority of Gulf of Mexico seeps) as a source of methane to the atmosphere.

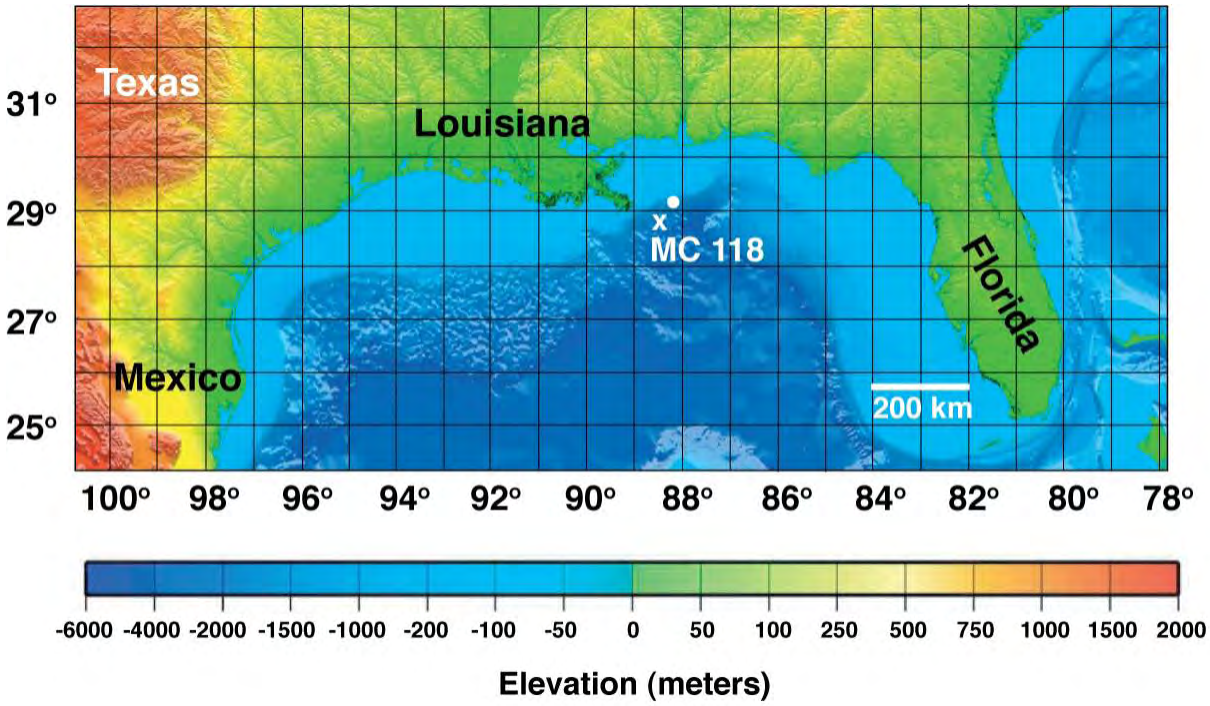

Figure 4.1: *Location of the MC 118 seep site.*

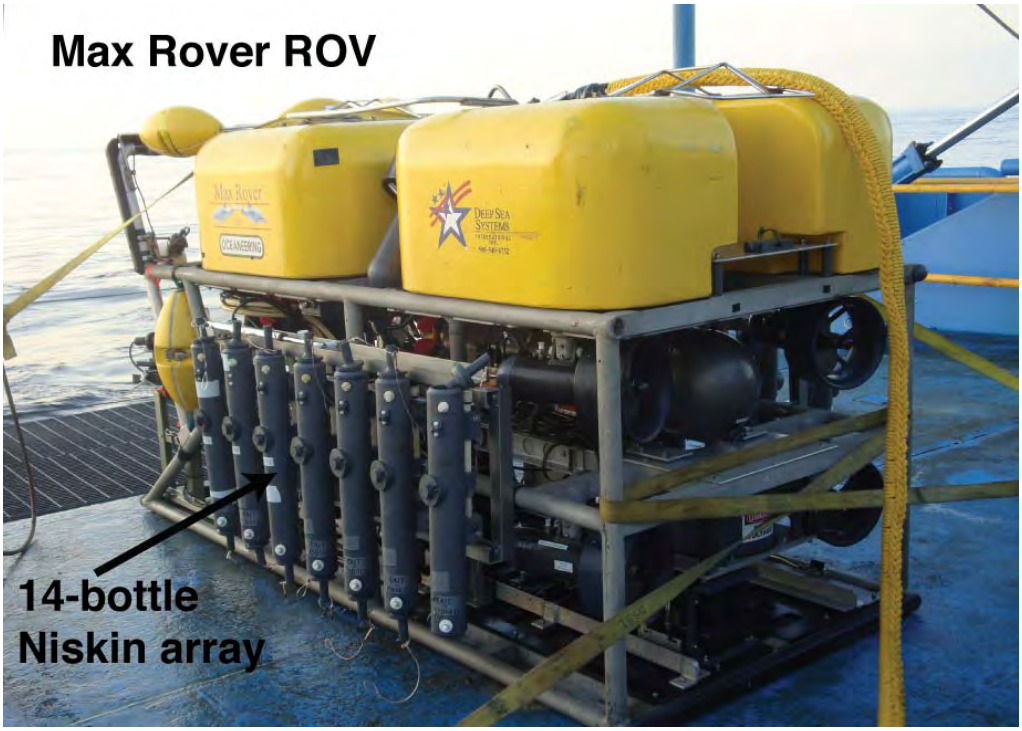

Figure 4.2*. The Max Rover ROV used to sample immediately adjacent to the bubble plumes at MC 118. Water samples were collected by an array of 14 bottles (7 on each side of the ROV) attached to the chassis. The Niskin bottles were tripped remotely one-by-one from the control room onboard the research vessel.*

4.2 SITE DESCRIPTION

The northern Gulf of Mexico is a prolific hydrocarbon province where rapid migration of oil, gases, and brines from deep subsurface petroleum reservoirs occurs through faults generated by salt tectonics [*H. H. Roberts and Carney*, 1997]. In the Gulf of Mexico, the focused expulsion of hydrocarbons is manifested at the seafloor by gas vents, gas hydrates, oil seeps, chemosynthetic biological communities, and mud volcanoes. Hydrocarbon gas is emitted as bubble plumes from focused vents within the larger hydrocarbon seep sites.

MC 118 is located east of the Mississippi Canyon and is on the continental slope at water depths ranging from 820-990 m (*Figure 4.3*). The swath bathymetry at MC 118 (*Figure 4.3A*) shows that the seafloor is smooth and featureless except for a submarine canyon crossing its northeastern portion and an area of irregular relief in its southwest portion [*Lutken et al.*, 2006; *McGee et al.*, 2008]. The area of irregular topography to the southeast is the focus of this study, and is a 1 km^2 mound that contains three crater complexes (*Figure 4.3A*).

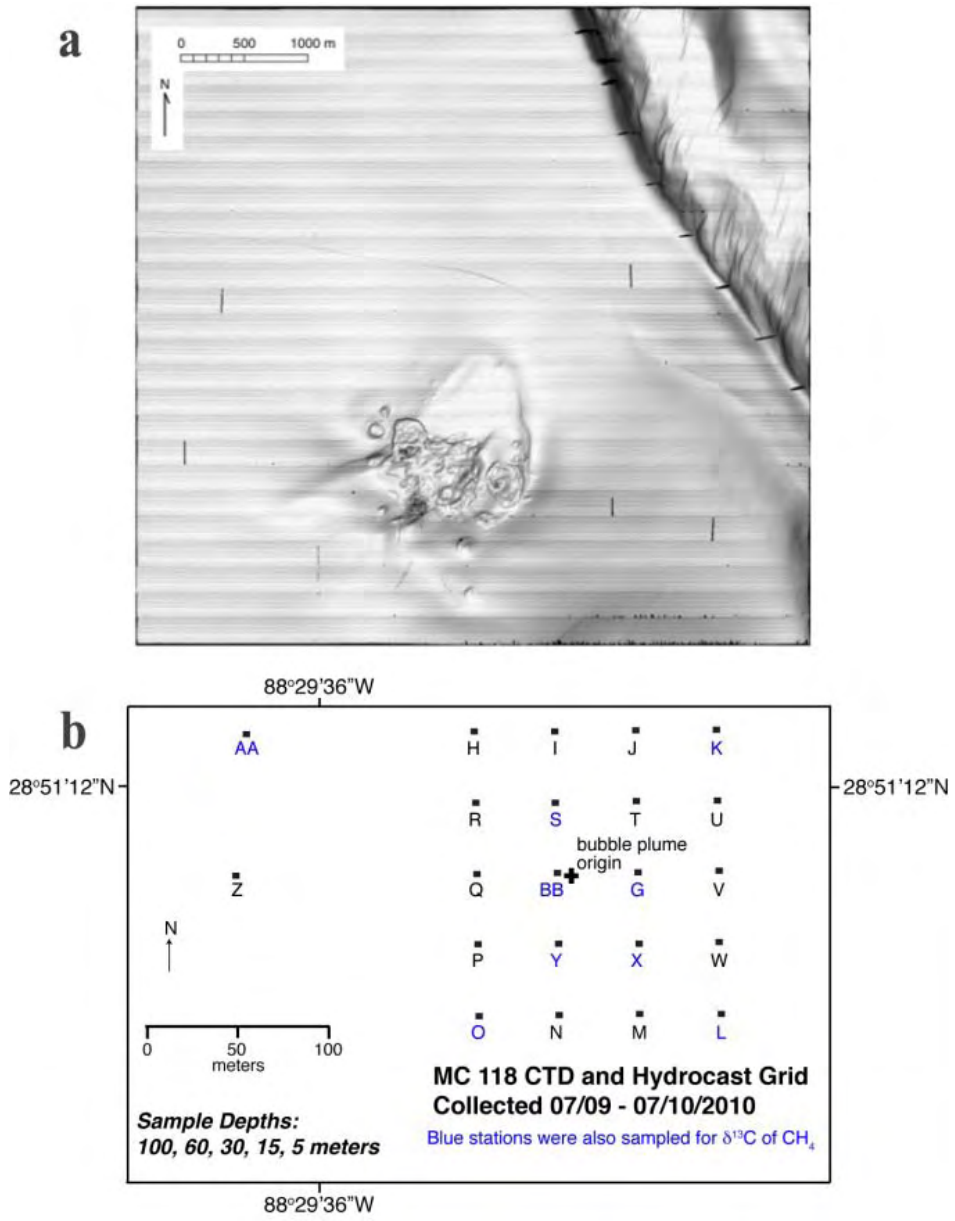

Figure 4.3 A: *Bathymetric image of MC 118 (from [Lutken et al., 2006]) showing region of irregular topography to the southwest.* ***B.*** *Hydrocast grid collected above a bubble plume emitted from the mound at MC 118. The distance between stations is 50 m, and the cross represents the plume origin.*

The mound supports a chemosynthetic biological community dominated by *Beggiatoa* mats, tubeworms, and mussels [*R. Sassen and Roberts*]. Fluid and gas venting at the mound is associated with fractures that originate from an underlying salt diapir that is estimated to be greater than 350 m deep [*McGee et al.*, 2008]. There are large Structure II gas hydrate outcrops associated with the region of high methane flux.

4.3 METHODS

Water Column Sampling and Analysis

Water column samples adjacent to the bubble plumes were collected by a Max Rover ROV operated by Oceaneering and the CTD/hydrocasts were deployed from the RV Brooks McCall, operated by TDI Brooks International. Complete analytical results for the water column samples collected are provided in ***Appendix IV***. Operations at MC 118 were conducted from July 5 to July 13, 2009. A total of five water column transects were made with the ROV at MC 118. The ROV samples were collected immediately adjacent to the bubble plumes (~3-4 m) to ensure the bubbles were not directly sampled. Navigation through the water column was based on visual identification of bubbles during ascent from the seafloor. During times when we lost visual contact with the bubbles, the ROV's forward-looking sonar was used to reacquire the plume. In general, we were unable to detect the bubbles with both the sonar and camera system above depths of ~300-150 meters below sea level (mbsl). This indicates that either the bubbles do not reach depths above ~150 mbsl and dissolve or they were advected away from the ROV at shallow water depths. Samples were collected roughly every 50 m from the seafloor at 895 m to 450 mbsl, and a frequency of one sample per 100 m above this depth. Due to restrictions imposed by the ROV's clump weight, samples could not be collected at depths shallower than ~25 mbsl.

The water samples were collected by an array of 14 Niskin bottles mounted to the ROV chassis, with seven bottles mounted to the port side and seven mounted to the starboard side of the vehicle (*Figure 4.2*). Bottles were triggered at a given depth remotely from the ROV control room onboard the RV Brooks McCall. The bottles were actuated on the ROV by a mechanical track that depresses the release button on the bottles triggering the springs that close the caps. Each Niskin bottle was immediately sub-sampled on deck upon recovery of the vehicle.

In addition to water sampling via ROV, six full water column CTD/hydrosts were deployed adjacent to the bubble plumes and at background locations. An additional 22 CTD/hydrocasts were deployed in the upper 120 m of the water column in a grid above the seafloor vent source (*Figure 4.3B*). Stations were spaced ~50 m apart and comprise a grid of about 150 × 150 m. These hydrocasts sampled across the pycnocline and into the mixed layer above the bubble plume, and were used to map out the spatial distribution of the methane saturation anomaly in the surface mixed layer, as well as to constrain the dynamics of methane transfer across the pycnocline.

Water samples collected via ROV and hydrocast were immediately transferred to serum bottles that were capped and crimped on deck. Duplicate samples were collected for hydrocarbon concentration analyses, and sub-samples were also collected for $\delta^{13}C\text{-}CH_4$ determinations. Both the concentration and isotope sub-samples were poisoned with a saturated $HgCl_2$ solution to halt microbial production and oxidation of methane. C_1-C_4 compounds were analyzed on a gas chromatograph equipped with a flame ionization detector (initially with a GC 14A, Shimadzu Corp. and later with a SRI Instruments 8610C GC-FID). C_1-C_4 compounds were resolved with a temperature program and using ultra-high purity He as a carrier gas through a stainless steel ShinCarbon ST 100/120 micropacked column. The standard error of the CH_4 analyses was ± 2%, and was < 3% for the C_2-C_4 analyses. $\delta^{13}C\text{-}CH_4$ analyses were carried out on a Finnigan MAT 252 mass spectrometer with a GC1 interface with a standard deviation of 0.6‰.

Estimation Diffusive Hydrocarbon Fluxes

The contemporaneous diffusive fluxes of methane, ethane, and propane from the mixed layer to the atmosphere were computed using the diffusive exchange equation:

$$\text{Flux} = k_{avg}(C_{plume} - C_{eq})$$

where k_{avg} is the gas transfer coefficient at the average wind speed and C_{eq} is the seawater hydrocarbon concentration in equilibrium with air at ambient conditions. The gas transfer coefficient for the diffusive flux equation was computed using the following empirical relationship [*Wanninkhof*, 1992]:

$$k_{avg} = 0.31u^2_{avg}(Sc/660)^{-0.5}$$

where u_{avg} is the average wind speed at 10 m above the sea surface and Sc is the Schmidt number. The equilibrium C_1-C_3 concentrations and Sc were computed on the basis of the CTD temperature and salinity profiles at MC 118 (*Figure 4.4)*. The diffusion coefficients for ethane and propane were estimated by the Wilke and Chang method [*Wilke and Chang*, 1955]. Due to the placement of the shipboard anemometer a few meters directly aft of the wheelhouse, wind coming from the ship's bow was blocked and created eddies and vortices behind the wheelhouse, thus these wind speed measurements were deemed unusable. For the contemporaneous wind speed at the study area, wind speed data from nearby NOAA National Data Buoy Center Station 42040 (~45 km from MC 118) was used. The local atmospheric methane concentration during the study period was measured every day, and was constant at 1.82 ppmv.

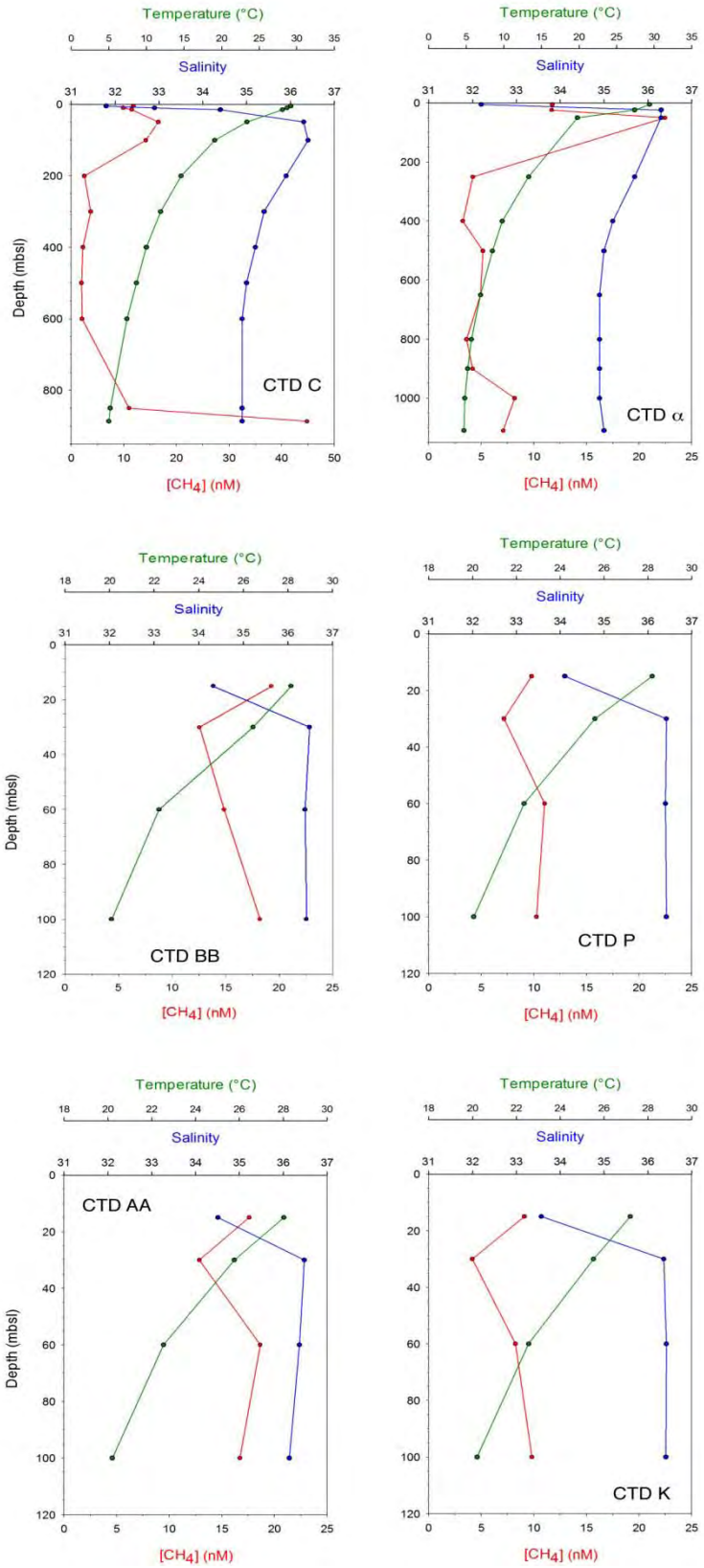

***Figure 4.4**: Profiles of temperature (green), salinity (blue), and methane concentrations (red) in the upper 120 m of the water column.*

Uncertainties in the estimated diffusive fluxes arise from inherent variations in u_{avg} affecting the k_{avg} estimation, and the various relationships between u_{avg} and k_{avg} in the literature. For instance, an increase in the wind speed from 4 to 5 cm/s (daily average) increases the methane flux estimate by ~50%. In addition, for a given u_{avg}, use of the various other parameterizations for k_{avg} produces differences in the methane flux of 10-40% [*Mau et al.*, 2007]. Surface films such as floating oil can also reduce gas exchange by as much as 50% [*Frew et al.*, 2004]. Given that there is some oil associated with the MC 118 seep site, the diffusive flux estimates at MC 118 should be considered high values.

4.4 RESULTS

Bottom water sampled by ROV had CH_4 concentrations ranging from 158 to 38,150 nM (*Figure 4.5*). Bottom water collected by traditional hydrocast adjacent to the bubble plumes contained methane concentrations ~0.2% of those sampled by ROV (*Figure 4.5*). The bottom water concentrations measured at MC 118 are ~three times those measured at the bubble plumes emitted at 550-m water depth at Bush Hill (GC 185; [*E Solomon et al.*, 2009]). The GC 185 bubbles had a visible oil coating and the plume had associated drops of oil, whereas the bubbles emitted at MC 118 did not appear to have an oily coating.

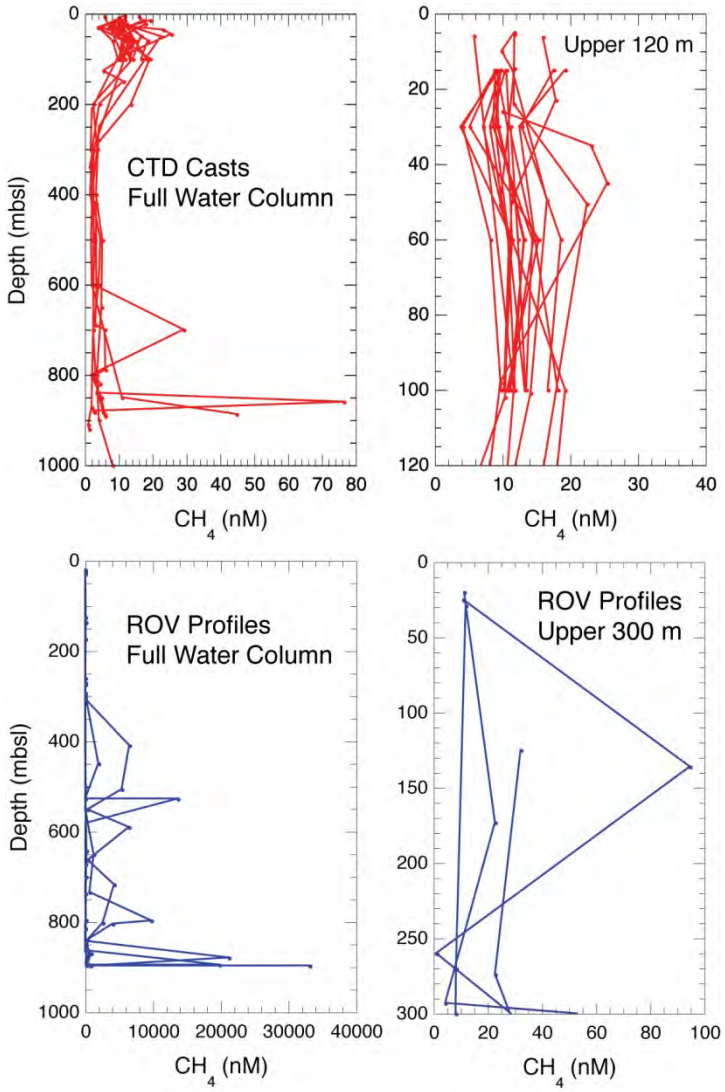

Figure 4.5. *Methane concentration profiles sampled by CTD/hydrocast and ROV.*

Methane concentrations measured in samples collected by the ROV decrease abruptly from the seafloor to ~800 mbsl, are variable between 800 and 600 m, then increase again between 550 and 500 m, coincident with the upper boundary of the gas hydrate stability field at this site. Bubbles were not detected by the ROV camera system and sonar above depths of ~300 to 150 m (dependent on the specific ROV dive). Between the top of the gas hydrate stability field and 300 m, CH_4 concentrations decrease sharply reaching near steady values of 10-40 nM above this depth. Thus, CH_4 concentrations sampled by the ROV near the mixed layer are 0.2% of the CH_4 concentrations at the seafloor.

Methane concentrations sampled by CTD/hydrocast are relatively constant from ~800 m to 200 m (*Figure 4.5*) ranging from 2 to 10 nM. Above ~200 m, CH_4 concentrations increase abruptly and remain elevated into the mixed layer with near surface CH_4 concentrations ranging from 6 to 24 nM. The zone of increasing methane concentrations above 200 m is coincident with an increase in the temperature gradient (*Figure 4.4*). Methane concentrations are supersaturated with respect to seawater in equilibrium with air at the in situ conditions at each station comprising the hydrocast grid in the upper water column at MC 118 (*Figure 4.3*). Methane concentrations range from 3.8 times saturation in the northeastern portion of the grid to 15 times saturation immediately above the seafloor location of the bubble plume (Station BB, *Figure 4.3*).

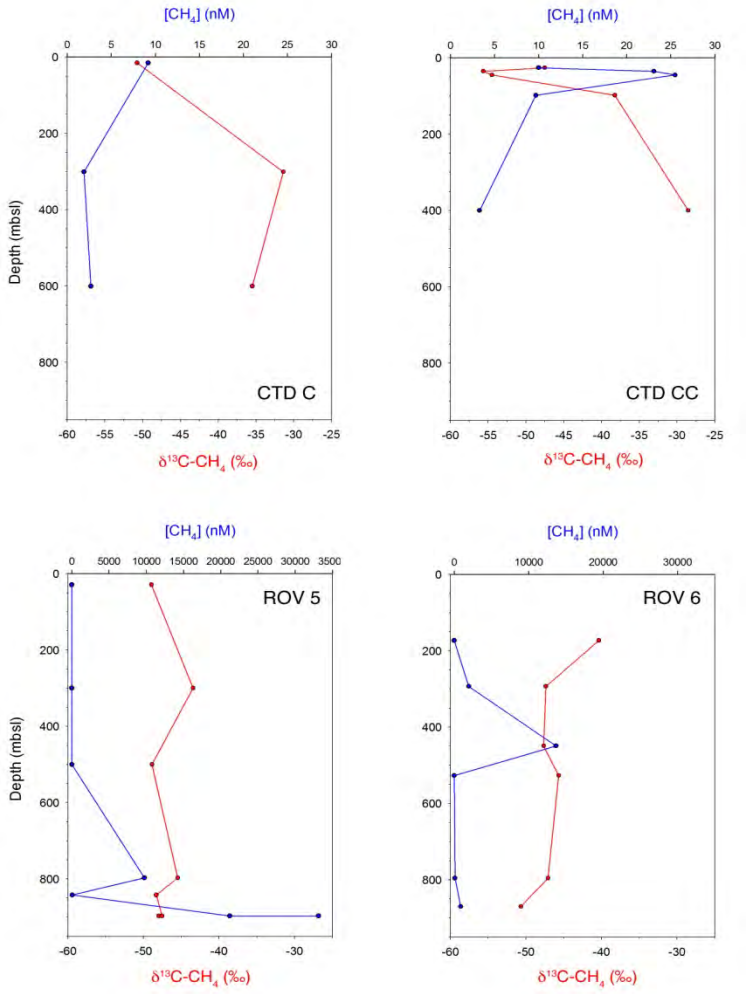

***Figure 4.6**: Water column δ^{13}C-CH_4 (red) and CH_4 profiles sampled by CTD/hydrocast and ROV.*

The strongest gradient in temperature occurs from ~200 m to 15 m, above which temperature is almost constant, signifying the top of the thermocline during the study period. Salinity, however, increases from ~400 m to 30 m, then rapidly decreases reaching ~32 at the sea surface (*Figure 4.4*). The strong salinity gradient of ~0.15/m was consistent from sampling station to sampling station and over the duration of the field campaign at MC 118. Variations in methane concentrations above ~120 m are related to these variations in temperature and salinity in the upper water column. Methane concentrations reach minimum values at ~30 m at most stations, coincident with the peak in salinity and immediately below the halocline extending to the sea surface. At the base of the halocline, CH_4 concentrations increase (*Figure 4.4*). At a few of the stations, however, the opposite trend is observed, where CH_4 reaches a local maximum before the halocline and decreases slightly within the halocline (*Figure 4.4*).

Bottom water $\delta^{13}C$-CH_4 values range from -51 to -48‰ (*Figure 4.6*), indicating the gas venting at MC 118 is a mixture between a biogenic and thermogenic source. Different methane sources were also measured in the sediment column at MC 118 where the upper 50 cm below the seafloor (cmbsf) was dominated by in situ microbial production of CH_4 and the methane below 50 cmbsf was predominantly thermogenic [*Lutken et al.*, 2006]. The $\delta^{13}C$-CH_4 of samples collected immediately adjacent to the bubble plume via ROV are relatively constant with depth, but, in some cases, do increase by ~10‰ toward the mixed layer. This increase in $\delta^{13}C$-CH_4 towards the sea surface indicates some microbial oxidation of CH_4 near the bubble plumes.

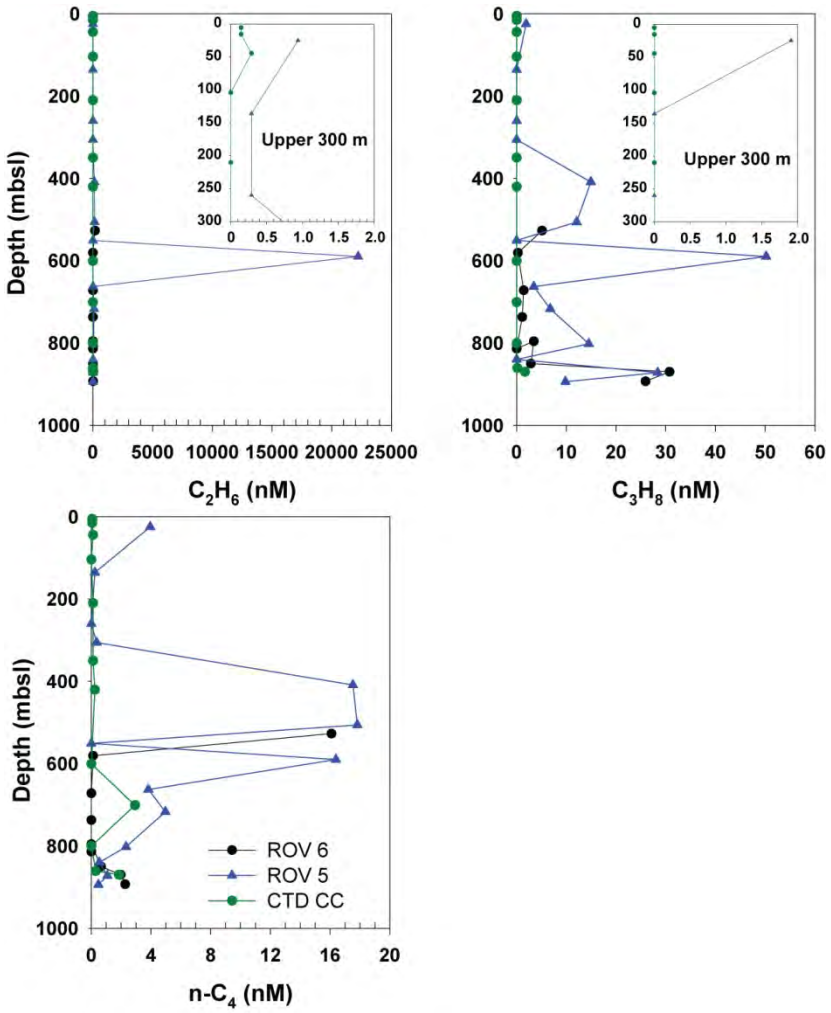

Figure 4.7: *Profiles of ethane, propane, and n-butane.*

The $\delta^{13}C$-CH_4 profiles collected by hydrocasts are a mirror image of the CH_4 concentration profiles (*Figure 4.6*). In general, the $\delta^{13}C$-CH_4 sampled by the hydrocasts is enriched in the lower water column to mid-water column with values ranging from -35 to -25‰, clearly indicating aerobic methane oxidation at greater lateral distances from the bubble plume. The zone of most extensive CH_4 oxidation occurs from ~800-200 m depth. Above 200 m, where methane concentrations start to increase (*Figure 4.5*), $\delta^{13}C$-CH_4 decreases indicating the input of fresh, non-oxidized methane to the upper water column.

C_2-C_4 concentrations are moderately elevated and variable from the seafloor to ~600 m, and they increase and remain highly elevated from 600 to 450 m (*Figure 4.7*). This depth range encompasses the top of the gas hydrate stability field at this site. Above this depth, C_2-C_4 concentrations decrease dramatically. Nevertheless, ethane, propane, and butane migrate all the way from the seafloor at ~900 m to the mixed layer with mixed layer ethane and propane concentrations up to 626 and 9,500 times saturation with respect to seawater in equilibrium with air at the ambient conditions.

4.5 SUMMARY AND DISCUSSION

This was the first study where hydrocarbons were directly sampled from the seafloor to the sea surface by ROV from a seep site deeper than 600 m. This comprehensive dataset provides constraints on the source of the methane, the dissolution depth of the bubbles, the extent of methane oxidation in the water column, the fraction of CH_4 that reaches the mixed layer, and the contemporary diffusive flux of hydrocarbons to the atmosphere. The $\delta^{13}C$ of methane immediately adjacent to the seafloor source indicates that the CH_4 venting to the water column at MC 118 is a mixture between a biogenic and a thermogenic source. To test whether the bubbles had an oily coating, a push core was inverted over the bubble plume with the ROV's manipulator. We allowed gas hydrate to form within the push core over a ~15 minute period, and, upon visual inspection with the ROV camera system, the gas hydrate was white and there were no clear signs of oily gas hydrate or oil droplets. Thus, unlike the bubble plumes at Bush Hill [*E Solomon et al.*, 2009], the plumes at this site were only associated with minor amounts of oil during the sampling period.

From visual observations at the seafloor, the bubble plume has high bubble fluxes, upwelling flow of fluids, and a relatively broad bubble size distribution in comparison to vents that produce a single stream of bubbles. The bubbles emitted at MC 118 also appear to be coated with a thin gas hydrate skin. All of these are critical factors that enhance bubble-mediated hydrocarbon transfer through the water column [*I. Leifer et al.*, 2006; *G. Rehder et al.*, 2009; *E Solomon et al.*, 2009]. The sharp decrease in CH_4 concentrations from the seafloor to ~800 mbsl is likely a manifestation of the broad bubble size distribution; in this depth range the small bubbles (radius < 1mm) likely completely dissolve. The peak in C_1-C_4 concentrations observed between ~550-500 m coincides with the top of the gas hydrate stability field at this site. Below this depth, the thin gas hydrate skin coating the bubbles inhibits bubble dissolution and gas transfer across the bubble surface, enhancing hydrocarbon transfer through the water column. At the top of the gas hydrate stability field, the thin gas hydrate skin dissociates, enabling the transfer of hydrocarbons across the bubble surface and enhancing bubble dissolution. Methane concentrations remain highly elevated from ~550-350 m then decrease, indicating that most of the bubbles have dissolved by this depth as a result of the loss of the protective gas hydrate barrier. This indicates that the bubbles travel an additional ~200 m through the water column after gas hydrate dissociation before dissolution; this is consistent with observations presented in ref. [*G. Rehder et al.*, 2009] above the gas hydrate stability field. A fraction of the methane emitted at the seafloor seep, however, is transferred to the mixed layer as observed in the elevated C_1-C_4 concentrations at ~20 m in the ROV transects and the increase in CH_4 concentrations above 200 m in the hydrocast survey (*Figure 4.5*).

As methane concentrations increase towards the mixed layer there is a concomitant decrease in $\delta^{13}C$-CH_4. Below ~200 m, $\delta^{13}C$ is enriched indicating a significant amount of methane oxidation occurs in the water

column. This is especially evident in the hydrocasts collected at background locations away from the bubble plume. The values of $\delta^{13}C\text{-}CH_4$ in the upper water column are almost equivalent to the $\delta^{13}C\text{-}CH_4$ of the vent fluid at the seafloor, suggesting the methane transferred into the mixed layer is from a source with a short residence time in the water column that has not undergone a significant amount of oxidation. This source could be from residual bubbles that are transported the entire water column distance from the seafloor or from dissolved plume methane that upwells into the upper water column. In most cases, this methane-rich fluid intrudes into the base of the halocline at ~25 m, indicating plume detrainment and deposition. Once deposited at the base of the halocline, the methane migrates to the sea surface by vertical mixing when the halocline breaks down and by diffusion. These results show that hydrocarbons can be transferred from depths of ~1000 m to the sea surface, and that the transfer is much faster than the rate of microbial methane oxidation. Furthermore, the results indicate that the diffusive flux of this methane into the atmosphere is much faster than the methane oxidation rate in the upper water column.

Methane concentrations near the sea surface collected by the grid of hydrocast stations above the plume are above saturation with respect to seawater in equilibrium with air at in situ conditions. Methane concentrations range from 3.8 times saturation at the northeastern portion of the grid to 15 times saturation at the station closest to the inferred surfacing location of the bubble plume. The average methane saturation anomaly for the stations adjacent to the inferred plume surfacing location (grid stations R, S, T, G, BB, Q, P, Y, X) is 700%. Likewise, C_2H_6 and C_3H_8 concentrations are highly elevated above those expected for equilibrium with air, and average 630 and 92,540 times saturation, respectively. From the near sea surface hydrocarbon concentrations and the average wind speed at the study area of 5.37 m/s, the contemporary (day of sampling) diffusive methane fluxes to the atmosphere were estimated (*Table 4.1*). The estimated average diffusive flux of methane, ethane, and propane to the atmosphere are 26.5, 2.1, and 2.78 $\mu mol/m^2d$, respectively. The estimated CH_4 flux is a small fraction of the flux measured at the 500-m seep at GC 185 [*E Solomon et al.*, 2009], and is about ½ to 1/3 of the CH_4 flux rom shallow water seeps in the Black Sea [*Schmale et al.*, 2005]. Though the methane concentration and estimated flux above the 900-m seep at MC 118 is much lower than the fluxes measured at shallow water seep sites like Coal Oil Point, the concentrations are still highly elevated above background levels over a fairly large area (30,000 m^2). Considering that the majority of seeps in the Gulf of Mexico are deep (>700 m), elevated CH_4 concentrations in near-surface waters resulting from bubble-mediated CH_4 transport in the water column are expected to be widespread in the Gulf of Mexico.

Table 4.1. *Estimated contemporary diffusive fluxes of methane, ethane, and propane to the atmosphere at MC 118.*

Hydrocarbon	Avg. Near-Surface Concentration (nM)	Times Saturation	Contemporary Diffusive Flux ($\mu mol\ m^{-2}\ d^{-1}$)
CH_4	11.6	7	26.5
C_2H_6	1.00	630	2.10
C_3H_8	1.91	92,540	2.78

The concentration of the heavier hydrocarbons ethane and propane in surface waters are greatly elevated with respect to background concentrations (background = 1.5-2.0 pM). Very few studies have investigated the natural emission of C_2H_6 and C_3H_8 from natural seeps and their potential contribution to global atmospheric ethane and propane budgets. The contemporary fluxes of C_2H_6 and C_3H_8 at MC 118 are 2-3 orders of magnitude greater than previous estimates from the marine environment [*Plassdulmer et al.*, 1995; *Plassdulmer et al.*, 1993]. Atmospheric mixing ratios of ethane and propane range from a fraction of a part per billion to a few parts per billion, making ethane the second most abundant trace gas in the atmosphere after methane. The mean atmospheric lifetime of ethane is ~2 months, but can be as long as ~10 months in the winter, and the lifetime of propane in the atmosphere is ~2 weeks. The global

flux of ethane and propane to the atmosphere based on tropospheric removal rates are 13-15 Tg/yr and 12 Tg/yr, respectively [*Etiope and Ciccioli*, 2009; *Stein and Rudolph*, 2007]. Current emission inventories for C_2H_6 and C_3H_8 include fossil fuel production and transmission, biomass burning, biofuel consumption, waste treatment, and soil microseepage. Bottom-up estimates of the global fluxes based on these emission inventories underestimate the global flux of C_2H_6 by 3-6 Tg/yr and C_3H_8 by ~3 Tg/yr. Based on the high diffusive fluxes associated with the deepwater seep at MC 118 measured in this study, it is possible that fluxes from marine seeps fill part of the gap in the global atmospheric ethane and propane budgets.

5. AIR-SEA FLUX ANALYSIS

The information in results in this chapter have been published in the following journal article:
Hu, L., S. A. Yvon-Lewis, J. D. Kessler, and I. R. MacDonald (2012), Methane fluxes to the atmosphere from deepwater hydrocarbon seeps in the northern Gulf of Mexico, J. Geophys. Res., 117(C1), C01009.

5.1. INTRODUCTION

Methane (CH_4), one of the most important greenhouse gases, has a warming potential 23 times that of carbon dioxide over a 100-year time horizon [*Ramaswamy et al.*, 2001]. It is also actively involved in tropospheric ozone production and stratospheric ozone destruction. The total amount of methane reserved in the form of gas hydrate is about 15 X 10^6 Tg in a global inventory [*Kvenvolden and Rogers*, 2005]. It is comparable to about 3000 times the total mass of the global atmospheric methane, 4850 (±242) Tg [*IPCC*, 2001]. Although the gas hydrate is an enormous methane reservoir, the contribution of the gas hydrate from the seafloor to the atmospheric methane budget is poorly characterized. It was estimated that marine seeps emit 8 – 65 Tg yr^{-1} of methane from the continental shelves to the overlying water column. If all of this methane was transported to the atmosphere, it could account for as much as 1 – 11 % of the total annual methane emission in the atmosphere [*Hornafius et al.*, 1999; *Hovland et al.*, 1993; 2001; *Kvenvolden and Rogers*, 2005]. However, these estimates are based on methane seafloor fluxes.

Methane released from the seafloor or produced in microenvironments in the water column [*Cynar and Yayanos*, 1991; *Deangelis and Lee*, 1994] can reach the atmosphere through turbulent diffusion or rising bubbles. In shallow water, rising bubbles are the predominant pathway for delivering methane from seeps to the atmosphere, while the net sea-to-air fluxes via diffusion are also considerable [*Mau et al.*, 2007; *Schmale et al.*, 2005]. In deep water systems, turbulent diffusion is a commonly cited pathway to deliver methane to the atmosphere, whereas it is still debatable whether or not bubbles are capable of surviving from the seafloor to the surface and, if so, how much methane would be displaced by other gases (i.e. oxygen, nitrogen etc.) as they are stripped out of the water as the bubble moves to the surface [*McGinnis et al.*, 2006; *G. Rehder et al.*, 2002; *G. Rehder et al.*, 2009]. Methane transport via rising bubbles from the deepwater seeps to the atmosphere depends on a variety of geological and physical parameters, including intensity and composition of the seepages, bubble initial size, release depth, bubble path, and dissolution rate [*I. Leifer and MacDonald*, 2003]. Most previous studies reported that the diffusive net sea-to-air fluxes of methane from deepwater seep systems (water depth > 200 m) are insignificant [*Kessler et al.*, 2006; *Reeburgh et al.*, 1991; *Schmale et al.*, 2005; *Yvon-Lewis et al.*, 2011]. However, one recent study suggests that the diffusive net sea-to-air flux of methane from the deepwater hydrocarbon seeps to the atmosphere could be considerable [*E Solomon et al.*, 2009].

To better understand and quantify the diffusive net sea-to-air fluxes of methane from deepwater hydrocarbon seeps, we investigated three deepwater seeps featuring near-seafloor gas hydrate in the northern Gulf of Mexico. High spatial and temporal resolution measurements were made to determine the net sea-to-air fluxes of methane over these hydrocarbon seeps.

5.2 METHOD

Location and Measurements

The HYFLUX cruise took place in the northern Gulf of Mexico during July of 2009 (4 July – 19 July, 2009) aboard the *R/V Brooks McCall*. Intensive surface surveys were conducted above three active seeps, MC118 (Rudyville, 28.8522° N, 88.4928° W, 900 meters below sea level (mbsl)), GC600 (Oil Mountain, 27.3652° N, 90.5642° W, 1250 mbsl), and GC185 (Bush Hill, 27.7823° N, 91.5080° W, 550 mbsl) (*Figure 5.1*), which were characterized by seafloor gas hydrate deposits that were partly exposed to seawater. A complete inventory of these analytical results is provided in ***Appendix V***.

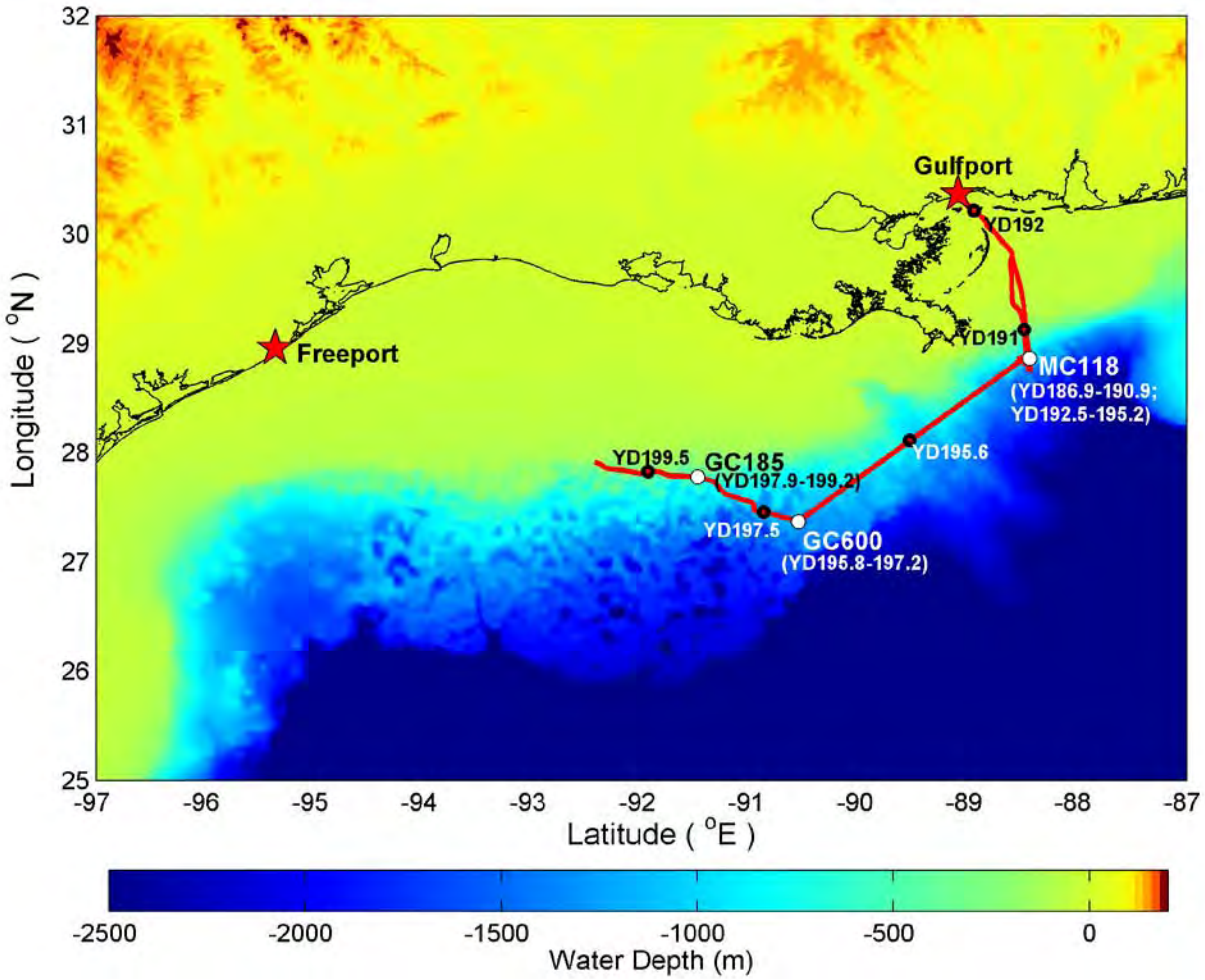

Figure 5.1: *Cruise track (red line) of HYFLUX cruise in July of 2009 (4 July – 19 July, 2009). Colored surface of the map indicates the water depths and land surface elevations. The bathymetric data are from the NOAA National Geophysical Data Center (http://www.ngdc.noaa.gov/mgg/bathymetry/relief.html). White circles denote the locations of the three seep sites; black circles mark the year days (YD) along the cruise track; red stars stand for the ports where the ship departed or arrived.*

Active oil and gas venting was confirmed by the ROV at fixed locations within all three sampling sites. Air and surface seawater samples were analyzed continuously (except for brief maintenance intervals) during occupation of the sites and transits. The air-sea sampling plan had two modes: 1) a coarse regular grid, where samples were spaced at a kilometer scale, and 2) a fine sampling scale that occurred as the ship loitered above the ROV, where samples were spaced ≤ 10 m. The ship speed was kept below 4 knots over most of the seep areas (*Figure 5.2e*).

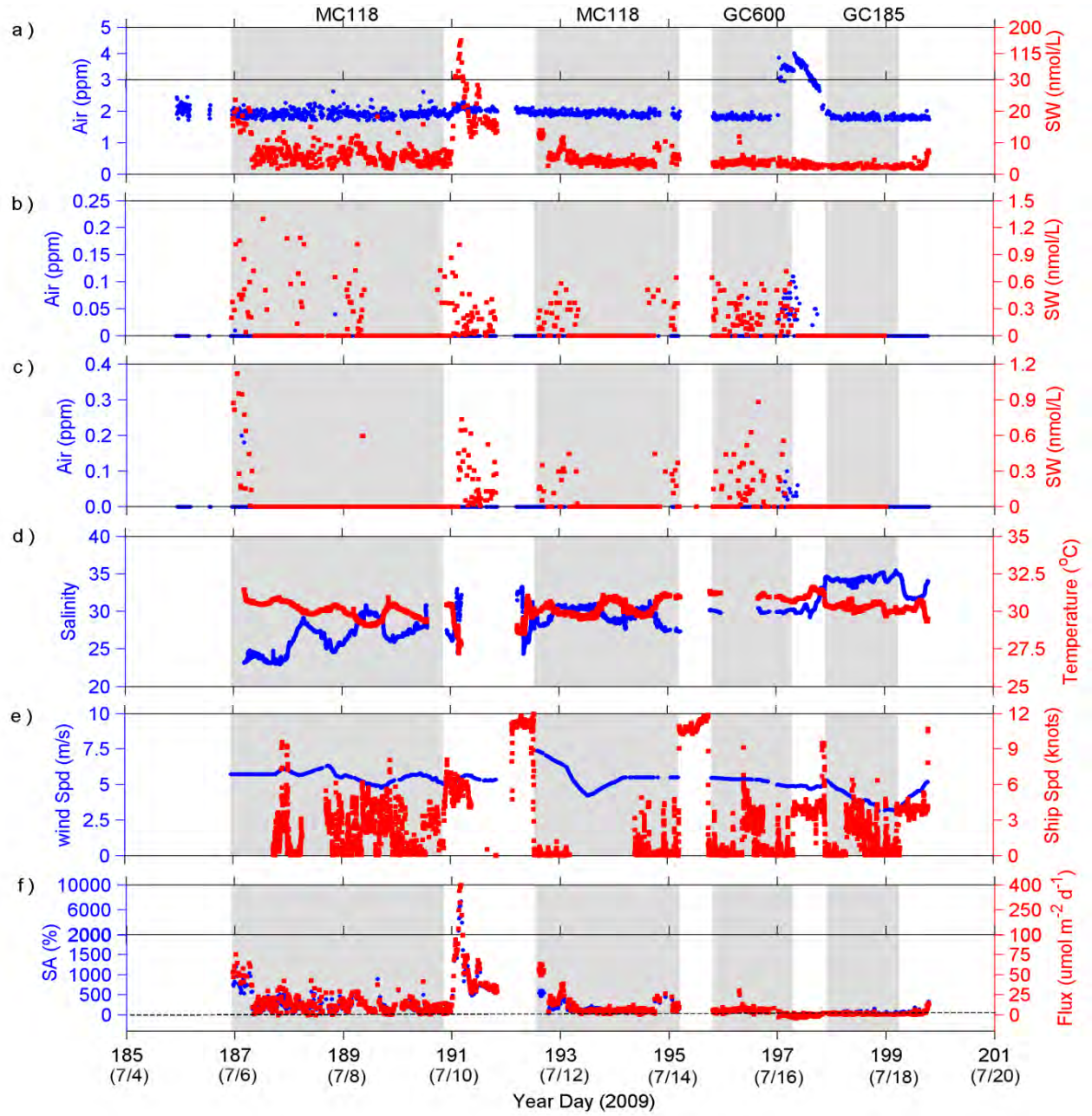

Figure 5.2: ***(a)*** *Atmospheric mixing ratios (blue) and surface seawater concentrations (red) of methane; the scales for surface seawater methane in ranges of 0 – 30 nmol L^{-1} and 30 – 200 nmol L^{-1} are different.* ***(b - c)*** *Atmospheric mixing ratios (blue) and surface seawater concentrations (red) of ethane (b) and propane (c).* ***(d)*** *Sea surface salinity (blue) and temperature (red);* ***(e)*** *24 hour averaged wind speeds at 10 m above sea level prior to sampling (blue) and ship speeds along the cruise track (red).* ***(f)*** *Saturation anomalies (blue) and net sea-to-air fluxes (red) of methane; different scales for saturation anomalies in ranges of -40 – 2000 % and 2000 – 10000 % and fluxes in ranges of -20 – 100 µmol m^{-2} d^{-1} and 100 - 400 µmol m^{-2} d^{-1}; dash line marks zero saturation anomaly and zero flux. Concentrations of zeros for panels a – c indicate concentrations below the instrument detection limit. Grey shadows mark the time periods over three seep sites. X-axis is the year day of 2009 and the corresponding month/day is labeled in the brackets.*

To measure the diffusive net sea-to-air fluxes of methane and possibly estimate its origin, atmospheric and surface seawater dissolved C_1 - C_3 hydrocarbons were measured continuously with an automated sampling system coupled to a Weiss-type equilibrator and a Gas Chromatograph/Flame Ionization Detector (GC/FID, Agilent 6850) system. This technique only quantifies the diffusive net sea-to-air flux

of dissolved methane and not the direct bubble injection of methane to the atmosphere; however, direct bubble injection to the atmosphere could be manifested in the data as enhanced atmospheric concentrations relative to surface seawater.

Air samples were pumped continuously at ~ 6 L min^{-1} through 0.63 cm ID Synflex tubing (Motion Industries, TX) mounted on the railing on the top of flying bridge and running to the laboratory. Surface seawater (about 4 m below the sea surface) was pumped into the Weiss-type equilibrator at 15 L min^{-1}. Equilibrator headspace and ambient air were alternately sampled every 6 minutes using a stream select valve. The sample stream passed through a 20 μL sampling loop after being dehumidified by a Nafion dryer (Permapure Inc). The Nafion dryer and the 20 μL sampling loop were flushed with the sample air at a rate of 25 mL min^{-1} for 90 seconds before injection into the GC/FID, which was equipped with a 15 m long, 32 μm ID GS-GasPro column (1 m pre-column and 14 m main-column) with nitrogen carrier gas. Prior to the cruise, a series of standard mixtures (C_1 - C_3) ranging from 0 – 1000 ppm were made using two known concentration standards (15 ppm and 1000 ppm) from Scott Specialty Gases. Standards with methane concentrations at 0.09 (± 0.01) ppm, 1.09 (± 0.02) ppm, 1.69 (± 0.02) ppm and 2.88 (± 0.06) ppm were also calibrated against a whole air tank, which was calibrated to the NOAA-04 methane scale. The standards with methane concentrations at 0.09 – 2.88 ppm were used to create a standard curve to calibrate the instrument. Higher concentration standards 15 (± 1.5) ppm, 503 (± 25) ppm, 1000 (± 50) ppm were also run and used as an alternate calibration curve if the measured concentration exceeded our lower calibration range. The precision of the system was determined from five standard injections. The precision for concentrations ≤ 3 ppm was 3 % for methane, 2 % for ethane and 3 % for propane. The precision for concentrations > 3 ppm was less than 1 % for methane, ethane and propane.

The sea surface temperature and salinity were continuously measured by a CTD sensor from Sea-Bird Electronics (SBE 19 plus) at the outflow of the equilibrator. Wind speeds and directions were continuously measured by an anemometer at a height of ~ 9 m above the sea level.

Equilibrator concentration correction

Over the past 20 years, the equilibrator headspace technique has been used for the determination of the net sea-to-air fluxes of many dissolved gases including, but not limited to, halocarbons [*Butler et al.*, 2007] and references therein];[*Hu et al.*, 2010], CO_2 [*Takahashi et al.*, 2009] and references therein], and methane [*Amouroux et al.*, 2002; *Bange et al.*, 1996; *Bange et al.*, 1994; *Bange et al.*, 1998; *Kourtidis et al.*, 2006; *Rhee et al.*, 2009].

Due to the different solubilities for different gases, the time needed for the trace gas concentration in the headspace to reach equilibrium with the incoming seawater is different for each trace gas. The headspace mass concentration, C_e, at a time, t, can be expressed with the following equation when the equilibrator vent flow, Q_v, is zero [*Johnson*, 1999].

$$C_e = \left(C_i - \frac{C_w}{\alpha}\right) e^{-(t/\tau_1)} + \frac{C_w}{\alpha} \quad (1)$$

where, $\tau_1 = \frac{v_e}{Q_w \varepsilon \alpha}$; V_e is the volume of the headspace, 12.5 L; Q_w is the volumetric flow rate of the seawater, 15 L min^{-1}; ε is a dimensionless equilibrator coefficient, which is typically about 0.3 - 0.4 [*Johnson*, 1999]; α is the Oswald solubility coefficient; C_i is the initial mass concentration in the headspace and C_w is the mass concentration of the trace gas in the incoming seawater.

When the equilibrator vent flow, Q_v, is not zero, the air in the headspace is removed and replaced by the ambient air at a rate of Q_v. The trace gas concentration in the headspace can then be expressed by the following equation [*Johnson*, 1999].

$$C_e = \frac{\frac{c_w}{\alpha\tau_1}\left(1-e^{-\frac{t}{\tau_2}}\right)+\frac{C_a}{\tau_v}\left(1-e^{-\frac{t}{\tau_2}}\right)+\frac{C_i}{\tau_2}e^{-\frac{t}{\tau_2}}}{\frac{1}{\tau_2}} \quad (2)$$

where, $\tau_v = \frac{v_e}{Q_v}$ and $\frac{1}{\tau_2} = \frac{1}{\tau_1} + \frac{1}{\tau_v}$; C_a is the mass concentration of the trace gas in the ambient air.

Under normal operating conditions, the equilibrator vent flow is off between two surface seawater measurements except the duration when the instrument is flushing the dryer and sample loop (i.e. collecting the headspace air sample). Assuming the equilibrator vent flow is off for a period of t_1 (min) and on for a period of t_2 (min) at a rate of Q_v (ml min^{-1}), the trace gas concentration in the headspace at t_1 + t_2 can be expressed as:

$$C_e = \frac{\frac{c_w}{\alpha\tau_1}\left(1-e^{-\frac{t_2}{\tau_2}}\right)+\frac{C_a}{\tau_v}\left(1-e^{-\frac{t_2}{\tau_2}}\right)}{1/\tau_2} + \left(\left(C_i - \frac{C_w}{\alpha}\right)e^{-\frac{t_1}{\tau_1}} + \frac{C_w}{\alpha}\right)e^{-\frac{t_2}{\tau_2}} \quad (3)$$

Since the trace gas concentrations in the ambient air and in the equilibrator headspace were measured, C_a, C_i, and C_e are known. The trace gas concentration in seawater can be expressed as a function of C_a, C_i, and C_e (Equation 4).

$$C_w = \frac{C_e - \tau_2/\tau_v\left(1-e^{-\frac{t_2}{\tau_2}}\right)C_a - e^{-\left(\frac{t_1}{\tau_1}+\frac{t_2}{\tau_2}\right)}C_i}{\frac{\tau_2\left(1-e^{-\frac{t_2}{\tau_2}}\right)}{\alpha\tau_1} + \frac{\left(1-e^{-\frac{t_1}{\tau_1}}\right)e^{-\frac{t_2}{\tau_2}}}{\alpha}} \quad (4)$$

In this study, the vent flow, 25 ml min^{-1}, was only on for 2.5 min between two seawater measurements, resulting in only 1 % of difference in the C_w compared to the case without the vent flow. Given such a small effect, we can simplify equation (4) by assuming the vent flow is 0 during t_1 to t_2. Then τ_v is equal to 0, and τ_1 is equal to τ_2. Equation (4) can be expressed as:

$$C_w = \frac{C_e - C_i e^{-\left(\frac{t_1-t_2}{\tau_1}\right)}}{\frac{1-e^{-\frac{t_1+t_2}{\tau_1}}}{\alpha}} \quad (5)$$

In equations (1 - 5), it is assumed that the trace gas concentration in the seawater is constant during t_1 and t_2. However, in reality, this assumption may not be true especially when the ship speed is fast. Therefore, assuming the seawater concentration is constant during a very short time period (Δt) (i.e. < 1 second) and the seawater concentrations are $C_{w_1}, C_{w_2}, \ldots, C_{w_{n-1}}, C_{w_n}$ for each Δt ($n\Delta t = t_1+t_2$), the trace gas concentration in the headspace can be expressed by:

$$C_e = \left(C_i - \frac{C_{w_1}}{\alpha}\right)e^{-\frac{n\Delta t}{\tau_1}} + \left(\frac{C_{w_1}-C_{w_2}}{\alpha}\right)e^{-\frac{(n-1)\Delta t}{\tau_1}} + \left(\frac{C_{w_2}-C_{w_3}}{\alpha}\right)e^{-\frac{(n-2)\Delta t}{\tau_1}} + \ldots + \left(\frac{C_{w_{n-1}}-C_w}{\alpha}\right)e^{-\frac{\Delta t}{\tau_1}} + \frac{C_{w_n}}{\alpha} \quad (6)$$

By substituting the C_e in equation (5) with equation (6), C_w can be expressed by:

$$C_w = \frac{1-e^{-\frac{\Delta t}{\tau_1}}}{1-e^{-\frac{n\Delta t}{\tau_1}}}\left(C_{w_1}e^{-\frac{n-1}{\tau_1}\Delta t} + C_{w_2}e^{-\frac{n-2}{\tau_1}\Delta t} + C_{w_3}e^{-\frac{n-3}{\tau_1}\Delta t} + \cdots + C_{w_{n-1}}e^{-\frac{1}{\tau_1}\Delta t} + C_{w_n}\right) \quad (7)$$

Assuming $a_i = \frac{1-e^{-\frac{\Delta t}{\tau_1}}}{1-e^{-\frac{n\Delta t}{\tau_1}}} e^{-\frac{n-i}{\tau_1}\Delta t}$ (i = 1, 2, 3, … , n), C_w can be rewritten as:

$$C_w = a_1 C_{w_1} + a_2 C_{w_2} + a_3 C_{w_3} + \cdots + a_{n-1} C_{w_{n-1}} + a_n C_{w_n} \quad (8)$$

Therefore, the fractional contributions of the true seawater concentrations, $C_{w_1}, C_{w_2}, \ldots, C_{w_{n-1}}, C_{w_n}$, to the corrected seawater concentration (C_w) are $a_1, a_2, \ldots, a_{n-1}, a_n$. For the very soluble gases (i.e. CO_2, N_2O), $a_1, a_2, \ldots, a_{n-1}, a_n$ exponentially increase from 0 to 1 as a_1 goes to a_n, and C_w is more representative of an instantaneous incoming seawater concentration. For the less soluble gases (i.e. CH_4, CO), $a_1, a_2, \ldots, a_{n-1}, a_n$ are close to 1/*n* and C_w is more representative of an average seawater concentration during the last $n\Delta t$ min. In this study, the seawater concentrations were calculated using equation (4), and they represent average seawater concentrations over a period of 12 min. As the ship speed was in a range of 0 – 4 knots when sampling, 12 min represents a distance of 0 – 1480 m.

Net sea-to-air flux calculation

The net sea-to-air flux (F) is calculated by:

$$F = k_w(C_w - \alpha C_a) \quad (9)$$

where, k_w is the gas transfer velocity (m d^{-1}) [*Sweeney et al.*, 2007], and C_w, C_a and α are defined above. The gas transfer velocity parameterization from [*Sweeney et al.*, 2007] is an improvement over the typical [*Wanninkhof*, 1992] parameterization since they closed the previous gap between field measurements [*Liss and Merlivat*, 1986; *Nightingale et al.*, 2000] and radiocarbon estimates [*Tans et al.*, 1990; *Wanninkhof*, 1992] on this parameter.

The gas transfer velocity (k_w) from [*Sweeney et al.*, 2007] is expressed as:

$$k_w = 0.27 u_{10}^2 \left(\frac{Sc}{660}\right)^{-0.5} \quad (10)$$

where, *Sc* is the Schmidt Number of methane in seawater from [*Wanninkhof*, 1992] and u_{10} is the 10 m normalized wind speed (m s^{-1}) determined using the equation given by [*Large and Pond*, 1982].

5.3. RESULTS

Atmospheric methane during this cruise ranged from 1.70 ppm to 4.01 ppm, with a mean of 2.01 ppm (*Figure 4.2a*). The atmospheric methane fluctuated around a background concentration of 1.92 ppm during the occupation of the sites and transits, except at the end of GC600 and the transit to GC185 (*Figure 4.2a*). The surface seawater methane concentrations ranged from 1.76 to 23.5 nmol L^{-1} at MC118, 1.76 to 11.9 nmol L^{-1} at GC600, and 1.72 to 4.48 nmol L^{-1} at GC185 (*Table 4.1*). The presence of ethane and propane in the surface seawater over the seep area (mainly at MC118 and GC 600) indicates a thermogenic source, which suggests the surface seawater methane may be, at least partly, attributable to transport from the deepwater hydrocarbon seeps. The maximum methane concentration observed in surface seawater during this study, 156 nmol L^{-1}, was observed on YD 191 (10 July, 2009) on the continental shelf offshore from Louisiana (*Figures 4.1 and 4.2a*). The corresponding atmospheric methane concentrations reached 2.10 ppm due to the net sea-to-air flux (*Figure 4.2a*). Increased ethane and propane along with elevated salinity and decreased temperature (*Figures 4.2b, 4.2c and 4.2d*) suggest that the elevated methane in the surface seawater may be associated with upwelling which was enriched with hydrocarbons. A similar feature in the surface seawater was observed in the same region in June 2010 during the Persistent Localized Underwater Methane Emission Study (PLUMES) [*Yvon-Lewis et al.*, 2011], which suggests that the elevated C_1 - C_3 hydrocarbons in the sea surface might be associated with an undocumented thermogenic hydrocarbon source in this region.

Table 5.1: *Mean atmospheric methane mixing ratios, seawater methane concentrations, saturation anomalies and net sea-to-air fluxes of methane at the three seep sites (ranges of values in parentheses).*

Sites	Atmospheric CH_4 mixing ratio (ppm)	Seawater CH_4 concentration (nmol L^{-1})	Saturation anomaly (%)	Averaged wind speed (m s^{-1})	Flux (μmol m^{-2} d^{-1})	
					W92[a]	S07[b]
MC118	1.93 (1.70-2.32)	5.94 (1.76-23.5)	212 (-6.42-1196)	5.6	15.4 (-0.52-86.1)	13.4 (-0.45-75.0)
GC600	2.18 (1.72-4.01)	3.61 (1.76-11.9)	90.5 (-46.0-598)	5.3	5.41 (-4.19-34.9)	4.71 (-3.65-30.4)
GC185	1.81 (1.70-2.01)	2.40 (1.72-4.48)	39.6 (2.33-156)	4.0	1.25 (0.08-4.13)	1.09 (0.07-3.6)

[a] *W92 refers to the flux calculated using the [Wanninkhof, 1992] gas transfer velocity parameterization;*
[b] *S07 refers to the flux calculated using the [Sweeney et al., 2007]gas transfer velocity parameterization.*

The methane saturation anomaly is defined as the percent difference between the partial pressures of methane in surface seawater and air. They ranged from -51.8 to 7.43 X 10^3 % (*Figure 4.2f*). The calculated net sea-to-air fluxes ranged from - 4.68 to 416 μmol m^{-2} d^{-1} (*Figure 4.2f*). The mean net sea-to-air flux at each of the three seep areas was 13.4 μmol m^{-2} d^{-1} (MC118), 4.71 μmol m^{-2} d^{-1} (GC600) and 1.09 μmol m^{-2} d^{-1} (GC185) (*Table 4.1*). To compare the results from this study to those from previous studies, we calculated the flux using the gas transfer velocity from [*Wanninkhof*, 1992] in addition to using the [*Sweeney et al.*, 2007] relationship described earlier. The calculated net sea-to-air methane fluxes from the deepwater hydrocarbon plume areas are one to two orders of magnitude lower than those from shallow water seep plume areas (*Table 4.2*; [*Mau et al.*, 2007; *Schmale et al.*, 2005]). For the deep water environment, the calculated fluxes from this study are in the same range as those determined from most previous studies (*Table 4.2*; [*Reeburgh et al.*, 1991; *Schmale et al.*, 2005; *Yoshida et al.*, 2004; *Yvon-Lewis et al.*, 2011]). However, they are three orders of magnitude lower than those reported by [*E Solomon et al.*, 2009] who investigated the same region as the current study including one of the same identified seep sites.

Table 5.2: *Diffusive net sea-to-air fluxes of methane from different environments.*

Location	Water Depth (m)	Flux (μmol m^{-2} d^{-1}) [a]	Reference
Deep water environments (> 200 m)			
Deepwater hydrocarbon plume area in the northern GOM	550 – 1250	-4.19 - 86.1	This study
Deepwater hydrocarbon plume area in the northern GOM	500 - 600	200 - 10,500	[*E Solomon et al.*, 2009]
Plume area during the Deepwater Horizon oil spill	1500	-0.055 - 1.83	[*Yvon-Lewis et al.*, 2011]
Sorokin Trough and Dnepr Area in Black Sea	>200	40.6 - 49.2	[*Schmale et al.*, 2005]
Central Black Sea	>200	27	[*Reeburgh et al.*, 2006]
Sea of Okhotsk	>200	0.36 - 88	[*Yoshida et al.*, 2004]
Baltic and North Seas	>200	-6.6 - 13.89	[*Bange et al.*, 1994]
Aegean Sea	>200	1.81	[*Bange et al.*, 1996]
Northwestern Levantine Basin	>200	3.02	[*Bange et al.*, 1996]
Open Ocean in the Atlantic	>200	0.3	[*Rhee et al.*, 2009]
Open Ocean in the Pacific	>1000	0.9 - 3.5	[*Tilbrook and Karl*, 1995]
Shallow water environments (≤ 200 m)			
Coal Oil Point	<70	195	[*Mau et al.*, 2007]
Northwest Black Sea	<200	53	[*Amouroux et al.*, 2002]
Northwestern continental shelf of the Sea of Okhotsk	<200	0.47 - 11	[*Yoshida et al.*, 2004]
Shelf waters of Dnepr Area	<200	67	[*Schmale et al.*, 2005]
Coastal region of the Atlantic	<200	3.2	[*Rhee et al.*, 2009]

[a] *Fluxes were calculated using the gas transfer velocity parameterization of [Wanninkhof, 1992].*

5.4. DISCUSSION

Based on the results above, four main issues will be addressed in the following discussion: 1) the source for the elevated atmospheric methane during the transit from GC600 to GC185; 2) the diffusive net sea-to-air fluxes of methane from three seep sites and their temporal and spatial variability; 3) potential causes for the large discrepancy between the results from this study and those reported by [*E Solomon et al.*, 2009]; and 4) the impact of small areas of high methane concentration hotspots on our regional air-sea flux estimate if extremely high concentrations existed in the surface seawater over a deepwater hydrocarbon plume area and were missed in this study.

Elevated atmospheric methane

An area of elevated atmospheric methane with a maximum concentration of 4.01 ppm was observed on YD 197 (16 July) at GC600. The elevated atmospheric methane persisted for 19 hours and extended over 50 kilometers to the northwest of GC600 during the transit to GC185 (*Figure 4.2a*). Elevated ethane and propane in the atmosphere suggest a thermogenic source for the elevated methane (*Figures 4.2b and 4.2c*). The 24 h air-mass back-trajectories obtained from the NOAA Air Resources Laboratory (http://www.ready.noaa.gov/ready/open/hysplit4.html) show that the air masses with increased atmospheric methane came from the same region as those with background concentrations of 1.81 ppm (*Figure 4.3*), suggesting a localized source rather than long-range transport. Since the methane concentrations in the underlying seawater were close to a seawater background concentration of 2.40 nmol L^{-1} (*Figure 4.2a*), methane transport via diffusive sea-to-air gas exchange is not the source of these high atmospheric concentrations.

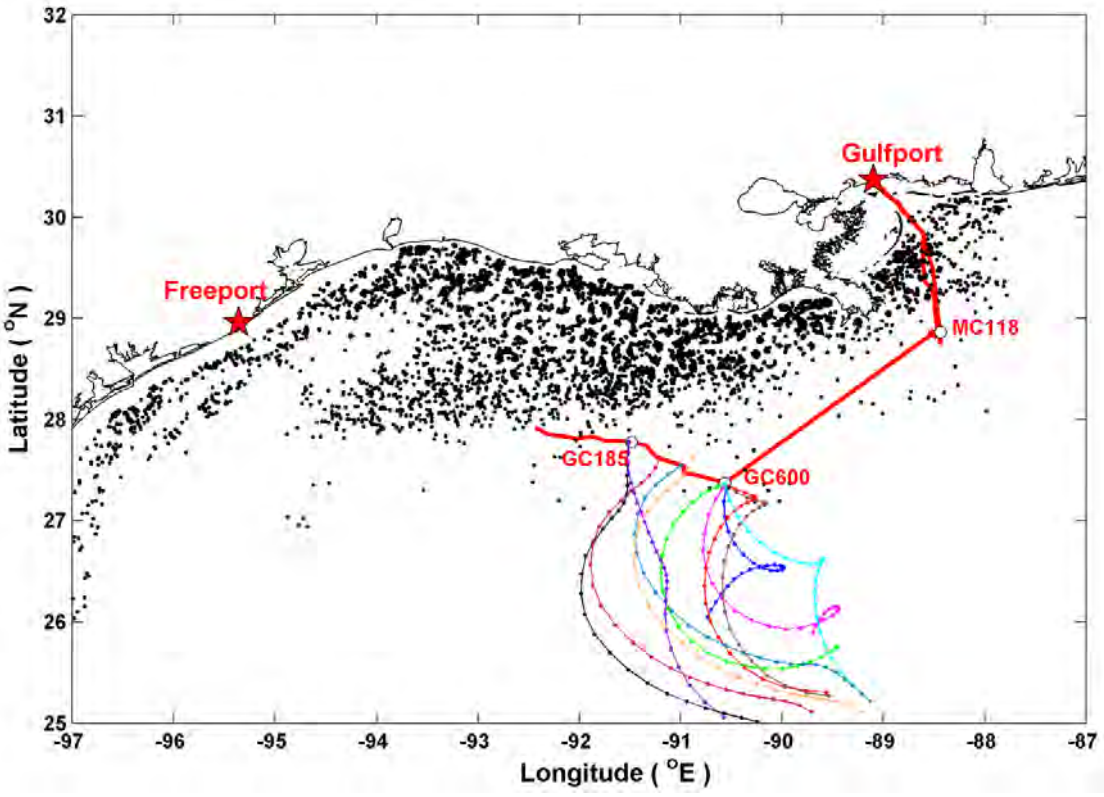

Figure 5.3: *24-hour back-trajectories of air masses (dot lines) and locations of oil platforms (black dots) in the northern Gulf of Mexico. Back-trajectories downloaded from the NOAA Air Resources Laboratory (http://www.ready.noaa.gov/ready/open/hysplit4.html) and platform locations are from MMS GOM regional database (http://www.gomr.mms.gov/homepg/pubinfo/repcat/arcinfo/index.html). White circles denote the locations of three seep sites. Red stars stand for the ports where the ship departed or arrived.*

Although bubbles traveling over 1000 m from a deepwater seep site have been observed [*Greinert et al.*, 2006], whether or not they can reach the surface is still debated [*McGinnis et al.*, 2006; *G. Rehder et al.*, 2009]. In this study, in order to increase the atmospheric methane concentration to 4.01 ppm (3.25 ppm averaged over the area with elevated methane concentrations), 3 X 10^5 mol d^{-1} of methane would need to be released to the atmosphere assuming a boundary layer height of 700 m (data from *http://ready.arl.noaa.gov/READYamet.php*) and assuming the elevated methane only spread out in a circle 100 m in diameter centered on the ship as it moved along the cruise track in the marine boundary layer. It is not likely for direct methane transport via gas bubbles at GC600 to contribute such a large amount of methane to the atmosphere due to the strong pycnocline during the summer (*Figure 4.4*) and the 1200 m water depth at this site. While slicks were observed from the ship at this site along with intermittent oil droplets rising to the surface, surface water concentrations were 2.85 ± 0.73 (1 σ) nmol L^{-1}, suggesting that these droplets were not carrying high concentrations of methane. Since the observation of the elevated atmospheric methane to the northwest of GC600 does coincide with satellite data from 20 July showing very extensive oil slicks over this broad region of the Gulf, we could not completely exclude the possibility that methane could be transported inside of the oily bubbles to the atmosphere. However, we cannot provide an appropriate mechanism for this possibility.

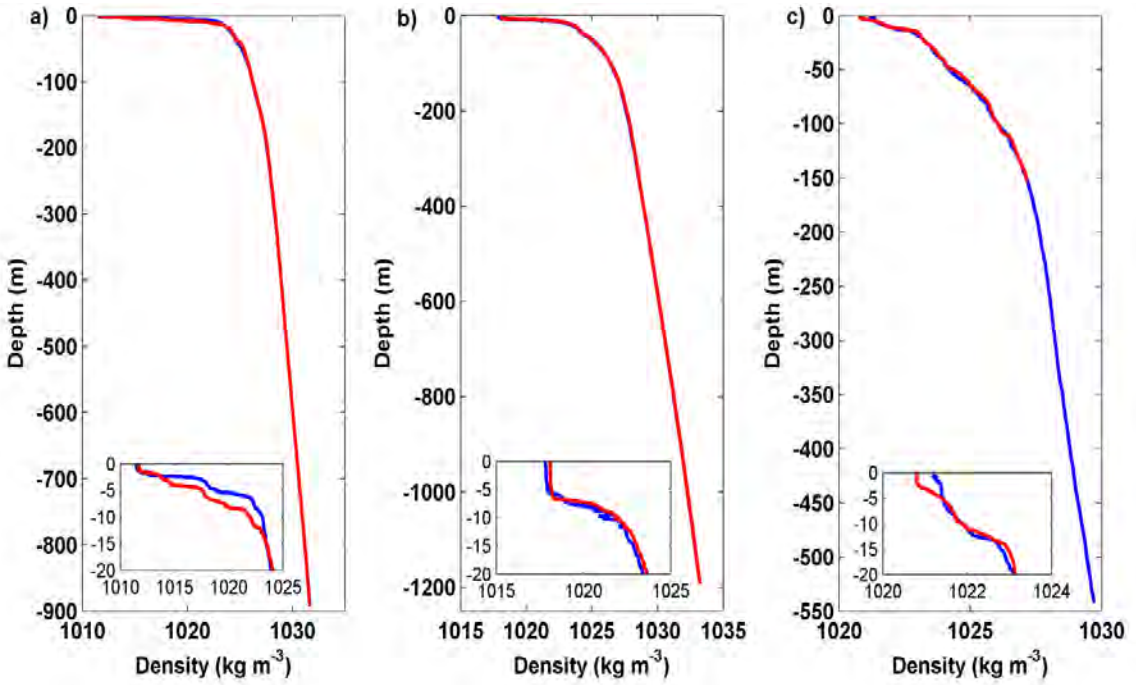

Figure 5.4: *Vertical profiles of density at MC118 (a), GC600 (b) and GC185 (c). Red and blue lines stand for two randomly selected CTD casts from each site.*

Fugitive release to the atmosphere directly from oil platforms around GC600 is possible (*Figure 4.3*). Given the fact that no significantly elevated atmospheric methane concentrations were observed near the recovery ships during the Deepwater Horizon oil spill, which were flaring tremendous amounts of gas [*Yvon-Lewis et al.*, 2011], flaring itself is an unlikely source of methane to the atmosphere. Not flaring or intentionally releasing gas from the drilling oil platform during this time is not likely to be the explanation either based on the drilling records from the Drilling Rig OCEAN MONARCH (the rig close to GC 600). A likely explanation could be an undetected leak from the nearby oil platform.

Methane net sea-to-air flux over the seeps

High temporal and spatial variability was observed in sea surface methane and net sea-to-air fluxes over the three seep areas (*Figures 5.5 and 5.6*). As the ship was conducting the surface survey, it kept crossing some of the same locations, and the concentrations were different at different times. This variability is not surprising and could happen on the order of seconds to hours due to variability in seepage rates, currents, wind speeds, surface wave action, etc. [*Jordan F. Clark et al.*, 2010; *J. F. Clark et al.*, 2003; *Greinert et al.*, 2006; *I. Leifer and Boles*, 2005; *I. Leifer et al.*, 2006; *Quigley et al.*, 1999]. Spatial variability within one seep site is associated with the rising angle of the bubbles and the directions of mid-depth and surface currents. Spatial variability also exists from site to site (*Figures 4.5 and 4.6*), which is associated with characteristics of their geological and physical environment, e.g. seep intensity, oil-water ratio, water depth, currents, mixed layer depth.

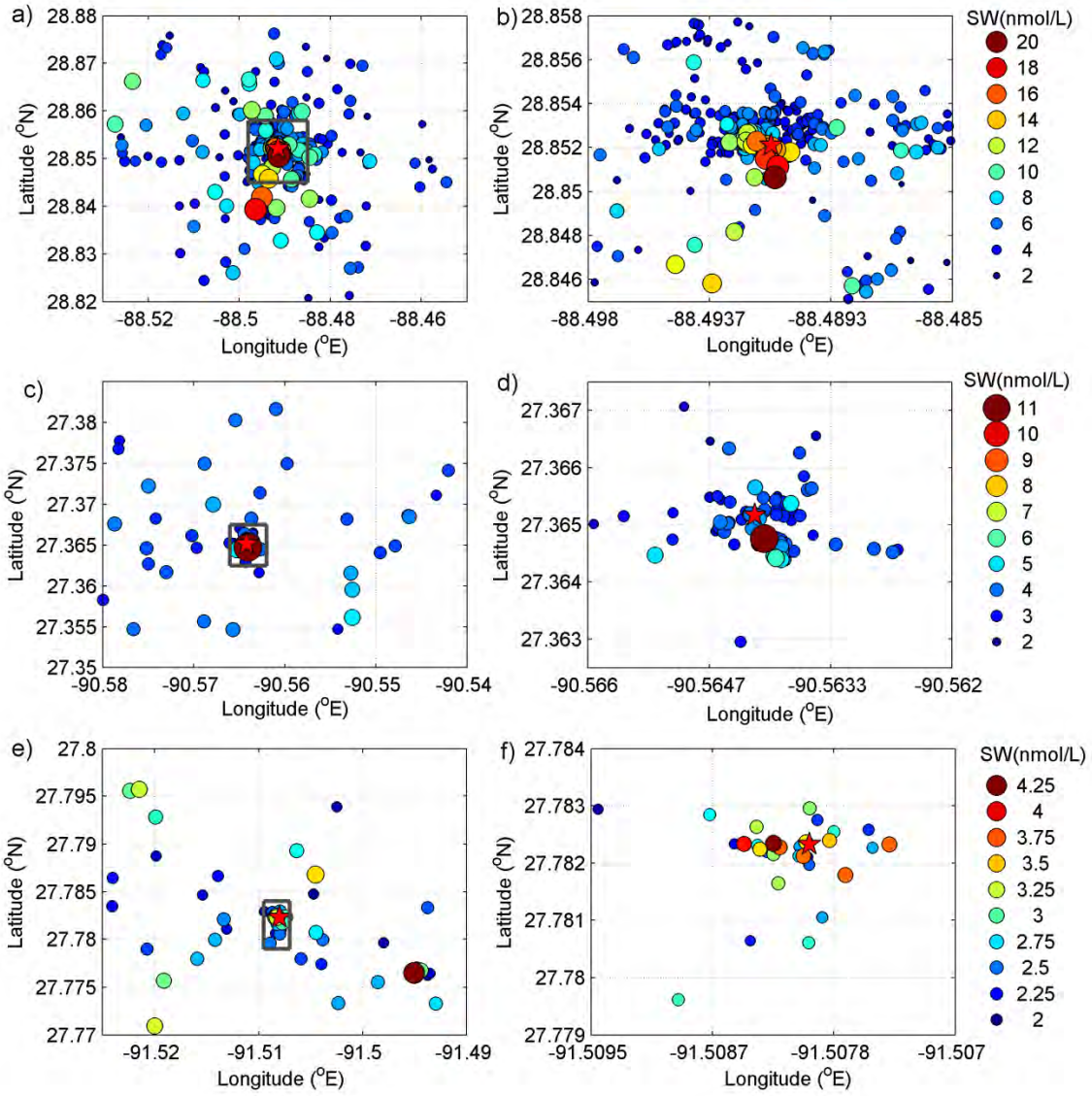

Figure 5.5: *Methane concentrations in surface seawater at MC118 (a-b), GC600 (c-d) and GC185 (e-f). Grey rectangles in the lefthand panels indicate the blown-up regions, which are plotted in the righthand panels. Red stars indicate the locations of the seeps.*

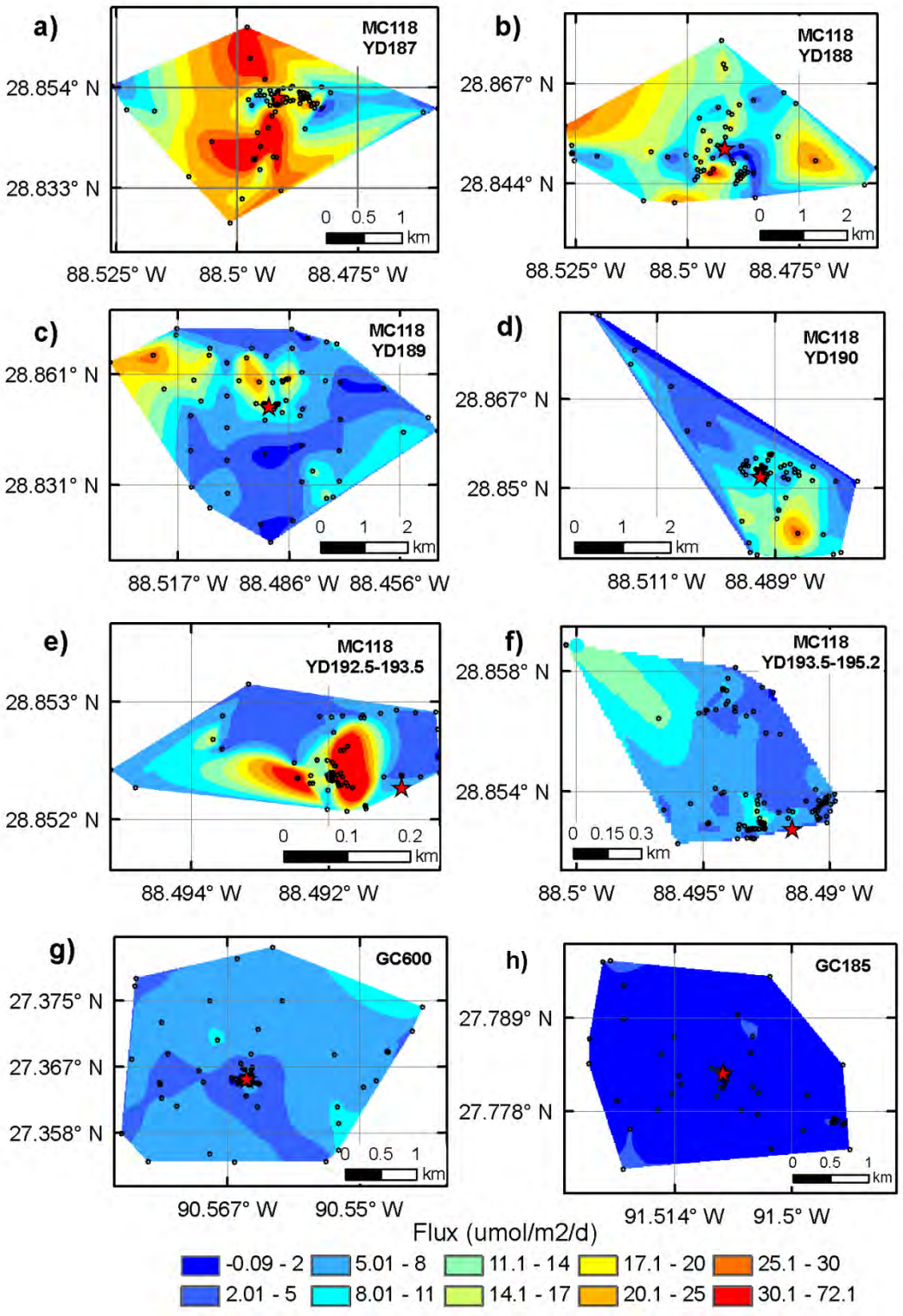

Figure 5.6: *Contour plots of methane net sea-to-air fluxes at the three seep sites using natural neighbor. Red stars indicate the locations of the seeps. Black circles stand for the locations of the flux measurements.*

Overall, MC118 had higher sea surface methane concentrations and higher net sea-to-air fluxes than those observed at either GC600 or GC185 (*Tables 4.1 and 4.3; Figures 4.5 and 4.6*), especially on YDs 187 – 189, and 192 (*Table 4.3; Figure 4.6*). On YD 192, the elevated methane flux was located in a very confined area, which was three orders of magnitude smaller than the area of elevated flux observed on YDs 187 – 189 (*Table 4.3*).

Table 5.3. *Mass fluxes over the survey area using different interpolation gridding methods. The boundaries for the gridded fluxes are shown in Figure 4.6.*

Sites	Survey Area (km^2)	Area with fluxes ≥ 8 μmol m^{-2} d^{-1} (km^2)	Natural Neighbor		Inverse Distance Weighted		Krigging	
			Area weighted mean flux (μmol m^{-2} d^{-1})	Mass Flux (mol d^{-1})	Area weighted mean flux (μmol m^{-2} d^{-1})	Mass Flux (mol d^{-1})	Area weighted mean flux (μmol m^{-2} d^{-1})	Mass Flux (mol d^{-1})
MC118								
YD 187	15.15	14.00	19.8	300	21.5	326	23.2	352
YD 188	16.27	13.91	13.2	215	12.0	195	11.3	183
YD 189	34.64	12.31	7.82	271	8.68	301	9.11	316
YD 190	8.530	3.430	7.75	66.1	8.70	74.2	8.82	75.2
YD 192.5 - 193.5	0.06155	0.03014	12.1	0.744	15.5	0.954	18.7	1.15
YD 193.5 -195.2	0.5318	0.0055	6.98	3.71	6.36	3.38	6.23	3.31
GC 600	8.571	0.407	6.05	51.9	5.53	47.4	5.26	45.1
GC 185	6.686	0.000	1.02	6.85	1.03	6.86	1.00	6.69

GC 600 is the oiliest site surveyed during this study. A large oil seep with a hydrate mound and a series of vents spaced about 75 m apart were found during ROV dives at GC 600. Large areas of oil slicks or oil sheen were observed on the sea surface at GC600. Although surfactants can inhibit bubble dissolution and enhance the methane transport, lower surface seawater methane concentrations and lower diffusive fluxes were observed than those at MC118. As discussed earlier, another big difference between GC 600 and the other two seep areas is the presence of high atmospheric methane concentrations (as high as to 4.01 ppm) observed on YD 197, resulting in a net air-to-sea flux in this area (*Figures 4.2 and 4.6*).

GC 185 is the shallowest site occupied during this study. During a prior study at this site, a methane concentrations of 608 nmol L^{-1} at a water depth of ~ 20 m and a net sea-to-air flux of 3420 μmol m^{-2} d^{-1} in the plume area was reported [*E Solomon et al.*, 2009]. Therefore, higher methane concentrations in the air and sea surface as well as higher fluxes were anticipated. However, both the atmospheric methane and the sea surface methane were near background concentrations with atmospheric concentrations from 1.70 to 2.01 ppm and surface water concentrations ranging from 1.72 to 4.48 nmol L^{-1} over the entire survey area. The methane net sea-to-air flux was 0.07 - 3.6 μmol m^{-2} d^{-1} (*Table 4.1*).

The daily methane mass flux distribution for each survey area was determined by interpolation using natural neighbor, inverse distance weighted interpolation, and kriging (*Table 4.3*). The three different interpolation methods do not produce significantly different fluxes. Since the natural neighbor method produced a smoother shape, we chose this algorithm as our main interpolation method for plotting the mass flux distribution over the seep sites. Due to the high temporal and spatial variability of the methane fluxes within and between sites, it is difficult to extrapolate the observed net sea-to-air fluxes to other periods or to other hydrocarbon seeps (*Figures 4.5 and 4.6*). However, we can approximate the upper limit of the diffusive net sea-to-air flux of methane from the deepwater hydrocarbon seeps in the northern Gulf of Mexico under normal conditions (i.e. no mud volcanoes or submarine earthquake) by assigning the highest daily flux determined in this study, 300 mol d^{-1} (per seep site), to other deepwater hydrocarbon seeps in this region. Large uncertainty exists in the number of active seeps in the northern Gulf of

Mexico. Geophysical anomalies generated by seeps in the geologic past exceed 5000 possible sites [*Frye*, 2008] whereas preliminary results for seeps detected by remote sensing (see the detailed method in [*Garcia-Pineda et al.*, 2010]) suggest a maximum number of active vents at about 1500. Assuming that each of the 1500 - 5000 seeps in the northern Gulf of Mexico has a daily net sea-to-air flux of 300 mol d^{-1}, and they persistently emit methane to the atmosphere at the same rate over a one-year period, the total diffusive net sea-to-air flux from deepwater hydrocarbon seeps in the northern Gulf of Mexico is about 3 - 9 Gg yr^{-1}. Compared with the total annual emission of methane to the atmosphere, 6 X 10^5 Gg yr^{-1} [*Lelieveld et al.*, 1998], the contribution of the net diffusive sea-to-air flux from deepwater hydrocarbon seeps in the northern Gulf of Mexico is insignificant to the atmospheric methane budget.

Investigating the large discrepancy

Three orders of magnitude of discrepancy exist between the mean fluxes presented in [*E Solomon et al.*, 2009] and the mean fluxes from this study. This large difference in net sea-to-air flux is mainly attributable to the differences in the reported surface seawater methane concentrations and the distinction of a surface concentration that can or cannot be used to determine the air-sea flux of a gas. Besides the possible temporal variability, the difference in "surface" sampling depths between the two studies is a key factor in the differences in seawater concentrations and fluxes reported. The results presented here are for seawater collected at around 4 m water depth continuously as the ship was moving. A submersible vehicle or rosette samples seawater at discrete depths periodically, and the shallowest sample the submersible collected in [*E Solomon et al.*, 2009] was around 20 m. The temperature and salinity profiles in the supplementary materials of [*E Solomon et al.*, 2009] did not show a clear mixed layer depth at or below 20 m depth, suggesting they were sampling below the mixed layer or that a mixed layer did not exist. In the current study, the mean mixed layer depths were 4.8 m (0 – 28.8 m; median: 3.5 m; 32 CTD casts) at MC118, 4.9 m (4.2 – 5.5 m; 2 CTD casts) at GC 600, and 2.1 m (1.4 – 2.6 m; 3 CTD casts) at GC185 (*Figure 4.4*). We were sampling within or close to the bottom of the mixed layer at all times. When determining the air-sea flux using the air-sea concentration gradient, the dissolved concentrations must be measured as close to the surface as possible especially for gases that may not be well mixed even within the mixed layer due to mixing time scales and reaction rates.

A contributing but minor factor to the differences in net sea-to-air fluxes reported in the two studies involves the atmospheric methane concentrations used in the flux calculation. [*E Solomon et al.*, 2009] used an averaged atmospheric methane concentration for their flux calculations, while the atmospheric mixing ratios were measured once every 12 minutes locally during the current study. Atmospheric methane ranged from 1.70 ppm to 4.01 ppm over the seep sites during the current study. At times, the atmospheric methane concentrations were over twice the average background concentration. In some places during the occupation of GC600, the surface ocean acted as a sink for atmospheric methane and would have been misinterpreted as a source to the atmosphere if average atmospheric methane concentrations were used in the flux calculations. Fluxes of methane from the ocean to the atmosphere or other incidental hydrocarbon emissions could result in perturbations to the local atmospheric methane concentrations, and these perturbations should be accounted for in the calculation of the flux.

Impact of small area high concentration hotspots on the regional air-sea flux

To determine if the regional air-sea flux results from continuous air-sea measurements are more representative than discrete measurements, we investigate whether or not the technique used in this study could have missed a high methane concentration hotspot that is large enough to impact the overall flux from the plume area. To address this in more detail, the sensitivity of the corrected seawater concentration (C_w) to the size and concentration of a potential hotspot is determined using equation (7). We assumed: 1) that any corrected seawater concentration $\geq$ 4 nmol L^{-1} (twice the background concentration) indicated an observable hotspot; and 2) that the ship left a background concentration of 2 nmol L^{-1} and immediately crossed a methane hotspot with a concentration ranging from 4 to 1609 nmol L^{-1} (the highest 20 m value

reported by [*E Solomon et al.*, 2009]). Under these conditions, a surface hotspot with a concentration of 1609 nmol L^{-1} is observable with a diameter ≥ 5 cm when the ship speed is 0.1 knots (e.g. when the ship was holding a station), and a diameter ≥ 2 m when the ship speed is 4 knots (e.g. when the ship is conducting coarse surveys) (*Figure 4.7*). As the concentration of the hotspot decreases, the size of the observable hotspot would exponentially increase (*Figure 4.7*).

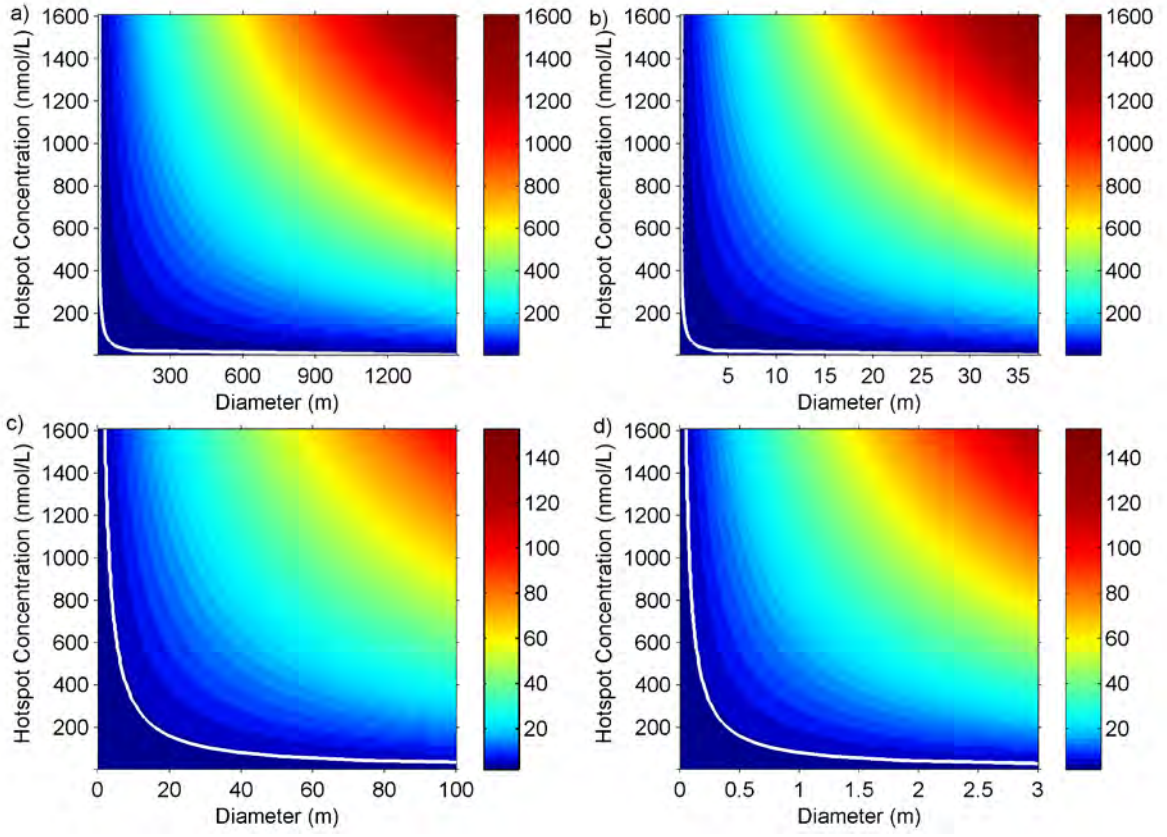

Figure 5.7: *Corrected seawater methane concentration (C_w) as a function of a hotspot concentration and a hotspot size.* ***(a)*** *A scenario when the ship crosses a hotspot from a background concentration of 2 nmol L^{-1} at a ship speed of 4 knots (e.g. when ship is doing coarse survey).* ***(b)*** *A scenario when the ship crosses a hotspot from a background concentration of 2 nmol L^{-1} at a ship speed of 0.1 knots (e.g. when ship is holding station).* ***(c) and (d)*** *are the blown-up plots for (a) and (b). White lines indicate 4 nmol L^{-1} contours. 4 nmol L^{-1} is our defined boundary for an observable hotspot signal.*

Since the corrected seawater concentration (C_w) is close to an average concentration over 12 min (see equation 7), it averages out the high and low seawater concentrations. Here, we will assess the possible impact of missed hotspots along the survey track. Assuming the three seep sites only contain hotspots with methane concentrations of 1609 nmol L^{-1} and waters with background concentrations of 2 nmol L^{-1}, the possible sizes of the missed hotspots can be determined by equation 7 using the actual ship speeds and the observed concentrations. The area of each possible missed hotspot ranges from 5.24 cm^2 to 77 m^2 and the total area of missed hotpots in each of the three plume areas is 181 – 930 m^2 (MC118), 51 m^2 (GC600) and 20 m^2 (GC185), corresponding to fluxes of 0.80 – 5.16 mol d^{-1} (MC118), 0.24 mol d^{-1} (GC600) and 0.05 mol d^{-1} (GC185) (*Table 5.4*). The mean flux over each plume area resulting from hotspots that might have been missed using the current survey technique accounts for only 1.7 % (MC118), 0.5 % (GC600) and 0.7 % (GC185) of the integrated regional flux (*Table 5.4*).

Table 5.4. *The integrated net mass flux of methane from each survey area each day and the total potential mass flux from hotspots at those sites.*

Sites	Survey Area (km^2)	Mass Flux [a] ($mol\ d^{-1}$)	Total Hotspot Area (km^2)	Hotspots Mass Flux [b] ($mol\ d^{-1}$)
MC118				
YD 187	15.15	300	0.930×10^{-3}	5.16
YD 188	16.27	215	0.238×10^{-3}	1.34
YD 189	34.64	271	0.444×10^{-3}	1.82
YD 190	8.53	66.1	0.181×10^{-3}	0.82
YD 192.5 - 193.5	0.062	0.74	0.597×10^{-3}	4.66
YD 193.5 -195.2	0.53	3.71	0.181×10^{-3}	0.80
Mean		142		2.43
GC 600	8.57	51.9	0.051×10^{-3}	0.24
GC 185	6.69	6.85	0.020×10^{-3}	0.05

[a] *integrated mass flux using natural neighbor;*
[b] *the total methane flux from hotspots assuming relatively small areas of hotspots exist on the survey tracks*

Another potential limitation of the survey technique used in this study is the possibility of missing hotspots existing between the survey tracks and never sampled. Since the extremely high surface water methane concentrations reported in [*E Solomon et al.*, 2009] were from GC 185, we use this site to investigate the impact of missed hotspots between the survey tracks. Assuming that either the missed hotspots or our sampling pattern were randomly distributed throughout the survey area, we estimate the probability that a hotspot was completely missed. For each surface water measurement, the probability (P) that a hotspot was missed is calculated as a function of the total integrated hotspot area (A_h) and the total survey area (A; 6.686 km^2) of GC 185.

$$P = (A - A_h)/A \tag{11}$$

Since we sampled 71 times, and the probability that the hotspot was completely missed on all 71 measurements is P^{71}. This calculation clearly shows that as the area of the hotspot increases, the probability that it was missed rapidly decreases (*Figure 4.8*). While there is an increased probability that a relatively small total integrated hotspot area was missed, this relatively small area leads to a relatively small flux from hotspots. Interestingly, even if we assume a background flux of 50 times the observed value for GC 185, a total integrated hotspot area of only 1.92 % of the survey area is necessary to produce a daily flux similar to our "background" observations. And at a hotspot area of 1.92 %, there is only a 25 % chance that hotspots containing this total integrated area were missed during our sampling campaign.

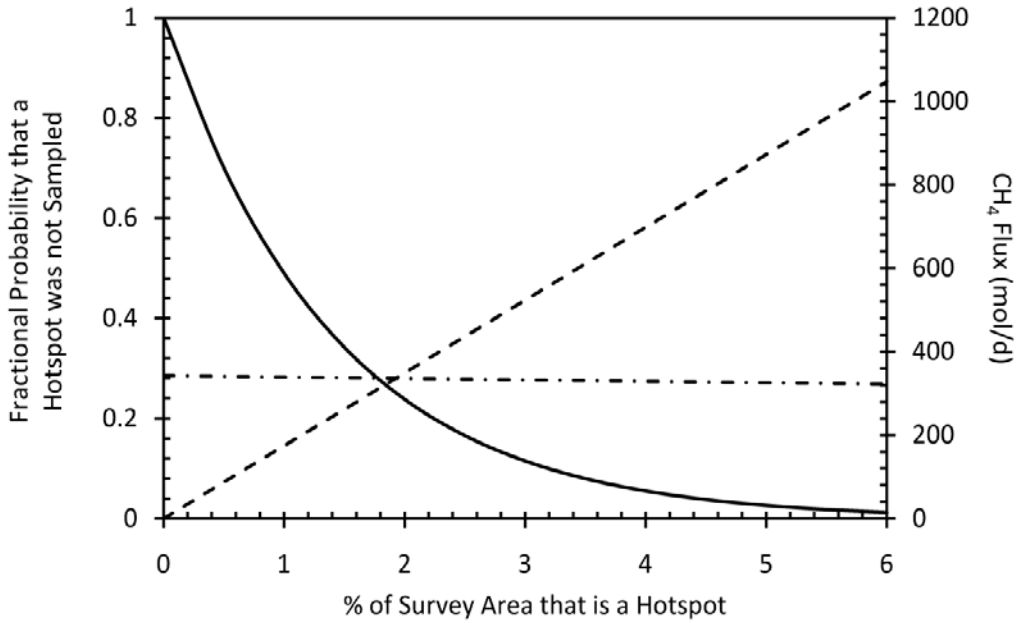

Figure 5.8: *Hotspots potentially missed between sampled locations at GC185 as a function of assumed total hotspot area. Probability that a hotspot was missed during the survey (n = 71) (solid line). CH_4 flux from the total integrated hotspot area (dashed line). CH_4 flux from the 50- times the background (i.e. non-hotspot) area at GC185 (dashed-dotted line).*

5.5 CONCLUSIONS

Elevated methane concentrations in surface seawater were observed, and elevated net sea-to-air methane fluxes were determined at all three seep sites (MC118, GC 600 and GC185) surveyed in this study. The net sea-to-air methane fluxes ranged from - 4.19 μmol m^{-2} d^{-1} to 86.1 μmol m^{-2} d^{-1} over the deepwater hydrocarbon plume areas, agreeing with most previous studies. Variations in the atmospheric methane concentrations suggest the need for measuring atmospheric methane concentration when assessing the net sea-to-air fluxes. High temporal and spatial variability in the methane fluxes was observed over the three seep areas. Extrapolating the highest flux from this study to other deepwater hydrocarbon seeps in the northern Gulf of Mexico suggests that the diffusive net sea-to-air fluxes from deepwater hydrocarbon seeps in the northern Gulf of Mexico is an insignificant source to atmospheric methane. However, the elevated air concentrations on GC600 require about 3 X 10^5 mol d^{-1} of methane released in this area. This tremendous methane source could not be characterized during this study.

Three orders of magnitude of discrepancy exist between the results from this study and those reported in [*E Solomon et al.*, 2009] for the estimation of the diffusive net sea-to-air flux of methane from deepwater hydrocarbon seeps in the northern Gulf of Mexico. The large discrepancy between these two studies is mainly attributable to the different concentrations observed and the depths of those concentrations. The concentrations reported here are all from within or close to the surface mixed layer and appropriate for use in air-sea flux calculations. However, assuming that extremely high methane concentrations existed as relatively small hotspots in the surface seawater over deepwater hydrocarbon seep area, the impact of those hotspots on the regional diffusive air-sea flux would be small.

6. SEDIMENT ANALYSIS

6.1 INTRODUCTION

From a geologic perspective the flux of CH_4 from sources such as marine gas hydrates and mud volcanoes, terrestrial methane seeps, and geothermal/volcanic emissions are likely to comprise a significant fraction of the fossil methane flux to the atmosphere. Of these geologic sources, the flux of methane from marine hydrocarbon seeps and mud volcanoes, probably the most significant sources, is the least constrained because they are difficult to detect. A significant fraction of the methane that migrates from subsurface reservoirs to the water column is sequestered in shallow deposits of gas hydrate that can interact with the water column at the margin of the hydrate stability regime [*I.R. MacDonald et al.*, 2005; *I. R. MacDonald et al.*, 1994; *A.V. Milkov and Sassen*, 2001].

The current budget contains a fossil (^{14}C-depleted) CH_4 flux from fossil fuel-related anthropogenic emissions such as coal mining and crude oil exploitation of ~100 Tg CH_4 yr^{-1} [*K L Denman et al.*, 2007]. This flux is based on the ^{14}C-dead methane in the atmosphere, thus is a top-down estimate. A significant fraction of natural methane from geologic sources is also ^{14}C-depleted, yet is not included in the atmospheric methane budget because the methane fluxes from these sources remain poorly quantified. Thus, the distribution of these marine sources is not well known and they are difficult to sample with traditional techniques. Recent literature reviews have indicated that the CH_4 flux from marine seeps could be as high as 20-40 Tg CH_4 yr^{-1}, which would amount to ~1/3 of the current estimated fossil fuel-related anthropogenic emission to the atmosphere [*Etiope et al.*, 2008a; *Alan G. Judd*, 2003]. These estimates, however, are mainly based on approximations of seafloor CH_4 fluxes and water column acoustic surveys, thus are not constrained by direct water column sampling and flux determinations from the oceanic mixed layer to the atmosphere. These estimates also do not account for possible changes in the stability of shallow gas hydrate due to increased water temperatures [*Kennett and Cannariato*, 2000] or cascading pressure changes resulting from slope failure and turbidity flow [*Dillon and Max*, 2000a]. Most recent studies focused on direct plume sampling in the water column have occurred at water depths <100 m, and in particular have concentrated on the prolific seeps at Coal Oil Point, California. These studies have indicated that the bubble plumes at Coal Oil Point retain a significant fraction of the CH_4 during water column transit and that they emit a considerable amount of methane locally [*Hornafius et al.*, 1999; *Mau et al.*, 2007]. The aerial extent of the Coal Oil Point seeps, however, is small at ~280 km^2; thus, with ~1.3 Gg CH_4 yr^{-1}, these seeps do not contribute a significant amount of methane to the atmosphere [*Hornafius et al.*, 1999; *Mau et al.*, 2007]. There have been only a few studies quantifying CH_4 fluxes from deepwater (>200 m) hydrocarbon seeps [*Kessler et al.*, 2006; *Schmale et al.*, 2010; *Valentine et al.*, 2001], which cover a much larger area than the shallow water seeps. These preliminary studies have indicated that CH_4 in bubble plumes emanating from water depths greater than 200 m is entirely consumed before reaching the mixed layer as a result of bubble dissolution, aerobic methane oxidation, and gas exchange, thus are not a significant source of methane to the atmosphere [*Greinert et al.*, 2006; *Valentine et al.*, 2001]., These studies that are limited in spatial extent, relied on inaccurate sampling techniques that typically fail in sampling the bubble plumes, but sample the background concentrations instead. Thus, the question of whether marine hydrocarbon plumes represent a significant source of CH_4 to the atmosphere that should be included in the global atmospheric methane budget remains unresolved. However, it is also important to consider factors that will constrain the release of CH_4 from the sediments or from shallow deposits of gas hydrate.

There are several processes that consume methane as it ascends from seafloor seeps to the sea surface. A highly important CH_4 loss processes is anaerobic oxidation of methane (AOM) in the sediment column, bubble dissolution, aerobic CH_4 oxidation in the water column, and gas transfer across the bubble-water interface with N_2 and O_2 during bubble ascent through the water column. During AOM, methane rich fluids, derived either from bacterial or thermogenic sources, rise toward the sediment-water interface and

are met by sulfate rich pore fluids derived from bottom water. This methane-sulfate interaction is mediated by a consortium of microorganisms [*Antje Boetius et al.*, 2000; *Orphan et al.*, 2001]. During AOM methane and sulfate are both consumed resulting in a production of hydrogen sulfide and an increase in carbonate alkalinity of the pore fluids:

$$CH_4 + SO_4^{2-} => HCO_3^- + HS^- + H_2O$$

One consequence of AOM is the creation of a sulfate-methane interface (SMI) [e.g., *W. S. Borowski et al.*, 1996; *W. S. Borowski et al.*, 1997; *Iversen and Jorgensen*, 1985]. The SMI is an interval at the base of the sulfate reduction zone that separates sulfate-bearing pore fluids above from sulfate-depleted but methane-rich pore fluids below.

Carbon that was originally part of the methane pool is transformed to bicarbonate, which causes increases in DIC and carbonate alkalinity of the pore fluids at the SMI. Higher carbonate alkalinity, in turn, will stimulate authigenic carbonate precipitation at and immediately below the SMI [e.g., *Thomas H. Naehr et al.*, 2007a; *Orphan et al.*, 2004] via the following reaction [*Baker and Burns*, 1985]:

$$2HCO_3^- + Ca^{2+} => CaCO_3 + CO_2 + H_2O$$

The formation of carbonates in methane-rich and methane-gas-hydrate-bearing marine sediments will sequester a portion of the methane-derived carbon in these systems. The sequestration of carbon will mean that there will be less “free” methane available for interaction with the ocean and atmosphere and more tied up in carbonates; this in turn will affect the global carbon cycle.

To date, little is known about the quantitative aspects of carbon sequestration by authigenic carbonate precipitation. Rates of DIC production through AOM are not well constrained, and current estimates for rates of AOM vary by four orders of magnitude [for a review see *Ussler III and Paull*, 2008]). However, knowing rates of DIC production via AOM is necessary to estimate rates at which authigenic carbonates may form. Recently, two biogeochemical models have been published, which may help to address these questions [*Luff et al.*, 2004; *Ussler III and Paull*, 2008]. These models indicate that $CaCO_3$ precipitation rates may be as high as 120 μmol cm^{-2} a^{-1} [*Luff and Wallmann*, 2003; *Luff et al.*, 2004]. In addition, formation of authigenic carbonate in the subsurface may also contribute to the focusing of fluid flow and ultimately enhance methane fluxes into the water column, because methane can escape only at high fluid flow rates [*Luff et al.*, 2005]. Regardless of the net effect of authigenic carbonate formation (sequestration of methane-derived carbon, or increase of methane fluxes into the water column), AOM-driven carbonate precipitation in gas-hydrate-bearing marine sediments must be considered when assessing the impact of gas-hydrate-derived methane on the global carbon cycle.

In the context of this study, we analyzed pore water and sediment samples for sulfate, sulfide, total alkalinity, DIC, calcium concentrations, carbonate content, bulk carbon and oxygen isotopic composition to constrain the degree of AOM and carbonate precipitation at different sediment depths. This was done for three different gas hydrate bearing sites in the northern Gulf of Mexico. Results from this study will contribute to a modeling effort aimed at constraining carbonate precipitation rates at gas hydrate sites in the Gulf of Mexico and elsewhere.

6.2 REGIONAL SETTING

In the Gulf of Mexico, a thick sequence of continental margin sediments overlies enormous reservoirs of liquid and gaseous hydrocarbons that rest upon Jurassic-age salt deposits. Salt-driven tectonics generate fault networks that act as conduits for the rapid transfer of oil, gas and brines from deep reservoirs through the overlying sediments and into the water column [*H. H. Roberts*, 2001]. On the sea floor, these conduits give rise to gas vents and seeps, subsurface and surficial methane hydrates (*Figure 2.1a*), brine pools and mud volcanoes [*Aharon*, 1994; *Ian R. MacDonald et al.*, 2003; *H. H. Roberts*, 2001].

Sediments around areas of active seepage are characterized by elevated concentrations of simple (C_1–C_5) and high-molecular weight hydrocarbons (oils) and hydrogen sulfide. Complex chemosymbiotic communities proliferate in this cold, high-pressure environment by exploiting the abundance of energy-rich, reduced substrates including CH_4 and H_2S, the latter produced by anaerobic oxidation of hydrocarbons in gas, liquid, and gas hydrate phases [*Aharon and Fu*, 2000; *Ian R. MacDonald et al.*, 2003] .

Recent seismic studies based on detection of anomalous reflectors at the sediment there may be 5,000 seep sites in the northern Gulf of Mexico where carbonate has formed during recent geologic time [*Frye*, 2008]. However, the present day release rates from these sites have not been well constrained and cannot be confirmed from seismic evidence alone. Ground truth operations reported by [*De Beukelaer et al.*, 2003; *Frye*, 2008; *I. R. MacDonald*, 1997; *A.V. Milkov and Sassen*, 2001; *H. H. Roberts and Carney*, 1997] demonstrate that active oil seeps universally include shallow deposits of gas hydrate. In many ways the Gulf of Mexico has also served as a case study for understanding gas hydrate deposits and hydrocarbon seeps, which have more recently been investigated on other continental margins. The HYFLUX sites in the Gulf of Mexico that were investigated in this study are Green Canyon 600 (GC 600; 1200 m water depth), Mississippi Canyon 118 (MC 118; 900 m water depth), and Green Canyon 185 (GC 185; 550 m water depth).

6.3 MATERIALS AND METHODS

Sediments were collected using push cores, piston cores and gravity cores in the three active gas hydrate sites visited. Push cores were taken using a Remotely Operated Vehicle (ROV). Three piston cores, one gravity core and one push core were taken. Two of the piston cores were taken at GC 600 and one was taken at GC 185. One gravity core and one push core were collected at site MC 118. Once on board, cores were cut into segments that were stored in a temperature-controlled environment for analysis at an onshore laboratory, where the segments were sectioned at predetermined intervals. (One piston cores was given to Florida State University for sediment analysis.) Piston core number one (PC 1) measured 325 cm and the upper 290 cm was sectioned and squeezed for pore fluids using a Reeburgh-style pore water press with the increments ranging from 3 cm at the surface layer to 20 cm at greater depths. Piston core number three (PC 3) measured 200 cm in total length. The top 50 cm were split lengthwise. One half of the core was squeezed with the pore water press and the remaining half was used to extract pore water by means of Rhizon sampling. Equal increments were used for both halves and ranged from 6 cm to 20 cm. Piston core number four (PC 4) was 500 cm in length and was also split lengthwise in order to allow one half to be squeezed by the pore water press and the other half to use Rhizons as means of pore water extraction. One 43 cm gravity core was taken from site MC 118 and the sections were divided into increments ranging from 3-20 cm. All of the squeeze cakes taken from the pore water press were labeled and stowed for further onshore analysis. Pore water samples were analyzed on board via gas chromatograph for alkalinity.

Pore fluid samples were filtered through disposable 0.45 μm Gelman polysulfone filters for analysis of Ca^{2+}, Mg^{2+}, total sulfur (TS), K^+, and Na. Dissolved inorganic carbon (DIC) samples were poisoned with an $HgCl_2$ solution and stored in vacutainers. Aliquots for sulfate analyses were added to centrifuge tubes containing a 50% $CdNO_3$ solution to precipitate the sulfide. Ca, Mg, SO_4, and K concentrations were determined at Scripps Oceanography Institution via inductively coupled plasma-optical emission spectrometry (ICP-OES). The analytical reproducibility of the analyses expressed as percent precision from multiple determinations of IAPSO standard seawater are: Ca^{2+} = 0.63%, SO_4^{2-} = 0.7%. For details regarding the analytical procedure see [*E A Solomon et al.*, 2008].

Sediment samples were analyzed for percent carbonate [expressed as weight percent (wt.%) CaCO3] using a C/N elemental analyzer at TAMUCC. Bulk sedimentary carbonate stable isotope ratios for carbon

and oxygen were determined by reacting samples with 100% orthophosphoric acid in vacuo at 90°C. The purified CO_2 gas was analyzed using a Finnigan MAT 252 mass spectrometer at the Texas A&M University stable isotope facility. Results are reported in standard δ notation relative to the PDB standard. Precision is on the order of 0.03‰ for both oxygen and carbon.

Our modeling approach to constrain the rate of AOM needed to generate the observed DIC concentrations followed the method described in [*Ussler III and Paull*, 2008]. As outlined by these authors, the DIC pool was assumed to comprise only bicarbonate anions because this is the dominant chemical species of the carbonate system at typical porewater pH values and simplified the selection of the diffusion coefficient. The details of how DIC is acquired by various microbes in the pore water do not affect the model. The bicarbonate free solution diffusion coefficient (D_o=11.8×10^{-6} cm^2 s^{-1} at 25 °C) was adjusted to the in situ temperature (5.5 °C) using the Stoke–Einstein equation [*Iversen and Jørgensen*, 1993]. The model assumes that the sediment was isothermal from the seafloor to 290 cmbsf. The effective sediment diffusion coefficient (D_s) was computed using porosity (Φ) and the relationship $D_s=D_o \Phi^2$, assuming an average porosity of 50% over the depth range of the model (0–290 cmbsf). DIC production was modeled as a 15-cm-thick vertical zone in which AOM occurred at a uniform rate. For further details regarding the modeling framework and assumptions see [*Ussler III and Paull*, 2008]

6.4 RESULTS

Pore water analysis

Results of the pore water analyses described above are presented in *Table 1* and *Figure 2.1 through 2.7.*

Table 6 1. *Pore water analyses from Gulf of Mexico sites GC 600, GC 185, and MC 118.*

Site	Core segment cm below top)	SO_4 (mM)	Sulfide (mM)	Alkalinity (mM)	Ca^{2+} (mM)
GC600	**PC1**				
	0-3	21.34	1.62	10.27	8.96
	3-6	2.51	7.91	32.49	4.42
	6-9	1.09	4.06	33.11	4.85
	9-15	1.91	19.39	41.02	6.01
	15-25	0.00	32.11	41.13	5.48
	50-65	0.00	24.96	39.69	6.31
	150-170	0.03	1.41	42.50	9.01
	225-245	0.00	10.60	42.85	10.40
	275-290	0.00	3.05	35.59	12.27
	PC3				
	0-6	21.93	1.04	5.34	8.28
	6-12	19.22	1.66	8.20	7.97
	12-20	10.93	4.82	16.04	6.03
	20-30	8.63	5.00	19.87	6.06
	30-40	4.00	6.60		4.69
	40-49	3.00	27.26	26.44	4.80
GC185	**PC4**				
	0-6	24.99	1.91	4.26	10.20
	6-12	23.05	3.65	4.74	10.05
	12-20	24.72	2.14	3.85	10.15
	20-30	23.72	3.29	4.38	10.30
	30-40	25.05	2.21	4.43	10.37

Site	Core segment cm below top)	SO_4 (mM)	Sulfide (mM)	Alkalinity (mM)	Ca^{2+} (mM)
	40-49	23.56	3.45	4.74	10.20
MC118	**GC8**				
	0-3	25.20	3.02	3.63	10.55
	3-6	25.32	1.51	4.38	9.89
	6-9	25.56	0.59	4.49	9.44
	9-15	18.05	0.00	11.87	6.64
	15-25	9.81	4.45	19.30	5.75
	30-43	1.91	8.97	27.80	4.87
	RC8				
	0-3	26.47	1.32	3.01	10.25
	3-6	24.93	2.66	3.40	10.47
	6-10	22.29	4.06	5.79	10.12

GC 600: PC 1

GC 600 PC 1 displayed SO_4^{2-} concentrations that decreased from 21.34 mM at 0 cm to 0 mM at 282.5 cm. HS^- concentrations for this piston core began to increase to a concentration of 32.11 mM up to 20 cm but then began to decrease down to 3.05 mM at a subsurface depth of 282.5 cm. Alkalinity concentrations start as 10.27 mM at a depth of 1.5 cm and increase to a concentration of 35.59 mM at 282.5 cm subsurface. Ca^{2+} also increases from 8.96 mM at 1.5 cm to 12.27 mM at 282.5 cm. See *Figure 2.1*.

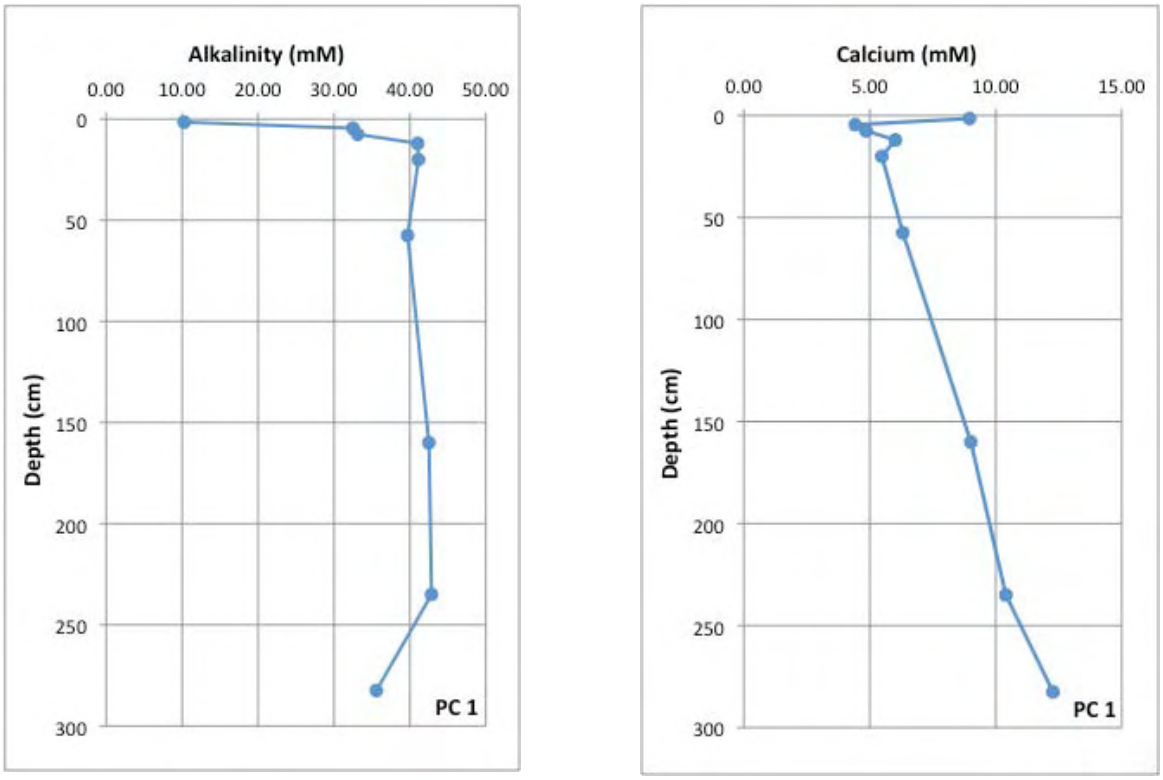

Figure 6.1: *SO_4^{2-}, HS^-, Alkalinity and Ca^{2+} concentrations for PC 1 at site GC 600.*

GC 600: PC 3

The sulfate concentration at 3 cm subsurface was 21.93 mM and decreased to 3.00 mM at 44.5 cm subsurface. HS^- concentrations increased from 1.04 mM at 3 cm subsurface to 27.26 at a depth of 44.5 cm. Alkalinity concentrations yielded a steady increase from 5.34 mM at 3 cm subsurface to 26.44 mM at 44.5 cm and Ca^{2+} depletion in the same subsurface range from 8.28 mM to 4.80 mM. See *Figure 2.2.*

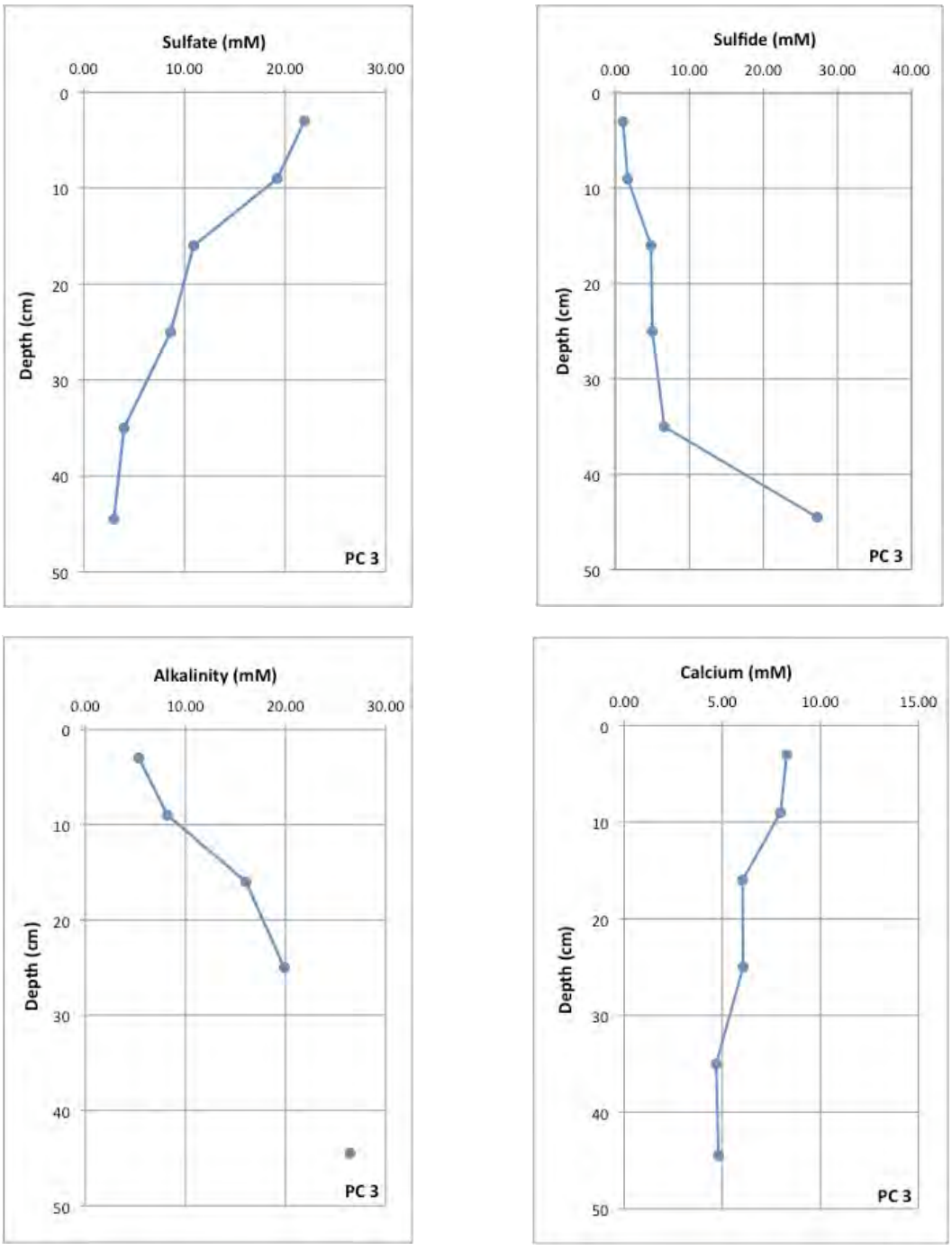

Figure 6.2: *SO_4^{2-}, HS^-, Alkalinity and Ca^{2+} concentrations for PC 3 at site GC 600.*

GC 185: PC 4

The piston core at site GC 185 showed SO_4^{2-} concentrations that ranged from 22.99 mM at 3 cm to 23.56 mM at 44.5 cm sediment depth. Measurements at this site fluctuated slightly but did not show any large reduction. HS^- concentrations similarly showed minute changes with an initial increase from 1.91 mM at 3 cm and ending with a concentration of 3.45 mM at a subsurface depth of 44.5 cm. Alkalinity concentrations at 3 cm were 4.26 mM and increased slightly to 4.47 mM over the 44.5 cm distance. Ca^{2+} concentrations were equal at the first and last intervals, measuring 10.20 mM, and showed only small fluctuations throughout the sediment (*Figure 6.3*).

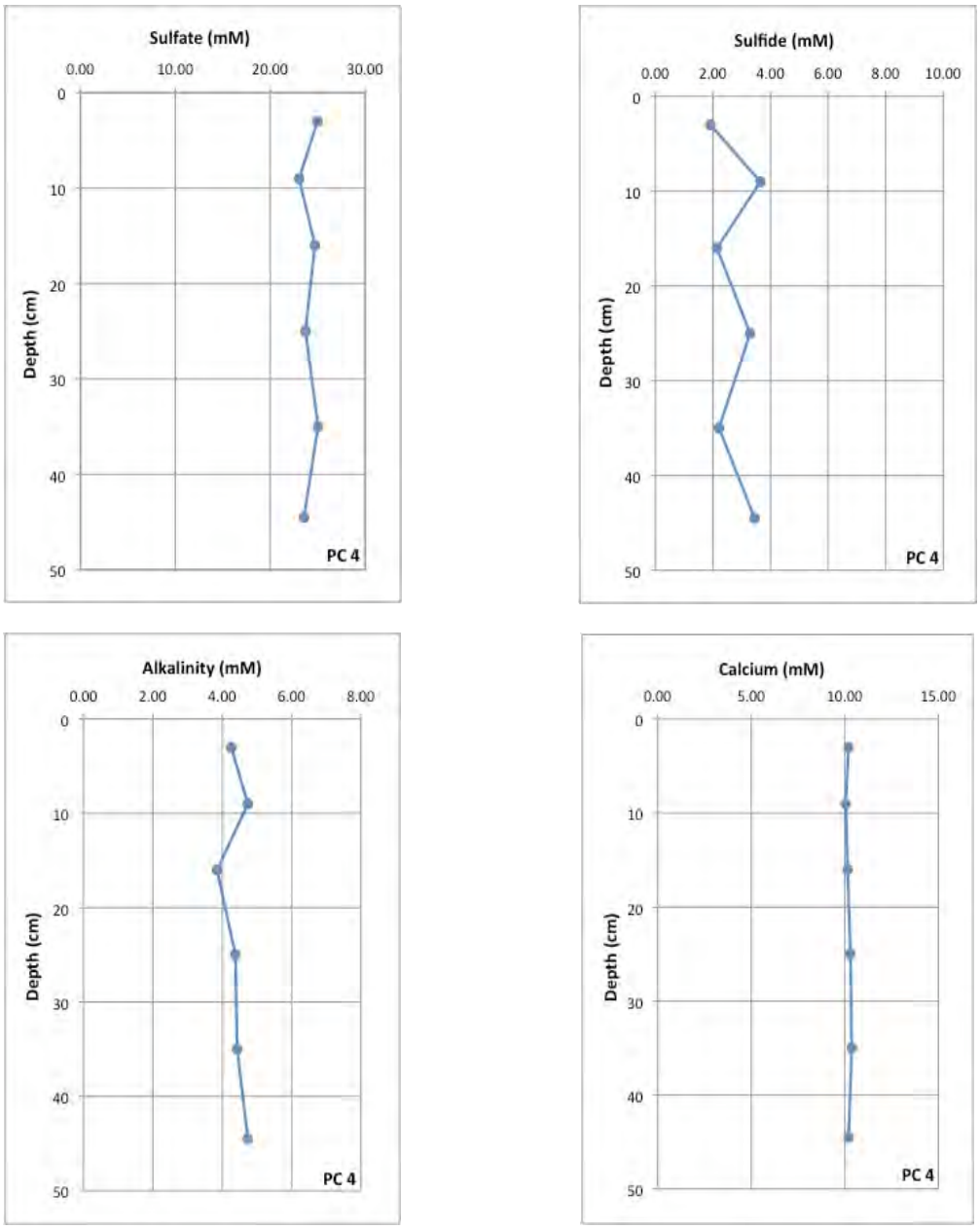

Figure 6.3: *SO_4^{2-}, HS^-, Alkalinity and Ca^{2+} concentrations for PC 4 at site GC 185.*

Results from the Rhizone sampling (not shown) were very similar to the data collected using standard pore water extraction techniques except there was no increase in HS^-.

MC 118: GC 8 and RC 8

Site MC 118 shows a decrease of SO_4^{2-} in the sediment from 25.2 mM at 1.5 cm depth to concentrations of 1.91 mM at 36.5 cm. Sulfide concentrations increase below 12 cm depth to 8.82 mM at 36.5 cm. Alkalinity concentrations show an increase with subsurface depth from 3.63 mM at 1.5 cm to 27.8 mM at 36.5 cm, and decrease in Ca^+ concentrations from 10.55 mM at 1.5 cm subsurface to 4.87 mM at 36.5 cm. The push core taken from site MC 118 shows a decrease in SO_4^{2-} from 26.47 mM at 1.5 cm to 22.29 mM at 8 cm, along with HS^- a concentration increase from 1.32 mM at 1.5 cm to 4.06 mM at 8 cm. Alkalinity increases from 3.01 mM at 1.5 cm to 5.79 mM at 8 cm and Ca^+ decreases from 10.25 mM at 1.5 cm to 10.12 mM at 8 cm. See *Figure 6.4* and *Figure 6.5*.

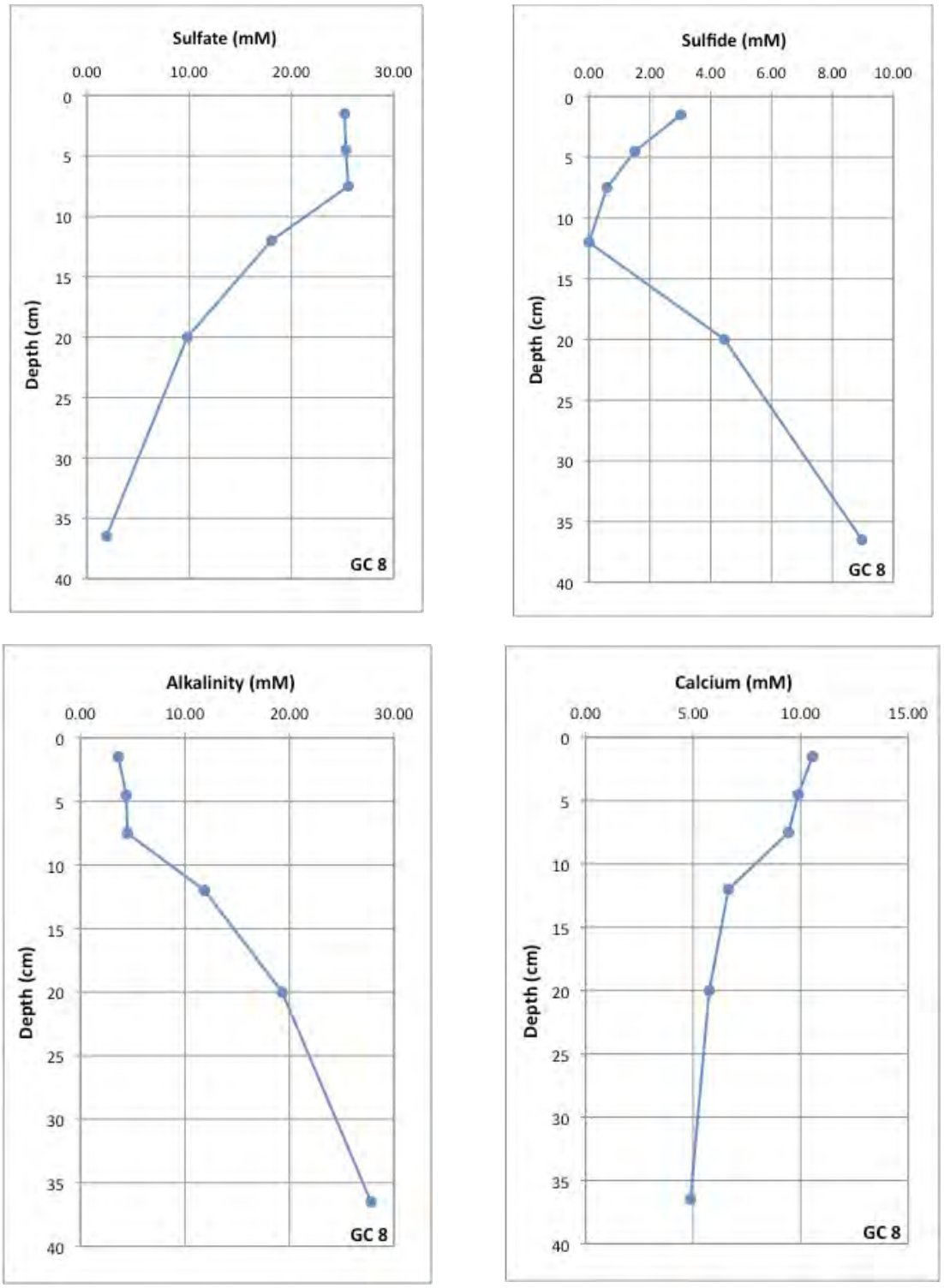

Figure 6.4: *SO_4^{2-}, HS^-, Alkalinity and Ca^{2+} concentrations for GC 8 at site MC 118.*

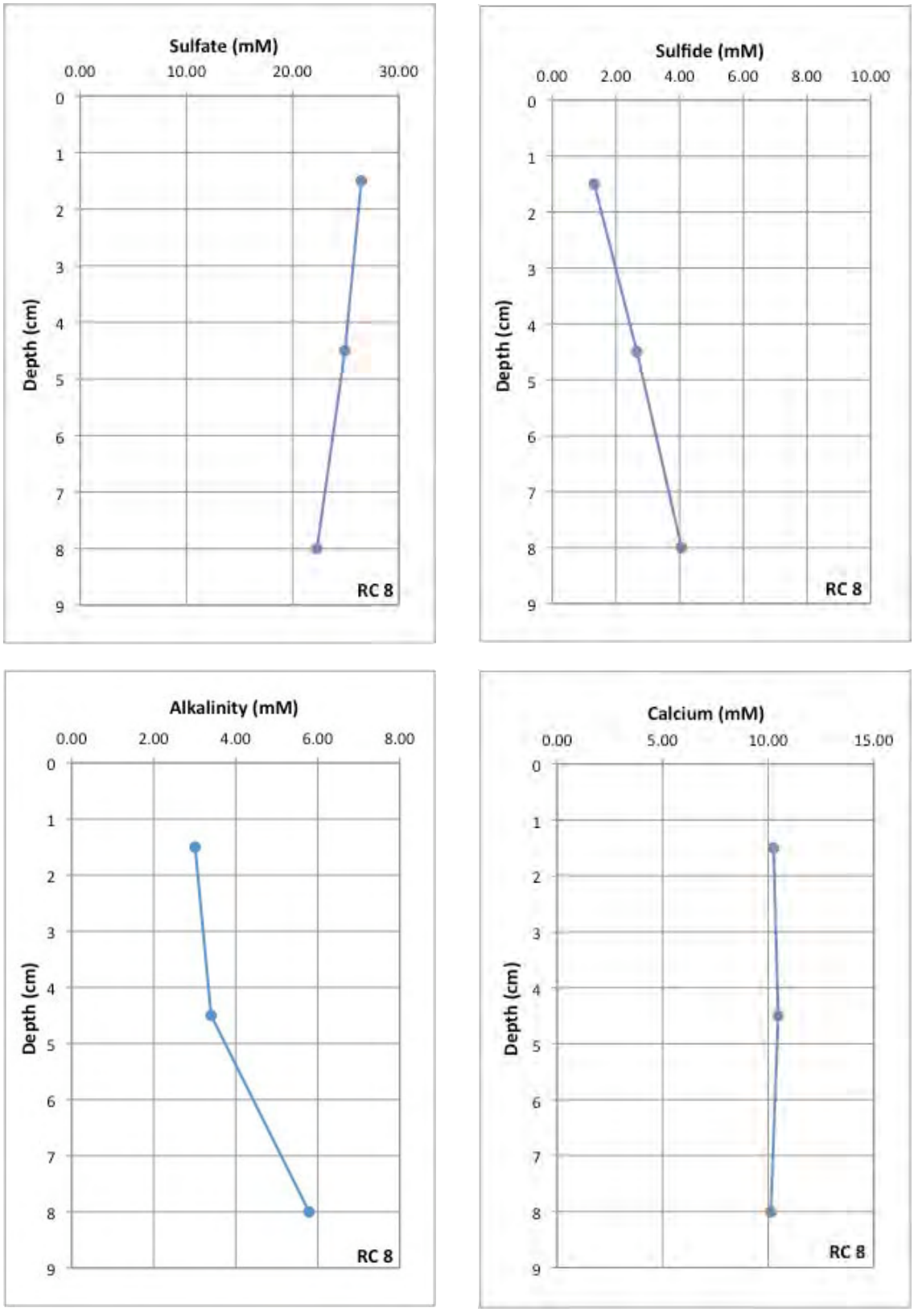

Figure 6.5: *SO_4^{2-}, HS^-, Alkalinity and Ca^{2+} concentrations for RC 8 at site MC 118.*

Sediment Analysis

Results of the sediment analyses are presented in *Table 6.2* and *Figure 6.6.*

Table 6.2. *Sediment analyses from Gulf of Mexico sites GC 600, GC 185, and MC 118. PC 1, PC3, and PC 4 were collected with a piston corer, GC 8.*

Site	Core segment (cm below top)	Carbonate [wt. %]	Carbonate ∂^{13}C ‰ (PDB)	Carbonate ∂^{18}O ‰ (PDB)
GC 600	**PC 1**			
	0-3	4.30	-0.05	-1.12
	3-6	8.70	-10.12	-0.82
	6-9	15.60	-39.45	0.76
	9-15	9.80	-21.67	0.52
	15-25	14.90	-36.89	0.84
	50-65	6.20	-5.82	-4.79
	150-170	4.90	-1.47	-3.98
	225-245	8.40	-4.32	-4.27
	275-290	5.60	-0.87	-5.02
	PC 3			
	0-6	2.30	-0.57	-0.37
	6-12	3.10	-1.58	-0.79
	12-20	5.10	-1.47	0.84
	20-30	6.70	-5.82	-0.53
	30-40	5.80	-8.73	1.05
	40-49	8.20	-17.74	-0.83
GC 185	**PC4**			
	0-6	3.60	-0.78	-1.73
	6-12	2.80	-0.26	-0.82
	12-20	4.50	-0.59	-0.51
	20-30	2.30	-0.69	0.68
	30-40	3.70	-1.53	0.34
	40-49	4.10	-0.42	-1.12
MC 118	**GC 8**			
	0-3	4.40	-0.81	-1.02
	3-6	5.60	-0.44	0.54
	6-9	3.70	-0.56	-0.78
	9-15	5.20	-3.67	0.98
	15-25	6.90	-6.89	-1.47
	30-43	6.50	-12.63	-1.32
	RC 8			
	0-3	3.1	-1.63	-0.76
	3-6	4.2	-0.91	-0.32
	6-10	3.7	-2.78	0.33

GC 600: PC 1

Carbonate contents at GC 600 PC 1 ranged from 4.3 to 15.6 weight percent and bulk sedimentary carbonate ∂^{13}C values are between −39.45‰ and −0.05‰. Sharp increases in carbonate content below the SMI correlate with large changes in the ∂^{13}C of the bulk carbonate. Throughout much of the core sedimentary carbonate ∂^{13}C values are close to values for pelagic carbonate (~0‰), except for the interval between 3 to 25 cmbsf.

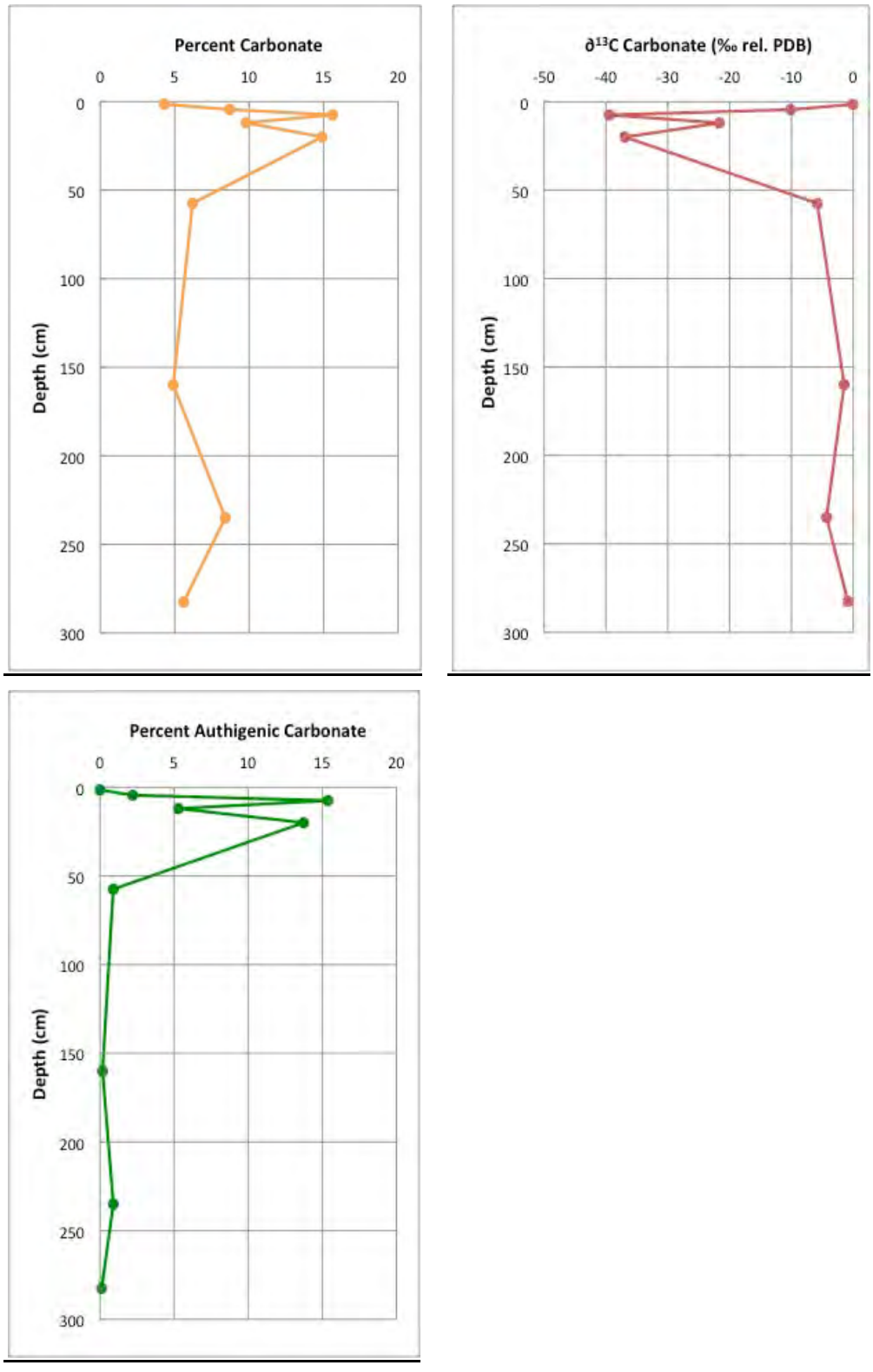

Figure 6.6: *Percent carbonate, bulk sedimentary carbonate $\partial^{13}C$, and percent authigenic carbonate by weight calculated from simple mass balance plotted versus depth. See text for discussion.*

GC 600: PC 3

Carbonate contents for piston core PC 1 ranged from 2.3 to 8.2 weight percent and bulk sedimentary carbonate ∂^{13}C values are between −17.74‰ and −0.57‰. Slight increases in carbonate content below 12 cmbsf correlate with changes in the ∂^{13}C of the bulk carbonate.

GC 185: PC 4

The piston core at site GC 185 showed carbonate contents that ranged from 2.3 to 4.5 weight percent and bulk sedimentary carbonate ∂^{13}C values are between −1.53‰ and −0.26‰. Slight increases in carbonate content below 12 cmbsf correlate with changes in the ∂^{13}C of the bulk carbonate. Throughout the core sedimentary carbonate ∂^{13}C values are close to values for pelagic carbonate (~0‰).

MC 118: GC 8

Carbonate contents at MC 118 GC 8 ranged from 4.4 to 6.9 weight percent and bulk sedimentary carbonate ∂^{13}C values are between −12.63‰ and −0.44‰. Slight increases in carbonate content below 9 cmbsf correlate with changes in the ∂^{13}C of the bulk carbonate.

MC 118: RC 8

Carbonate contents for ROV core GC 8 at MC 118 ranged from 3.1 to 4.3 weight percent and bulk sedimentary carbonate ∂^{13}C values are between −2.78‰ and −0.91‰. Throughout the core sedimentary carbonate ∂^{13}C values are close to values for pelagic carbonate (~0‰).

6.5 DISCUSSION

Seafloor seepage of hydrocarbons from leaky subsurface reservoirs and its impact on the geology and biology of the Gulf of Mexico basin is a well-known phenomenon and the co-migration of oil and gas creates a unique biogeochemical regime at Gulf of Mexico cold seeps [e.g., *Ian R. MacDonald et al.*, 2003; *H.H. Roberts and Aharon*, 1994; *R. Sassen et al.*, 1993]. Biogeochemical reactions triggered by the interaction of hydrocarbon, in this case mostly methane gas, including the anaerobic reduction of sulfate, leads to increases in carbonate alkalinity and sulfide concentrations in the pore fluids:

$$CH_4 + SO_4^{2-} \Rightarrow HCO_3^- + HS^- + H_2O \quad (1)$$

This increase in carbonate alkalinity causes carbonate precipitation, which consumes dissolved Ca^{2+}:

$$2HCO_3^- + Ca^{2+} \Rightarrow CaCO_3 + CO_2 + H_2O. \quad (2)$$

The above pore water figures demonstrate the relationship between SO_4^{2-}, alkalinity, HS^-, and Ca^{2+}. Sites of active methane seepage, such as GC 600 and MC 118, typically show a sharp decrease in SO_4^{2-} at deeper sediment depths with values approaching zero close to the sulfate-methane interface (SMI) where all SO_4^{2-} is consumed. In turn HS^- increases with depth according to reaction (1) described above. As methane is consumed, bicarbonate is produced and this reaction increases alkalinity and DIC concentrations. High alkalinity and DIC causes dissolved calcium to precipitate as calcium carbonate [e.g., *Thomas H. Naehr et al.*, 2000; *Thomas H. Naehr et al.*, 2007a; *Orphan et al.*, 2004]. The combination of pore water sulfate, sulfide, alkalinity, DIC, and calcium data reveals biogeochemical processes at hydrocarbon seeps.

Site GC 600: PC 1 and PC 3

Pore water samples from GC 600 PC 1 show SO_4^{2-} concentrations that decrease rapidly in the upper 25 cm below the sediment surface. This pronounced drop in SO_4^{2-} is caused by the anaerobic oxidation of methane, demonstrating that this is an active seep site. The rapid decrease in pore water sulfate concentration with depth and the general shape of the sulfate profile is consistent with consumption of

sulfate within a narrow SMI zone at ~20 cm below sea floor (cmbsf), but is not strictly linear as seen at other locations with SMIs at comparable depths [e.g., Blake Ridge, *Walter S. Borowski et al.*, 2000]. The general concave upward curvature of the sulfate profile between the SMI and the seafloor may suggest a recent increase in the upward methane flux occurred [*Hensen et al.*, 2003]. An increase in upward methane flux would cause the SMI to be located closer to the seafloor and increase the rate of sulfate reduction [*W. S. Borowski et al.*, 1996], creating a concave upward sulfate profile. Sulfide concentrations reach a maximum at SMI depth, which supports the hypothesis that SO_4^{2-} is depleted and HS^- produced. Alkalinity and DIC concentrations sharply increase with depth within the first 20 cmbsf and then remain fairly constant with depth throughout the remainder of the core. Ca^{2+} concentrations sharply decrease with depth from the sediment surface to about 5 cm, then increase with depth throughout the remaining core. This may be due to the presence of another Ca^{2+} source, such as the dissolution of calcareous shell material at depth. Methane $\partial^{13}C$ values at site GC 600 average ~ −54‰ (Lapham, pers. communication), with DIC $\partial^{13}C$ values as low as −40‰. Assuming that authigenic carbonates precipitating from pore water DIC without isotopic fractionation, a simple isotope mass balance calculation using an end member authigenic carbonate isotopic value of −40‰ (PDB) suggests that up to about 15 weight percent of the bulk sediment contains authigenic carbonate (*Figure2.8*).

The second piston core (PC 3) from site GC 600 also showed concentration gradients with depth typical of seep areas, yet the SO_4^{2-} concentrations did not decrease as sharply. Sulfate concentrations decreased steadily with depth throughout the core, placing the SMI at roughly 50 cmbsf. SO_4^{2-} concentrations were inversely related to HS^- concentrations. In this case too, alkalinity concentrations increased while Ca^{2+} depletion was observed indicating carbonate precipitation within the sediment. Rhizone sampling conducted on this core allowed comparison with pore water samples extracted via the pore water press. Data from the Rhizone method showed the same general concentration gradients with depth as the pore water press samples.

Site GC 185: PC 4

This site seemed to be fairly inactive in terms of methane seepage. Only small variations in SO_4^{2-} concentration with depth in the sediment were measured along with a small change in alkalinity. Calcium concentrations stayed almost constant with depth in the sediment. No evidence of gas hydrate was found and we can conclude that this site is currently not an active methane seep. However, Green Canyon block 185 is known to contain a number of active hydrocarbon seeps [*Roger Sassen et al.*, 2003], so the lack of geochemical indicators in this core is most likely the result of inaccurate targeting of the gravity corer. These results corroborate the fact that hydrocarbon seeps are very limited in their lateral extent and that it is easy to miss the most active locations during sample collection.

Site MC 118: GC 8 and RC 8

Site MC 118 is the location of the first gas hydrate observatory in the Gulf of Mexico [*Lapham et al.*, 2008; *Woolsey et al.*, 2005]. At site MC 118, SO_4^{2-} decreases from seawater concentrations (28 mM) to close to zero at 40 cmbsf. Sulfide concentrations show an initial decrease, which may be due to bioirrigation, flushing the sediment with oxygenated bottom water. After 12 cmbsf there is a substantial increase in HS^- due to SO_4^{2-} reduction. Alkalinity concentrations increase with subsurface depth, mirrored by a decrease in Ca^+ concentrations due to the precipitation of calcium carbonate [*Thomas H. Naehr et al.*, 2007a]. Data obtained from analyzing one 10-cm-long push core taken at site MC 118 also showed the same general trends in SO_4^{2-} reduction, a decrease in Ca^{2+} concentrations, along with alkalinity increase and HS^- production.

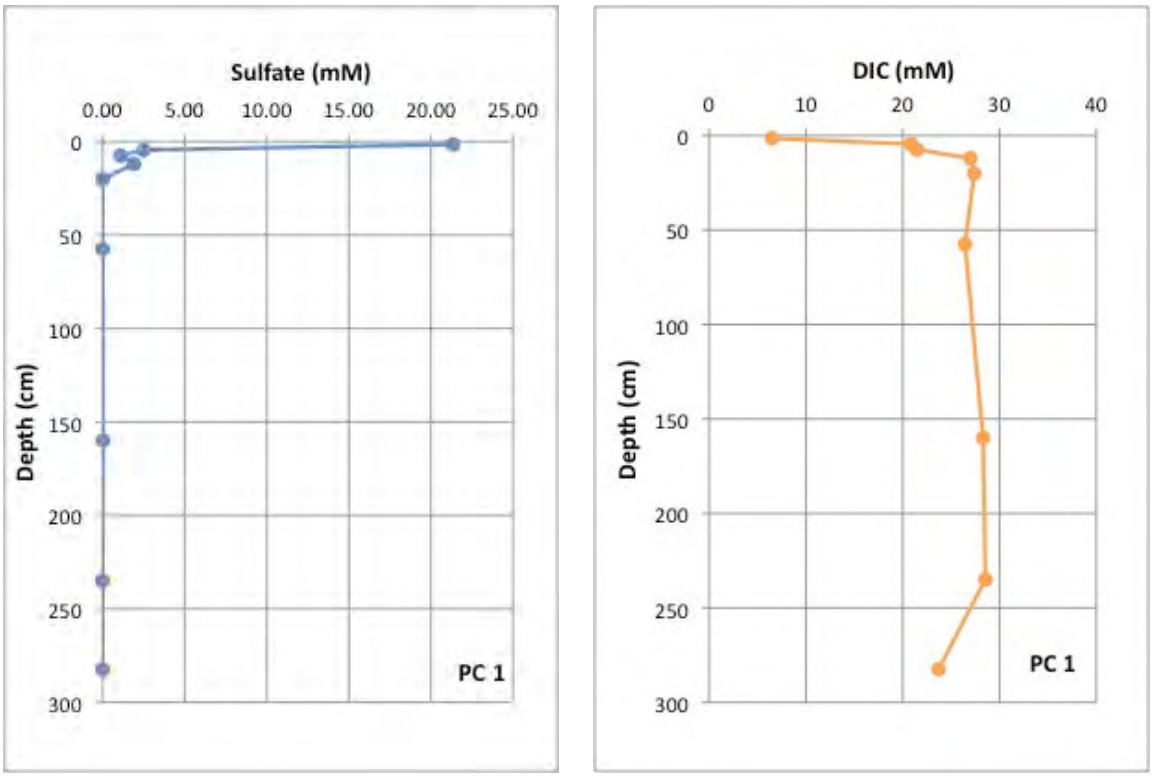

Figure 6.7: *SO_4^{2-} and DIC concentrations for PC 1 at site GC 600.*

Numerical Modeling

Based on the discussion above, PC 1 from site GC 600 was selected for further study, as none of the other cores had penetrated the sedimentary section deep enough to reach the base of the sulfate reduction zone. The model used in this study is a simple, transient numerical model, where DIC production occurs uniformly over a 15-cm-thick vertical zone where present-day DIC concentration is greatest. The model was run until the maximum DIC concentration value matched the measured peak value at the center of the SMI. The DIC production rate used in this model (2.6×10^{-14} mol DIC/cm^3 s) was computed from the flux of sulfate to the center depth of the 15-cm-thick zone of AOM. The model assumes that a linear sulfate gradient extended from the seafloor to 15 cmbsf and no loss of sulfate occurred in the overlying sediments by sulfate reduction of organic matter. This provides a maximum estimate of the amount of sulfate that can be delivered to the zone of AOM. This rate of DIC production is comparable to rates determined from other deep-sea sediment cores summarized by [*Ussler III and Paull*, 2008]. At the DIC production rates used to model DIC accumulation, it would take roughly 2900 yr for the 15% authigenic carbonate calculated for core PC 1 to precipitate, assuming 100% efficiency throughout the process beginning with the delivery of sulfate to the zone of AOM.

6.6 CONCLUSIONS

Anaerobic oxidation of methane at three gas hydrate bearing sites in the northern Gulf of Mexico has produced pore water gradients of dissolved sulfate, sulfide, alkalinity, and calcium indicative of active hydrocarbon seepage. Among the sites studied, GC 600 showed the most active upward flux of hydrocarbons, leading to a complete depletion of pore water sulfate below 20 cmbsf. Sulfide, alkalinity, DIC, and calcium gradients corroborate these findings and are indicative of authigenic carbonate precipitation in shallow subsurface sediments. Pore water data from site MC 118 also showed evidence for active hydrocarbon seepage, although pore water gradients indicate lower methane flux rates, which

lead to sulfate reduction and the development of a SMI at roughly 40 cmbsf. Finally, site GC185 revealed pore water gradients typical of background sediments in the area, demonstration the small lateral extent of active hydrocarbon seepage.

Geochemical profiles from site GC 600 indicate that microbially-driven anaerobic oxidation of methane is active now. Microbial production rates of DIC are controlled by the diffusion of sulfate to the zone of AOM and the overall stochiometry of the anaerobic oxidation of methane process. Modeled rates of DIC production (~10^{-14} mol DIC/cm^3 s) are comparable to published rates from field studies and laboratory incubations. Anaerobic oxidation of methane will produce DIC pore water gradients that will lead to subsurface carbon sequestration through authigenic carbonate precipitation in geologically short time intervals of several thousand years.

REFERENCES

Aharon, P. (1994), Geology and biology of modern and ancient submarine hydrocarbon seeps and vents: An introduction, *Geo-Marine Letters*(14), 69-73.

Aharon, P., and B. Fu (2000), Microbial sulfate reduction rates and sulfur and oxygen isotope fractionations at oil and gas seeps in deep water Gulf of Mexico, *Geochimica et Cosmochimica Acta*, *64*(2), 233-246.

Alpers, W., and H. Hühnerfuss (1988), Radar signatures of oil films floating on the sea surface and the Marangoni effect, *Journal of Geophysical Research*, *93*(C4), 3642-3648

Amouroux, D., G. Roberts, S. Rapsomanikis, and M. O. Andreae (2002), Biogenic gas (CH4, N2O, DMS) emission to the atmosphere from near-shore and shelf waters of the north-western Black Sea, *Estuarine Coastal and Shelf Science*, *54*(3), 575-587.

Baker, P. A., and S. J. Burns (1985), Occurrence and formation of dolomite in organic-rich continental margin sediments, *AAPG Bulletin*, *69*(11), 1917-1930.

Bange, H. W., S. Rapsomanikis, and M. O. Andreae (1996), The Aegean Sea as a source of atmospheric nitrous oxide and methane, *Marine Chemistry*, *53*(1-2), 41-49.

Bange, H. W., U. H. Bartell, S. Rapsomanikis, and M. O. Andreae (1994), METHANE IN THE BALTIC AND NORTH SEAS AND A REASSESSMENT OF THE MARINE EMISSIONS OF METHANE, *Global Biogeochemical Cycles*, *8*(4), 465-480.

Bange, H. W., S. Dahlke, R. Ramesh, L. A. Meyer-Reil, S. Rapsomanikis, and M. O. Andreae (1998), Seasonal study of methane and nitrous oxide in the coastal waters of the southern Baltic Sea, *Estuarine Coastal and Shelf Science*, *47*(6), 807-817.

Ben-Avraham, Z., G. Smith, M. Reshef, and E. Jungslager (2002), Gas hydrate and mud volcanoes on the southwest African continental margin off South Africa, *Geology*, *30*(10), 927-930.

Bergquist, D. C., T. Ward, E. E. Cordes, T. McNelis, S. Howlett, R. Kosoff, S. Hourdez, R. Carney, and C. R. Fisher (2003), Community structure of vestimentiferan-generated habitat islands from Gulf of Mexico cold seeps, *Journal of Experimental Marine Biology and Ecology*, *289*(2), 197-222.

Boetius, A., K. Ravenschlag, C. J. Schubert, D. Rickert, F. Widdel, A. Gieseke, R. Amann, B. B. Jorgensen, U. Witte, and O. Pfannkuche (2000), A marine microbial consortium apparently mediating anaerobic oxidation of methane, *Nature*, *407*(6804), 623-626.

Boetius, A., K. Ravenschlag, C. J. Schubert, D. Rickert, F. Widdel, A. Gleseke, R. Amann, B. B. Jørgensen, U. Witie, and O. Pfannkuche (2000), A marine microbial consortium apparently mediating anaerobic oxidation of methane, *Nature*, *407*, 623-626.

Bohrmann, G., et al. (2003), Mud volcanoes and gas hydrates in the Black Sea: new data from Dvurechenskii and Odessa mud volcanoes, *Geo-Marine Letters*, *23*(3-4), 239-249.

Borowski, W. S., C. K. Paull, and W. U. III (1996), Marine pore-water sulfate profiles indicate in situ methane flux from underlying gas hydrates, *Geology*, *24*(7), 655-658.

Borowski, W. S., C. K. Paull, and W. Ussler III (1997), Carbon cycling within the upper methanogenic zone of continental rise sediments: An example from the methane-rich sediments overlying the Blake Ridge gas hydrate deposits, *Marine Chemistry*, *57*, 299-311.

Borowski, W. S., T. M. Hoehler, M. J. Alperin, N. M. Rodriguez, and C. K. Paull (2000), Significance of anaerobic methane oxidation in methane-rich sediments overlying the Blake Ridge gas hydrates, *Proceedings of the Ocean Drilling Program, Scientific Results*, *164*, 87-99.

Brooks, J. M., M. C. Kennicutt, II, R. R. Fay, T. J. McDonald, and R. Sassen (1984), Thermogenic gas hydrates in the Gulf of Mexico., *Science*, *223*, 696-698.

Bryant, R. B., J. Lugo, C. Cordova, and A. Salvador (1991), Physiography and bathymetry, in *The Geology of North America, The Gulf of Mexico Basin*, edited by A. Salvador, Geol. Soc. of Am., Boulder, CO.

Buffett, B. A., and O. Y. Zatsepina (2000), Formation of gas hydrate from dissolved gas in natural porous media, *Mar Geol*, *164*(1-2), 69-77.

Butler, J. H., D. B. King, J. M. Lobert, S. A. Montzka, S. A. Yvon-Lewis, B. D. Hall, N. J. Warwick, D. J. Mondeel, M. Aydin, and J. W. Elkins (2007), Oceanic distributions and emissions of short-lived halocarbons, *Global Biogeochemical Cycles*, *21*(1).

Chen, D.-F., Z. Su, and L. M. Cathles (2006), Types of gas hydrates in marine environments and their thermodynamic characteristics, *Terrestrial Atmospheric and Oceanic Sciences*, *17*(4), 723-737.

Chernick, M. R. (1999), *Bootstrap methods, A practicioner's guide*, Wiley, New York, NY.

Clark, J. F., L. Washburn, and K. S. Emery (2010), Variability of gas composition and flux intensity in natural marine hydrocarbon seeps, *Geo-Marine Letters*, *30*(3-4), 379-388.

Clark, J. F., I. Leifer, L. Washburn, and B. P. Luyendyk (2003), Compositional changes in natural gas bubble plumes: observations from the Coal Oil Point marine hydrocarbon seep field, *Geo-Marine Letters*, *23*(3-4), 187-193.

Cordes, E. E., S. L. Carney, S. Hourdez, R. S. Carney, J. M. Brooks, and C. R. Fisher (2007), Cold seeps of the deep Gulf of Mexico: Community structure and biogeographic comparisons to Atlantic equatorial belt seep communities, *Deep-Sea Res Pt I*, *54*(4), 637-653.

Cynar, F. J., and A. A. Yayanos (1991), ENRICHMENT AND CHARACTERIZATION OF A METHANOGENIC BACTERIUM FROM THE OXIC UPPER LAYER OF THE OCEAN, *Current Microbiology*, *23*(2), 89-96.

De Beukelaer, S. M., I. R. MacDonald, N. L. Guinnasso, and J. A. Murray (2003), Distinct side-scan sonar, RADARSAT SAR, and acoustic profiler signatures of gas and oil seeps on the Gulf of Mexico slope, *Geo-Marine Letters*, *23*(3-4), 177-186.

de Miranda, F. P., A. M. Q. Marmol, E. C. Pedroso, C. H. Beisl, P. Welgan, and L. M. Morales (2004), Analysis of RADARSAT-1 data for offshore monitoring activities in the Cantarell Complex, Gulf of Mexico, using the unsupervised semivariogram textural classifier (USTC), *Canadian Journal of Remote Sensing*, *30*(3), 424-436.

Deangelis, M. A., and C. Lee (1994), METHANE PRODUCTION DURING ZOOPLANKTON GRAZING ON MARINE-PHYTOPLANKTON, *Limnology and Oceanography*, *39*(6), 1298-1308.

Delisle, G. (2004), The mud volcanoes of Pakistan, *Environ. Geol.*, *46*(8), 1024-1029.

Denman, K. L., et al. (2007), Climate Change 2007: The Physical Science Basis. Contribution of working group 1 to the fourth assessment report of the Intergovernmental Panel on Climate Change, chap. Changes in Atmospheric Constituents and in Radiative Forcing, edited, pp. 499-587, Cambridge University Press, Cambridge and New York.

Denman, K. L. e. a. (2007), Couplings Between Changes in the Climate System and Biogeochemistry. In: Climate Change 2007: The Physical Science Basis. Contribution of Working Group I to the Fourth Assessment Report of the Intergovernmental Panel on Climate Change [Solomon, S.D. et al. (eds.)]. *Rep.*, 67 pp, Cambridge University Press, Cambridge, UK and New York, NY, USA.

Deonier, R., S. Tavaré, and M. S. Waterman (2005), *Computational Genome Analysis: An Introduction*, Springer, New York, NY USA.

Dickens, G. R., J. R. Oneil, D. K. Rea, and R. M. Owen (1995), Dissociation of Oceanic Methane Hydrate As a Cause of the Carbon-Isotope Excursion At the End of the Paleocene, *Paleoceanography*, *10*(6), 965-971.

Dillon, W. P., and M. D. Max (2000a), Oceanic gas hydrates, in *Natural Gas Hydrate in Oceanic and Polar Environments*, edited by M. D. Max, pp. 61-76, Kluwer Academic Publishers, Dordrecht.

Dillon, W. P., and M. D. Max (2000b), Oceanic gas hydrate, in *Natural Gas Hydrates in Oceanic and Permafrost Environments*, edited by M. D. Max, pp. 61-76, Kluwer Academic Press, The Netherlands.

Ding, F., V. Spiess, I. R. MacDonald, M. Bruening, N. Fekete, and G. Bohrmann (2010a), Shallow sediment deformation styles in north-western Campeche Knolls, Gulf of Mexico and their controls on the occurrence of hydrocarbon seepage, *Marine and Petroleum Geology*, *27*(4), 959-972.

Ding, F., V. Spiess, N. Fekete, B. Murton, M. Bruening, and G. Bohrmann (2010b), Interaction between accretionary thrust faulting and slope sedimentation at the frontal Makran accretionary prism and its implications for hydrocarbon fluid seepage, *Journal of Geophysical Research-Solid Earth*, *115*.

Egorov, A. V., K. Crane, P. R. Vogt, and A. N. Rozhkov (1999), Gas hydrates that outcrop on the sea floor: stability models, *Geo-Mar Lett*, *19*(1-2), 68-75.

Egorov, A. V., K. Crane, P. R. Vogt, and A. N. Rozhkov (1999), Gas hydrates that outcrop the sea floor: stability models, *Geo-Mar Lett*, *19*(1/2), 68-75.

Etiope, G., and P. Ciccioli (2009), Earth's Degassing: A Missing Ethane and Propane Source, *Science*, *323*(5913), 478-478.

Etiope, G., A. V. Milkov, and E. Derbyshire (2008a), Did geologic emissions of methane play any role in Quaternary climate change?, *Global and Planetary Change*, *61*(1-2), 79-88.

Etiope, G., K. R. Lassey, R. W. Klusman, and E. Boschi (2008b), Reappraisal of the fossil methane budget and related emission from geologic sources, *Geophysical Research Letters*, *35*(9).

Fortuny-Guasch, J. (2003), Improved Oil Slick Detection and Classification with Polarimetric SAR, *Proceedings of the Workshop on POLinSAR - Applications of SAR Polarimetry and Polarimetric Interferometry (ESA SP-529). 14-16 January 2003, Frascati, Italy. Editor: H. Lacoste. Published on CDROM., p.27.1*.

Frew, N. M., et al. (2004), Air-sea gas transfer: Its dependence on wind stress, small-scale roughness, and surface films, *Journal of Geophysical Research-Oceans*, *109*(C8).

Frye, M. (2008), Preliminary Evaluation of In-Place Gas Hydrate Resources: Gulf of Mexico Outer Continental Shelf, *U.S. Dept. Interior, Minerals Management Service, Resource Evaluation Division*, *OCS Report MMS 2008-004*, 192 pages, appendices.

Garcia-Pineda, O., I. MacDonald, B. Zimmer, B. Shedd, and H. Roberts (2010), Remote-sensing evaluation of geophysical anomaly sites in the outer continental slope, northern Gulf of Mexico, *Deep-Sea Research Part Ii-Topical Studies in Oceanography*, *57*(21-23), 1859-1869.

Gay, A., M. Lopez, H. Ondreas, J. L. Charlou, G. Sermondadaz, and P. Cochonat (2006), Seafloor facies related to upward methane flux within a Giant Pockmark of the Lower Congo Basin, *Mar Geol*, *226*(1-2), 81-95.

Ginsburg, G. D. (1998), Gas hydrate accumulation in deep-water marine sediments, *Geological Society*, *137*, 51-62.

Gordon, C. S., J. Hurely, and B. Shawan (1998), Coastal Zone Monitoring with RADARSAT-1, *GIS Development Proceedings*, *23*, 3.

Granin, N., M. Makarov, K. Kucher, and R. Gnatovsky (2010), Gas seeps in Lake Baikal—detection, distribution, and implications for water column mixing, *Geo-Marine Letters*, *30*(3), 399-409.

Greinert, J., Y. Artemov, V. Egorov, M. De Batist, and D. McGinnis (2006), 1300-m-high rising bubbles from mud volcanoes at 2080 m in the Black Sea: Hydroacoustic characteristics and temporal variability, *Earth and Planetary Science Letters*, *244*(1-2), 1-15.

Henschel, M., R. Olsen, and P. Hoyt (1997), The ocean monitoring workstation: Experience gained with Radarsat., *Geomatics in the Era of Radarsat*.

Hensen, C., M. Zabel, K. Pfeifer, T. Schwenk, S. Kasten, N. Riedinger, H. D. Schulz, and A. Boetius (2003), Control of sulfate pore–water profiles by sedimentary events and the significance of anaerobic oxidation of methane for the burial of sulfur in marine sediments., *Geochimica et Cosmochimica Acta*, *67*, 2631-2647.

Hine, A. C., G. R. Brooks, R. A. Davis, D. S. Duncan, S. D. Locker, D. C. Twichell, and G. Gelfenbaum (2003), The west-central Florida inner shelf and coastal system: a geologic conceptual overview and introduction to the special issue, *Mar Geol*, *200*(1-4), 1-17.

Hood, K. C., L. M. Wenger, O. P. Gross, and S. C. Harrison (2002), Hydrocarbon systems analysis of the northern Gulf of Mexico: Delineation of hydrocarbon migration pathways using seeps and seismic imaging, in Surface exploration case histories: Applications of geochemistry, magnetics, and remote sensing,, *AAPG Studies in Geology*, *No. 48*(Geophysical References Series No. 11,), 25–40.

Hornafius, J. S., D. Quigley, and B. P. Luyendyk (1999), The world's most spectacular marine hydrocarbon seeps (Coal Oil Point, Santa Barbara Channel, California): Quantification of emissions, *Journal of Geophysical Research-Oceans*, *104*(C9), 20703-20711.

Hovland, M., A. G. Judd, and R. A. Burke (1993), THE GLOBAL FLUX OF METHANE FROM SHALLOW SUBMARINE SEDIMENTS, *Chemosphere*, *26*(1-4), 559-578.

Hu, L., S. A. Yvon-Lewis, Y. Liu, J. E. Salisbury, and J. E. O'Hern (2010), Coastal emissions of methyl bromide and methyl chloride along the eastern Gulf of Mexico and the east coast of the United States, *Global Biogeochemical Cycles*, *24*.

Huang, C.-Y., C.-W. Chien, M. Zhao, H.-C. Li, and Y. Iizuka (2006), Geological study of active cold seeps in the syn-collision accretionary prism Kaoping slope off SW Taiwan, *Terrestrial Atmospheric and Oceanic Sciences*, *17*(4), 679-702.

IPCC (2001), Appendix VIII in Climate Change 2001: The Scientific Basis, Third Assessment Report of the Intergovernmental Panel on Climate Change (IPCC) *Rep.*, 881 pp, Cambridge, U.K.

Ivanov Andrei, M.-X. H., Ming-Qiang FANG (2002), Oil spill detection with the RADARSAT SAR in the waters of the Yellow and East China Sea: A case study, *Proc. 23rd Asian Conference on Remote Sensin*.

Iversen, N., and B. B. Jorgensen (1985), Anaerobic Methane Oxidation Rates at the Sulfate-Methane Transition in Marine Sediments from Kattegat and Skagerrak (Denmark), *Limnology and Oceanography*, *30*(5), 944-955.

Iversen, N., and B. B. Jørgensen (1993), Diffusion coefficients of sulfate and methane in marine sediments: Influence of porosity, *Geochimica et Cosmochimica Acta*, *57*(3), 571-578.

Jain, A. K., and R. C. Dubes (1988), *Algorithms for Clustering Data*, 320 pp., Prentice Hall, Inc., Engelwood Cliffs, NJ.

Jingxuan, L., L. Hock, B. Mingquan, C. L. Soo, and K. K. Leong (2002), Mapping Ocean Oil Pollution with ERS SAR Imagery *Centre for Remote Imaging, Sensing and Processing, National University of Singapore*.

Johnson, J. E. (1999), Evaluation of a seawater equilibrator for shipboard analysis of dissolved oceanic trace gases, *Analytica Chimica Acta*, *395*(1-2), 119-132.

Joye, S. B., A. Boetius, B. N. Orcutt, J. P. Montoya, H. N. Schulz, M. J. Erickson, and S. K. Lugo (2004), The anaerobic oxidation of methane and sulfate reduction in sediments from Gulf of Mexico cold seeps, *Chemical Geology*, *205*(3-4), 219-238.

Judd, A. G. (2003), The global importance and context of methane escape from the seabed, *Geo-Marine Letters*, *23*(3), 147-154.

Judd, A. G., M. Hovland, L. I. Dimitrov, S. G. Gil, and V. Jukes (2002), The geological methane budget at Continental Margins and its influence on climate change, *Geofluids*, *2*(2), 109-126.

Kasten, S., R. Schneider, V. Spiess, and C. P. o. M56 (2003), From black hole to hydrate hole: gas hydrates, authigenic carbonates and vent biota as indicators of fluid migrations at pockmark sites of the northern Congo Fan, *Geophysical Research Abstracts*, *5*, 08832.

Kennett, J. P., and K. G. Cannariato, Hendy, Ingrid L., Behl, Richard J. (2000), Carbon isotopic evidence for methane hydrate instability during quaternary interstadials, in *Science*, edited, pp. 128-133.

Kessler, J. D., W. S. Reeburgh, J. Southon, R. Seifert, W. Michaelis, and S. C. Tyler (2006), Basin-wide estimates of the input of methane from seeps and clathrates to the Black Sea, *Earth and Planetary Science Letters*, *243*(3-4), 366-375.

Klapp, S. A., M. M. Murshed, T. Pape, H. Klein, G. Bohrmann, P. G. Brewer, and W. F. Kuhs (2010), Mixed gas hydrate structures at the Chapopote Knoll, southern Gulf of Mexico, *Earth and Planetary Science Letters*, *299*(1-2), 207-217.

Klapp, S. A., G. Bohrmann, W. F. Kuhs, M. M. Murshed, T. Pape, H. Klein, K. S. Techmer, K. U. Heeschen, and F. Abegg (2010), Microstructures of structure I and II gas hydrates from the Gulf of Mexico, *Mar Petrol Geol*, *27*(1), 116-125.

Klaucke, I., H. Sahling, W. Weinrebe, V. Blinova, D. Buerk, N. Lursmanashvili, and G. Bohrmann (2006), Acoustic investigation of cold seeps offshore Georgia, eastern Black Sea, *Mar Geol*, *231*(1-4), 51-67.

Kourtidis, K., I. Kioutsioukis, D. F. McGinnis, and S. Rapsomanikis (2006), Effects of methane outgassing on the Black Sea atmosphere, *Atmospheric Chemistry and Physics*, *6*, 5173-5182.

Kvenvolden, K. A. (2000), Gas hydrate and humans, in *Gas Hydrates: Challenges For the Future*, edited, pp. 17-22.

Kvenvolden, K. A., and B. W. Rogers (2005), Gaia's breath - global methane exhalations, *Marine and Petroleum Geology*, *22*(4), 579-590.

Lapham, L. L., J. P. Chanton, C. S. Martens, K. Sleeper, and J. R. Woolsey (2008), Microbial activity in surficial sediments overlying acoustic wipeout zones at a Gulf of Mexico cold seep, *Geochem. Geophys. Geosyst.*, *9*(6), 1-17.

Large, W. G., and S. Pond (1982), SENSIBLE AND LATENT-HEAT FLUX MEASUREMENTS OVER THE OCEAN, *Journal of Physical Oceanography*, *12*(5), 464-482.

Leifer, I. (2010), Characteristics and scaling of bubble plumes from marine hydrocarbon seepage in the Coal Oil Point seep field, *Journal Geophysical Research*, *115*, C11014.

Leifer, I., and A. G. Judd (2002), Oceanic methane layers: The hydrocarbon seep bubble deposition hypothesis, *Terra Nova*, *14*(6), 417-424.

Leifer, I., and I. MacDonald (2003), Dynamics of the gas flux from shallow gas hydrate deposits: interaction between oily hydrate bubbles and the oceanic environment, *Earth and Planetary Science Letters*, *210*(3-4), 411-424.

Leifer, I., and J. Boles (2005), Measurement of marine hydrocarbon seep flow through fractured rock and unconsolidated sediment, *Marine and Petroleum Geology*, *22*(4), 551-568.

Leifer, I., B. P. Luyendyk, J. Boles, and J. F. Clark (2006), Natural marine seepage blowout: Contribution to atmospheric methane, *Global Biogeochemical Cycles*, *20*(GB3008), doi:10.1029/2005GB002668.

Leifer, I., H. Jeuthe, S. H. Gjøsund, and V. Johansen (2009), Engineered and natural marine seep, bubble-driven buoyancy flows, *J. Phys. Oceanography*, *39*(12), 3071-3090.

Lelieveld, J., P. J. Crutzen, and F. J. Dentener (1998), Changing concentration, lifetime and climate forcing of atmospheric methane, *Tellus Series B-Chemical and Physical Meteorology*, *50*(2), 128-150.

Lemckert, C. J., and J. Imberger (1993), Energetic bubble plumes in arbitrary stratification, *Journal Hydraulic Engineering*, *19*, 680-703.

Lessard-Pilon, S., M. D. Porter, E. E. Cordes, I. MacDonald, and C. R. Fisher (2010), Community composition and temporal change at deep Gulf of Mexico cold seeps, *Deep-Sea Research Part Ii-Topical Studies in Oceanography*, *57*(21-23), 1891-1903.

Liss, P. S., and L. Merlivat (1986), Air-sea gas exchange rates: Introduction and synthesis, in *The Role of Air-Sea Exchange in Geochemical Cycling* edited by P. Buat-Menard, pp. 113-127, Springer, N.Y.

Luff, R., and K. Wallmann (2003), Fluid flow, methane fluxes, carbonate precipitation and biogeochemical turnover in gas hydrate-bearing sediments at Hydrate Ridge, Cascadia Margin: Numerical modeling and mass balances, *Geochimica et Cosmochimica Acta*, *67*(18), 3403-3421.

Luff, R., K. Wallmann, and G. Aloisi (2004), Numerical modeling of carbonate crust formation at cold vent sites: significance for fluid and methane budgets and chemosynthetic biological communities, *Earth and Planetary Science Letters*, *221*(1-4), 337.

Luff, R., J. Greinert, K. Wallmann, I. Klaucke, and E. Suess (2005), Simulation of long-term feedbacks from authigenic carbonate crust formation at cold vent sites, *Chemical Geology*, *216*(1-2), 157-174.

Lutken, C. B., C. A. Brunner, L. Lapham, J. Chanton, R. Rogers, R. Sassen, J. Dearman, and L. Lynch (2006), Analyses of core samples from Mississippi Canyon 118, in *Offshore Technology Conference*, edited, Paper OTC 18208, Houston, TX.

MacDonald, I., J. Reilly, S. Best, R. Venkataramaiah, N. Guinasso, and J. Amos (1996), Remote sensing inventory of active oil seeps and chemosynthetic communities in the Northern Gulf of Mexico., *AAPG Memoir*(66), 27-37.

MacDonald, I. R. (1997), Bottom line for hydrocarbons, *Nature*, *385*(30), 389-390.

MacDonald, I. R. (2011), edited.

MacDonald, I. R., W. W. Sager, and M. B. Peccini (2003), Gas hydrate and chemosynthetic biota in mounded bathymetry at mid-slope hydrocarbon seeps: Northern Gulf of Mexico, *Marine Geology*, *198*(1-2), 133-158.

MacDonald, I. R., L. C. Bender, M. Vardaro, B. Bernard, and J. R. Brooks (2005), Thermal and Visual Time-Series at a Seafloor Gas Hydrate Deposit on the Gulf of Mexico Slope., *Earth and Planetary Science Letters*, *233*, 45-59.

MacDonald, I. R., N. L. Guinasso, R. Sassen, J. M. Brooks, L. Lee, and K. T. Scott (1994), Gas Hydrate That Breaches the Sea-Floor on the Continental-Slope of the Gulf-of-Mexico, *Geology*, *22*(8), 699-702.

MacDonald, I. R., I. Leifer, R. Sassen, P. Stine, R. Mitchell, and N. Guinasso (2002), Transfer of hydrocarbons from natural seeps to the water column and atmosphere, *Geofluids*, *2*(2), 95-107.

MacDonald, I. R., N. L. Guinasso, Jr., S. G. Ackleson, J. F. Amos, R. Duckworth, R. Sassen, and J. M. Brooks (1993), Natural oil slicks in the Gulf of Mexico visible from space, *Journal of Geophysical Research*, *98 C9*, 16351-16364.

MacDonald, I. R., J. F. Reilly, Jr., S. E. Best, R. Venkataramaiah, R. Sassen, J. Amos, and N. L. Guinasso, Jr. (1996), A remote-sensing inventory of active oil seeps and chemosynthetic communities in the northern Gulf of Mexico, in *Hydrocarbon migration and its near-surface expression*, edited by D. Schumacher and M. A. Abrams, pp. 27-37, American Association of Petroleum Geologists.

MacDonald, I. R., et al. (2004), Asphalt volcanism and chemosynthetic life, Campeche Knolls, Gulf of Mexico, *Science*, *304*, 999-1002.

Mau, S., D. L. Valentine, J. F. Clark, J. Reed, R. Camilli, and L. Washburn (2007), Dissolved methane distributions and air-sea flux in the plume of a massive seep field, Coal Oil Point, California, *Geophysical Research Letters*, *34*(22).

McDougall, T. (1978), Bubble plumes in stratified environments, *Journal of Fluid Mechanics 85*(655–672).

McGee, T., et al. (2008), Structure of a carbonate/hydrate mound in the northern Gulf of Mexico, paper presented at 6th International Conference on Gas Hydrates, Vancouver, BC, Canada.

McGinnis, D. F., J. Greinert, Y. Artemov, S. E. Beaubien, and A. Wuest (2006), Fate of rising methane bubbles in stratified waters: How much methane reaches the atmosphere?, *Journal of Geophysical Research-Oceans*, *111*(C9).

Milkov, A. V. (2000), Worldwide distribution of submarine mud volcanoes and associated gas hydrates, *Mar Geol*, *167*(1-2), 29-42.

Milkov, A. V. (2004), Global estimates of hydrate-bound gas in marine sediments: how much is really out there?, *Earth-Science Reviews*, *66*(3-4), 183-197.

Milkov, A. V., and R. Sassen (2000), Thickness of the gas hydrate stability zone, Gulf of Mexico continental slope, *Mar Petrol Geol*, *17*(9), 981-991.

Milkov, A. V., and R. Sassen (2001), Estimate of gas hydrate resource, northwestern Gulf of Mexico continental slope, *Marine Geology*, *179*, 71-83.

Milkov, A. V., R. Sassen, I. Norikova, and E. Mikhailov (2000), Gas hydrates at minimum stability water depths in the Gulf of Mexico: significance to geohazard assessment, *Gulf Coast Association of Geological Societies Transactions*, *L*, 217-224.

Mink, R. M., B. L. Bearden, and E. A. Mancini (1989), Regional Jurassic geologic framework of Alabama coastal waters area and adjacent Federal waters area, *Mar Geol*, *90*(1–2), 39-50.

Naehr, T. H., N. M. Rodriguez, G. Bohrmann, C. K. Paull, and R. Botz (2000), Methane-derived authigenic carbonates associated with gas hydrate decomposition and fluid venting above the Blake Ridge Diapir, in *Proc. ODP, Sci. Results*, edited by C. K. Paull, R. Matsumoto, P. J. Wallace and W. P. Dillon, pp. 285-300, Ocean Drilling Program, College Station, TX.

Naehr, T. H., D. Birgel, G. Bohrmann, I. R. MacDonald, and S. Kasten (2009), Biogeochemical controls on authigenic carbonate formation at the Chapopote "asphalt volcano", Bay of Campeche, *Chemical Geology*, *266*(3-4), 399-411.

Naehr, T. H., P. Eichhubl, V. J. Orphan, M. Hovland, C. K. Paull, W. Ussler Iii, T. D. Lorenson, and H. G. Greene (2007a), Authigenic carbonate formation at hydrocarbon seeps in continental margin sediments: A comparative study, *Deep Sea Research Part II: Topical Studies in Oceanography*, *54*(11-13), 1268-1291.

Naehr, T. H., P. Eichhubl, V. J. Orphan, M. Hovland, C. K. Paull, W. Ussler, III, T. D. Lorenson, and H. G. Greene (2007b), Authigenic carbonate formation at hydrocarbon seeps in continental margin sediments: A comparative study, *Deep-Sea Research Part Ii-Topical Studies in Oceanography*, *54*(11-13), 1268-1291.

National Commission (2011), The Amount and Fate of the Oil, *National Commission on the BP Deepwater Horizon Oil Spill and Offshore Drilling*, *11 January 2011*(http://www.oilspillcommission.gov/document/amount-and-fate-oil).

Nightingale, P. D., P. S. Liss, and P. Schlosser (2000), Measurements of air-sea gas transfer during an open ocean algal bloom, *Geophysical Research Letters*, *27*(14), 2117-2120.

Nikolovska, A., H. Sahling, and G. Bohrmann (2008), Hydroacoustic methodology for detection, localization, and quantification of gas bubbles rising from the seafloor at gas seeps from the eastern Black Sea, *Geochem Geophy Geosy*, *9*, -.

Orphan, V. J., C. H. House, K.-U. Hinrichs, K. D. McKeegan, and E. F. DeLong (2001), Methane-Consuming Archea Revealed by Directly Coupled Isotopic and Phylogenetic Analysis, *Science*, *293*(5529), 484-487.

Orphan, V. J., W. U. III, T. H. Naehr, C. H. House, K.-U. Hinrichs, and C. K. Paull (2004), Geological, geochemical, and microbiological heterogeneity of the seafloor around methane vents in the Eel River Basin, offshore California, *Chemical Geology*, *205*, 265-289.

Plassdulmer, C., R. Koppmann, M. Ratte, and J. Rudolph (1995), LIGHT NONMETHANE HYDROCARBONS IN SEAWATER, *Global Biogeochemical Cycles*, *9*(1), 79-100.

Plassdulmer, C., A. Khedim, R. Koppmann, F. J. Johnen, J. Rudolph, and H. Kuosa (1993), EMISSIONS OF LIGHT NONMETHANE HYDROCARBONS FROM THE ATLANTIC INTO THE ATMOSPHERE, *Global Biogeochemical Cycles*, *7*(1), 211-228.

Quigley, D. C., J. S. Hornafius, B. P. Luyendyk, R. D. Francis, J. Clark, and L. Washburn (1999), Decrease in natural marine hydrocarbon seepage near Coal Oil Point, California, associated with offshore oil production, *Geology*, *27*(11), 1047-1050.

Quintero-Marmol, A. M., E. C. Pedroso, C. H. Beisl, R. G. Caceres, F. P. de Miranda, K. Bannerman, P. Welgan, and O. L. Castillo (2003), Operational applications of RADARSAT-1 for the monitoring of natural oil seeps in the South Gulf of Mexico, *Geoscience and Remote Sensing Symposium, 2003. IGARSS '03. Proceedings. 2003 IEEE International*, *4*, 2744- 2746

Ramaswamy, V., O. Boucher, J. Haigh, D. Hauglustaine, J. Haywood, G. Myhre, T. Nakajima, G. Shi, and S. Solomon (2001), Radiative forcing of climate change in Climate Change 2001: The Scientific Basis, Third Assessment Report of the Intergovernmental Panel on Climate Change (IPCC)*Rep.*, 349-416 pp, Cambridge, U.K.

Raney, R. K., A. P. Luscombe, E. J. Langham, and S. Ahmed (1991), Radarsat *IEEE, Proceedings 79,*, 839-849.

Reeburgh, W. S., S. C. Tyler, and J. Carroll (2006), Stable carbon and hydrogen isotope measurements on Black Sea water-column methane, *Deep-Sea Research Part Ii-Topical Studies in Oceanography*, *53*(17-19), 1893-1900.

Reeburgh, W. S., B. B. Ward, S. C. Whalen, K. A. Sandbeck, K. A. Kilpatrick, and L. J. Kerkhof (1991), Black-Sea Methane Geochemistry, *Deep-Sea Research Part a-Oceanographic Research Papers*, *38*, S1189-S1210.

Rehder, G., R. S. Keir, E. Suess, and M. Rhein (1999), Methane in the northern Atlantic controlled by microbial oxidation and atmospheric history, *Geophysical Research Letters*, *26*(5), 587-590.

Rehder, G., P. W. Brewer, E. T. Peltzer, and G. Friederich (2002), Enhanced lifetime of methane bubble streams within the deep ocean, *Geophysical Research Letters*, *29*(15).

Rehder, G., I. Leifer, P. G. Brewer, G. Friederich, and E. T. Peltzer (2009), Controls on methane bubble dissolution inside and outside the hydrate stability field from open ocean field experiments and numerical modeling, *Marine Chemistry*, *114*(1/2), 19-30.

Rehder, G., S. H. Kirby, W. B. Durham, L. A. Stern, E. T. Peltzer, J. Pinkston, and P. G. Brewer (2004), Dissolution rates of pure methane hydrate and carbon-dioxide hydrate in undersaturated seawater at 1000-m depth, *Geochimica et Cosmochimica Acta*, *68*(2), 285-292.

Rhee, T. S., A. J. Kettle, and M. O. Andreae (2009), Methane and nitrous oxide emissions from the ocean: A reassessment using basin-wide observations in the Atlantic, *Journal of Geophysical Research-Atmospheres*, *114*.

Ripley, B. D. (1981), *Spatial Statistics*, John Wiley & Sons, Inc., Hoboken, New Jersey.

Roberts, H. H. (2001), Fluid and gas expulsion on the northern Gulf of Mexico continental slope: Mud-prone to mineral-prone responses, in *Natural Gas Hydrates: Occurrence, distribution and dynamics*, edited by C. K. Paull and W. P. Dillon, pp. 131-143, American Geophysical Union.

Roberts, H. H., and P. Aharon (1994), Hydrocarbon-derived carbonate buildups of the northern Gulf of Mexico continental slope: A review of submersible investigations, *Geo-Marine Letters*, *14*, 135-148.

Roberts, H. H., and R. S. Carney (1997), Evidence of episodic fluid, gas, and sediment venting on the northern Gulf of Mexico continental slope, *Economic Geology and the Bulletin of the Society of Economic Geologists*, *92*(7-8), 863-879.

Roberts, H. H., D. Feng, and S. B. Joye (2010), Cold-seep carbonates of the middle and lower continental slope, northern Gulf of Mexico, *Deep-Sea Research Part Ii-Topical Studies in Oceanography*, *57*(21-23), 2040-2054.

Sager, W. W., C. S. Lee, I. R. Macdonald, and W. W. Schroeder (1999), High-frequency near-bottom acoustic reflection signatures of hydrocarbon seeps on the northern Gulf of Mexico continental slope, *Geo Marine Letters*, *18*(4), 267-276.

Sahling, H., G. Bohrmann, V. Spiess, J. Bialas, M. Breitzke, M. Ivanov, S. Kasten, S. Krastel, and R. Schneider (2008), Pockmarks in the Northern Congo Fan area, SW Africa: Complex seafloor features shaped by fluid flow, *Mar Geol*, *249*(3-4), 206-225.

Sassen, R., and H. H. Roberts Site selection and characterization of vent gas, gas hydrate and associated sediments, in Final Technical Progress Report of the Gulf of Mexico Seafloor Stability and Gas Hydrate Monitoring Station Project. *Rep.*, 28-227 pp.

Sassen, R., H. H. Roberts, P. Aharon, J. Larkin, E. W. Chinn, and R. Carney (1993), Chemosynthetic bacterial mats at cold hydrocarbon seeps, Gulf of Mexico continental slope, *Organic Geochemistry*, *Vol. 20*, 77 - 89.

Sassen, R., A. V. Milkov, E. Ozgul, H. H. Roberts, J. L. Hunt, M. A. Beeunas, J. P. Chanton, D. A. DeFreitas, and S. T. Sweet (2003), Gas venting and subsurface charge in the Green Canyon area, Gulf of Mexico continental slope: evidence of a deep bacterial methane source?, *Organic Geochemistry*, *34*(10), 1455-1464.

Sauter, E. J., S. I. Muyakshin, J.-L. Charlou, M. Schlüter, A. Boetius, K. Jerosch, E. Damm, J.-P. Foucher, and M. Klages (2006), Methane discharge from a deep-sea submarine mud volcano into the upper water column by gas hydrate-coated methane bubbles, *Earth and Planetary Science Letters*, *243*(3-4), 354-365.

Schmale, O., J. Greinert, and G. Rehder (2005), Methane emission from high-intensity marine gas seeps in the Black Sea into the atmosphere, *Geophysical Research Letters*, *32*(7).

Schmale, O., S. E. Beaubien, G. Rehder, J. Greinert, and S. Lombardi (2010), Gas seepage in the Dnepr paleo-delta area (NW-Black Sea) and its regional impact on the water column methane cycle, *Journal of Marine Systems*, *80*(1-2), 90-100.

Sibuet, M., and A. Vangriesheim (2009), Deep-sea environment and biodiversity of the West African Equatorial margin, *Deep-Sea Research Part Ii-Topical Studies in Oceanography*, *56*(23), 2156-2168.

Sloan Jr., E. D. (1998), *Clathrate Hydrates of Natural Gases*, 2nd ed., 705 pp., Marcel Dekker, Inc., New York, NY.

Sloan., E. D. (1998), *Clathrate Hydrates of Natural Gases*, 2nd ed., 705 pp., Marcel Dekker, Inc., New York, NY.

Solomon, E., M. Kastner, I. R. MacDonald, and I. Leifer (2009), Considerable methane fluxes to the atmosphere from hydrocarbon seeps in the Gulf of Mexico, *Nature Geoscience*, *2*, 561-565.

Solomon, E. A., M. Kastner, H. Jannasch, G. Robertson, and Y. Weinstein (2008), Dynamic fluid flow and chemical fluxes associated with a seafloor gas hydrate deposit on the northern Gulf of Mexico slope, *Earth and Planetary Science Letters*, *270*(1-2), 95-105.

Spiess, V. (2008), SHORT CRUISE REPORT R/V METEOR Cruise M76/3a, *Personal Communication*, *MARUM, University of Bremen*, 1-4.

Spiess, V., and Y. Artemov (2010), Fine Scale sediment and water column structure at deep sea seepage sites derived from spatial seismoacoustic surveys, paper presented at 10th International Conference on Gas in Marine Sediments, Lake Baikal, Russia, 6-12 Sept 2010.

Stein, O., and J. Rudolph (2007), Modeling and interpretation of stable carbon isotope ratios of ethane in global chemical transport models, *Journal of Geophysical Research-Atmospheres*, *112*(D14).

Sweeney, C., E. Gloor, A. R. Jacobson, R. M. Key, G. McKinley, J. L. Sarmiento, and R. Wanninkhof (2007), Constraining global air-sea gas exchange for CO2 with recent bomb (14)C measurements, *Global Biogeochemical Cycles*, *21*(2).

Takahashi, T., et al. (2009), Climatological mean and decadal change in surface ocean pCO(2), and net sea-air CO(2) flux over the global oceans, *Deep-Sea Research Part Ii-Topical Studies in Oceanography*, *56*(8-10), 554-577.

Tans, P. P., I. Y. Fung, and T. Takahashi (1990), OBSERVATIONAL CONSTRAINTS ON THE GLOBAL ATMOSPHERIC CO2 BUDGET, *Science*, *247*(4949), 1431-1438.

Thomanek, K., O. Zielinski, H. Sahling, and G. Bohrmann (2010), Automated gas bubble imaging at sea floor - a new method of in situ gas flux quantification, *Ocean Science*, *6*(2), 549-562.

Tilbrook, B. D., and D. M. Karl (1995), METHANE SOURCES, DISTRIBUTIONS AND SINKS FROM CALIFORNIA COASTAL WATERS TO THE OLIGOTROPHIC NORTH PACIFIC GYRE, *Marine Chemistry*, *49*(1), 51-64.

Ussler III, W., and C. K. Paull (2008), Rates of anaerobic oxidation of methane and authigenic carbonate mineralization in methane-rich deep-sea sediments inferred from models and geochemical profiles, *Earth and Planetary Science Letters*, *266*(3-4), 271-287.

Valentine, D. L., D. C. Blanton, W. S. Reeburgh, and M. Kastner (2001), Water column methane oxidation adjacent to an area of active hydrate dissociation, Eel river Basin, *Geochim. Cosmochim. Acta*, *65*(16), 2633-2640.

Vardaro, M., I. R. MacDonald, L. C. Bender, and J. Guinasso, N.L (2005), Dynamic biological and physical processes observed at a gas hydrate outcropping on the continental slope of the Gulf of Mexico, *Geo-Marine Letters*(26(1)), 6-15.

Wanninkhof, R. (1992), Relationship Between Wind-Speed and Gas-Exchange Over the Ocean, *Journal of Geophysical Research-Oceans*, *97*(C5), 7373-7382.

Watanabe, S., N. Tsurushima, M. Kusakabe, and S. Tsunogai (1995), Methane in the Izena Cauldron, Okinawa Trough, *Journal of Oceanography*, *51*, 239.

Watkins, J. S., J. W. Ladd, R. T. Buffler, F. J. Shaub, Houston, M. H., and J. L. Worzel (1978), Occurrence and evolution of salt in deep Gulf ofMexico, in *Framework, Facies and Oil-Trapping Characteristics of the Upper Continental Margin*, edited by A. H. Bouma, G. T. Moore and J. M. Coleman, AAPG Studies in Geol. , Tulsa, OK.

Wilke, C. R., and P. Chang (1955), CORRELATION OF DIFFUSION COEFFICIENTS IN DILUTE SOLUTIONS, *Aiche Journal*, *1*(2), 264-270.

Woolsey, J. R., P. Higley, L. L. Lapham, J. P. Chanton, C. Lutken, K. Sleeper, R. Culp, S. Sharpe, and D. Ross (2005), Operations report of cruise GOM2-05-MC118 deployment of the initial components of the sea floor monitoring station–the pore-fluid array and the geophysical line array–via the sea floor probe system and collection of core samplers, Mississippi Canyon 118*Rep.*, 11 pp.

Yoshida, O., H. Y. Inoue, S. Watanabe, S. Noriki, and M. Wakatsuchi (2004), Methane in the western part of the Sea of Okhotsk in 1998-2000, *Journal of Geophysical Research-Oceans*, *109*(C9).

Yvon-Lewis, S. A., L. Hu, and J. Kessler (2011), Methane flux to the atmosphere from the Deepwater Horizon oil disaster, *Geophysical Research Letters*, *38*.

Zahn, C. T. (1971), GRAPH-THEORETICAL METHODS FOR DETECTING AND DESCRIBING GESTALT CLUSTERS, *Ieee Transactions on Computers*, *C 20*(1), 68-&.

LIST OF ACRONYMS AND ABBREVIATIONS

AOM - anaerobic oxidation of methane

ASF - Alaska Satellite Facility

Cmbsf - cm below seafloor

CH_4 - Methane

DIC – Dissolved inorganic carbon

ESA - European Space Administration

FSU - Florida State University

GC – Green Canyon

GOM - Gulf of Mexico

HCT - Hierarchical Cluster Tree

HYFLUX - HYdrate FLUX

IC - Inconsistency Coefficient

ICP-OES - inductively coupled plasma-optical emission spectrometry

MBSL - meters below sea level

MC – Mississippi Canyon

NASA - National Aeronautic Space Administration

NODC - National Ocean Data Center

OSO - Oil Slick Origin

PC – piston core

PLUMES - Persistent Localized Underwater Methane Emission Study

ROV - remote operated vehicle

SAR - synthetic aperture radar

SBE - Sea-Bird Electronics

SIO - Scripps Institute for Oceanography

SMI - sulfate-methane interface

TAMU - Texas A&M University

TAMUCC - Texas A&M University - Corpus Christi

TS – total sulfur

UCSB - University of California Santa Barbara

YD – year days

Appendices

Appendix I: HYFLUX cruise report

Appendix II: Inventory of SAR images analyzed for HYFLUX results

Appendix III: Preliminary report on persistent oil seep and gas hydrates in the Black Sea

Appendix IV: Analytical results of water column samples

Appendix V: Analytical results of air-sea continuous sampling

APPENDIX I:
HYFLUX CRUISE REPORT

Table of Contents

Summary 2
Participating Organizations 3
Major Equipment 4
Cruise participants 6
Operations summary and preliminary results 7
Daily narrative of cruise operations 17
Written dive notes. 28

List of Figures

Figure 1. Map shows locations of principal sampling stations 3
Figure 2. Principal equipment used during HYFLUX cruise. 5
Figure 3 Operations at MC118. 8
Figure 4 Locations of ROV dives (logged events) and CTD-rosette profiles 9
Figure 5. Methane concentrations at MC118: 10
Figure 6 Huey camera system. 11
Figure 7. Deployment of Dewey camera system 12
Figure 8. GC600 site. 14
Figure 9 Hydrate features at the GC600 study site 15
Figure 10. Summary of operations and collections at GC185 site. 16

List of Tables

Table 1. Ports and sampling sites in cruise sequential order. 2
Table 2. Cruise participants for Legs 1 & 2 with roles and affiliations. 6
Table 3. Gravity cores(GC) and piston cores (PC) collected 27

Summary

The objective of this research cruise was to collect data concerning the concentrations of methane derived from natural seeps and deposits of gas hydrate in the Gulf of Mexico. Collections were planned at the air-sea interface, the water column, and the seafloor. Team members developed innovated techniques and equipment for accomplishing these collections. The HYFLUX Hydrate observatory cruise was completed with the scientific team having occupied all of the planned sampling sites and accomplishing the great majority of planned collections. Collection of sediment cores during the first phase of the expedition was curtained due to operational constraints including weather and equipment malfunction. This deficit was repaid during subsequent days of the expedition. By the conclusion of the expedition, the science team had fulfilled their objectives. Table 1 provides a list of the major study areas occupied by the cruise. Figure 1 provides a map of the vessel track and the principal sampling sites. This report describes the major equipment used, science personnel, and summarizes the operations and preliminary results from each of the study sites. A detailed narrative lists daily activities during the cruise. Finally, the hand-written notes of the ROV dives are copied for future reference.

Study Sites

Sites were identified based on satellite remote sensing and previous knowledge of seep locations.

Table 1. Ports and sampling sites in cruise sequential order. Distance shows approximate distance from previous site.

Site	Longitude	Latitude	Water depth (m)	Dates occupied
GULFPORT	-89.0927778	30.3672222	na	Departure 4 July
MC118	-88.43859900	28.86541200	900	4-9 July
GULFPORT	-89.0927778	30.3672222	na	Repairs 10 July
MC118	-88.43859900	28.86541200	900	11-13 July
GC600	-90.56233200	27.36990000	1200	14-15 July
GC185	-91.48406200	27.77517900	550	16-17 July
FREEPORT	-95.3594444	28.9538889		Demobilize 19 July

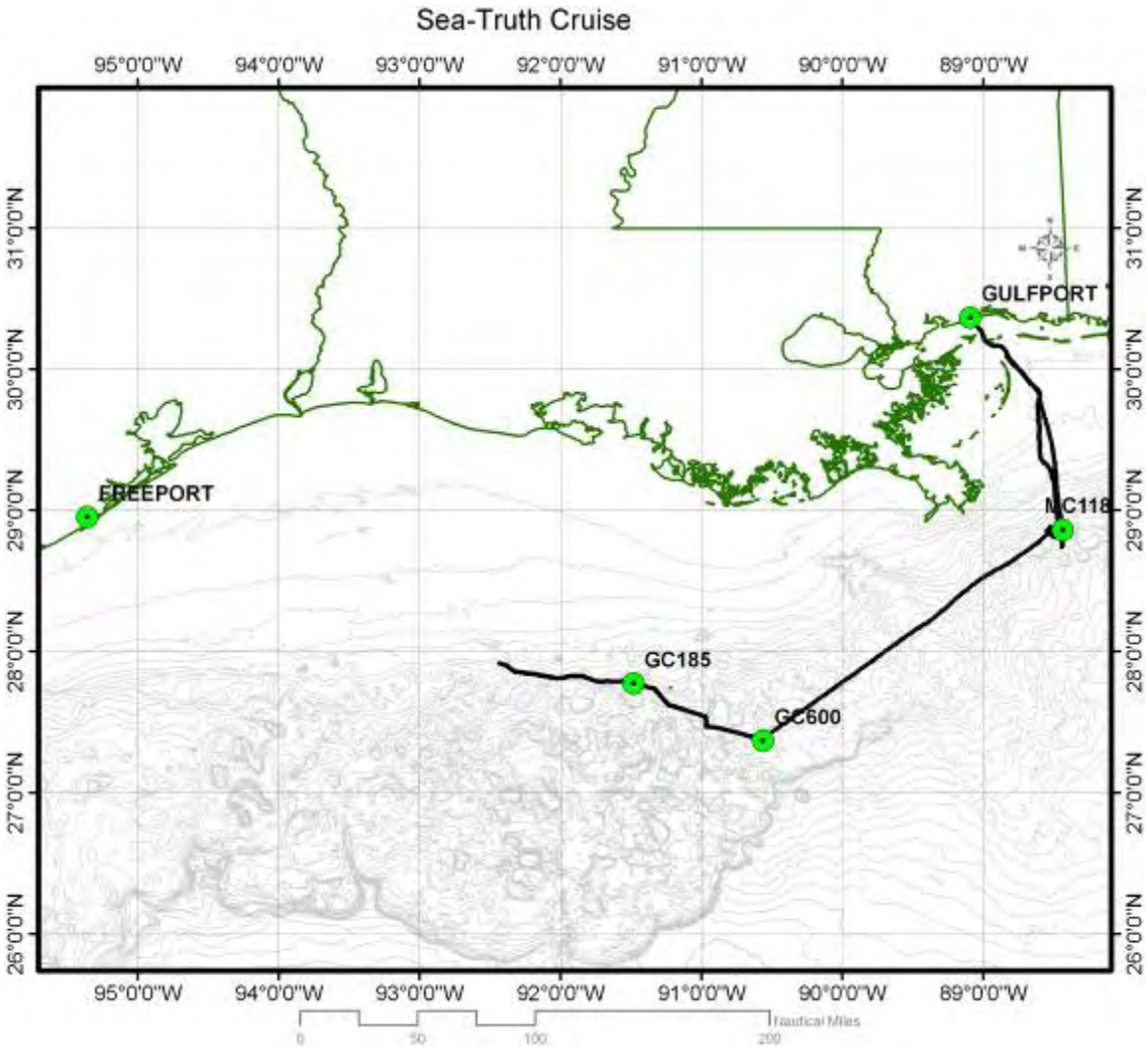

Figure 1. Map shows locations of principal sampling stations and the staging points for the cruise. Trackline indicates collections of air-sea methane concentration data, which was suspended when the expedition during the final transit to Freeport.

Participating Organizations

The HYFLUX Sea-Truth Cruise was a joint effort of the following institutions, agencies, and

- DOE National Energy Technology Lab*
- NOAA Center for Satellite Applications*
- NOAA National Institute for Undersea Science and Technology*
- Texas A&M University (TAMUCC)
- Texas A&M University – College Station (TAMU)
- Scripps Institute of Oceanography (SIO)

* Consulting on cruise planning and program execution. No cruise personnel participating.

- University of California Santa Barbara (UCSB)
- University of Southern Mississippi (USM)
- Florida State University (FSU)
- University of Mississippi, Methane Hydrate Consortium (and participating institutions)
- TDI BROOKS INTERNATIONAL (TDI-BROOKS)
- DEEPSEA SYSTEMS INTERNATIONAL (DSSI)

Major Equipment

Completing of the HYLUX cruise required charters and/or rental agreements to obtain use of several major equipment items. These

Vessel

- TDI-BI Ship, RV BROOKS McCALL was chartered for the expedition (Figure 2A).
- This ship is 155 ft, with 22 Berths available (for Sentry crew; science crew)
- Included with vessel were two winches and piston/gravity-coring equipment as well as a ultra-short baseline (USBL) submersible navigation system.

ROV

- The Max Rover work-class ROV Global Explorer (GE) was operated by a three-person team from Deepsea Systems International (Figure 2B).
- Imaging systems included video cameras recording in MiniDV and Panasonic DVCPro HD formats, Kongsberg Sector-Scanning Sonar, and digital still camera.
- Developed and fabricated specially for this expedition was a 14-bottle niskin array individually fired by commands from the ROV pilot and science staff.

Water Sampling Rosette

- This is 24-bottle rosette with a SBE911 conductivity-temperature-depth (CTD) sensor. Sampling depths were individually selected and bottles were closed with single commands (Figure 2C)

Elevator

- This device was used to deploy autonomous instruments and to recover devices previously left on the MC118 site (Figure 2D)

Surface water sampling

- The surface ocean was monitored continuously using a shipboard seawater pumping system, a Weiss-style Plexiglas equilibrator, and a fully automated GC/FID instrument, which will draw samples from a Weiss-style Plexiglas equilibrator (Fig. 2E).
- The instrument cycled continuously between ambient air, seawater-equilibrated air, and a gas standard, with a 5-7 minute cycle time from the start of one sample to the start of the next.

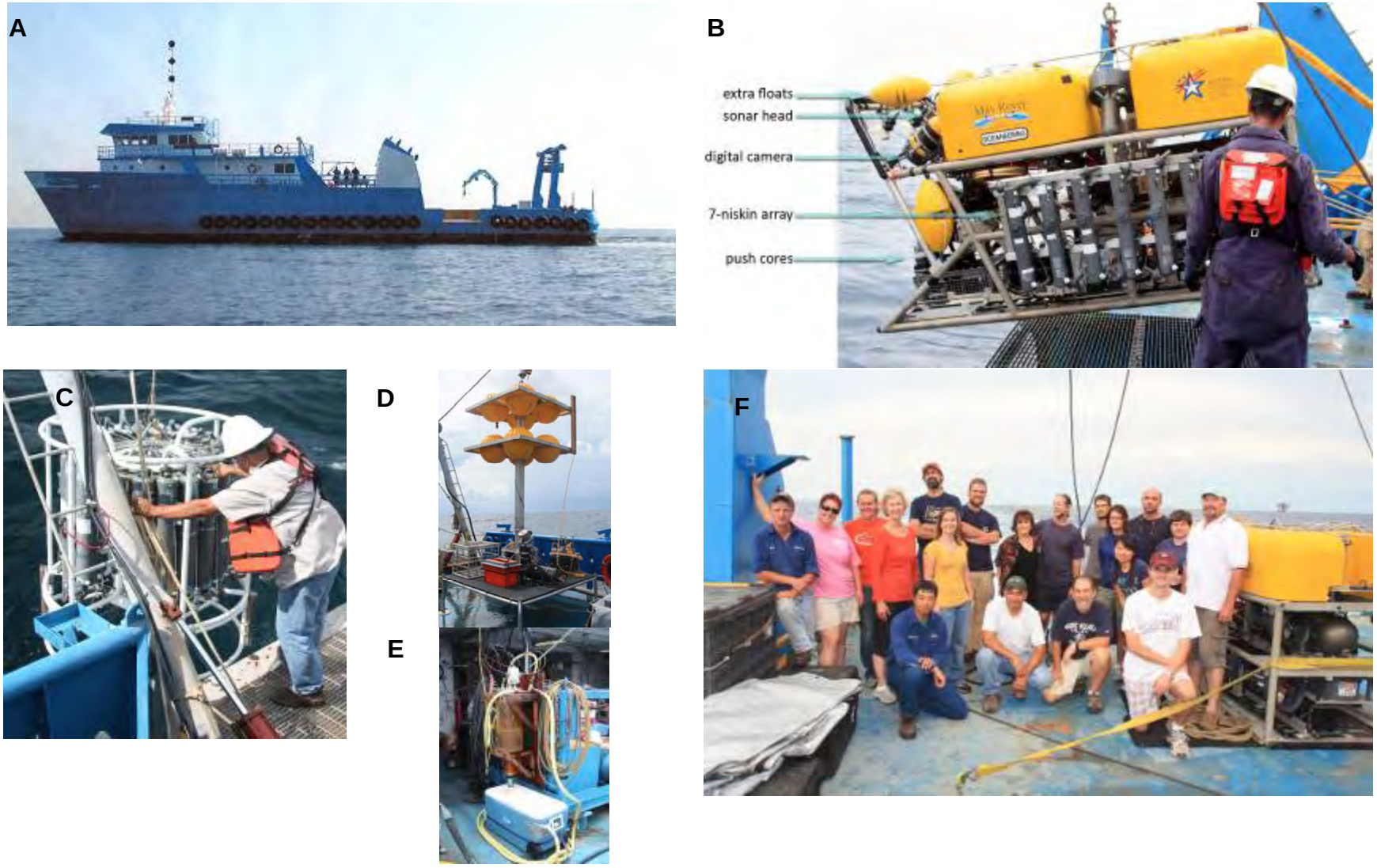

Figure 2. Principal equipment used during HYFLUX cruise. A. RV BROOKS McCALL, B. Global Explorer ROV with niskin sampler array. C. Rosette. D. Elevator with instruments and sampling equipment. E. Seawater equilibrator for surface sampling. F. Science party

Cruise participants

A total of 25 scientists and technicians staffed the cruise (Table 2).

Table 2. Cruise participants for Legs 1 & 2 with roles and affiliations.

	Name	Gender	Group	Role	Transfer
	Leg 1 MC118, Microbiology Participants				
1	**Laura Laphanm**	**F**	**FSU**	**Micro**	**off**
2	Gretchen Robertson	F	Scripps	Water chem	no
3	Miriam Kastner	F	Scripps	Water chem	no
4	Nichole Beasley	F	Scripps	Water chem	no
5	Emily Bockman	F	Scripps	Air/sea	no
6	Shari Yvon-Lewis	F	TAMU	Air/sea	no
7	Lei Hu	F	TAMU	Air/sea	no
8	Rosalie Shapiro	F	TAMUCC	Geochem	no
9	**Julia Doe**	**F**	**UGA**	**Micro**	**off**
10	**Jen Biddle**	**F**	**UNC**	**Micro**	**off**
11	Toshi Mikagawa	M	DSSI	ROV pilot	no
12	Kevin MacArthey	M	DSSI	ROV tech	no
13	ROV 3	M	DSSI	ROV pilot	no
14	Evan Solomon	M	Scripps	Water chem	no
15	John Kessler	M	TAMU	Air/sea	no
16	Paul Clark	M	TAMU	Technician	no
17	Ian MacDonald	M	TAMUCC	Chief Scientist	no
18	Oscar Garcia	M	TAMUCC	Navigation	no
19	Thomas Naehr	M	TAMUCC	Geochem	no
20	Ira Leifer	M	UCSB	Bubbles	no
21	**Marshall Bowles**	**M**	**UGA**	**Micro**	**off**
22	**Kevin Martin**	**M**	**USM**	**Bubbles**	**off**
	Leg 2 GC600, GC852, GC185, HYFLUX only				
1	Emily Bockman	F	Scripps	Air/sea	no
2	Gretchen Robertson	F	Scripps	Water chem	no
3	Miriam Kastner	F	Scripps	Water chem	no
4	Nichole Beasley	F	Scripps	Water chem	no
5	Lei Hu	F	TAMU	Air/sea	no
6	Shari Yvon-Lewis	F	TAMU	Air/sea	no
7	Rosalie Shapiro	F	TAMUCC	Geochem	no
8	**Melissa Miller**	**F**	**Scripps**	**Water chem**	**on**
9	Toshi Mikagawa	M	DSSI	ROV pilot	no
10	Chris Nicholson	M	DSSI	ROV tech	no
11	Kevin MacArthey	M	DSSI	ROV pilot	no
12	**Jeff Chanton**	**M**	**FSU**	**Micro**	**on**
13	Evan Solomon	M	Scripps	Water chem	no
14	John Kessler	M	TAMU	Air/sea	no
15	Paul Clark	M	TAMU	Technician	no
16	Ian MacDonald	M	TAMUCC	Chief Scientist	no
17	Oscar Garcia	M	TAMUCC	Navigation	no
18	Thomas Naehr	M	TAMUCC	Geochem	no
19	**Chris Stubbs**	**M**	**UCSB**	**Bubbles**	**on**
20	Ira Leifer	M	UCSB	Bubbles	no

Operations summary and preliminary results

Operations summary at MC118 (hydrate observatory)

This portion of the expedition was a cooperative effort between the HYFLUX science team and investigators in the Hydrate Observatory (HO) Consortium. Operations during the first week of our cruise were challenged by weather that made safe ROV operations temporarily unfeasible. We also had some critical equipment malfunctions. We had two ROV dives that were prematurely terminated due to buoyancy problems. We completed one ROV dive on 6 July. During this dive we located the "Rudyville" site, which had a vigorous gas plume. We collected several short cores for microbiology and made a series of water collections using the niskin racks mounted on the ROV. Despite problems, the scientific results from MC118 were very positive and the science party was in agreement that we should extend our operations there to complete a full suite of sampling.

We had to shut down diving for two days after that while we waited for improvement in the weather and worked on better procedures for safe ROV launch/recovery. Four members of the HO Consortium transferred off the ship on 9 July and were replaced by two more HYFLUX team members and Dr. Jeff Chanton from the HO Consortium. TDI-BI (the vessel operator) cooperated fully with our efforts to improve ROV operations and sent Dr. James Howell out to assist with this, but we obliged to return to Gulfport on 9 July because the ship's steering gear failed.

We left Gulfport at 9pm on 10 July and arrived at MC118 next morning. No further problems were experienced with traction winch, A-frame, crane, or rudder gear. Weather remained flat calm. We completed four more dives at MC118. Also took two short gravity cores and about 12 rosette casts. We found the active gas vent and were able to sample it several times with niskin bottles on the ROV. Surface surveys showed peaks of methane to 15ppm. The ROV niskin sampling produced peaks of methane to about 1000 nM in the water column. We were able to recover Laura Lapham's equipment using the elevator. We recovered a time-lapse camera that had been deployed in June 2008 as a free vehicle by cutting its anchor line. The camera had ~300 bottom photographs and a temperature record as was in good condition despite having been out for over a year. We recovered additional in-situ instruments that had been deployed by Chanton and Laura Lapham as part of the HO effort. We deployed an “elevator” to recover instruments and to briefly deploy the scanning sonar for acoustic quantification of bubble flow. We collected 7 gravity cores targeting sites of anomalous seismic character.

Preliminary sampling results at MC118 (hydrate observatory)

The station markers and devices deployed during previous efforts at this site were crucial aids to navigation that allowed us to locate hydrate site deposits and gas plumes. Figure 3A shows the array of stations at MC118 (Figure 3A). Surface water sample and air samples were automatically collected during most of the operations at MC118. The results showed water concentrations elevated above an expected background value of ~2nM across much of the site, with a concentration of elevated values over the seafloor locations of gas hydrate and bubble plumes (Figure 3B). ROV operations were also focused in this area (Figure 4).

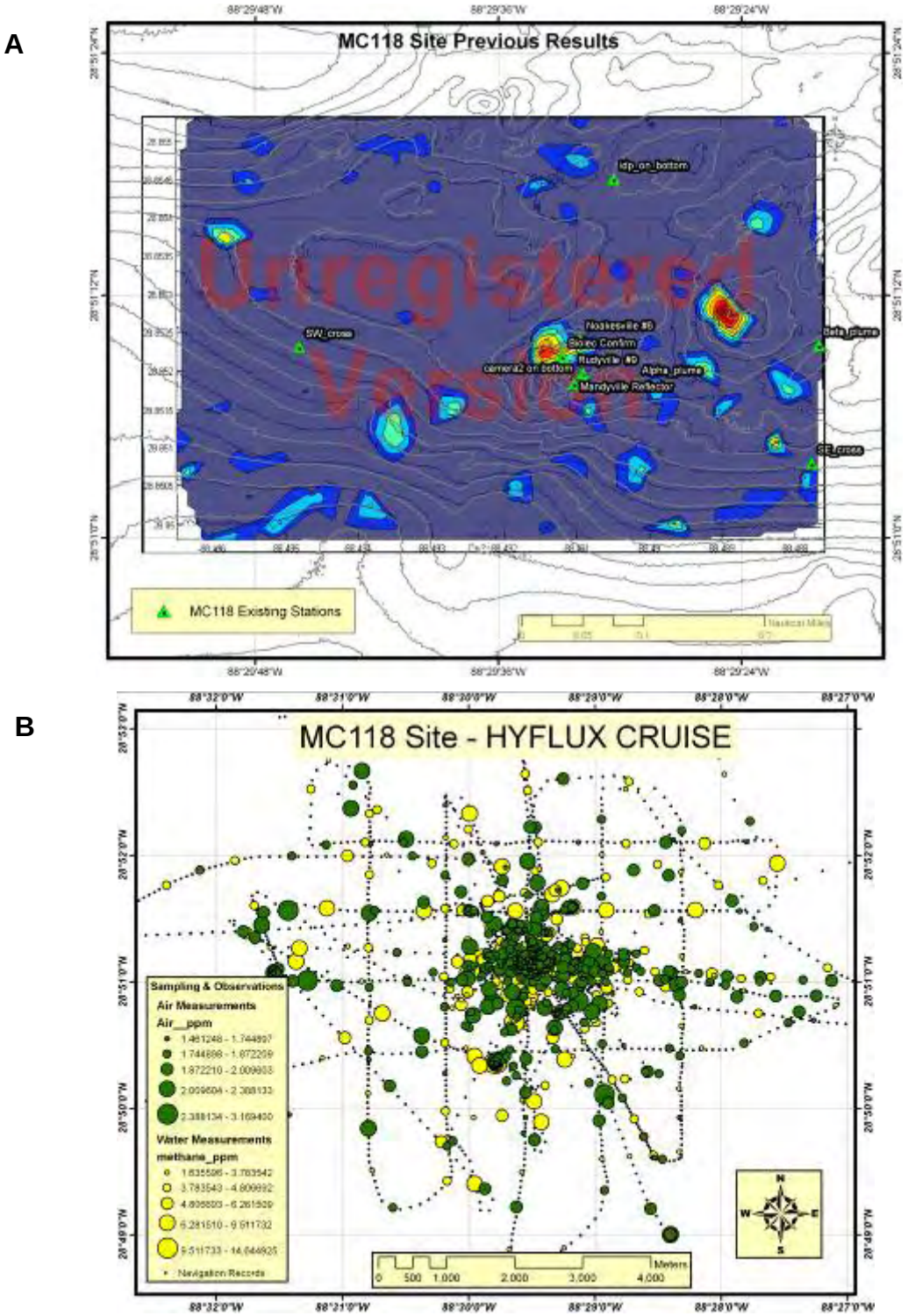

Figure 3 Operations at MC118 re-occupied many of the stations previously established at the site. An AUV survey had identified regions of high CH4 concentrations (A). Surface sampling of air-sea methane concentrations was completed in coarse and fine-scale surveys (B).

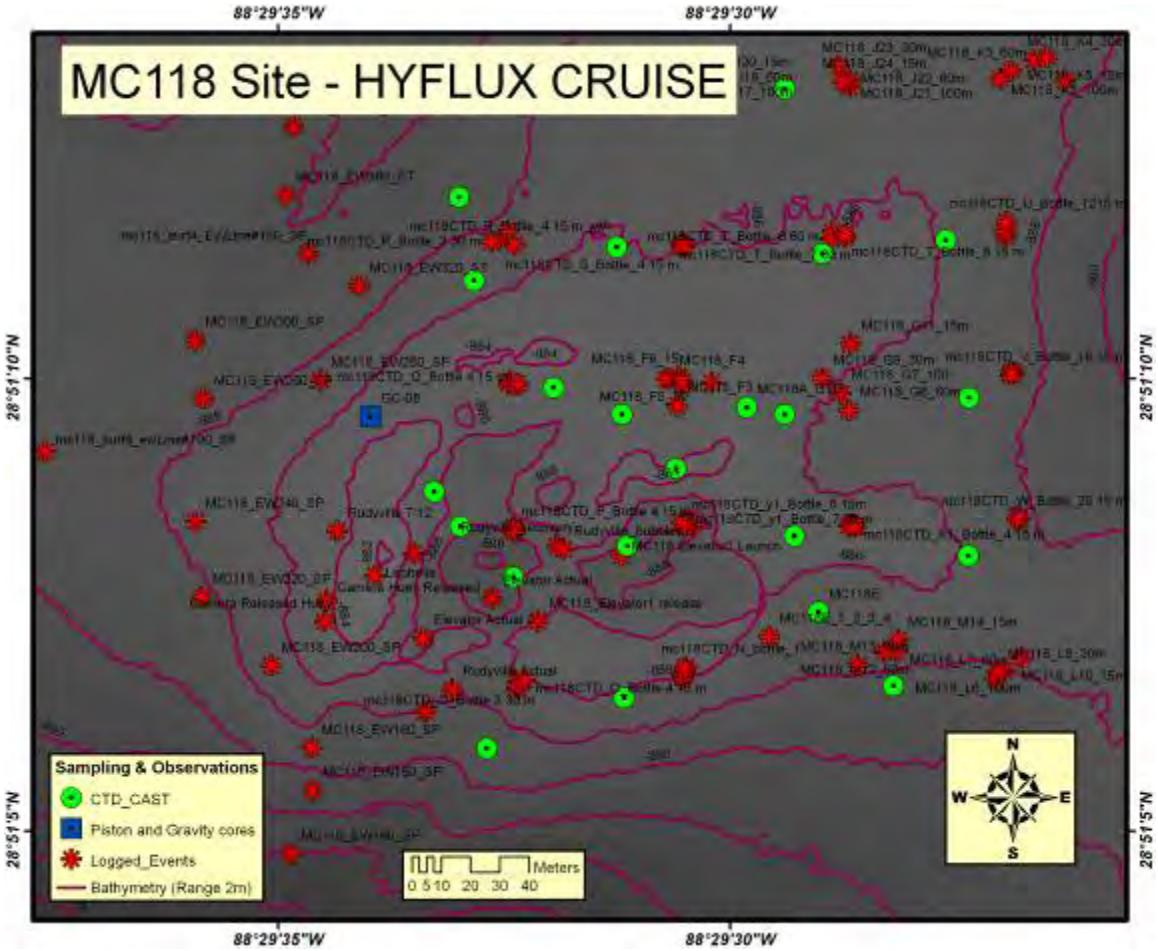

Figure 4 Locations of ROV dives (logged events) and CTD-rosette profiles concentrated near the Rudyville site.

We received a preliminary plot of bottom-water methane concentrations collected by the Hydrate Consortium with Richard Camilli's mass-spectrometer mounted on an AUV. This group had identified two plumes (Alpha and Beta) where they detected peak CH_4 concentrations. We georectified this plot (as a bit-map) based on the coordinates provided and then adjusted the position so that the bathymetric features on the Camilli map corresponded to our navigation--this resulted in a 130 m offset to the west-northwes between the two grids. One of the regions of high CH_4 corresponded closely to the location of active venting at the #9 Rudyville site (Figure 3A).

Oil drops and sheen were frequently observed reaching the surface in the vicinity of the Rudyville gas vent, where they produced a persistent oil slick. A gridded plot of the surface water CH4 concentrations showed regions of high concentrations that corresponded closely to the apparent origin of the oil on the surface (Figure 5A).

We confirmed the presence of CH_4 in the water column with ship-board analyses using a gas chronometer operated by Jeff Chanton (Figure 5B and 3C). Water samples were collected by lowering the rosette over the gas plume location at Rudyville (Figure 3B) and by visually targeting the gas plume using the ROV video and collecting water with the ROV niskin array.

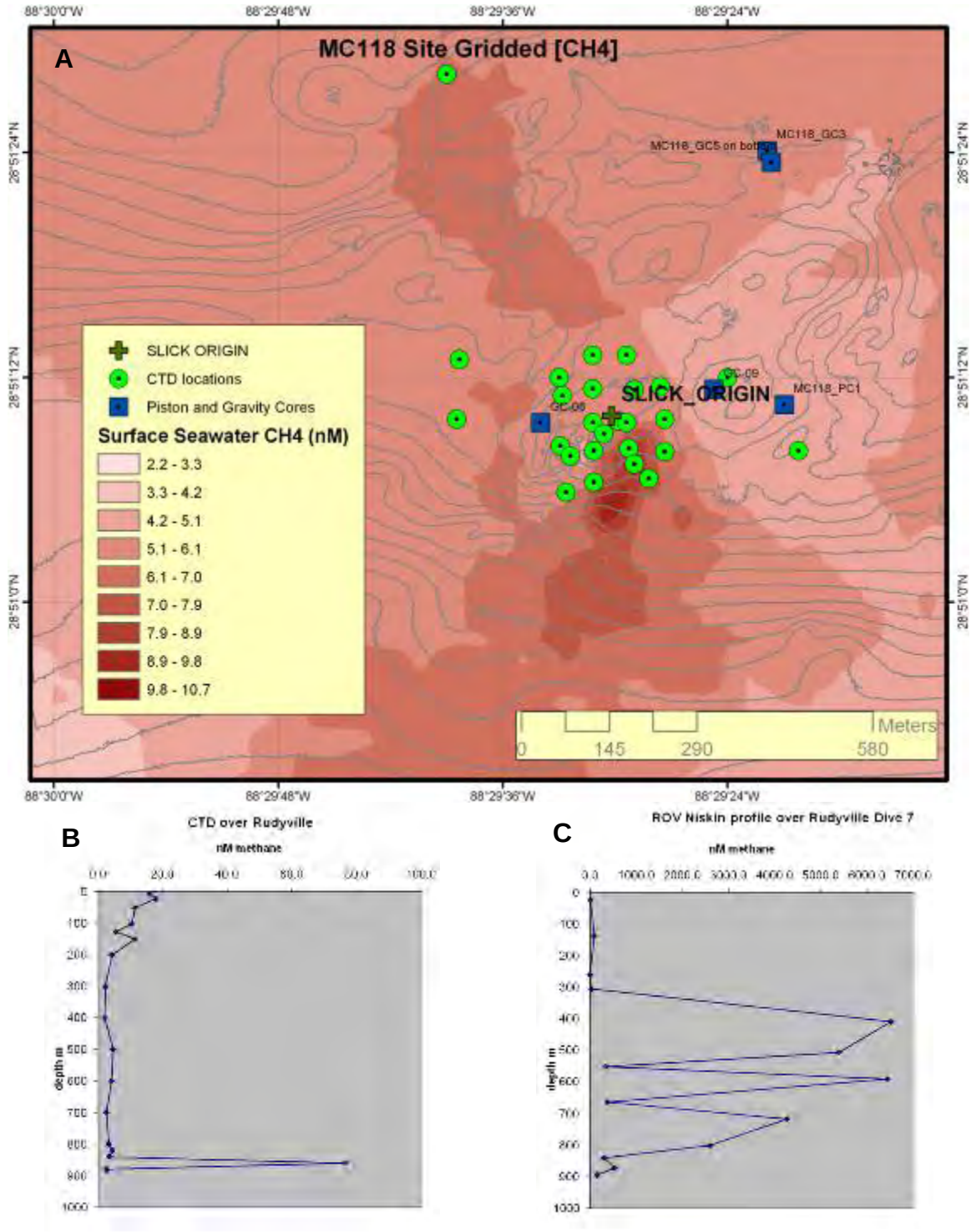

Figure 5. Methane concentrations at MC118: A. Gridded surface show preliminary distribution of surface water methane anomalies.

These preliminary results show that the water column has generally elevated CH4 values over a large area with patchy areas of highly elevated concentrations (Figure 5B).

Targeting the plume with the ROV niskin sampler, however, produced values two to three orders of magnitude greater (Figure 5C). The ROV results also demonstrate conclusively that the niskin bottles were sampling a highly localized water column feature because the values fluctuated sharply at several points in the profile where the ROV deviated slightly from the main portion of the gas plume.

Time-lapse camera deployments at MC118 (hydrate observatory)

In July 2009, during the HYFLUX cruise on board RV Brooks McCall, the Dewey System was found using the Global Explorer ROV. Further attempts to release the system acoustically were unsuccessful. The ROV then released the camera by cutting the anchor tether so that it was able to float to the surface.

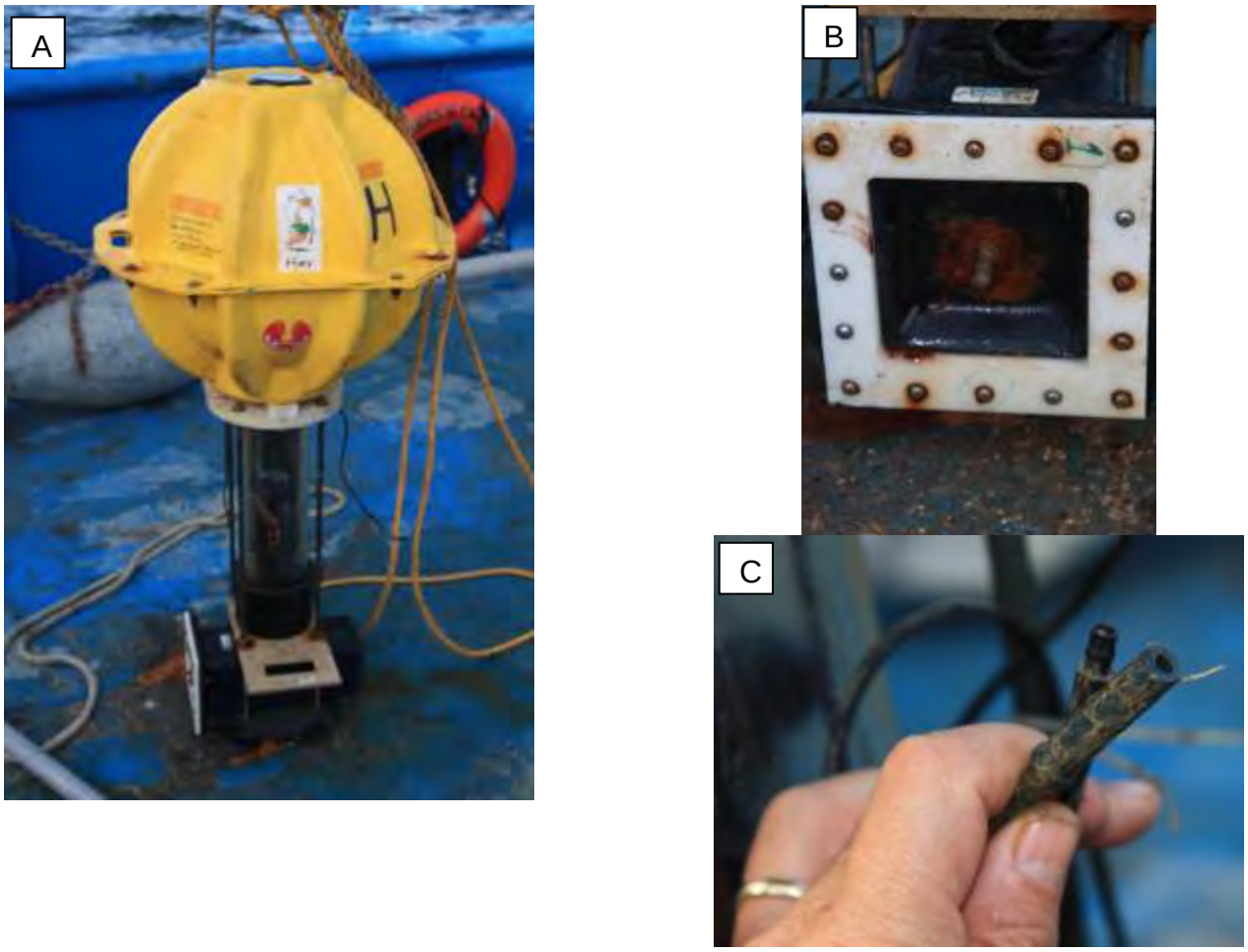

Figure 6 Huey camera system after recover from MC118, 10 July 2009 (A). B. Battery pack was flooded and corroded beyond repair. C. System failed to release because the grounding connector and corroded through--probably damage during deployment.

The camera was found to be intact and functional--no flooding or mechanical damage to the main components (Figure 6A). The battery suffered membrane failure and will need to be replaced (Figure 6 B). Failure mode for the release mechanism was a connector on

the grounding cable from the Benthos transponder (Figure 6 C). The photographs record the connector as having been broken in the earliest images from the sequence (Fig. 2). It is most likely that the connector was damaged during the deployment process and did not complete the circuit for the burn-wire release.

The camera had recorded 25 complete rotations during a 7-day interval. Unfortunately, the "blind" deployment had landed on a steep hill, so half of the images in each revolution did not show the seafloor. The seafloor in view consisted of soft mud with shells. A crab (*Chaceon sp*) and a bathygadid fish (*Coryphaenoides sp*) were captured in multiple images from the site. There were no clearly distinguishable bacterial mats visible in the images.

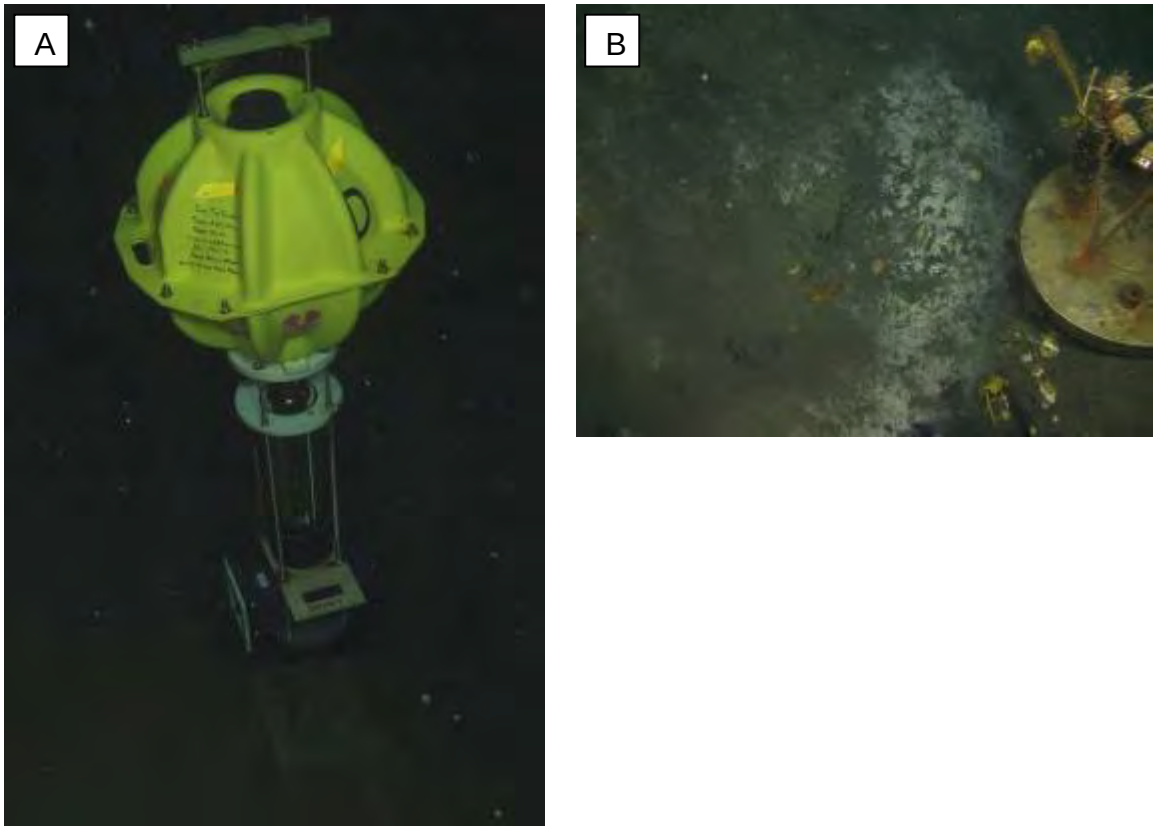

Figure 7. Deployment of Dewey camera system 12 July 2009. A. system in place on bottom. B. approximate field of view for camera (prior to removal of disused instrument array)

System Dewey had been refurbished during the interim. This system was redeployed by the ROV at the active gas vent near the Rudyville vent (Figure 7A). Rotation was fixed (no movement) and the recording interval was set to 30 min. The ROV was able to position the camera to oversee a patch of exposed hydrate, a large bacterial mat, and an active gas seep (Figure 7B). The time-base of the camera was UTC. First flash was 15:44UTC. Depth of site was The strobe was seen to flash repeatedly while the ROV was operating near the site. The depth of the site was 895 m, position 28°51.13'N

88°29.57'W. The transponder for Dewey receives on channel 14.0 and transmits on 11.0. Enable is D and release is E.

Operations summary and results for GC600 (Deep-water site)

This site targeted the source of large, persistent oil slicks observed in satellite SAR data (Figure 8A). The ship departed MC118 on the night of July 13 and transited 12h to GC600. We dived on targets developed from satellite SAR analysis and found very large oil seep with huge hydrate mound after less than 20 min of searching. The seep was less than 50m from the predicted location (Figure 8B). Further exploration located three additional vents spaced about 75m apart along a ridge-line trending to the south. This is also consistent with the satellite observations, which predicted an array of four, closely-spaced oil sources.

The hydrate mounds were associated with mussels and clam shells (no living specimens seen). Three were no tube worms and the bacterial mats were restricted to areas where apparent brine flows had reworked the surface sediment. Extensive carbonate pavements were observed near some of the hydrate mounds, including karsts-like frameworks where gas hydrate has dissolved, leaving behind carbonate lined crevices.

The exposed hydrate was unlike anything previously seen (Figure 9A). Although hydrate is typically white or stained orange-yellow if oil is present, this hydrate was black in color and appeared to be completely saturated with oil. Oil could be seen rising in continuous drops all along the edge of the big mound--which we call Oil Mountain. Also in a steady stream of large, very oil bubbles mixed relatively clean bubbles. Oily bubbles were also observed issuing in a continuous stream from a small vent located about 20 m south of the large mound.

We completed three dives at GC600. The ROV took a push core for microbiology. We collected two piston cores. We located a position where oil drops were arriving at the surface at a high rate and took a rosette cast into that position. We continued diving on July 15, collecting push cores and water samples with the ROV-mounted niskin bottles.

The transit to GC185 (Bush Hill) was conducted at ~4kt and was routed to traverse five sites where satellite data show persistent oil seepage.

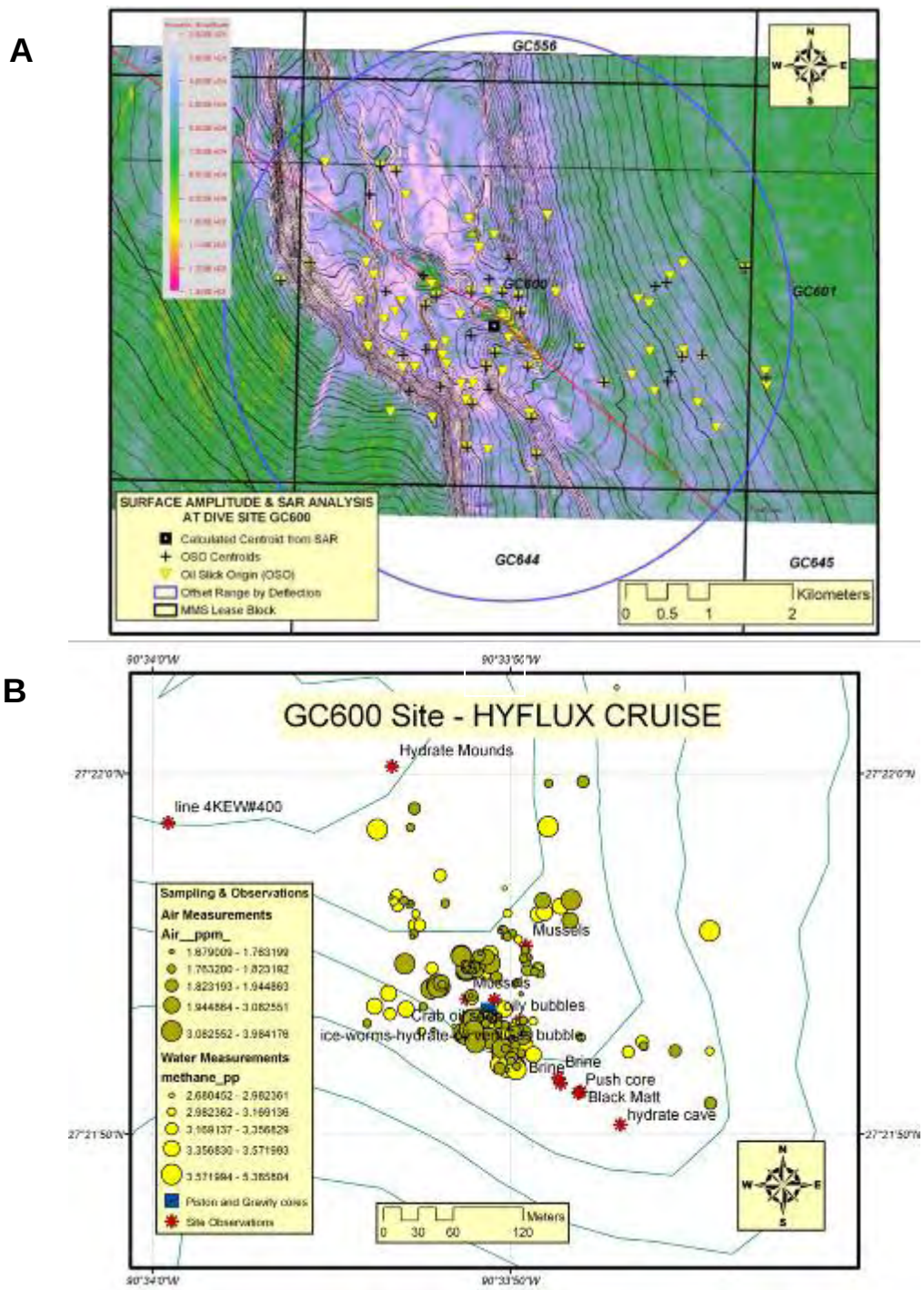

Figure 8. GC600 site. A. Results of satellite SAR analysis predicted a seep located near the center of the GC600 lease block. B. Summary of operations and findings at the GC600 site, which confirmed predictions.

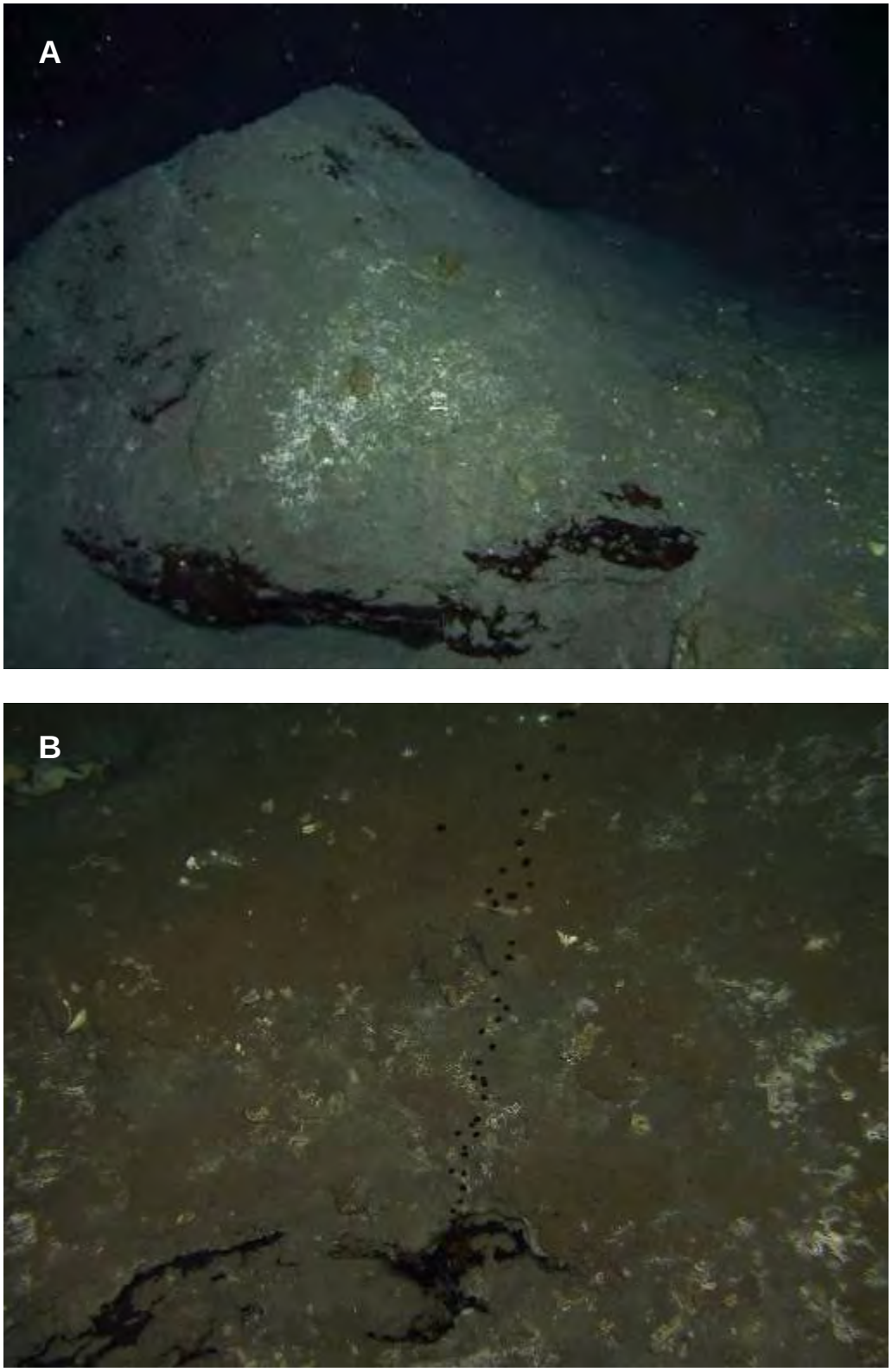

Figure 9 Hydrate features at the GC600 study site. A. Large mound of oil-saturated gas hydrate. B. Discharge of oily bubbles from vent.

Operations summary and results for GC185— (Shallow-water site)

This site (also known as Bush Hill) has been sampled in very many science projects beginning in 1986. It was chosen to provide a shallow-water example of the seep process and because the location of the gas vents was well known. The ROV collected imagery for quantifying bubble flow rates and gas flux. Four push cores were collected in bacterial mats for the microbiology effort. Four profiles of water samples (12-14 samples per profile) were collected as the ROV maneuvered in the bubble stream. Effort at GC185 concluded at 00:00 on July 17. A surface survey visiting several seeps identified in satellite data was completed during the transit back to Freeport, Texas. The cruise demobilized on 19-20 July 2009.

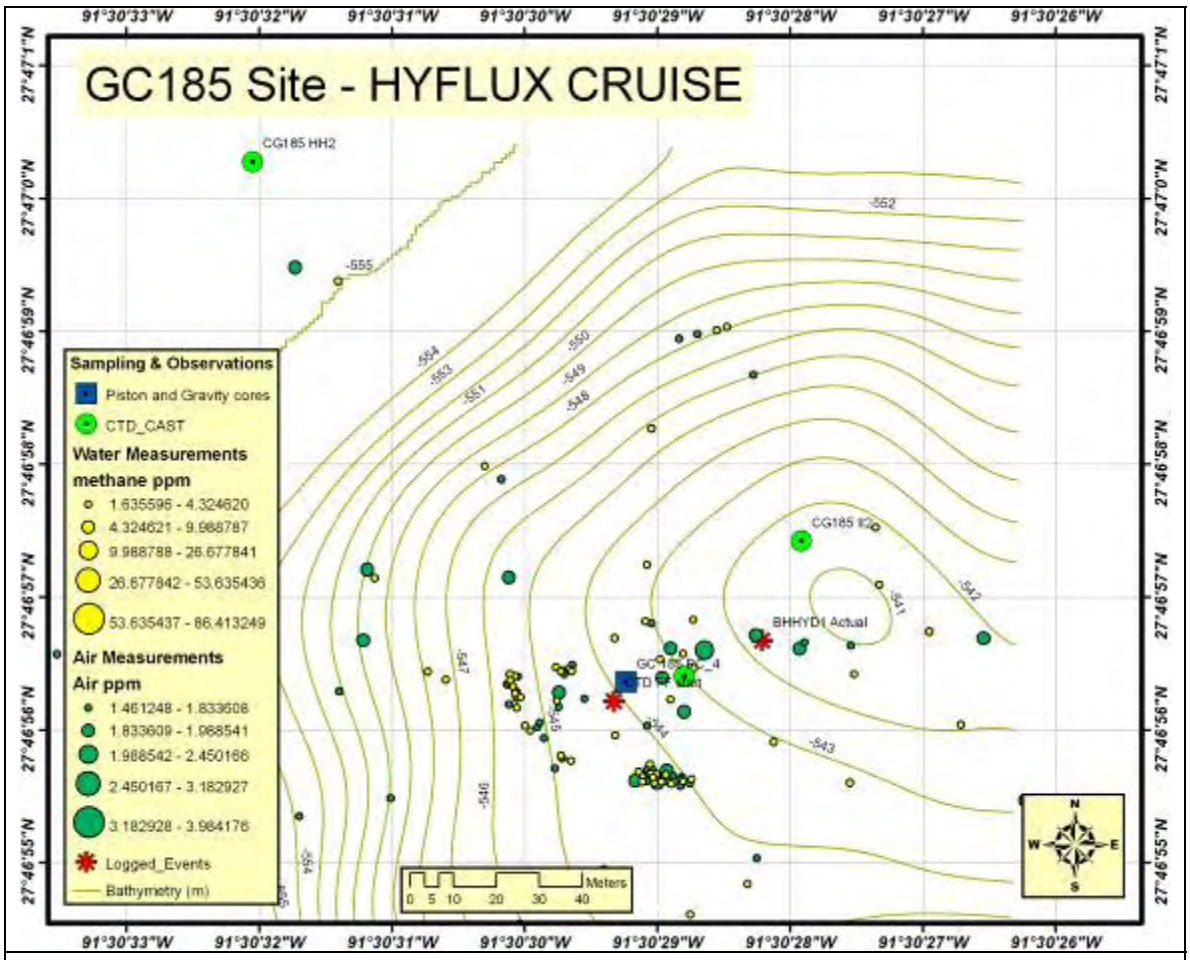

Figure 10. Summary of operations and collections at GC185 site.

Daily narrative of cruise operations

Wednesday, 1-3 July, 2009

Location and general activities

The RV Brooks McCall (BMCC hereafter) was mobilized with the ROV Global Explore (ROV hereafter) onboard. These operations were completed at the East Pier, Dock 3 of the Gulfport Municipal Port. The ROV team set up the deck winch and the top-side control system. The SeaBird 911 niskin rosette and CTD (rosette hereafter) had previously been placed onboard the BMCC and were made ready for sea. We took onboard a second oceanographic winch with conducting cable for operating the rosette. Repairs to the traction winch--used for piston and gravity coring--were completed. The Kongsberg ultra-short baseline navigation system (USBL) transponder was installed in the ship's moonpool. All science personnel reported. We completed safety briefings and orientations.

Major problems or delays

Departure was delayed by about 6 hours due to recurring problems with the traction winch. A critical piece of gear needed for piston coring was found to be missing, but there was no time to have a replacement sent. Determined to conduct gravity coring instead.

Saturday, 04 July

Location and general activities

Arrived on-station in MC118 site at 10:00 (all times in this narrative are local Cental-daylight saving time). Continued set-up of ROV in preparation for launch. There were continued problems with the traction winch and uncertainty as to whether it would function sufficiently to support coring.

ROV operations

HYFLUX 1 21:15 to 23:50 at 28°51.17' 88°29.5'
Test-fired niskin bottle array successfully.
ROV too heavy--recovery by hauling in on umbilical cable.

Air-Sea surface sampling

Not yet initiated. Set-up for instruments still in progress

Rosette-CTD samples

Two CTD casts were carried out:

mc118.cal	Jul 04 2009 15:29:30	28 51.3594	88 25.4793
mc1189acal	Jul 04 2009 23:46:24	28 51.3574	88 25.2663

Other scientific activity

Not Applicable (NA hereafter)

Major problems or delays

NA

Sunday, 05 July

Location and general activities

On station at MC118 completing background rosette casts, refining ROV configuration and USBL calibration

ROV operations

Several tests adjust ballasting. These are listed as HYFLUX 2 15:15-21:55

Air-Sea surface sampling

Initiated at end of day. Total of 13 water and equilibrator samples collected.

Rosette-CTD samples

Five rosette casts completed:

Sample designation	Date & time	Latitude N	Longitude W
mc1189acal	Jul 05 2009 14:03:42	28 50.6505	88 32.5467
mc1189acal	Jul 05 2009 15:13:10	28 50.6505	88 32.5467
mc118alfa	Jul 05 2009 17:29:15	28 51.1613	88 29.4970
mc118alfaA	Jul 05 2009 18:16:32	28 51.1357	88 29.3376
mc118E	Jul 05 2009 22:17:17	28 51.1236	88 29.4838

Other scientific activity

Preparing elevator and acoustic bubble monitoring devices.

Major problems or delays

ROV requires extended testing to adjust buoyancy. One issue is that the surface waters are relative low-salinity, so buoyancy changes significantly with depth. Traction winch continues to present problems, which has prevented calibration of the USBL system. Launch and recovery of the ROV is very difficult over the p

Monday, 06 July

Location and general activities

On station at MC118 site. Attempted elevator launch; unsuccessful due to heavy seas.

ROV operations

HYFLUX 3 19:26-23:48. Located Rudyville station despite difficulty with USBL navigation. Found timelapse camera from June 2008 deployment. Collected push cores (three successful) at Rudyville vent from bacterial mats. Collected 10 niskin bottles with ROV.

Air-Sea surface sampling

Air-sea system active all day. Processed a total of 218 water and equillibrator samples.

Rosette-CTD samples

None

Other scientific activity

Successful collection of three push cores for microbiology.

Major problems or delays

Elevator launch was unsuccessful due to heavy seas and difficulties deploying the elevator over the starboard side with the deck crane. Recovery of the ROV was difficult due to excessive movement during transit from water to deck.

Tuesday, 07 July

Location and general activities

On station at MC118. Attempting to rectify problems with ROV launch and recovery. Collected gravity cores at MC118 site

ROV operations

Suspended due to heavy weather

Air-Sea surface sampling

Completed surface survey in 5km grid covering the larger MC118 area. A total of 104 air and 103 equillibrator samples were processed.

Rosette-CTD samples

None

Other scientific activity

Collected two gravity cores near point Bravo. Both attained better than 3 m penetration. One was sulfurous.

Major problems or delays

Weather delay

Wednesday, 08 July

Location and general activities

On station at MC118. Continued heavy weather and problems with ROV launch/recovery. Collected gravity cores at MC118 site

ROV operations

Suspended due to weather and launch/recovery prolems

Air-Sea surface sampling

Totals of 105 air and 103 water samples were processed.

Rosette-CTD samples

None

Other scientific activity

Preparing elevator for launch.

Major problems or delays

ROV cannot be safely deployed or recovered using the deck crane over the port side of the ship. We are working to adapt the A-frame for launch recovery. This requires functioning traction winch and a refit of the back-deck area such a welding grating over the instrument launch shoot. In light of on-going problems, we have delayed the crew change until 9 July.

Thursday, 09 July

Location and general activities

On station at MC118. Continued heavy weather and problems with ROV launch/recovery. Personnel change. TDI representative Lara Miles has been replaced by Dr. James Howell. Conducting detailed operations review to guarantee safe and effective ROV operations.
Returned to Gulfport to repair steering gear and traction winch

ROV operations

Suspended pending operational review.

Air-Sea surface sampling

Totals of 59 air and 59 water samples were processed. A number of these samples were collected during the transit to Gulfport and revealed extremely high methane values.

Rosette-CTD samples

Completed a grid of rosette profiles and CTD casts over so-called Bravo site where oil drops were seen surfacing.

Sample designation	Date & time	Latitude N	Longitude W
mc118F	Jul 09 2009 05:48:21	28 51.16 N	088 29.52 W
mc118F2	Jul 09 2009 05:59:18	28 51.15 N	088 29.51 W
mc118G	Jul 09 2009 06:24:52	28 51.16 N	088 29.49 W
mc118H	Jul 09 2009 06:49:56	28 51.20 N	088 29.55 W
mc118I	Jul 09 2009 07:14:44	28 51.22 N	088 29.52 W
mc118J	Jul 09 2009 08:13:11	28 51.22 N	088 29.49 W
mc118M	Jul 09 2009 11:26:35	28 51.11 N	088 29.47 W

Other scientific activity

Launched elevator with acoustic bubble measurement device. Used survey information from previous dives to attempt to position it near the gas vent at Rudyville. However, it proves difficult to get it within the required ~40m of the vent.

Major problems or delays

Safety review of ROV and all deck operations. Because the cruise is short-handed, we need to ensure that all scientific personnel working on deck are aware of and following safety procedures. At 15:00 the ship's steering gear failed. Problem was traced to hydraulic rams that control rudders. Replacement parts are on-hand at Freeport Texas and were trucked over-night to Gulfport to meet the vessel.

Friday, 10 July

Location and general activities

Transit and port: Arrived in Gulfport at 11:30 to make repairs. Departed at 21:00 and transited back toward MC118.

ROV operations

None

Air-Sea surface sampling

A total of 54 air and 53 water samples were processed. Most of these samples were collected along the transit back to MC118, which followed a different route from the transit to Gulfport.

Rosette-CTD samples

None

Other scientific activity

Major problems or delays

We have lost fully over 24 hours from our schedule over and above the weather down-time. It will be necessary to extend the cruise by 2 days to make up this deficit.

Saturday, 11 July

Location and general activities

Arrived at MC118 site, operating in the vicinity of the Rudyville station 28°51.129' and 88°29.53'. Completed rosette cast and ROV dive. Released elevator with push cores and acoustic bubble sensor.

ROV operations

HYFLUX 4-- 10:24-23:30. Collected 10 niskin samples in the main plume at Rudyville vent. Found and released elevator. Found time-lapse camera that had been stuck on bottom since June. Released it by cutting the anchor tether. Recovered "peeper" pore

fluid sampler deployed during past operations at this site. Digital photographs of vent site.

Air-Sea surface sampling

A total of 108 air and 103 water samples were processed. Samples from over Rudyville during ROV operations and in a large-scale grid after vehicle was recovered.

Rosette-CTD samples

CTD cast for sound velocity.

Mc118-svp	Jul 11 2009 13:21:33	28 51.13 N	088 29.54 W

Other scientific activity

Deployed second time-lapse camera using winch and acoustic release. Camera is set for sampling at 30-s intervals. The timebase for photographs is UTC. The Benthos acoustic release is set at Rx=14.0, Tx=11.0, Enable="D", Release="E". Camera will be positioned with ROV on next dive.

Major problems or delays

Elevator was damaged during launch--one of the glass floats was broken. Further use during this cruise is not contemplated. Did successfully deploy and recover acoustic bubble sensor with this device as well as recovered Laura Lapham's pore sampling instruments.

Sunday, 12 July

Location and general activities

Continued operations in the vicinity of the Rudyville station 28°51.129' and 88°29.53'. Completed rosette casts and ROV dive.

ROV operations

HYFLUX 5-- 15:05 - 22:00, 890m depth. Deployed University of Southern Mississippi acoustic bubble sensor mounted on ROV. Collected 11 ROV niskin samples from gas plume at Rudyville. Successfully tracked bubbles to 300 m depth with use of ROV sonar. Positioned time-lapse camera at Rudyville vent site. Collected digital photographs. Avoided bottom contact to limit contact with potentially methane-contaminated sediments.

Air-Sea surface sampling

Completed large area grid over MC118 site during night-time. Totals of 84 air and 84 water samples were processed.

Rosette-CTD samples

Completed 15 rosette profiles--again attempting to collect a gridded array over locations where oil can be seen surfacing.

Sample designation	Date & time	Latitude N	Longitude W
Mc118- N	Jul 12 2009 04:37:15	28 51.1078	88 29.5196

Mc118- O	Jul 12 2009 05:01:15	28 51.0985	88 29.5449
Mc118- P	Jul 12 2009 05:22:24	28 51.1394	88 29.5498
Mc118- Q	Jul 12 2009 05:47:06	28 51.1599	88 29.1570
Mc118- R	Jul 12 2009 06:08:38	28 51.1847	88 29.5473
Mc118- S	Jul 12 2009 07:04:05	28 51.1908	88 29.5209
Mc118- T	Jul 12 2009 07:25:21	28 51.1896	88 29.4830
Mc118- U	Jul 12 2009 07:45:41	28 51.1921	88 29.4603
Mc118- V	Jul 12 2009 08:06:42	28 51.1631	88 29.4560
Mc118- W	Jul 12 2009 08:26:51	28 51.1340	88 29.4562
Mc118- X2	Jul 12 2009 10:31:06	28 51.1376	88 29.4882
Mc118- Y1	Jul 12 2009 10:51:19	28 51.1358	88 29.5190
Mc118- Z	Jul 12 2009 11:12:10	28 51.1630	88 29.6415
Mc118- AA	Jul 12 2009 11:31:51	28 51.2167	88 29.6394
Mc118- BB	Jul 12 2009 11:52:33	28 51.1636	88 28.5177

Other scientific activity

Bubble-quantification with

Major problems or delays

None

Monday, 13 July

Location and general activities

Continued operations in the vicinity of the Rudyville station 28°51.129' and 88°29.53'. Completed rosette casts and ROV dive. Gravity coring over night.Deployed University of Southern Mississippi acoustic bubble sensor mounted on ROV. Launched the ROV twice to increase niskin sampling. Transited to GC600 site at conclusion of ROV operations.

ROV operations

HYFLUX 6-- 15:00 - 19:30, 890m depth. Collected 13 ROV niskin bottles in plume. Successfully following bubbles to ~100m depth using video and sonar. Avoided bottom contact.
HYFLUX 7 20:00 - 21:54 880m depth. Short dive to collect push core for U. Georgia, Athens. Collected single short core at Rudyville vent. Collected 14 niskin bottles in plume. Successfully tracked bubbles to 136m depth. Final niskin bottle at 25 m.

Air-Sea surface sampling

Totals of 39 air and 39 water samples were processed. System suspended for maintenance and to allow rapid transit.

Rosette-CTD samples

Collected 4 background rosette profiles.

Sample designation	Date & time	Latitude N	Longitude W
Mc118- SEEPC	Jul 13 2009 12:44:28	28 51.47	88 29.65
Mc118- SEEPB	Jul 13 2009 14:14:37	28 51.20	88 29.40
Mc118- SEEPBG	Jul 13 2009 16:08:35	28 51.1458	88 29.5546

Mc118- SEEPBG3	Jul 13 2009 16:31:43	28 51.1649	88 29.5326

Other scientific activity

Two gravity cores collected during the night.

Major problems or delays

Tuesday, 14 July

Location and general activities

Transit to GC600 sampling site at 27°21.91' and 90°33.85'. ROV dives to explore suspected seep location successfully located major seep vents along ridge-line.

ROV operations

HYFLUX 8-- 16:10 - 23:52, 1230m depth. Found very active oil and seep with massive gas hydrate deposit. Seep was found at precisely the predicted location on the seafloor--confirming the predictive ability of the satellite interpretation. Gas hydrate was noteworthy for being saturated with oil to the point that it was black in color. Collected 11 ROV niskin bottle in plume. Following this plume was difficult, but samples near bottom were in plume. Chemosynthetic fauna was restricted to mussels and Calyptogena shells.

Air-Sea surface sampling

Totals of 92 air samples and 94 water samples were processed.

Rosette-CTD samples

One background rosette profile

Sample designation	Date & time	Latitude N	Longitude W
Mc118- CC	Jul 14 2009 04:06:31	28 25.5374	89 08.0172

Other scientific activity

Collected push core for microbiology. Piston cores for pore fluid sampling.

Major problems or delays

None

Wednesday, 15 July

Location and general activities

GC600 sampling site near 27°21.91' and 90°33.85'. Completed two ROV dives, air-sea sampling in vicinity of surfacing oil drops. Three piston cores.

ROV operations

HYFLUX 9-- 16:10 - 23:52, 1230m depth. Video and sonar quantification of bubble and oil plumes was completed with ROV at main site. Careful digital photo documentation of large hydrate deposit. Oil flow from hydrate and nearby vent continuous. Collected 13 ROV niskin bottles in plume.

HYFLUX 10-- 16:10 - 23:52, 1230m depth. Additional video documentation and quantification of bubble flows. Collected 14 ROV niskin bottles in plume.

Air-Sea surface sampling

A total of 96 air and 97 water samples were processed targeting location of surfacing oil drops.

Rosette-CTD samples

Sample	Date time	Latitude N	Longitude W
GC600EE	Jul 15 2009 15:00:28	27 22.12	90 32.78
GC600EE	Jul 15 2009 15:00:28	27 22.12	90 32.78

Other scientific activity

Piston cores (2) for pore fluid and hydrocarbon sampling.

Major problems or delays

UC-Santa Cruz acoustic instrument has proven inoperable despite numerous tries to make it work on the ROV. This portion of the project will have to be completed with visual data.

Thursday, 16 July

Location and general activities

Transiting slowly to GC185 site to allow surface air-sea survey. Arrived at GC185 at 15:00 27°46.9' and 91°30.5'. Completed ROV dives and other sampling operations.

ROV operations

HYFLUX 11-- 18:53 - 20:45, 545m depth. Located main vent at BHHYD1 station. Completed inspection of site where previous DOE work was carried out. Gas hydrate mound has disappeared although gas venting continues. Collected 13 ROV niskin samples in plume--tracked plume almost to surface.
HYFLUX 12-- 22:20 - 00:00, 540m depth. Collected 2 push cores in white mat. Collected 13 ROV niskin samples in plume. Were again about to track plume almost to surface.

Air-Sea surface sampling

Totals of 100 air and 101 water samples were processed.

Rosette-CTD samples

Collected one background rosette profile.

Sample	Date time	Latitude N	Longitude W
CG185 FF	Jul 16 2009 21:49:24	27 46.94	91 30.48

Other scientific activity

Found tube worm settlement array of Bob Carney. Appears intact. Juvenile tube worms were visible. Took piston core to East of main vent. Took piston core to east of main area.

Major problems or delays

Friday, 17 July

Location and general activities

Remained GC185 near 27°46.9' and 91°30.5'. Completed ROV dives and other sampling operations.

ROV operations

HYFLUX 13-- 16:37 - 19:30, 545m depth. Took push cores in orange and white mat. Relocated main vent and performed visual quantification of bubble flow. Collected 13 ROV niskin samples in plume.
HYFLUX 14-- 20:50 - 23:50, 545m depth. Survey of northern portion of GC185 site. Detailed video of large carbonate outcrop. Visual quantification of additional vent plumes. Collected 14 ROV niskin samples in plume

Air-Sea surface sampling

Totals of 87 air and 89 water samples were processed including samples in transit 55 nmi west from GC185 site.

Rosette-CTD samples

Collected profiles over site and targeting areas of surfacing oil drops.

Sample	Date time	Latitude N	Longitude W
CG185 GG	Jul 17 2009 18:02:30	27 47.728	91 31.297
CG185 HH	Jul 17 2009 18:06:22	27 46.609	91 29.682
CG185 HH2	Jul 17 2009 18:12:15	27 47.0046	91 30.5342
CG185 II	Jul 17 2009 18:33:10	27 46.591	91 29.705
CG185 II2	Jul 17 2009 18:55:23	27 46.9570	91 30.4653
Gc135JJ	Jul 17 2009 19:20:26	27 46.576	91 29.671
Gc135KK	Jul 17 2009 19:41:33	27 46.579	91 29.657
Gc135LL	Jul 17 2009 20:08:02	27 46.548	91 29.690
GC135MM	Jul 18 2009 06:12:48	27 49.7016	91 52.7985

Other scientific activity

NA

Major problems or delays

None

Saturday, 18 July

Location and general activities

Transit and demobilization

Sunday, 19 July

Location and general activities

Return to Freeport, Texas and demobilize cruise.

Table 3. Gravity cores(GC) and piston cores (PC) collected during the

Core	date	lat	long_	Latitude	Longitude
MC118_GC1	7/7/2009	28 51.1757	88 29.3495	28.852928	-88.4892
MC118_GC2	7/7/2009	28 51.6016	88 29.1663	28.860027	-88.4861
MC118_GC3	7/8/2009	28 51.4019	88 29.3646	28.856698	-88.4894
MC118_GC4	7/8/2009	28 50.7675	88 29.2871	28.846125	-88.4881
MC118_GC5	7/8/2009	28 51.3916	88 29.3610	28.856527	-88.4894
GC-08	7/13/2009	28 51.1596	88 29.5663	28.85266	-88.4928
GC-09	7/13/2009	28 51.1892	88 29.4122	28.853153	-88.4902
PC_GC600-1	7/15/2009	27 21.8909	90 33.8438	27.364848	-90.5641
PC_GC600-2	7/15/2009	27 21.8876	90 33.8428	27.364793	-90.564
PC_GC600-3	7/16/2009	27 21.8883	90 33.8461	27.364805	-90.5641
GC 185 PC_4	7/17/2009	27 46.9393	91 30.4873	27.782322	-91.5081

Written dive notes.

APPENDIX II:
INVENTORY OF SAR IMAGES ANALYZED FOR HYFLUX RESULTS

Image ID	Granule Name	Beam_Mode	Collection Date (UTC)
R107988379G3S008	R1_07988_SNA_F379	SNA	16-May-97 11:59:57
R107988388G3S009	R1_07988_SNA_F388	SNA	16-May-97 12:00:28
R108310070G3S007	R1_08310_SNA_F070	SNA	08-Jun-97 12:04:47
R108374378G3S004	R1_08374_SNA_F378	SNA	12-Jun-97 12:12:21
R108374384G3S005	R1_08374_SNA_F384	SNA	12-Jun-97 12:13:01
R108374388G3S006	R1_08374_SNA_F388	SNA	12-Jun-97 12:12:05
R108953066G3S007	R1_08953_SNA_F066	SNA	22-Jul-97 23:56:07
R108953070G3S008	R1_08953_SNA_F070	SNA	22-Jul-97 23:56:34
R109160384G3S004	R1_09160_SNA_F384	SNA	06-Aug-97 12:08:51
R109403379G3S002	R1_09403_SNA_F379	SNA	23-Aug-97 12:12:29
R109403384G3S003	R1_09403_SNA_F384	SNA	23-Aug-97 12:13:03
R109546388G3S004	R1_09546_SNA_F388	SNA	02-Sep-97 12:21:54
R110468069G1S005	R1_10468_ST3_F069	ST3	06-Nov-97 00:05:16
R110711067G3S009	R1_10711_SNA_F067	SNA	23-Nov-97 00:09:04
R111154069G1S010	R1_11154_ST3_F069	ST3	24-Dec-97 00:05:30
R111497069G1S007	R1_11497_ST3_F069	ST3	17-Jan-98 00:05:22
R111840069G1S010	R1_11840_ST3_F069	ST3	10-Feb-98 00:05:14
R112004381G1S008	R1_12004_ST3_F381	ST3	21-Feb-98 12:04:47
R112083069G1S003	R1_12083_ST3_F069	ST3	27-Feb-98 00:09:35
R113112069G1S003	R1_13112_ST3_F069	ST3	10-May-98 00:09:35
R114241068G3S005	R1_14241_SNA_F068	SNA	28-Jul-98 00:04:59
R118321379G1S015	R1_18321_ST1_F379	ST1	09-May-99 12:12:57
R118321381G1S016	R1_18321_ST1_F381	ST1	09-May-99 12:13:11
R118321383G1S017	R1_18321_ST1_F383	ST1	09-May-99 12:13:24
R118421380G1S012	R1_18421_ST2_F380	ST2	16-May-99 12:08:54
R118421382G1S013	R1_18421_ST2_F382	ST2	16-May-99 12:09:08
R118421384G1S014	R1_18421_ST2_F384	ST2	16-May-99 12:09:21
R118621383G3S010	R1_18621_SWB_F383	SWB	30-May-99 12:00:20
R118664383G3S015	R1_18664_SWB_F383	SWB	02-Jun-99 12:12:54
R118721382G3S001	R1_18721_SWB_F382	SWB	06-Jun-99 11:56:00
R118764382G3S006	R1_18764_SWB_F382	SWB	09-Jun-99 12:08:37
R118864382G3S010	R1_18864_SWB_F382	SWB	16-Jun-99 12:04:27
R119343069G1S046	R1_19343_ST1_F069	ST1	19-Jul-99 23:52:41
R119350381G1S012	R1_19350_ST2_F381	ST2	20-Jul-99 12:13:01
R126610384G3S002	R1_26610_SWB_F384	SWB	09-Dec-00 11:55:51
R128447050G3S006	R1_28447_SNA_F050	SNA	17-Apr-01 00:10:53
R128447052G3S007	R1_28447_SNA_F052	SNA	17-Apr-01 00:11:06
R129819052G3S003	R1_29819_SNA_F052	SNA	22-Jul-01 00:11:04
R129840399G3S007	R1_29840_SNA_F399	SNA	23-Jul-01 12:06:00
R129840399G3S009	R1_29840_SNA_F399	SNA	23-Jul-01 12:06:00
R129840401G3S008	R1_29840_SNA_F401	SNA	23-Jul-01 12:06:13
R130848050G3S003	R1_30848_SNA_F050	SNA	02-Oct-01 00:10:44
R131877050G3S008	R1_31877_SNA_F050	SNA	13-Dec-01 00:10:39
R132463050G3S006	R1_32463_SNA_F050	SNA	23-Jan-02 00:14:44
R133449069G1S007	R1_33449_ST2_F069	ST2	02-Apr-02 00:04:30
R133592050G3S004	R1_33592_SNA_F050	SNA	12-Apr-02 00:10:28

R133649069G1S024	R1_33649_ST2_F069	ST2	15-Apr-02 23:56:07
R133892069G1S006	R1_33892_ST2_F069	ST2	03-May-02 00:00:16
R134235069G1S010	R1_34235_ST2_F069	ST2	27-May-02 00:00:13
R134335069G1S016	R1_34335_ST2_F069	ST2	02-Jun-02 23:56:03
R134378050G3S004	R1_34378_SNA_F050	SNA	06-Jun-02 00:06:13
R134378056G3S005	R1_34378_SNA_F056	SNA	06-Jun-02 00:06:54
R134378061G3S006	R1_34378_SNA_F061	SNA	06-Jun-02 00:07:28
R134678069G1S013	R1_34678_ST2_F069	ST2	26-Jun-02 23:56:02
R135021069G1S019	R1_35021_ST2_F069	ST2	20-Jul-02 23:55:57
R135164069G1S006	R1_35164_ST2_F069	ST2	31-Jul-02 00:04:19
R135164071G1S007	R1_35164_ST2_F071	ST2	31-Jul-02 00:04:33
R135364069G1S019	R1_35364_ST2_F069	ST2	13-Aug-02 23:55:55
R135607069G1S015	R1_35607_ST2_F069	ST2	31-Aug-02 00:00:07
R136014380G3S006	R1_36014_SNA_F380	SNA	28-Sep-02 12:03:18
R136014400G3S003	R1_36014_SNA_F400	SNA	28-Sep-02 12:05:33
R136157380G3S007	R1_36157_SNA_F380	SNA	08-Oct-02 12:11:39
R136293069G1S016	R1_36293_ST2_F069	ST2	18-Oct-02 00:00:04
R137322069G1S010	R1_37322_ST2_F069	ST2	28-Dec-02 23:59:52
R137565069G1S008	R1_37565_ST2_F069	ST2	15-Jan-03 00:04:05
R137572394G3S003	R1_37572_SNA_F394	SNA	15-Jan-03 12:25:38
R137665069G1S008	R1_37665_ST2_F069	ST2	21-Jan-03 23:59:50
R137929389G3S003	R1_37929_SNA_F389	SNA	09-Feb-03 11:55:39
R138008069G1S010	R1_38008_ST2_F069	ST2	14-Feb-03 23:59:49
R138351069G1S011	R1_38351_ST2_F069	ST2	10-Mar-03 23:59:49
R138601394G3S005	R1_38601_SNA_F394	SNA	28-Mar-03 12:25:29
R138694069G1S010	R1_38694_ST2_F069	ST2	03-Apr-03 23:59:45
R138815391G3S003	R1_38815_SNA_F391	SNA	12-Apr-03 11:47:24
R138937069G1S016	R1_38937_ST2_F069	ST2	21-Apr-03 00:03:55
R138958378G1S001	R1_38958_ST2_F378	ST2	22-Apr-03 11:54:49
R138958380G1S001	R1_38958_ST2_F380	ST2	22-Apr-03 11:55:03
R138958382G1S001	R1_38958_ST2_F382	ST2	22-Apr-03 11:55:16
R138958384G1S001	R1_38958_ST2_F384	ST2	22-Apr-03 11:55:30
R139137069G1S009	R1_39137_ST2_F069	ST2	04-May-03 23:55:32
R139280069G1S011	R1_39280_ST2_F069	ST2	15-May-03 00:03:56
R139380069G1S009	R1_39380_ST2_F069	ST2	21-May-03 23:59:44
R139480069G1S009	R1_39480_ST2_F069	ST2	28-May-03 23:55:29
R139623069G1S015	R1_39623_ST2_F069	ST2	08-Jun-03 00:03:52
R139630388G3S004	R1_39630_SNA_F388	SNA	08-Jun-03 12:24:46
R139630394G3S005	R1_39630_SNA_F394	SNA	08-Jun-03 12:25:26
R139723067G1S013	R1_39723_ST2_F067	ST2	14-Jun-03 23:59:28
R139744378G1S001	R1_39744_ST2_F378	ST2	16-Jun-03 11:50:36
R139823069G1S025	R1_39823_ST2_F069	ST2	21-Jun-03 23:55:29
R139966069G1S010	R1_39966_ST2_F069	ST2	02-Jul-03 00:03:50
R140066068G1S012	R1_40066_ST2_F068	ST2	08-Jul-03 23:59:28
R140066070G1S013	R1_40066_ST2_F070	ST2	08-Jul-03 23:59:42
R140087383G1S001	R1_40087_ST2_F383	ST2	10-Jul-03 11:51:02
R140087385G1S001	R1_40087_ST2_F385	ST2	10-Jul-03 11:51:16

R140087387G1S001	R1_40087_ST2_F387	ST2	10-Jul-03 11:51:29
R140166069G1S003	R1_40166_ST2_F069	ST2	15-Jul-03 23:55:24
R140409069G1S011	R1_40409_ST2_F069	ST2	01-Aug-03 23:59:35
R140852069G1S033	R1_40852_ST2_F069	ST2	01-Sep-03 23:55:21
R140973387G1S001	R1_40973_ST2_F387	ST2	10-Sep-03 11:43:01
R141216379G1S001	R1_41216_ST2_F379	ST2	27-Sep-03 11:46:21
R141216388G1S001	R1_41216_ST2_F388	ST2	27-Sep-03 11:47:22
R141359380G1S001	R1_41359_ST2_F380	ST2	07-Oct-03 11:54:49
R141438069G1S017	R1_41438_ST2_F069	ST2	12-Oct-03 23:59:29
R141459383G1S001	R1_41459_ST2_F383	ST2	14-Oct-03 11:50:57
R141681069G1S026	R1_41681_ST2_F069	ST2	30-Oct-03 00:03:41
R141802379G1S001	R1_41802_ST2_F379	ST2	07-Nov-03 11:50:28
R141881069G1S018	R1_41881_ST2_F069	ST2	12-Nov-03 23:55:16
R142767072G1S001	R1_42767_ST2_F072	ST2	13-Jan-04 23:55:04
R142910069G1S029	R1_42910_ST2_F069	ST2	23-Jan-04 23:55:06
R143053069G1S034	R1_43053_ST2_F069	ST2	03-Feb-04 00:03:29
R143153069G1S031	R1_43153_ST2_F069	ST2	09-Feb-04 23:59:15
R143174383G1S001	R1_43174_ST2_F383	ST2	11-Feb-04 11:50:43
R143174385G1S001	R1_43174_ST2_F385	ST2	11-Feb-04 11:50:56
R143174387G1S001	R1_43174_ST2_F387	ST2	11-Feb-04 11:51:10
R143253069G1S017	R1_43253_ST2_F069	ST2	16-Feb-04 23:55:00
R143739069G1S019	R1_43739_ST2_F069	ST2	22-Mar-04 00:03:21
R143860379G1S001	R1_43860_ST2_F379	ST2	30-Mar-04 11:50:12
R143860381G1S001	R1_43860_ST2_F381	ST2	30-Mar-04 11:50:26
R143960382G1S001	R1_43960_ST2_F382	ST2	06-Apr-04 11:46:21
R144082069G1S019	R1_44082_ST2_F069	ST2	15-Apr-04 00:03:23
R144182069G1S042	R1_44182_ST2_F069	ST2	21-Apr-04 23:59:09
R144425069G1S025	R1_44425_ST2_F069	ST2	09-May-04 00:02:28
R144446377G1S001	R1_44446_ST2_F377	ST2	10-May-04 00:01:26
R144446379G1S001	R1_44446_ST2_F379	ST2	10-May-04 00:04:35
R144525067G1S016	R1_44525_ST2_F067	ST2	16-May-04 00:00:34
R144525069G1S017	R1_44525_ST2_F069	ST2	16-May-04 00:01:48
R144525071G1S018	R1_44525_ST2_F071	ST2	16-May-04 00:01:01
R144625069G1S010	R1_44625_ST2_F069	ST2	22-May-04 23:56:13
R144646381G1S001	R1_44646_ST2_F381	ST2	24-May-04 11:47:14
R144689381G1S002	R1_44689_ST3_F381	ST3	27-May-04 11:59:08
R144711050G3S003	R1_44711_SNB_F050	SNB	29-May-04 00:18:03
R144746389G1S001	R1_44746_ST2_F389	ST2	31-May-04 11:42:55
R144768067G1S019	R1_44768_ST2_F067	ST2	02-Jun-04 00:03:08
R144768069G1S020	R1_44768_ST2_F069	ST2	02-Jun-04 00:03:22
R144768071G1S021	R1_44768_ST2_F071	ST2	02-Jun-04 00:03:36
R144789377G1S001	R1_44789_ST2_F377	ST2	03-Jun-04 11:53:32
R144789379G1S001	R1_44789_ST2_F379	ST2	03-Jun-04 11:54:07
R144811056G3S004	R1_44811_SNA_F056	SNA	05-Jun-04 00:14:13
R144811066G3S005	R1_44811_SNA_F066	SNA	05-Jun-04 00:15:21
R144825071G1S001	R1_44825_ST2_F071	ST2	05-Jun-04 00:16:11
R144825073G1S001	R1_44825_ST2_F073	ST2	05-Jun-04 00:17:01

R144832380G1S006	R1_44832_ST1_F380	ST1	06-Jun-04 12:06:48
R144932381G1S007	R1_44932_ST2_F381	ST2	13-Jun-04 12:02:42
R144989387G1S001	R1_44989_ST2_F387	ST2	17-Jun-04 11:46:51
R145054050G3S002	R1_45054_SNB_F050	SNB	22-Jun-04 00:17:38
R145132377G1S001	R1_45132_ST2_F377	ST2	27-Jun-04 00:01:22
R145132379G1S001	R1_45132_ST2_F379	ST2	27-Jun-04 00:02:59
R145154056G3S006	R1_45154_SNA_F056	SNA	29-Jun-04 00:14:07
R145154066G3S007	R1_45154_SNA_F066	SNA	29-Jun-04 00:15:15
R145168073G1S001	R1_45168_ST2_F073	ST2	29-Jun-04 00:16:22
R145311069G1S018	R1_45311_ST2_F069	ST2	09-Jul-04 23:54:52
R145332379G1S001	R1_45332_ST2_F379	ST2	11-Jul-04 11:45:53
R145332381G1S001	R1_45332_ST2_F381	ST2	11-Jul-04 11:46:06
R145332383G1S001	R1_45332_ST2_F383	ST2	11-Jul-04 11:46:20
R145618381G1S008	R1_45618_ST2_F381	ST2	31-Jul-04 12:02:34
R145654069G1S019	R1_45654_ST2_F069	ST2	02-Aug-04 23:54:48
R145797067G1S002	R1_45797_ST2_F067	ST2	13-Aug-04 00:02:59
R145861380G1S004	R1_45861_ST1_F380	ST1	17-Aug-04 12:06:38
R145918379G1S001	R1_45918_ST2_F379	ST2	21-Aug-04 11:50:01
R145918381G1S001	R1_45918_ST2_F381	ST2	21-Aug-04 11:50:14
R145918385G1S001	R1_45918_ST2_F385	ST2	21-Aug-04 11:50:41
R145918387G1S001	R1_45918_ST2_F387	ST2	21-Aug-04 11:50:55
R146769050G3S002	R1_46769_SNB_F050	SNB	20-Oct-04 00:17:29
R151471049G3S002	R1_51471_SNB_F049	SNB	14-Sep-05 00:21:07
R151549381G1S003	R1_51549_ST3_F381	ST3	19-Sep-05 11:57:54
R154915064G1S014	R1_54915_ST1_F064	ST1	12-May-06 23:53:29
R154915066G1S015	R1_54915_ST1_F066	ST1	12-May-06 23:53:42
R154915068G1S016	R1_54915_ST1_F068	ST1	12-May-06 23:53:56
R154915069G1S017	R1_54915_ST1_F069	ST1	12-May-06 23:54:03
R154922380G1S032	R1_54922_ST1_F379	ST1	13-May-06 12:14:08
R154922382G1S033	R1_54922_ST1_F380	ST1	13-May-06 12:14:14
R154922384G1S034	R1_54922_ST1_F382	ST1	13-May-06 12:14:28
R154922395G1S036	R1_54922_ST1_F395	ST1	13-May-06 12:15:56
R155022380G1S019	R1_55022_ST1_F380	ST1	20-May-06 12:10:00
R155022382G1S020	R1_55022_ST1_F382	ST1	20-May-06 12:10:14
R155022383G1S021	R1_55022_ST1_F383	ST1	20-May-06 12:10:21
R155022385G1S022	R1_55022_ST1_F385	ST1	20-May-06 12:10:34
R155058068G1S009	R1_55058_ST3_F068	ST3	23-May-06 00:02:14
R155058070G1S010	R1_55058_ST3_F070	ST3	23-May-06 00:02:27
R155065381G1S009	R1_55065_ST1_F381	ST1	23-May-06 12:22:43
R155065385G1S011	R1_55065_ST1_F385	ST1	23-May-06 12:23:10
R155079379G1S011	R1_55079_ST3_F379	ST3	24-May-06 11:53:10
R155079381G1S012	R1_55079_ST3_F381	ST3	24-May-06 11:53:23
R155079383G1S013	R1_55079_ST3_F383	ST3	24-May-06 11:53:37
R155115067G1S009	R1_55115_ST1_F067	ST1	26-May-06 23:45:24
R155115069G1S010	R1_55115_ST1_F069	ST1	26-May-06 23:45:38
R155115071G1S011	R1_55115_ST1_F071	ST1	26-May-06 23:45:51
R155115073G1S012	R1_55115_ST1_F073	ST1	26-May-06 23:46:05

R155122380G1S018	R1_55122_ST1_F380	ST1	27-May-06 12:05:50
R155122381G1S024	R1_55122_ST1_F381	ST1	27-May-06 12:05:56
R155122382G1S019	R1_55122_ST1_F382	ST1	27-May-06 12:06:03
R155122383G1S020	R1_55122_ST1_F383	ST1	27-May-06 12:06:10
R155201065G1S003	R1_55201_ST1_F065	ST1	02-Jun-06 00:10:23
R155201068G1S005	R1_55201_ST1_F068	ST1	02-Jun-06 00:10:43
R155887063G3S001	R1_55887_SWB_F063	SWB	20-Jul-06 00:10:48
R155908385G3S001	R1_55908_SWB_F385	SWB	21-Jul-06 12:01:42
R156108379G3S010st	R1_56108_SWB_F379	SWB	04-Aug-06 11:52:37
R156144059G3S011	R1_56144_SWB_F059	SWB	06-Aug-06 23:43:53
R156187065G3S008st	R1_56187_SWB_F065	SWB	09-Aug-06 23:57:08
R156208379G3S010st	R1_56208_SWB_F379	SWB	11-Aug-06 11:48:24
R156230061G3S005	R1_56230_SWB_F061	SWB	13-Aug-06 00:09:16
R156230064G3S006	R1_56230_SWB_F064	SWB	13-Aug-06 00:09:36
R156244061G3S010st	R1_56244_SWB_F061	SWB	13-Aug-06 23:39:53
R156244071G3S011st	R1_56244_SWB_F071	SWB	13-Aug-06 23:41:00
R156251381G3S010st	R1_56251_SWB_F381	SWB	14-Aug-06 12:01:12
R156273064G3S009	R1_56273_SWB_F064	SWB	16-Aug-06 00:22:11
R156373060G3S009	R1_56373_SWB_F060	SWB	23-Aug-06 00:17:33
R156373064G3S010	R1_56373_SWB_F064	SWB	23-Aug-06 00:18:00
R156387060G3S010st	R1_56387_SWB_F060	SWB	23-Aug-06 23:48:10
R156387071G3S011st	R1_56387_SWB_F071	SWB	23-Aug-06 23:49:24
R156473066G3S007st	R1_56473_SWB_F066	SWB	30-Aug-06 00:14:03
R156530058G3S007	R1_56530_SWB_F058	SWB	02-Sep-06 23:56:22
R156530064G3S008	R1_56530_SWB_F064	SWB	02-Sep-06 23:57:02
R156530065G3S001	R1_56530_SWB_F065	SWB	02-Sep-06 23:57:09
R156551386G3S007	R1_56551_SWB_F386	SWB	04-Sep-06 11:49:12
R156551390G3S008	R1_56551_SWB_F390	SWB	04-Sep-06 11:49:40
R156573064G3S005	R1_56573_SWB_F064	SWB	06-Sep-06 00:09:38
R156594381G3S010	R1_56594_SWB_F381	SWB	07-Sep-06 12:01:14
R156616059G3S009	R1_56616_SWB_F059	SWB	09-Sep-06 00:21:40
R156616064G3S010	R1_56616_SWB_F064	SWB	09-Sep-06 00:22:14
R156651389G3S009	R1_56651_SWB_F389	SWB	11-Sep-06 11:45:21
R156730062G3S001	R1_56730_SWB_F062	SWB	16-Sep-06 23:49:41
R157059060G3S011	R1_57059_SWB_F060	SWB	10-Oct-06 00:17:34
R157059064G3S012	R1_57059_SWB_F064	SWB	10-Oct-06 00:18:00
R157073059G3S010	R1_57073_SWB_F059	SWB	10-Oct-06 23:48:04
R157073064G3S011	R1_57073_SWB_F064	SWB	10-Oct-06 23:48:37
R157216064G3S010	R1_57216_SWB_F064	SWB	20-Oct-06 23:57:01
R160410380G1S002	R1_60410_ST1_F380	ST1	01-Jun-07 12:13:57
R160410382G1S003	R1_60410_ST1_F382	ST1	01-Jun-07 12:14:10
R160410384G1S004	R1_60410_ST1_F384	ST1	01-Jun-07 12:14:24
R160446066G1S002	R1_60446_ST2_F066	ST2	04-Jun-07 00:06:00
R160446068G1S003	R1_60446_ST2_F068	ST2	04-Jun-07 00:06:13
R160446070G1S004	R1_60446_ST2_F070	ST2	04-Jun-07 00:06:27
R160446073G1S005	R1_60446_ST2_F073	ST2	04-Jun-07 00:06:47
R160460066G1S002	R1_60460_ST1_F066	ST1	04-Jun-07 23:36:38

R160467388G1S006	R1_60467_ST1_F388	ST1	05-Jun-07 11:58:05
R160546066G1S003	R1_60546_ST2_F066	ST2	11-Jun-07 00:01:49
R160546073G1S006	R1_60546_ST2_F073	ST2	11-Jun-07 00:02:37
R160567383G1S004	R1_60567_ST1_F383	ST1	12-Jun-07 11:53:20
R160689070G1S004	R1_60689_ST2_F070	ST2	21-Jun-07 00:10:41
R160703070G1S004	R1_60703_ST1_F070	ST1	21-Jun-07 23:41:19
R160703073G1S005	R1_60703_ST1_F073	ST1	21-Jun-07 23:41:39
R160710379G1S002	R1_60710_ST1_F379	ST1	22-Jun-07 12:01:17
R160710381G1S003	R1_60710_ST1_F381	ST1	22-Jun-07 12:01:31
R160710383G1S004	R1_60710_ST1_F383	ST1	22-Jun-07 12:01:44
R160753379G1S002	R1_60753_ST1_F379	ST1	25-Jun-07 12:13:53
R160789066G1S002	R1_60789_ST2_F066	ST2	28-Jun-07 00:06:01
R160789068G1S003	R1_60789_ST2_F068	ST2	28-Jun-07 00:06:15
R160789070G1S004	R1_60789_ST2_F070	ST2	28-Jun-07 00:06:28
R160803073G1S005	R1_60803_ST1_F073	ST1	28-Jun-07 23:37:26
R160810377G1S015	R1_60810_ST1_F377	ST1	29-Jun-07 11:56:51
R160810381G1S017	R1_60810_ST1_F381	ST1	29-Jun-07 11:57:18
R160810394G1S023	R1_60810_ST1_F394	ST1	29-Jun-07 11:58:46
R160846073G1S013	R1_60846_ST1_F073	ST1	01-Jul-07 23:50:01
R160853379G1S003	R1_60853_ST1_F379	ST1	02-Jul-07 12:09:39
R160853381G1S004	R1_60853_ST1_F381	ST1	02-Jul-07 12:09:53
R160853383G1S005	R1_60853_ST1_F383	ST1	02-Jul-07 12:10:07
R160889066G1S002	R1_60889_ST2_F066	ST2	05-Jul-07 00:01:48
R160889068G1S003	R1_60889_ST2_F068	ST2	05-Jul-07 00:02:01
R160896381G1S004	R1_60896_ST1_F381	ST1	05-Jul-07 12:22:28
R160896383G1S005	R1_60896_ST1_F383	ST1	05-Jul-07 12:22:41
R160910377G1S002	R1_60910_ST1_F377	ST1	06-Jul-07 11:52:37
R160910379G1S003	R1_60910_ST1_F379	ST1	06-Jul-07 11:52:51
R160953381G1S002	R1_60953_ST4_F381	ST4	09-Jul-07 12:05:43
R160953383G1S004	R1_60953_ST4_F383	ST4	09-Jul-07 12:05:57
R160953384G1S005	R1_60953_ST4_F384	ST4	09-Jul-07 12:06:04
R161110386G3S009	R1_61110_SWB_F386	SWB	20-Jul-07 11:44:46
R161410387G3S012	R1_61410_SWB_F387	SWB	10-Aug-07 11:32:18
R161439379G3S010	R1_61439_SWB_F379	SWB	12-Aug-07 12:13:23
R161439386G3S011	R1_61439_SWB_F386	SWB	12-Aug-07 12:14:10
R161782386G3S010	R1_61782_SWB_F386	SWB	05-Sep-07 12:14:10
R162768379G3S010	R1_62768_SWB_F379	SWB	13-Nov-07 12:00:46
R162768386G3S012	R1_62768_SWB_F386	SWB	13-Nov-07 12:01:33

APPENDIX III:
PRELIMINARY REPORT ON PERSISTENT OIL SEEP AND GAS HYDRATES IN THE BLACK SEA

Preliminary Results of the Black Sea SAR Project

Report prepared by Jan-Hendrik Körber
MARUM, University of Bremen, Germany
jkoerber@marum.de

In advance to the MSM 15/2 cruise to Ukrainian and Georgian parts of the Black Sea in May 2010 approximately 120 ENVISAT *Advanced Synthetic Aperture* (ASAR) *Image Mode Precision images* (IM_P) with a resolution of about 30 m were analyses in order to identify sites where natural oil seepage occurs. All images were loaded to a geographic information system and analysed manually. The origins of potential natural oil slick origins (OSOs) were marked in an image specific point shape file. All resulting point shape files were overlaid to identify OSO cluster. The cluster identification was done manually, since we struggled to get as nice results as you achieve applying the dendrogram and cluster analysis. In the Ukrainian parts of the Black Sea many *potential* OSOs were identified upon first image analyses, however no site showing persistent slicks could be identified. Also, no evidence for oil seepage in Ukrainian waters was found during the cruise, though many sites of gas seepage have been found and were known before. The situation is different for Georgia. The analysis of 40 ASAR IM_P scenes in the study area yielded clear evidence for oil seepage between 2003 and 2010 (the years images were available for). In the following a number of figures illustrating preliminary results of the image analyses, cruise MSM15/2 and archived data from the cruises M72/3 in 2007(Bohrmann et al. 2008) and TTR15 (IOC Technical Series No. 72*)* in 2005 are shown. The image analyses allowed identifyingg 8 sites where natural oil seepage occurs (Fig. 1). The most pronounced oil slicks and the highest persistency of oil slicks were found above two structures named Colkheti Seep and Pechori Mound, followed by site G1. Sites G2 to G6 do not show oil slicks on most of the analysed images, but the occurrence of seepage seems very likely. Tab. 1 gives an overview of how many images covering the different sites were available and how many of them showed oil slicks. Plate 1.1 and 1.2 present sub-scenes of ASAR images showing oil slicks at the different sites. The most prominent sites are Colkheti Seep and Pechori Mound which are shown in detail in Fig. 2, 3 and 4.

These sites have been known from previous cruises. Oil seepage has been observed at Colkheti Seep during one ROV dive in 2007 and the presence of oil in the shallow sediments was proven by gravity coring in 2005, 2007 and 2010. From cruise M72/3 (2007) hydroacoustic data acquired with the PARASOUND echosounder is available and a number of acoustic anomalies were detected. This *anomalies* do not appear as clear ‘flares’ but are rather blurred or undefined features and might thus not be useful to pinpoint locations of gas emanation. However, they are plotted in all following figures. Beside these sites, four distinct flares at Colkheti Seep and two at Pechori Mound were also found. Their locations are indicated on all maps as well. Plate 2a) to c) shows sample echograms of these flares. The location where oil and gas seepage was documented during a ROV dive in 2007 is also indicated on Fig. 2 and 3. During MSM15/2 cruise last year surfacing oily bubbles were observed (see Plate 3a) and b)). This location is marked in the figures, too. The bathymetry of Pechori Mound and surrounding areas was recorded with ship mounted MBES and processed to a 10 m resolution. The bathymetry of Colkheti Seep is based on an AUV survey in 2010, has a resolution of 1 m and shows the local morphology very detailed. As ancillary data Fig. 6 and 7 show details of two sidescan sonar lines acquired with the MAK system during TTR-15 cruise with RV Prof. Logachev. However, the sidescan records do not allow clearly identifying different sediment properties or small scale morphological features of the seep sites as most of the differences in backscatter intensity seem to originate from the main morphological structures. The site which follows Pechori and Colkheti in seepage intensity and persistency is G1 (see Fig. 1). This site was crossed by one PARASOUND line during the cruise in 2010 and a clear gas flare was found right at the location of the OSO cluster centre. An echogram of this flare is shown in Plate 2d). However, no further data is available for this location and neither for the sites G3 to G6.

Plate 3 shows again some images which confirm seepage at Colkheti seep. 3e) and g) give an impression how the seafloor and the crater structures in the bathymetry (Fig. 3) look like. The last Fig. 8 illustrates the

location of shale diapirs (originating from the Miocene Maikop formation (?)) which might create pathways and traps for the oil which is seeping out at the identified locations. The information on location and extent of these diapiric structures is taken from a map published by Tugolesov et al. (1985).

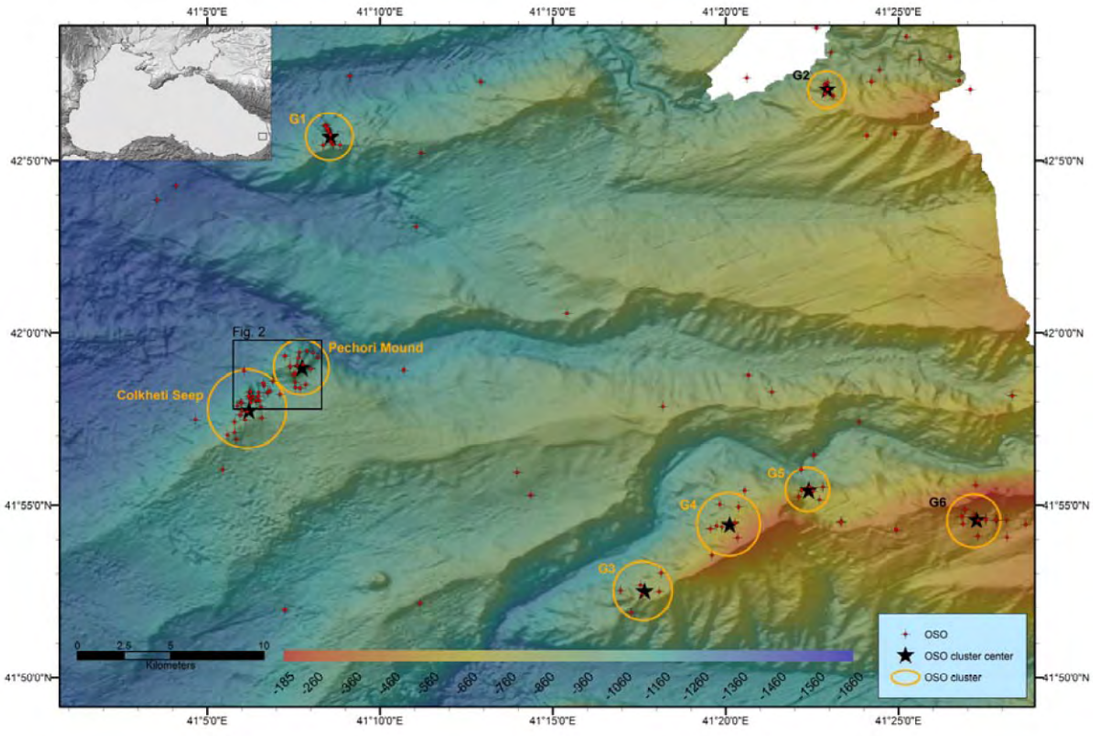

Figure 1. Shaded bathymetry of the study area offshore Georgia. Cluster of origins of natural oil slicks (OSOs) are indicated by circles, their spatial centres by stars. Individual OSOs are marked by crosses. The inset shows the location of the study area in the Black Sea.

Table. 1 Number of images covering the individual oil seep sites indicated in Fig. 1 and the number of images showing evidence of active oil seepage.

Site name	No. images covering site	No. images showing activity
Colkheti Seep & Pechori Mound	13	12
G1	12	9
G2	17	8
G3	17	8
G4	17	8
G5	17	12
G6	17	9

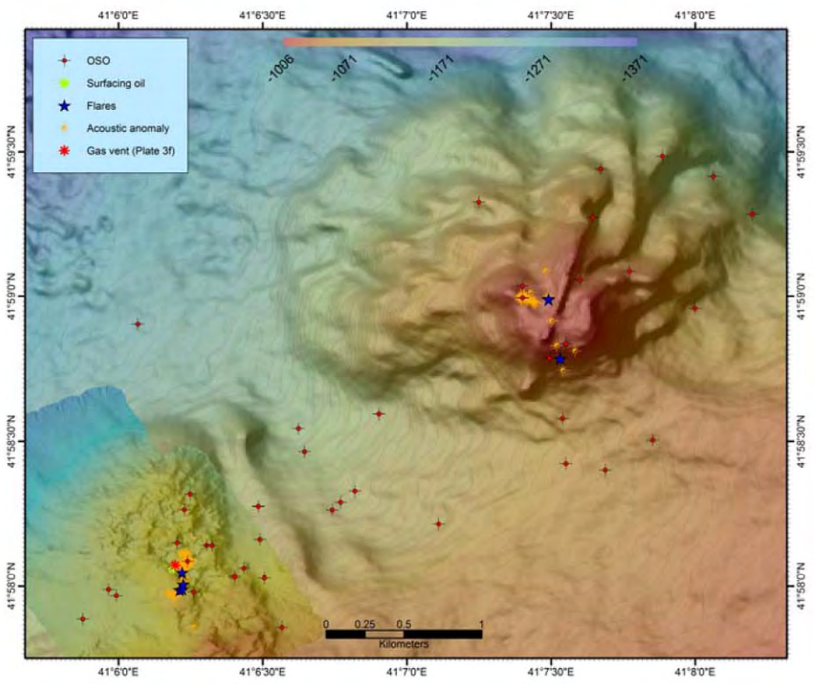

Fig. 2. Shaded bathymetry of Pechori Mound (upper right structure) and Colkheti Seep (lower left) (for location compare Fig. 1) with 5 m contour lines. Locations of acoustic anomalies and district gas flares detected with the PARASOUND echosounder are indicated as well as the location of one gas vent which was investigated during a ROV dive. Origins of sea surface oil slicks and the location of a site where surfacing oil bubbles were observed are shown.

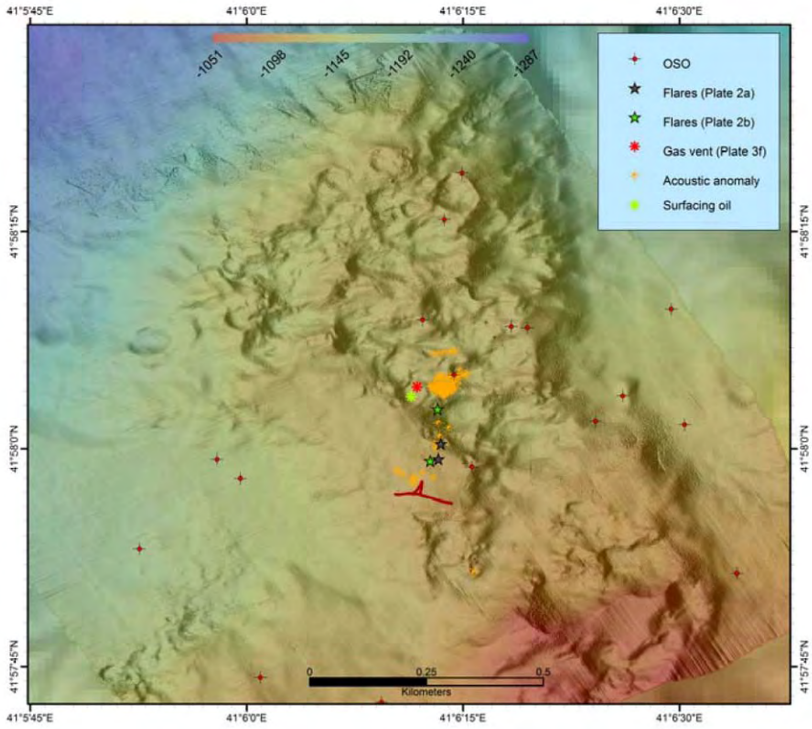

Fig 3. Shaded AUV bathymetry of the Colkheti Seep (1 m resolution) with 5 m contour lines showing the rough topography of the seep site. Acoustic anomalies in the water column detected by the PARASOUND echosounder are indicated. The red star shows a bubble stream found during a ROV dive (red and black line). Next to it the green star indicated the location of surfacing bubbles observed on the sea surface 3 years later.

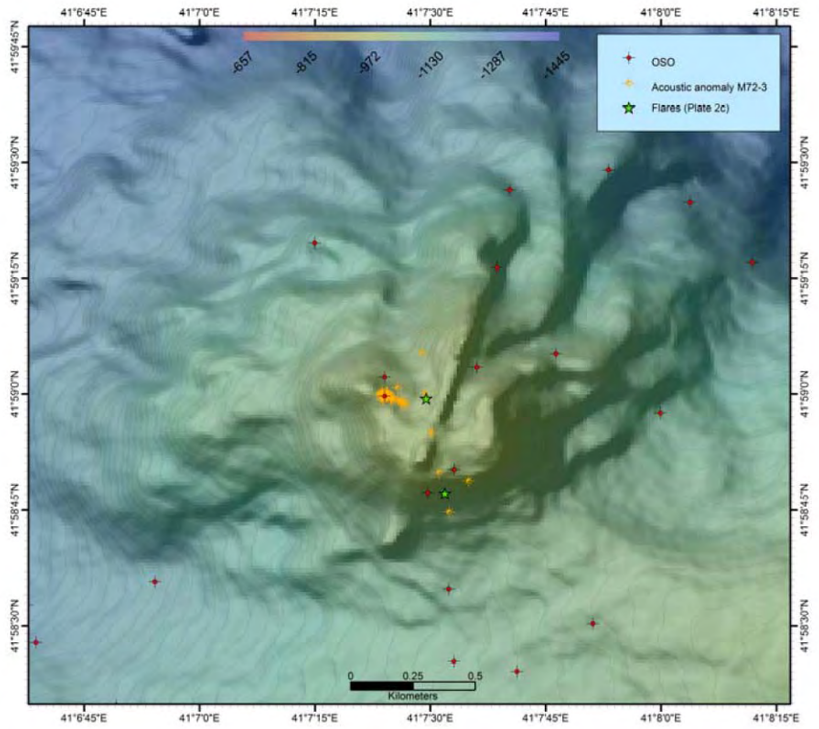

Fig 4. Shaded bathymetry with 5 m contour lines of Pechori Mound. Locations of acoustic anomalies and distinct flares in the water column detected by the PARASOUND echosounder are indicated.

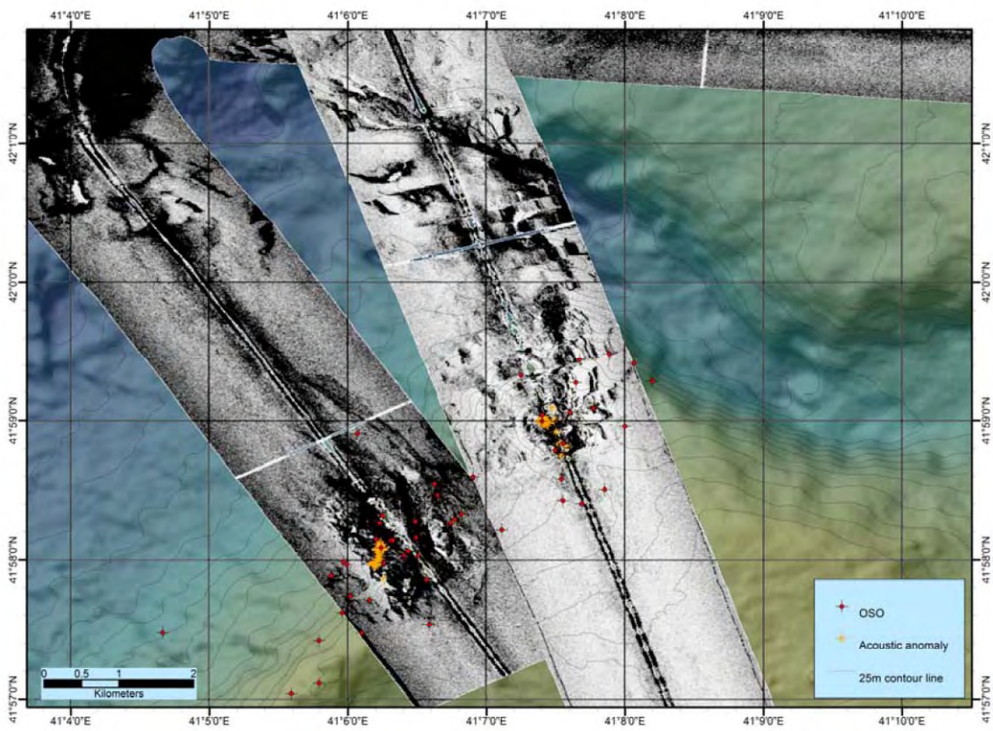

Fig 5. MAK sidescan sonar mosaic covering Colkheti Seep, Pechori Mound and the surrounding areas. OSOs and acoustic anomalies hinting to gas bubble release are shown (compare Fig. 3 and 4).

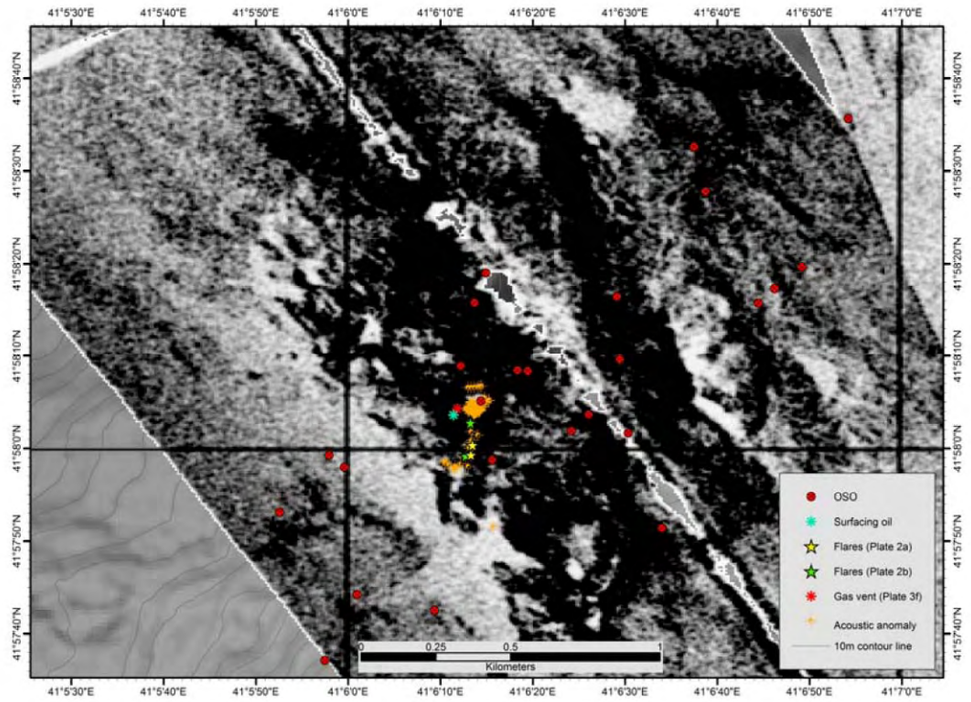

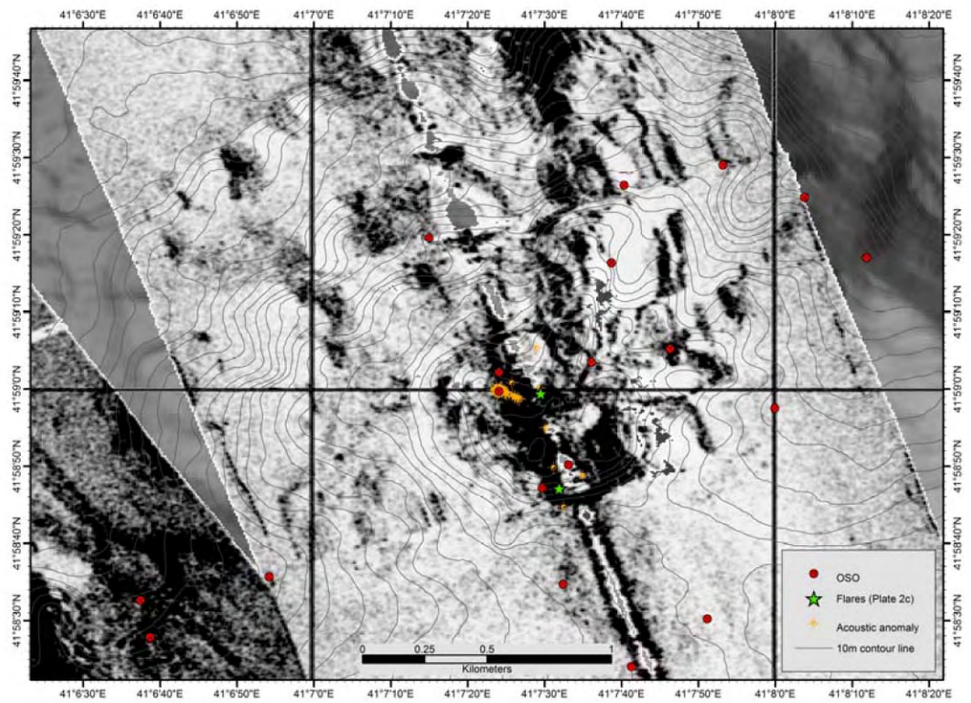

Fig 6. Detail of MAK sidescan sonar mosaic covering Colkheti Seep

Fig 7. Detail of MAK sidescan sonar mosaic covering Pechori Mound.

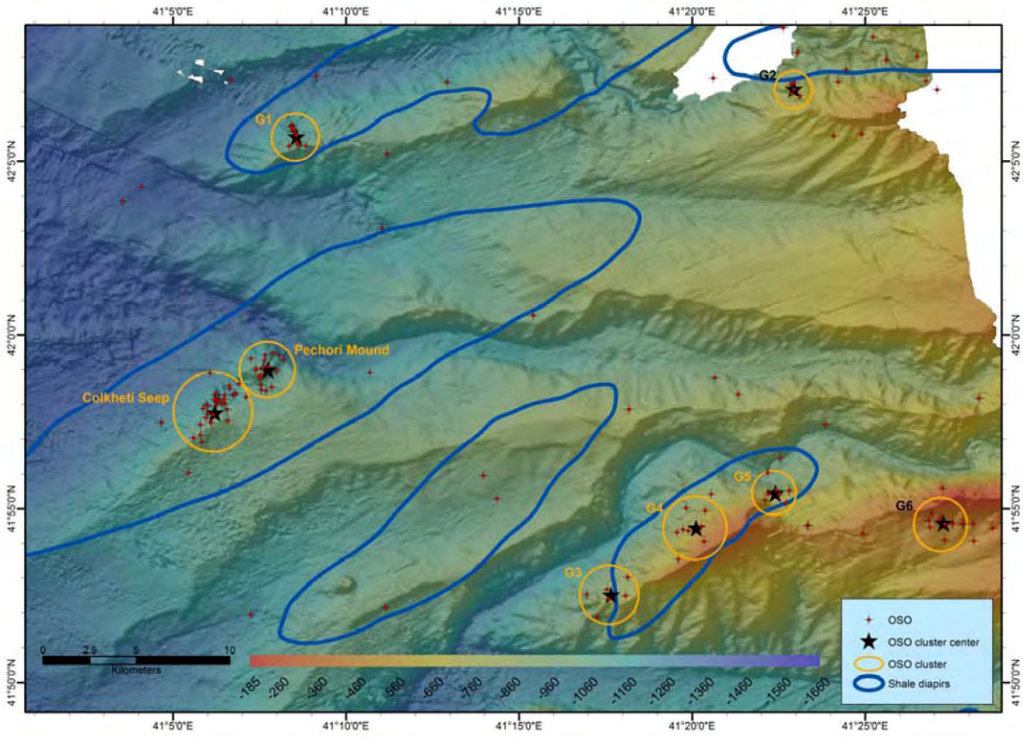

Fig 8. Overview map of the study area and oil seepage sites. The blue lines indicate the location of shale diapirs which might create pathways and traps for higher hydrocarbons originating from the Maikopian formation (location and shape of the diapiric structures from Tugolesov et al. 1985).

Plate 1.1. All images show sub-scenes of ENVISAT ASAR IMP images. Images a) to d) show oil slicks at Colkheti Seep and Pechori Mound. Images were acquired on 15 Sep 2003, 29 Dec 2003, 07 Feb 2007 and 14 May 2009. Images e) to h) show oil slicks at site G1 on 15 Sep 2003, 02 Jun 2004, 01 Aug 2007 and 14 May 2009. Note different scales of the sub-scenes. For location of the sites see Fig. 1. All images provided by the *European Space Agency*.

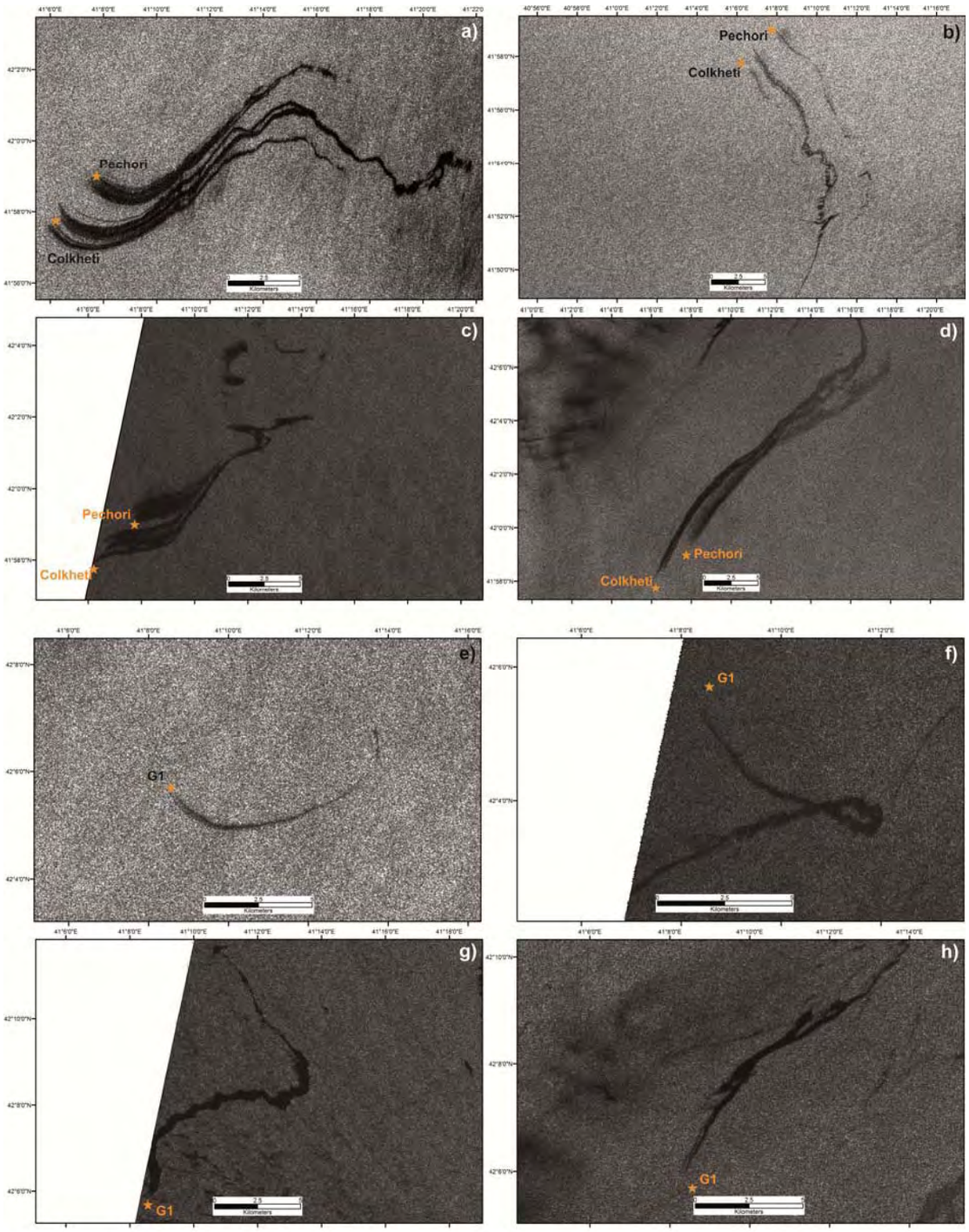

Plate 1.1. All images show sub-scenes of ENVISAT ASAR IMP images. Images a) to d) show oil slicks at Colkheti Seep and Pechori Mound. Images were acquired on 15 Sep 2003, 29 Dec 2003, 07 Feb 2007 and 14 May 2009. Images e) to h) show oil slicks at site G1 on 15 Sep 2003, 02 Jun 2004, 01 Aug 2007 and 14 May 2009. Note different scales of the sub-scenes. For location of the sites see Fig. 1. All images provided by the *European Space Agency*.

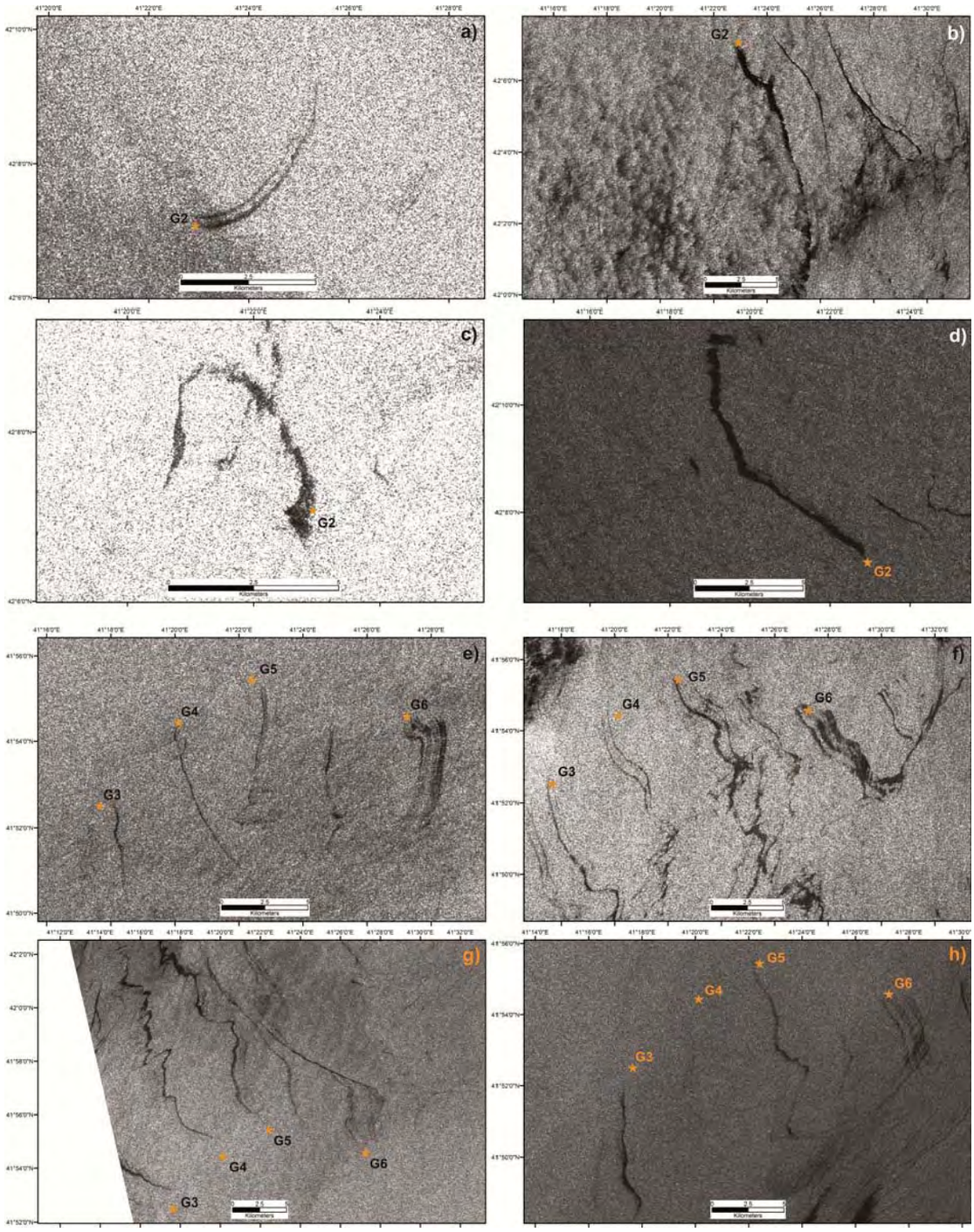

Plate 1.2. All images show sub-scenes of ENVISAT ASAR IMP images. Images a) to d) show oil slicks at site G2. Images were acquired on 15 Sep 2003, 29 Jul 2004, 31 Jul 2006 and 01 Aug 2007. Images e) to h) show oil slicks at sites G3 to G6 on 29 Dec 2003, 29 Jul 2004, 12 Oct 2006 and 08 Apr 2008. Note different scales of the sub-scenes. For location of the sites see Fig. 1. All images provided by the *European Space Agency*.

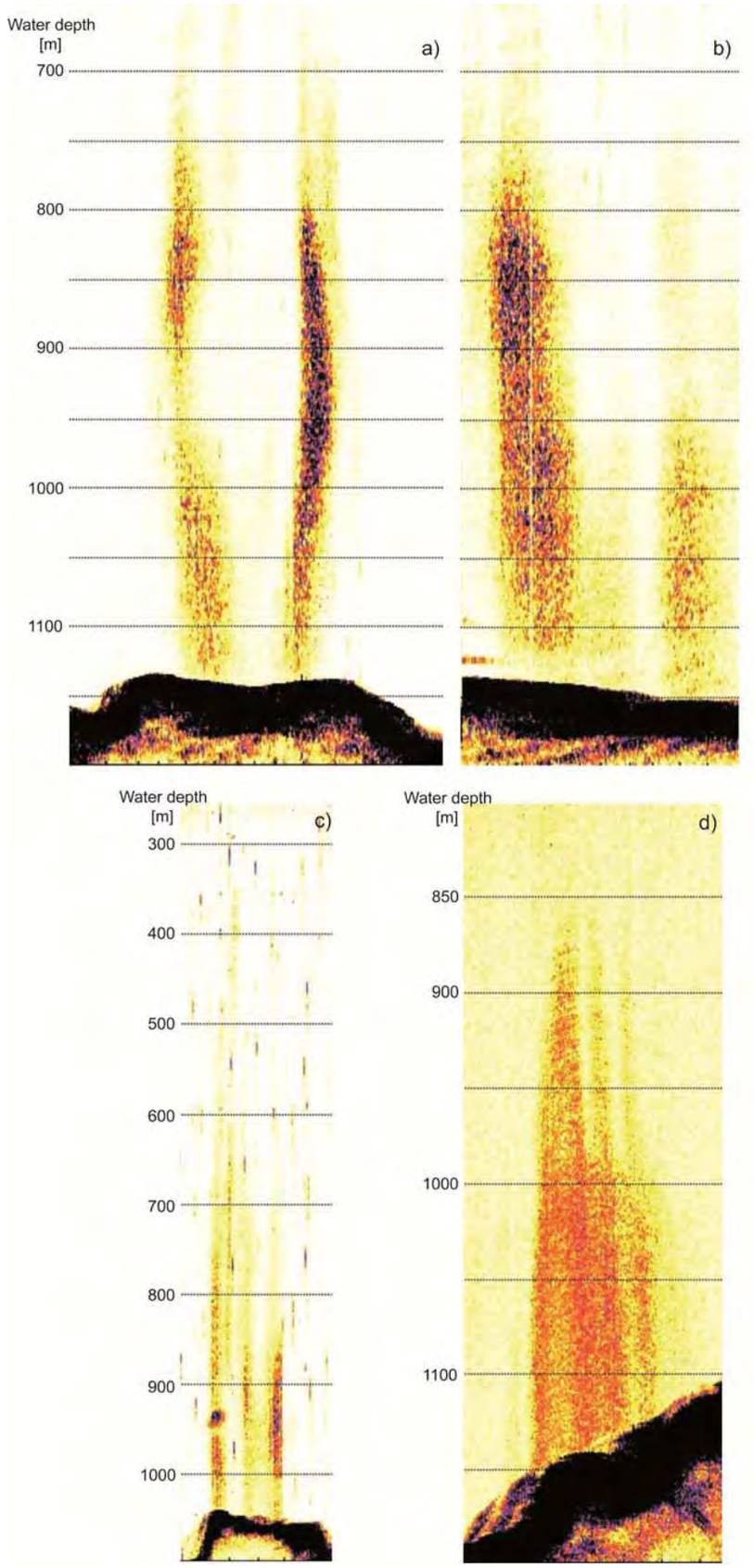

Plate 2. PARASOUND echograms showing acoustic anomalies (‘flares’) originating from rising gas bubbles or oil coated gas bubbles. Echograms a) and b) show two flares at the Colkheti seep (locations indicated in Fig. 2). Echogram c) shows flares emanating from Pechori Mound (locations indicated in Fig. 2). d) Depicts gas emissions at the G1 site (see Fig. 1).

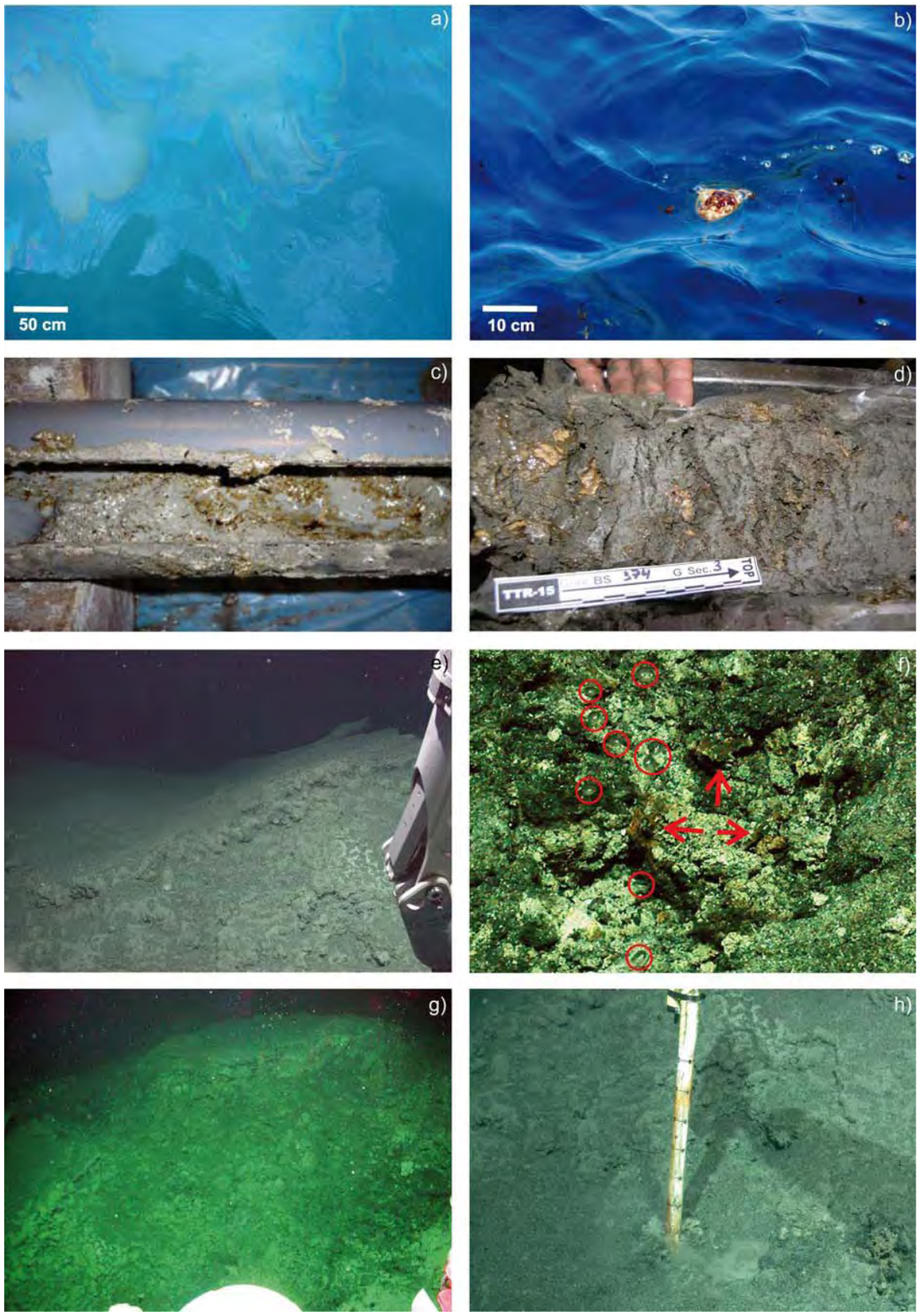

Plate 3. a) Thin (sub millimetre) film originating from oily bubbles reaching the sea surface above Colkheti Seep on May 26th 2010; location indicated on Fig. 2. b) Thick oil patch and 'lints' of oil; locations as in a). Image c) shows a section of a core liner from a Dynamic Autoclave Piston Corer, recovered at Colkheti seep. The brownish traces are an oil-water mix. d) Section o a gravity core recovered at Colkheti seep, showing oily sediments and gas hydrate flakes. e) Image taken by ROV QUEST 4000 next to a bubble emission site at Colkheti seep in 2007 (location indicated in Fig. 2); the image gives an impression on the rough morphology/ crater structures which can be identified on the AUV bathmetry in Fig. 3. f) Shows a close up of bubbles (red circles) and oily sediments (red arrows) at the vent location (e), Fig. 2 & 3). Image g) was taken at the same location as e) but towards the

bubble stream. h) A temperature lance deployed by the ROV next to the gas vent is covered by oil after recovery.

References:

Bohrmann G., T. Pape, and cruise participants (2007) Report and preliminary results of R/V METEOR Cruise M72/3, Istanbul – Trabzon – Istanbul, 17 March – 23 April, 2007. Marine gas hydrates of the Eastern Black Sea. Berichte, Fachbereich Geowissenschaften, Universität Bremen, No. 261, 176 pages. Bremen, 2007.

Deep-water cold seeps, sedimentary environments and ecosystems of the Black and Tyrrhenian Seas and Gulf of Cadiz. *IOC Technical Series No. 72, UNESCO, 2007 (English)*

Tugolesov, D.A., Gorshkov, A.S., Meisner, L.B., Soloviev, V.V., 1985.Tectonics of the Mesozoic–Cenozoic Deposits of the Black Sea Basin. Nedra, Moscow. 215 pp. (in Russian).

APPENDIX IV:
ANALYTICAL RESULTS OF WATER COLUMN SAMPLES

Analytical results of water column samples

Gulf of Mexico HyFlux Methane Concentration as of 11-25-2011

CTDs

CTD C

Bottle	Depth (m)	Methane (nM)	Ethane (nM)	Propane (nM)	Butane (nM)
1	891	6.0			
2	883	5.4		0.25	
3	800	10.52			0.18
4	788	6.1			
5	699	5.9			
6	689	3.35			
7	601	6.65	4.61		
8	589	3.4			
10	421	4.81			
11	400	1.6			
12	350	7.97			
13	340	1.88			
14	308	6.68			
15	301	3.50			
17	211	2.1			
19	98	11.01			
20	45	25.5			
21	35	23.22			

CTD B - measured Shipboard

Bottle	Depth (m)	Methane (nM)	Ethane (nM)	Propane (nM)	Butane (nM)
1	873	2.0			
2	685	2.5			
3	600	2.6			
4	300	2.6			
5	100	11.7			
6	5.9	5.8			
13	887	5.9			
14	850	4.9			
15	800	1.9			
16	700	29.2			
17	600	2.5			
18	499.3	3.0			
19	400	1.8			

Analytical results of water column samples

20	300.7	2.4
21	200.8	13.6
22	100	19.3
23	51.2	9.7
24	14.6	11.8

CTD D - measured Shipboard

Bottle	Depth (m)	Methane (nM)	Ethane (nM)	Propane (nM)	Butane (nM)
1	920	1.3			
2	910	1.0			
3	871	2.0			

CTD Over Rudyville - measured Shipboard

Bottle	Depth (m)	Methane (nM)	Ethane (nM)	Propane (nM)	Butane (nM)
1	883	2.8			
2	880	2.6			
3	860	76.5			
4	840	3.5			
5	820	4.5			
6	800	3.2			
9	700	2.5			
10	600	4.1			
11	500	4.6			
12	400	2.1			
13	300	2.2			
14	200	4.3			
15	150	11.4			
17	127	5.5			
18	102	10.4			
19	50	11.4			
20	23	17.9			
21	6.3	16.0			

CTD Seep C - measured Shipboard

Bottle	Depth (m)	Methane (nM)	Ethane (nM)	Propane (nM)	Butane (nM)
1	887	44.8			
2	850	11.0			
3	600.4	2.1			
4	500	1.9			

Analytical results of water column samples

5	400	2.2
6	300.3	3.7
7	200.4	2.5
8	100.9	14.2
9	49.6	16.6
10	15	11.5
11	10	9.9
12	5	11.8

CTD Background - measured Shipboard

Bottle	Depth (m)	Methane (nM)	Ethane (nM)	Propane (nM)	Butane (nM)
	1110	7.1			
	1000.2	8.2			
	900.4	4.2			
	800.7	3.6			
	650.7	4.9			
	501.4	5.2			
	400.3	3.3			
	250.8	4.2			
	50.6	22.5			
	24	11.7			
	5.5	11.8			

CTD AA

Bottle	Depth (m)	Methane (nM)	Ethane (nM)	Propane (nM)	Butane (nM)
1	100.1	16.93			
2	59.7	21.26			
3	30.5	16.54			
4	15	17.60			

CTD BB

Bottle	Depth (m)	Methane (nM)	Ethane (nM)	Propane (nM)	Butane (nM)
1	99.8	19.13			
2	59.7	17.49		0.28	
3	30.3	17.25	0.46	0.64	0.19
4	15	17.60	2.72		

Analytical results of water column samples

CTD CC

Bottle	Depth (m)	Methane (nM)	Ethane (nM)	Propane (nM)	Butane (nM)
1		5.53	0.51	1.70	0.84
2		4.53	0.43	0.14	0.00
3	800.5	10.56	0.00	0.55	0.12
4	790.4	6.76			
5		2.02	0.65		
6	691	3.86			
7		BDL			
8	590.9	10.85			
9		1.37			
10	401.1	6.64			
11		1.30			
12		Not Sampled			
13	309.9	11.04			
14	300.9	10.16			
15		1.58			0.24
16	200.8	5.68			
17		Not Sampled			
18		13.33	0.29		0.54
19	25.9	16.88			
20		11.20	0.14		0.48
21		6.42	0.14		0.42

CTD F

Bottle	Depth (m)	Methane (nM)	Ethane (nM)	Propane (nM)	Butane (nM)
1	100	10.35			
2	59.9	14.75			
3	29.2	6.72			
4	15	9.57			

CTD G

Bottle	Depth (m)	Methane (nM)	Ethane (nM)	Propane (nM)	Butane (nM)
1	100	10.72			
2	60	15.38			
3	29.5	7.92			
4	15.2	13.06			

Analytical results of water column samples

CTD H

Bottle	Depth (m)	Methane (nM)	Ethane (nM)	Propane (nM)	Butane (nM)
1	99.8	14.18			
2	60.4	17.20			
3	29	4.15			
4	15.3	15.10			

CTD I

Bottle	Depth (m)	Methane (nM)	Ethane (nM)	Propane (nM)	Butane (nM)
1	100.7	11.37			
2	56.9	15.60			
3	30.7	13.22			
4	15.2	15.52			

CTD J

Bottle	Depth (m)	Methane (nM)	Ethane (nM)	Propane (nM)	Butane (nM)
1	100.7	20.11			
2	60.4	16.23			
3	30.7	9.69			2.75
4	14.6	13.94			

CTD K

Bottle	Depth (m)	Methane (nM)	Ethane (nM)	Propane (nM)	Butane (nM)
1	100.6	16.12			
2	59.5	10.27			
3	30	4.16			
4	15.1	11.15	4.01	5.16	

CTD L

Bottle	Depth (m)	Methane (nM)	Ethane (nM)	Propane (nM)	Butane (nM)
1	100.4	17.52			
2	60	15.62			
3	30	3.88			
4	15.2	12.15			

CTD M

Analytical results of water column samples

Bottle	Depth (m)	Methane (nM)	Ethane (nM)	Propane (nM)	Butane (nM)
1	100	20.26			
2	60.7	17.81			
3	30	8.72			
4	15.6	12.27			

CTD N

Bottle	Depth (m)	Methane (nM)	Ethane (nM)	Propane (nM)	Butane (nM)
1	100	17.38			
2	60	20.52			
3	30	12.54			
4	15	12.32			

CTD O

Bottle	Depth (m)	Methane (nM)	Ethane (nM)	Propane (nM)	Butane (nM)
1	100	19.20			
2	60	17.65			
3	30	12.47			
4	15	12.47			

CTD P

Bottle	Depth (m)	Methane (nM)	Ethane (nM)	Propane (nM)	Butane (nM)
1	100	13.35			
2	60	11.02			
3	30	12.30			
4	13.5	11.05			

CTD Q

Bottle	Depth (m)	Methane (nM)	Ethane (nM)	Propane (nM)	Butane (nM)
1	100	10.21			
2	60	11.44			
3	30	10.76			
4	15	9.15			

CTD R

Bottle	Depth (m)	Methane (nM)	Ethane (nM)	Propane (nM)	Butane (nM)

Analytical results of water column samples

1	100	13.30			
2	60	10.97			
3	30	8.94			
4	15	9.77			

CTD S

Bottle	Depth (m)	Methane (nM)	Ethane (nM)	Propane (nM)	Butane (nM)
1	100	11.64			
2	60	13.14			
3	34.5	13.25			
4	15.3	15.13			

CTD T

Bottle	Depth (m)	Methane (nM)	Ethane (nM)	Propane (nM)	Butane (nM)
1	100	16.18			
2	60.1	20.34		0.10	
3	30.6	17.58			
4	14.6	13.45			

CTD U

Bottle	Depth (m)	Methane (nM)	Ethane (nM)	Propane (nM)	Butane (nM)
1	100.8	16.48			
2	60	13.24			
3	31.3	12.78			
4	15	8.83			

CTD V

Bottle	Depth (m)	Methane (nM)	Ethane (nM)	Propane (nM)	Butane (nM)
1	100	20.01			
2	59.5	16.28			
3	30.4	15.77			
4	15	10.59			

CTD W

Bottle	Depth (m)	Methane (nM)	Ethane (nM)	Propane (nM)	Butane (nM)
1	99.8	27.10			

Analytical results of water column samples

2	60	17.63			
3	31.1	13.52			
4	14.3	9.01			

CTD X

Bottle	Depth (m)	Methane (nM)	Ethane (nM)	Propane (nM)	Butane (nM)
1	100.7	19.14			
2	60.5	18.01			
3	28.5	15.78			
4	14.7	15.08			

CTD Y

Bottle	Depth (m)	Methane (nM)	Ethane (nM)	Propane (nM)	Butane (nM)
1	101.5	20.62			
2	59.9	18.38			
3	30.1	17.77			
4	13.9	13.07	3.59		

CTD Z

Bottle	Depth (m)	Methane (nM)	Ethane (nM)	Propane (nM)	Butane (nM)
1	99.6	14.30			0.25
2	60.3	26.66		0.262927846	
3	29.4	12.30		0.26	

APPENDIX V:
ANALYTICAL RESULTS OF AIR-SEA CONTINUOUS SAMPLING

Analytical results of air-sea continuous sampling

YD	Lat	Long	Air_ppm	SW_nM	fluxS07 (umol_m^{-2}_d^{-1})	SA (%)
197.9281	27.78238	-91.508	1.97	2.72	2.37	45.8
197.9549	27.78285	-91.5087	1.98	2.3	1.17	22.8
197.9813	27.78264	-91.5084	1.98	2.59	1.95	38.2
198.008	27.78211	-91.508	1.84	1.84	0.23	5.0
198.0344	27.78212	-91.508	1.89	2.92	2.76	62.6
198.0524	27.78213	-91.5081	1.83	1.88	0.32	7.7
198.0701	27.78165	-91.5082	1.77	2.57	2.06	52.1
198.0878	27.78276	-91.5079	1.84	2	0.58	14.5
198.1059	27.78296	-91.508	1.84	2.52	1.73	43.9
198.1236	27.78216	-91.5082	1.77	2.55	1.91	51.5
198.1323	27.78219	-91.5083	1.77	2.09	0.9	24.5
198.1503	27.78225	-91.5083	1.81	2.73	2.2	59.0
198.1771	27.78232	-91.5084	1.71	2.06	0.93	26.5
198.1858	27.78231	-91.5084	1.71	2.32	1.48	42.6
198.2219	27.78233	-91.5085	1.75	3.06	2.95	84.3
198.2306	27.78234	-91.5085	1.78	1.88	0.41	11.7
198.2483	27.78232	-91.5083	1.79	1.78	0.17	4.8
198.2573	27.78228	-91.5082	1.85	2.93	2.33	66.4
198.2753	27.78234	-91.5082	1.81	1.77	0.08	2.3
198.284	27.78235	-91.5082	1.79	3.3	3.09	93.9
198.3017	27.78877	-91.5199	1.72	1.89	0.48	15.6
198.3288	27.7939	-91.5025	1.83	1.86	0.21	6.5
198.3552	27.78931	-91.5064	1.8	2.78	1.89	62.0
198.3733	27.78647	-91.524	1.81	2.08	0.61	20.4
198.3823	27.78468	-91.5154	1.84	1.94	0.32	10.7
198.391	27.78476	-91.5048	1.78	1.76	0.11	3.9
198.3997	27.78334	-91.4938	1.78	2.27	0.99	34.7
198.4177	27.77999	-91.5038	1.83	2.35	0.97	34.2
198.4267	27.77996	-91.5142	1.92	2.55	1.13	38.8
198.4444	27.77571	-91.5191	1.77	3.03	2.06	79.0
198.4622	27.77556	-91.4986	1.83	2.54	1.17	45.1
198.4712	27.7733	-91.493	1.86	2.65	1.27	48.5
198.4979	27.77096	-91.52	1.8	3.3	2.26	91.5
198.5337	27.78679	-91.5045	1.79	3.5	2.43	104.4
198.5691	27.7821	-91.5134	1.92	2.43	0.86	33.3
198.5781	27.78294	-91.5095	1.83	1.79	0.07	3.0
198.5872	27.77968	-91.498	1.77	1.83	0.21	8.5
198.6135	27.78668	-91.5139	1.82	2.06	0.49	19.2
198.6316	27.7956	-91.5224	1.77	3	1.97	78.2
198.6497	27.79573	-91.5215	1.74	3.29	2.49	99.3
198.6851	27.79283	-91.5199	1.9	2.85	1.56	57.9
198.7031	27.77901	-91.5208	1.77	2.24	0.83	33.4
198.7118	27.77797	-91.5159	1.76	2.53	1.26	51.7
198.7205	27.77741	-91.504	1.76	2.13	0.66	27.7

Analytical results of air-sea continuous sampling

198.7295	27.777	-91.4949	1.84	2.3	0.77	31.9
198.7476	27.77676	-91.4944	1.83	3.05	1.76	75.1
198.7653	27.77677	-91.4949	1.96	2.04	0.23	9.4
198.783	27.77652	-91.4951	1.84	4.48	3.6	155.8
198.792	27.7765	-91.4951	1.72	2.63	1.32	60.7
198.8101	27.77651	-91.4947	1.81	2.43	0.94	41.4
198.8274	27.77648	-91.4936	1.91	1.91	0.13	5.6
198.8365	27.77624	-91.4938	1.82	1.9	0.22	10.2
198.8635	27.78074	-91.5045	1.83	2.71	1.13	56.5
198.8722	27.78105	-91.5079	1.78	2.18	0.55	29.8
198.9424	27.78227	-91.5076	1.71	2.19	0.58	35.4
199.0038	27.78233	-91.5075	1.74	2.93	1.27	76.7
199.0219	27.77335	-91.5024	1.83	2.49	0.74	41.9
199.0399	27.77799	-91.5059	1.81	2.25	0.53	29.6
199.0663	27.78061	-91.508	1.81	2.37	0.66	36.8
199.0844	27.78197	-91.508	1.84	2.07	0.32	17.5
199.0934	27.78234	-91.508	1.9	2	0.19	10.1
199.1021	27.78255	-91.5078	1.9	2.36	0.56	30.1
199.1378	27.78212	-91.5081	1.73	1.72	0.07	4.5
199.1469	27.78212	-91.5081	1.93	2.26	0.43	23.0
199.1556	27.78229	-91.5081	1.78	2.17	0.48	28.2
199.1642	27.78239	-91.5079	1.78	2.79	1.09	64.3
199.1823	27.7818	-91.5078	1.77	2.93	1.23	73.9
199.2003	27.78065	-91.5084	1.83	1.94	0.2	11.6
199.209	27.77962	-91.5089	1.73	2.39	0.74	45.5
199.2267	27.78112	-91.5131	1.8	1.94	0.23	13.5
199.2358	27.78352	-91.5241	1.74	2.02	0.37	22.1
		Min	1.71	1.72	0.07	2.3
		Mean	1.81	2.41	1.07	39.6
		Max	1.98	4.48	3.60	155.8

National Energy Technology Laboratory

626 Cochrans Mill Road
P.O. Box 10940
Pittsburgh, PA 15236-0940

3610 Collins Ferry Road
P.O. Box 880
Morgantown, WV 26507-0880

One West Third Street, Suite 1400
Tulsa, OK 74103-3519

1450 Queen Avenue SW
Albany, OR 97321-2198

2175 University Ave. South
Suite 201
Fairbanks, AK 99709

Visit the NETL website at:
www.netl.doe.gov

Customer Service:
1-800-553-7681